Dissertation zur Erlangung des Doktorgrades der Fakultät für Chemie und Pharmazie der Ludwig-Maximilians-Universität München

Two-Dimensional Hybrid Double Perovskites and Inspired Materials for Optoelectronic Applications

Rik Hendrik-Max Hooijer

aus

Heppenheim, Deutschland

2024

Erklärung

Diese Dissertation wurde im Sinne von § 7 der Promotionsordnung vom 28. November 2011 von Herrn Prof. Dr. Thomas Bein betreut.

Eidesstattliche Versicherung

Diese Dissertation wurde eigenständig und ohne unerlaubte Hilfe erarbeitet.

München, den 25.05.2024

Rik Hendrik-Max Hooijer

Dissertation eingereicht am: 05.06.24

Erstgutachter: Prof. Dr. Thomas Bein

Zweitgutachter: Prof. Dr. Achim Hartschuh

Mündliche Prüfung am: 11.07.24

'Über Halbleiter soll man nicht arbeiten, das ist eine Schweinerei; wer weiss, ob es überhaupt Halbleiter gibt.'

Wolfgang Pauli - Letter to Rudolf Peierls, 29 September 1931.[1]

[1] In *Wolfgang Pauli: Wissenschaftlicher Briefwechsel mit Bohr, Einstein, Heisenberg u.a. Band II: 1930–1939*, (Ed.: K. v. Meyenn), Springer Berlin Heidelberg, Berlin, Heidelberg, **1985**, pp. 49–104.

List of Abbreviations

E	energy
E_F	Fermi level
E_g	band gap
FF	fill factor
I	current
IV	current-voltage
I_D	diode current
I_S	reverse saturation current
J	current density
JV	current density-voltage
J_{sc}	short-circuit current density
P_{max}	maximum power point
QE	quantum efficiency
T	temperature
V_D	diode voltage
V_T	thermal voltage
V_{oc}	open-circuit voltage
α_c	critical angle
α_i	incidence angle
η	efficiency
λ	wavelength
ψ	wavefunction
σ	electrical conductivity
c	speed of light
h	Planck constant
k	wavevector
k_b	Boltzmann constant
q	scattering vector

v	frequency
NA	numerical aperture
2D	two-dimensional
3D	three-dimensional
AFM	atomic force microscopy
AM0	air mass 0 spectrum
AM1.5	air mass 1.5 spectrum
BA	butylammonium
BPhMA	biphenylmethylammonium
BSE	backscattered electron
BThMA	bithiophenemethylammonium
cAFM	conductive atomic force microscopy
CASI	$Cu_xAg_{1-x}SbI_4$
CB	conduction band
CBM	conduction band minimum
CBS	circular backscatter detector
CCD	charge-coupled device
CSD	Cambridge structural database
DFE	defect formation energie
DFT	density functional theory
DJ	Dion-Jacobson
DMF	dimethylformamide
DMSO	dimethylsulfoxide
DOS	density of states
EDTA	ethylenediaminetetraacetic acid
EDX	energy-dispersive X-ray spectroscopy
EQE	external quantum efficiency
ETM	electron transporting material
FA	formamidinium
FLIM	fluorescence-lifetime imaging microscopy
FTO	fluorine doped SnO_2
HOMO	highest occupied molecular orbital
HTM	hole transporting material
ICSD	inorganic crystal structure database
IPA	isopropylalcohol/2-propanol
LED	light-emitting diode

LUMO	lowest unoccupied molecular orbital
MA	methylammonium
n-i-p	negative-intrinsic-positive diode
OPTP	optical-pump terahertz-probe spectroscopy
p-i-n	positive-intrinsic-negative diode
p-n	positive-negative
P3HT	poly(3-hexylthiophene-2,5-diyl)
PBE	Perdew-Burke-Ernzerhof
PCE	power conversion efficiency
PDF	powder diffraction file database by the international centre for diffraction data
PEA	phenethylammonium
PL	photoluminescence
PLE	photoluminescence excitation
PXRD	powder X-ray diffraction
RP	Ruddlesden-Popper
SAXS	small-angle X-ray scattering
SCXRD	single-crystal X-ray diffraction
SE	secondary electron
SEM	scanning electron microscopy
SLME	spectroscopic limited maximum efficiency
SOC	spin-orbit-coupling
Spiro-O-MeTAD	2,2',7,7'-Tetrakis[N,N-di(4-methoxyphenyl)amino]-9,9'-spirobifluorene
TFXRD	thin-film X-ray diffraction
TIL	thermodynamic ionization level
TLD	through-the-lens detector
TRMC	time-resolved microwave conductivity
TU	thiourea
UV-Vis	ultraviolet-visible light
VB	valence band
VBM	valence band maximum
WAXS	wide-angle X-ray scattering
XPS	X-ray photoelectron spectroscopy
XRD	X-ray diffraction

Abstract

Perovskites have witnessed a grand rebirth over the last decade as the next generation photovoltaic materials. To be precise, metal halide perovskites and specifically lead-based halide perovskites have demonstrated exceptional properties as semiconductors for all kinds of optoelectronic applications. The two main downsides of these materials - the toxicity and the lack of long-term stability - stimulated the scientific community to look further into the world of perovskites and inspired materials to find alternatives with the aim to retain their exceptional optoelectronic properties.

This work explores double perovskites, two-dimensional double perovskites and perovskite-inspired rudorffites as potential alternative, lead-free materials with a focus on photovoltaic application. With their performances still far behind those of lead-based perovskites, understanding the reasons and fundamental photophysics is an important step towards finding and realizing the next generation of this material class.

In the first chapter, 2D double perovskites based on an Ag-Bi framework with 4-fluorophenethylammonium as the organic cation are investigated, demonstrating key advantages such as the change to a direct band gap and the ability to synthesize iodide phases through dimensional reduction. Strong orientational growth tendencies in crystalline thin films are observed and challenging charge-carrier properties such as the formation of excitonic, small polaronic and defect-mediated states are elucidated.

In the second chapter, a 2D/3D heterostructure is created to improve the performance of $Cs_2AgBiBr_6$ solar cells by adding a $(PEA)_4AgBiBr_8$ (PEA = phenethylammonium) layer before the hole-transport-layer. Through a combination of morphological and electronic structure optimization, the 2D/3D structure leads to improved contact selectivity and energy level alignment, resulting in a higher power conversion efficiency of 2.47%.

In the third chapter, the intrinsic limitations of the 2D perovskite structure are fundamentally addressed by employing electronically active, conjugated organic cations to modify the anisotropic electrical conductivity. Pyrene based cations demonstrate their influence on the electronic band structure, resulting in hybrid contributions to the frontier bands from both inorganic and organic layers. This, combined with a favorable organic intralayer alignment enables electrical out-of-plane conductivity in otherwise insulating 2D perovskites. $(POE)_4AgBiI_8$ with an inorganic layer thickness of n = 1 could ultimately be incorporated in the first reported, planar 2D double perovskite solar cell with a power conversion efficiency of 0.17%.

In the fourth chapter, a perovskite-inspired material class known as rudorffites is investigated as a solar cell material. With most reports being focussed on Ag-Bi-I rudorffites, in this work a synthesis route for Sb based rudorffite is established and further investigated upon inclusion of Cu into a $Cu_{1-x}Ag_xSbI_4$ based phase. The compositional substitution is investigated regarding the electronic structure, revealing the detrimental effect of Cu and Ag point defects. Improvements in the thin film morphology and charge-carrier mobility are found upon inclusion of Cu and fractional amounts of Bi, leading to a promising initial power conversion efficiency for solar cells of 0.7%.

Contents

Chapter 1

Introduction

1.1 Introduction

There is one physical quantity determining all life on earth, in fact, every other phenomenon in the universe - Energy. It can be neither destroyed nor created, only transformed or transferred. In our solar system, this transformation and transfer originates from our sun. The sun, radiating its energy onto earth, is solely responsible for every form of life and evolution on our planet. Nature has found many ways to use this energy throughout the evolution of the first lifeforms 3.42 billion years ago, the first plants 850 million years ago and the first animals 690 million years ago. Our species, the homo sapiens, only first showed up around 300,000 years ago, but still we have quickly become the most efficient and evolving transformers of energy on the planet. The ascension of humans can be easily visualized through the number of the global population shown in Figure 1.1 (left): 10,000 years ago there were only about 4.43 million people living on earth and as of today this number has soared up to 7.91 billion. It can be closely correlated to our ability to transform and use different types of energy as seen by the global energy consumption in Figure 1.1 (right).[1–6] For both, the sharp and exponential rise starts around the year 1900, directly linked to the industrial, the technological and from 1947 until now, the digital revolution. Until today, the biggest resources for energy production are still coal, oil and natural gas. Though, blinded by the success and rapid industrial expansion, one key underlying mechanism of these fossil fuels tended to be overlooked or ignored. The sought after exothermic reaction of these hydrocarbon based materials with oxygen releases amongst water, also carbon dioxide, a green-house gas (see Figure 1.2 (left)). Green-house gases such as methane, carbon dioxide or nitrous oxides are non-absorbing for the largest and most energetic part of the sun's spectrum, but not for the infrared region of the electromagnetic spectrum, meaning they absorb and reemit the space-bound heat from the Earth's surface, quantified through their radiative

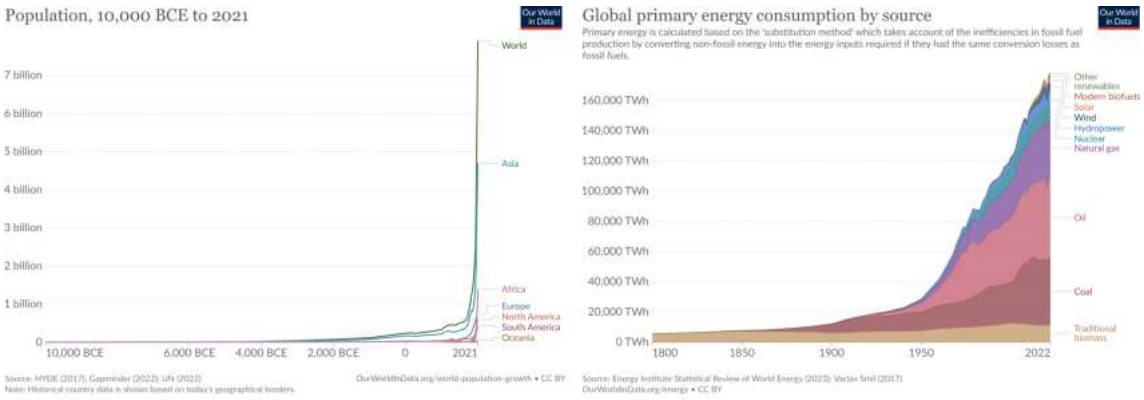

Figure 1.1: (Left) Global population from 10,000 BCE to 2021 (Right) Global primary energy consumption by source.[5,6]

forcing, leading to a warming of the Earth's atmosphere, as seen in Fig. 1.2 (right). While this effect in general is also responsible for making the temperature of the Earth's atmosphere habitable, too much of it is now leading to an unprecedented rise in average global temperatures, heralding the Anthropocene, the proposed, latest geological epoch dating from the large effect of humans and the anthropogenic climate change on Earth's geology and ecosystems. The projected risks and changes to ecosystems and our planet are increasingly motivating science, politics and industry to search for mitigation strategies and renewable alternatives to fossil fuel energy production in an urgent attempt to reduce global warming.[7–10]

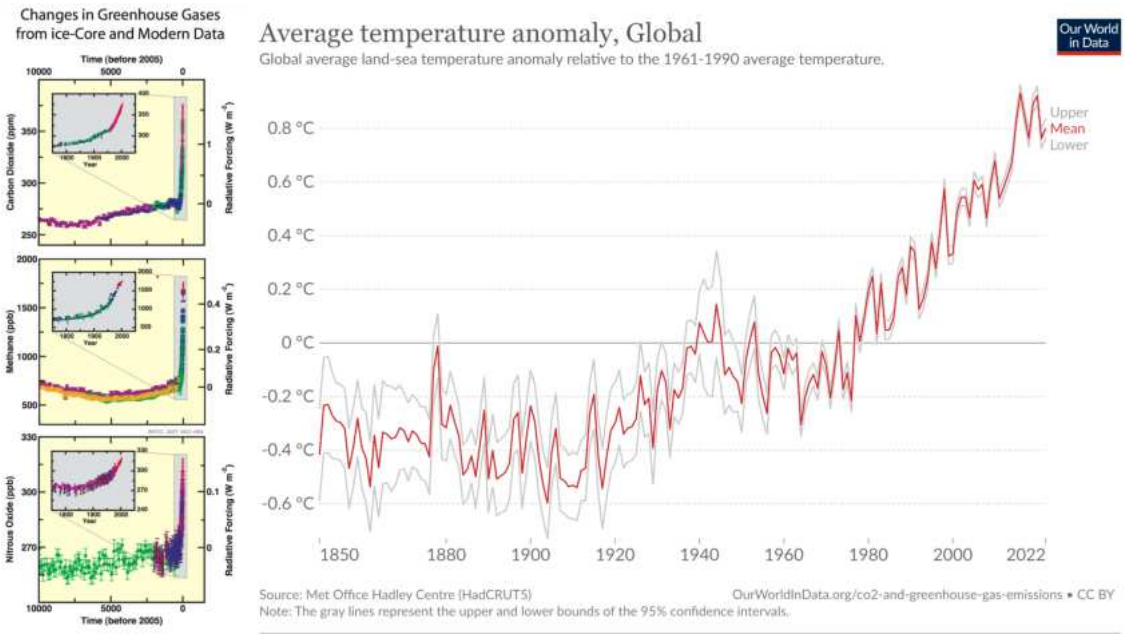

Figure 1.2: (Left) Changes in greenhouse gas concentrations from ice-core and modern data with corresponding radiative forcing on the right axis. Symbols with different colors from different studies (ice cores) and atmospheric studies (red lines). (Right) Average global temperature anomaly from 1850 to the present, relative to the 1961-1990 average temperature.[9,10]

1.1.1 Semiconductors

Possibly the most elegant solution for a renewable energy source is to harness the sun's light directly and convert it into a usable form of energy, such as electricity. This is achieved through the photovoltaic effect and is based on the discovery and the underlying physics of semiconductors. The properties of electric isolators and conductors, or metals, were common subjects of scientific research before semiconductors sparked the emergence of the new field of solid state physics and the introduction of the band theory to describe their electronic properties. The simplest classification of solids is based on their electrical conductivity, with semiconductor values lying inbetween that of insulators and conductors. Another important property is the negative temperature coefficient of semiconductors, i.e. with increasing temperature the resistivity decreases, opposite to metals or conductors. The explanation of these phenomena and a better general classification of materials is possible through the electronic band structure.[11–14]

Prior to the emergence of solid state physics, important landmarks in crystallography and quantum mechanics have been discovered, such as the identification of periodic lattices in crystals through diffraction by *Max von Laue* and the free electron model to describe charge carriers in metal solids by *Arnold Sommerfeld*. For crystalline solids, all atoms are arranged in a periodic lattice and thus the electronic structure can be described by solving the time-independent Schrödinger equation for electrons in a periodic potential. This is known as Bloch's theorem and can be written as the wavefunction ψ of a position r being equal to a periodic function u with a wave vector k:

$$\psi(r)_{nk} = e^{ikr} u_{nk}(r) \tag{1.1}$$

The band structure can then be expressed in three dimensions along the paths of the wavevector k in the Brillouin zone, a polyhedral representation related to the crystal lattice. For every wavevector k there are a number of solutions n resulting in the number of energy bands. The occupation probability of electrons in the band structure $f(\epsilon)$, is described through the Fermi-Dirac distribution in eq. 1.2. Here ϵ is the energy, μ the total chemical potential, k_b the Boltzmann constant and T the temperature:

$$f(\epsilon) = \frac{1}{1 + e^{(\epsilon-\mu)/k_B T}} \tag{1.2}$$

In solids, the total chemical potential μ is equivalent to the Fermi level E_F. It is the energy at a given temperature T, where the probability of an electron occupying an energetic state is 50%. At absolute zero temperature, it is equal to the Fermi energy, defined as the energy of the highest occupied state. While for metals, the Fermi level lies within at least one

band, for semiconductors and isolators it lies between the bands. The highest band below the Fermi level is called the valence band (VB) with the energy E_v and the lowest band above the Fermi level is the conduction band (CB) with the energy E_c. This energetic gap is separated by an amount ΔE_{cv}, which is called the band gap, denoted as E_g. This is schematically depicted in Figure 1.3:

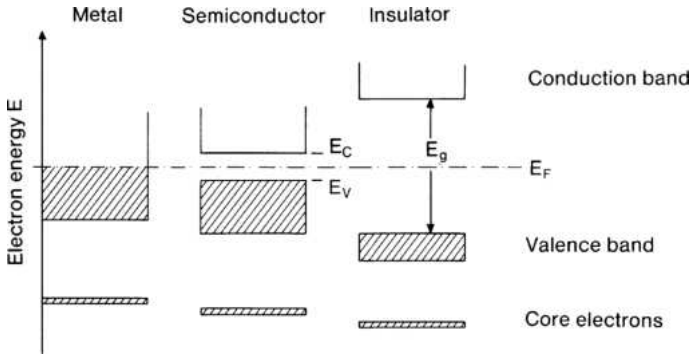

Figure 1.3: Schematic energy level diagrams for a metal, a semiconductor and an insulator. Reproduced with permission from Springer Nature.[13]

For band structures where the lowest energy state of the conduction band has the same k vector as the top of the valence band, it is classified as a direct band gap and if they are located at different k vectors it is classified as an indirect band gap. For an electron to change its state from the valence to the conduction band in a structure with a direct bang gap, only the required amount of energy for an optical transition with a photon is necessary. For an indirect band gap, additional vibrational energy for the crystal momentum in the k space in form of a phonon is required. This is shown in Figure 1.4 for two classic semiconductors, germanium (left) with an indirect band gap and gallium nitride (right) with a direct band gap. In band structure representations, the x-axis denotes the crystal momentum space with defined points in the Brillouin zone and the y-axis denotes the energy of the bands. Conventionally, the zero energy point is often set to the valence band maximum (VBM) value, as the interpretation is based not on absolute energies, but on energy differences.[11–14]

In addition to the band structure, the number of states in each band is an important property to describe the electronic structure. This density of states (DOS) is obtained by integrating in k-space over the first Brillouin zone and it is related to the orbital contributions of each atom in the crystal. Large densities of states are often correlated to flat parts of the bands and vice versa, while in the band gap the density of states will be zero, as seen in fig. 1.4 (left).

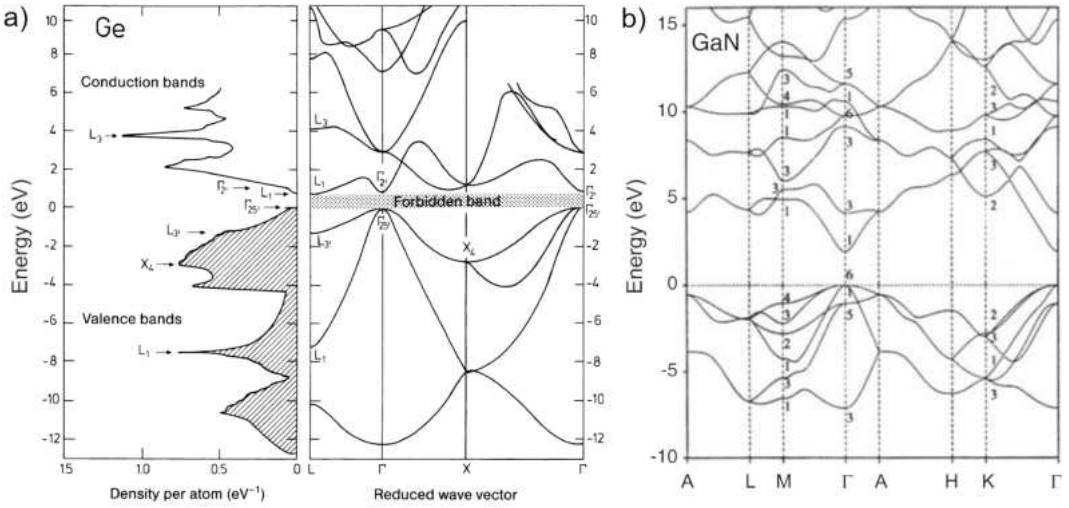

Figure 1.4: a) Density of states and band structure of germanium with an indirect band gap from Γ to close to the L point. b) Band structure of GaN with a direct band gap at Γ. Reproduced with permission from Springer Nature.[12,13]

The implication for the electrical conductivity σ of materials is, that for insulators σ is very small as E_F lies within a large band gap, with no occupied states that could conduct electrical current. For metals, σ is large, as E_F lies within a band and a large number of occupied states can conduct current. Semiconductors lie inbetween the two cases, where E_F is close enough to partially occupied states leading to a reasonable, non-zero σ. This leads to two important properties of semiconductors, the first being the dependence of intrinsic conductivity and carrier concentration on the ratio of E_g/k_BT, i.e. with increasing temperature, the concentration of intrinsic carriers also increases. Secondly, given sufficient energy an electron can be excited, bridging the band gap and creating a 'free', mobile charge carrier.

Since excited charge carriers are only conceptually free, hence the quotation marks, it is useful to describe the boundaries and types of excited charge carrier species in more detail. When an electron is excited into the conduction band, it quickly decays to the least energetic level, i.e. the conduction band minimum (CBM), emitting vibrational energy on a time order of femtoseconds. The relaxation back across the band gap on the other hand is many orders of magnitude slower, allowing the electron to be in a mobile state, being close to a large number of unoccupied band states. Importantly, the excited electron leaves behind a vacant state in the valence band; a hole, being a quasiparticle with positive charge that can be treated equivalent to the electron, as it is surrounded by a large number of occupied states. Electron and hole are thus created as pairs and due to their proximity and opposite charge they experience an attractive, coulombic force. If their energy, dependent on the product of k_BT, is insufficient to overcome this attraction a bound electron-hole pair is created, called an exciton.

After a photon is absorbed, the creation of a mobile electron-hole pair leads to a number of possible subsequent processes, shown in Figure 1.5. This reversal under thermal and chemical equilibrium for every mechanism must be exactly equivalent to the production rate, also called recombination and is referred to as the principle of detailed balance. The exact reverse process would be a radiative recombination, where the electron-hole pair recombines via the emission of a photon with the same energy as previously absorbed. If the recombination does not happen through the emission of a photon, the energy must be released through other particles, either via transition to other electrons or holes (Auger recombination) and finally or directly via phonons. This nonradiative recombination through multistep thermalization often involves defect or trap states in the band structure, making it the dominant recombination mechanism, as in reality semiconductors are never perfect crystals.

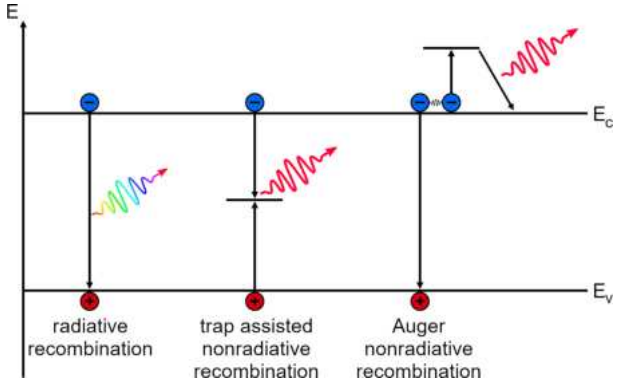

Figure 1.5: Schematic recombination mechanisms in a semiconductor: (left) radiative band to band recombination emitting a photon; (middle) trap assisted nonradiative recombination emitting phonons; (right) Auger nonradiative recombination emitting phonons.

The effective separation of electron-hole pairs thus requires a preferential flow direction of electric current. The elementary mechanism for this in semiconductor materials is accomplished through doping and the formation of a positive-negative (p-n) junction, or a heterojunction. Doping a crystalline semiconductor, by incorporating atoms of different valence state, creates additional charge carriers, increasing conductivity. In silicon, being a group IV element, this can be achieved by p-doping with group III elements such as boron, effectively creating mobile holes as they lack a fourth valence electron for the creation of all four bonds in the silicon lattice and vice versa by n-doping with group V elements such as phosphorus. In heterojunctions the principle is the same, but two different p- and n-type materials are connected. In a p-n junction, upon contact of the p- and n-type layer, the connecting region is depleted of mobile charge carriers as electrons will flow to the p-type region and holes to the n-type region, effectively recombining, making the region insulating. This depletion zone creates an electric field as the charged dopant atoms remain at their lattice positions, simultaneously limiting its width due to the

increasing gradient.

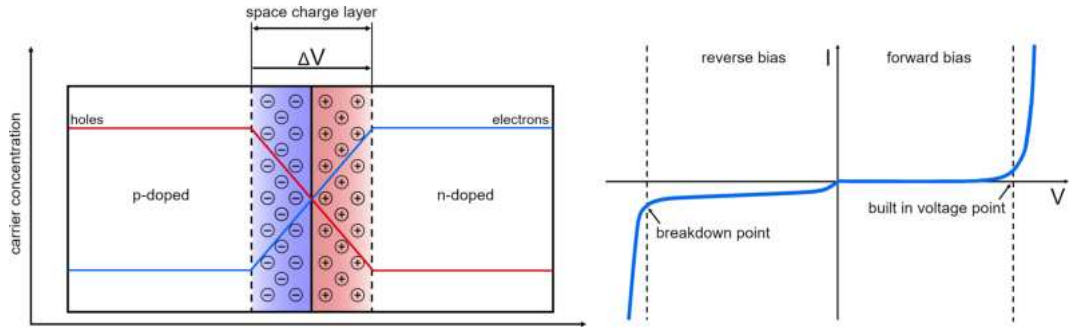

Figure 1.6: (Left) The space charge layer in the contact zone of a p-n junction schematically depicted with the charge carrier concentration as y-axis, charge carriers occupying the opposite charged dopant region in the boundaries of the space charge layer and the created potential ΔV at the top. (Right) Characteristic IV curve of a diode with no current flow under forward bias until the built in potential voltage is surpassed and small leakage current flow under reverse bias until the breakdown voltage point is surpassed.[15,16]

This space charge layer (Figure 1.6, left) governs such a diode's electrical characteristics, defined by its current-voltage (IV) curve (Figure 1.6, right), i.e. the behaviour of current flow dependent on the applied voltage bias. Under reverse bias, i.e. under the same polarity as the built-in potential, no current can flow through the diode up until a breakdown point where the potential reaches the peak inverse voltage, where large currents can flow in reverse, usually destroying the diode. Under forward bias, the current is zero up to the point where the built in potential is surpassed and then increases exponentially, following the Shockley diode equation, with the diode current I_D, the reverse saturation current I_S, the diode voltage V_D, the thermal voltage $V_T = \frac{kT}{q}$ and the ideality factor n (usually n = 1):

$$I_D = I_S(e^{\frac{V_D}{nV_T}} - 1) \tag{1.3}$$

These fundamental physical principles in semiconductors form the basis for all further applications. The diode is the elementary electrical component for these semiconductor circuits, as well as for more specialized cases such as the light-emitting diode (LED) or the photodiode in solar cells, which will be further explored in the following chapter.

1.1.2 Solar Energy

With the foundation of semiconductor physics laid out, a closer look at solar energy harvesting and the photovoltaic effect is now possible. As described in the foregoing chapter, the ability of a semiconductor to absorb energy allows it to lift an electron across the band gap, from its valence band into the conduction band. This not only increases the electrical conductivity of the semiconductor, but also creates the possibility for this charge to be extracted via an external circuit, ultimately allowing for the production of energy in the form of electricity.

Photovoltaic energy conversion requires the separation and extraction of the generated charges. As this competes directly with the natural recombination mechanisms, a driving force in the photovoltaic device is required. This driving force can effectively be achieved through an internal electric field, driving positive and negative charge carriers in opposite directions, or through large diffusive currents in asymmetric environments, i.e. interfaces with materials having much lower resistances for electrons or holes. In complete devices this is usually accomplished through either the use of a p-n junction, driving electrons into the positive charged side and holes into the negative charged side of the junction, or by placing the active absorber material inbetween two materials with very low specific resistances for electrons or holes, making them effective electron transporting materials (ETMs) or hole transporting materials (HTMs). Under load, i.e. illumination, the simplified electrical circuit and flow of current for a solar cell is shown in Fig. 1.7 (left).

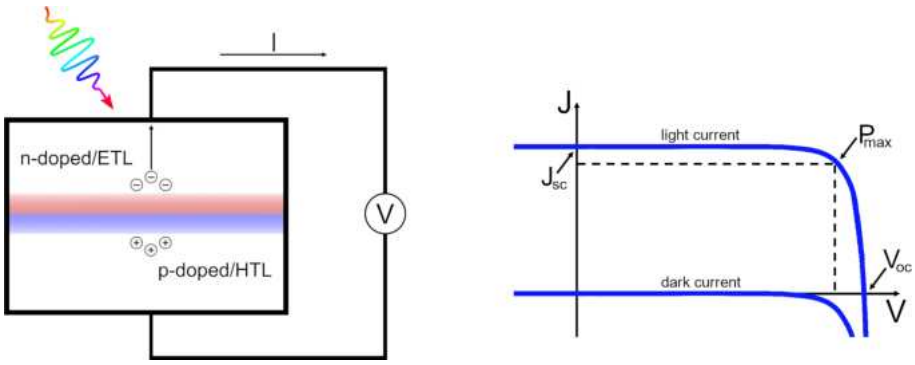

Figure 1.7: Simplified electrical circuit of a photovoltaic device (left). Current density voltage curve of a photodiode under light and dark conditions (right).

To describe the current-voltage characteristics of a photovoltaic device, a modified version of the diode current-voltage curve as shown in Fig. 1.6, can now be used for a photodiode, shown in Fig. 1.7 (right). Firstly, the conventional representation features the current density J instead of just the current I, as the extracted information is always in relation to the irradiance of the solar spectrum and the absorbing surface of the solar

cell. Secondly, as solar cells are operated under illumination, there are two cases for the current density-voltage (JV) curve to consider: a) under dark conditions, where the situation is equal to the standard diode curve shown in Fig. 1.6 and b) under light conditions, where the solar cell produces current through the absorbed light, which shifts the JV curve along the y-axis, proportional to the light induced current, as now there is a flow of current under zero bias voltage. This intersection point of the y-axis is denoted as the J_{sc}, the short-circuit current density, which in simple terms relates to the incident spectral photon flux b_s and the solar cell's quantum efficiency (QE), including the probability of an incident photon with energy E being converted to one electron to the external circuit and the electronic charge q:[15]

$$J_{sc} = q \int b_s(E) QE(E) dE \tag{1.4}$$

The quantum efficiency gives a ratio between the number of incident photons to the extracted electrons at a given energy. This depends strongly on the absorption by the absorber material, the charge separation and charge collection of the full device. With the J_{sc}, the ideal diode equation, shown in eq. 1.3, modifies slightly to:

$$J = J_{sc} - J_0(e^{\frac{qV}{k_B T}} - 1) \tag{1.5}$$

The maximum voltage a solar cell can deliver is denoted as the V_{oc}, the open circuit voltage. It is the point at which dark and light current exactly cancel each other out and can be expressed as:

$$V_{oc} = \frac{k_B T}{q} ln \frac{J_{sc}}{J_0} + 1 \tag{1.6}$$

As the output power of a solar cell does depend on both the current density and the voltage, the maximum power is reached at a point P_{max}, where the product of current density and voltage reaches its maximum. This characteristic is usually described through the fill factor FF:

$$FF = \frac{J_{Pmax} V_{Pmax}}{J_{sc} V_{oc}} \tag{1.7}$$

It is a ratio that can be visualized as the maximum rectangular area under the JV curve, as depicted by the dotted lines in fig. 1.7. Finally, the power conversion efficiency (PCE) η of a solar cell can be expressed by using the above introduced figures of merit, either in dependence of the maximum power point, or the J_{sc}, V_{oc}, FF and power of incident light P_{in}:

$$\eta = \frac{P_{max}}{P_{in}} = \frac{J_{sc} V_{oc} FF}{P_{in}} \tag{1.8}$$

To evaluate the maximum energy available from a photovoltaic device it is useful to make simplified assumptions to describe the system. Considering the ideal case of a two band system, separated by a band gap and perfectly absorbing material, the photocurrent of a solar cell is dependent on the solar spectrum or its photon flux at the energy equal or greater to the band gap of the absorber. Further considering perfect charge extraction of all electrons and holes to the external circuit, the maximum photocurrent can be calculated depending only on the band gap and the incident spectrum. The output power is then the potential energy of the extracted photo-electrons combined with the current from the absorbed photon flux.[17]

The sun emits energy that can be described as black body radiation at a temperature of T = 5900 K. This energy comes in the form of photons; massless, elementary particles without electrical charge. A photon's energy E is solely defined by its frequency v, or inversely its wavelength λ, with the Planck constant h and the speed of light c:

$$E = hv = \frac{hc}{\lambda} \tag{1.9}$$

Consequently, the spectrum of the sun can be displayed as irradiance, i.e. the current density per photon wavelength as a function of the photon wavelength in Figure 1.8.:

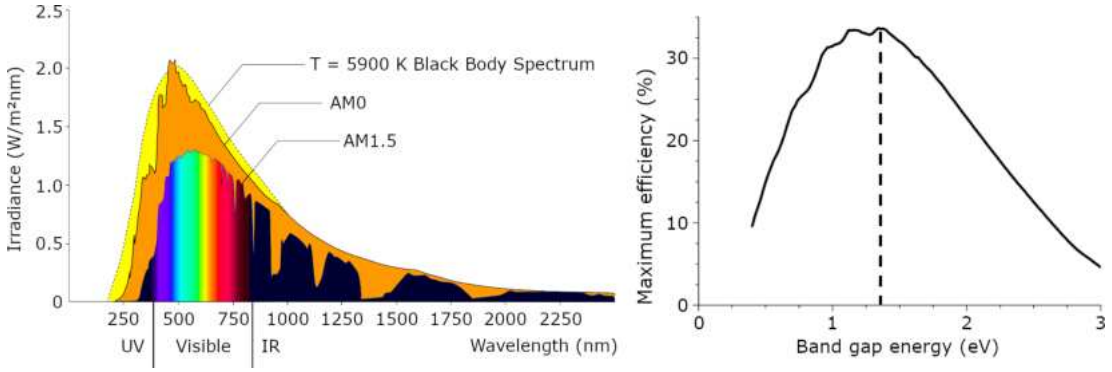

Figure 1.8: The solar spectrum at airmass 0 (AM0), airmass 1.5 (AM1.5) with black body radiation at T = 5900 K underlaid. The visible spectrum of light is illustrated in color in the AM1.5 spectrum (left).[18] The Shockley-Queisser limit showing the efficiency of a single-junction solar cell in dependence of the absorber material's band gap energy under the AM1.5 spectrum, with the maximum theoretical efficiency of 33.16% at 1.34 eV indicated by the dotted line (right).[17]

The complete, extraterrestrial solar spectrum is denoted as AM0, or air mass 0. As light penetrates the atmosphere of the earth, its molecules attenuate the light through scattering and absorption processes. The resulting spectrum at the earths surface, under an irradiation angle of 48 °, is denoted as AM1.5, or air mass 1.5. The dominant contribution to this spectrum lies in the range of the visible and near-infrared region of light, corresponding to photon energies between 0.6 - 2.0 eV. While the transition from conductor to semiconductor is clear, the transition from wide band gap semiconductor to insulator is somewhat

arbitrary. Most semiconductors thus have band gap energies that lie in the range of light in the context of the solar spectrum on earth.

With the figures of merit for the efficiency of a solar cell defined and the solar spectral flux, the maximum efficiency can now be calculated in dependence on the band gap energy. This limit was introduced by *William Shockley* and *Hans-Joachim Queisser* in 1961 and is known as the Shockley-Queisser limit, shown in Figure 1.8 (right).

It is calculated within the boundaries of a single p-n junction solar cell, with the key loss mechanisms being radiative recombination, thermalization, i.e. the loss of energy from excited electrons above the band gap through vibrational relaxation, and considering impedance matching. The used incident spectrum is the black body radiation model for the AM1.5 solar spectrum. This results in a theoretic maximum efficiency of 33.16% for a material with a band gap of 1.34 eV.[17]

Consequently, research for photovoltaic materials is often centered around the band gap of the material being as close as possible to this value, to approach the maximum efficiency for a single-junction solar cell. The most established solar cell technologies until now are based on first generation materials, mostly crystalline Si, second generation materials, such as amorphous Si, GaAs, CdTe or $CuIn_xGa_{1-x}Se_2$ and third generation materials, such as organic molecules and polymers, perovskites and perovskite inspired materials. The first two generations are already well into the stage of commercialisation and require high purity grade manufacturing processes based on wafer scale or solid state technologies. Third generation materials on the other hand are based on simpler thin film manufacturing processes but have not yet reached the stage of commercialisation, as their environmental stability and toxicity are still problematic and one of the main subjects of contemporary research. Nonetheless, perovskite solar cells have already reached maximum efficiencies of up to 26.1%, being on par with state of the art crystalline Si solar cells at 26.8% in 2023.[19]

1.1.3 Perovskites

Perovskites were first discovered in 1839 by *Gustav Rose* as the mineral $CaTiO_3$, which was later described crystallographically by *Victor Goldschmidt* in 1926, marking the origin to the ever-growing family of the perovskite structure.[20] It consists of the general formula ABX_3, where the A-site cation is located in the cuboctahedral cavity formed by B-site cation centered octahedra, cornered by the X-site anions, as shown in Figure 1.9 left. For charge neutrality, either the $A^{2+}B^{4+}X_3{}^{2-}$ or $A^{+}B^{2+}X_3{}^{-}$ configurations are possible. A-site cations are generally alkali, alkaline earth or transition metals, B-site cations are transition metals or group IV metalloids and X-site anions are either oxygen or halide ions. Perovskites often appear pseudocubic, but in reality the crystal system is mostly orthorombic, due to the twisted geometry of the octahedra. This distortion of the perovskite structure and its inherently connected intrinsic stability was described by *Victor Goldschmidt* in his aforementioned work in 1926. It is known as the Goldschmidt tolerance factor α, where the ionic radii of A-, B- and X-ions, r_A, r_B and r_X are put in context to give a descriptor ratio:

$$\alpha = \frac{r_A + r_X}{\sqrt{r_B + r_X}} \tag{1.10}$$

For a range of α between 0.71 and 1.0, perovskite structures are considered stable, with different degrees of distortion, producing structures of the following crystal systems: Orthorombic or rhombohedral for α = 0.71 - 0.9, cubic for α = 0.9 - 1.0 and hexagonal or tetragonal for $\alpha > 1$.[20]

The rapidly growing scientific interest for perovskite structures arose through the discovery of metal halide perovskites and hybrid perovskites, where organic cations such as methylammonium replace the B-site cation. Methylammonium lead halides, and in particular methylammonium lead iodide ($MAPbI_3$) (Fig. 1.9 right), feature outstanding optoelectronic properties as semiconductors.

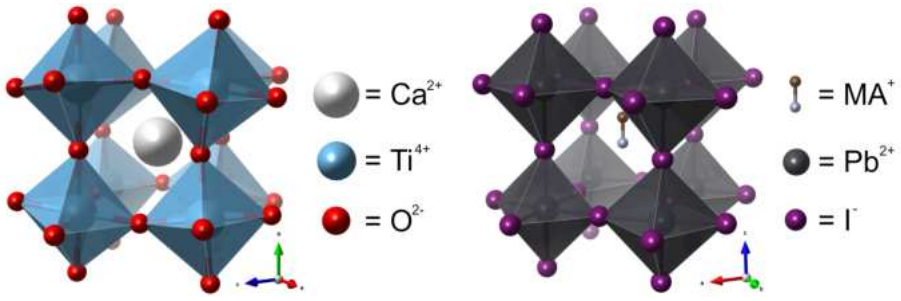

Figure 1.9: Crystal structures of $CaTiO_3$ (right) and of $MAPbI_3$ (right).[21,22]

The discovery of their excellent optoelectronic properties was initiated through the incorporation of $MAPbI_3$ in dye-sensitized solar cells, but was not limited to the field of photovoltaics, since the underlying properties enable their application in many semicon-

ductor devices such as light-emitting diodes (LEDs), photodiodes or transistors.[23] The dye-sensitized solar cell is based on a mesoporous TiO_2 film, prepared on a conductive, transparent oxide (fluorine-doped SnO_2 or FTO) on a glass substrate. The mesoporous TiO_2 is filled, or sensitized, by the $MAPbI_3$ and covered by an organic electrolyte solution, consisting of a lithium halide (LiI) and I_2 in methoxyacetonitrile, completed with a Pt coated FTO counterelectrode (Figure 1.10 left). The incoming light excites the $MAPbI_3$, the electron gets extracted by the TiO_2 and FTO anode, while the electrolytes redox couple $I_3^- + 2\,e^- \rightleftarrows 3\,I^- - 2\,e^-$ mediates electrons between Pt/FTO cathode and $MAPbI_3$.[24]

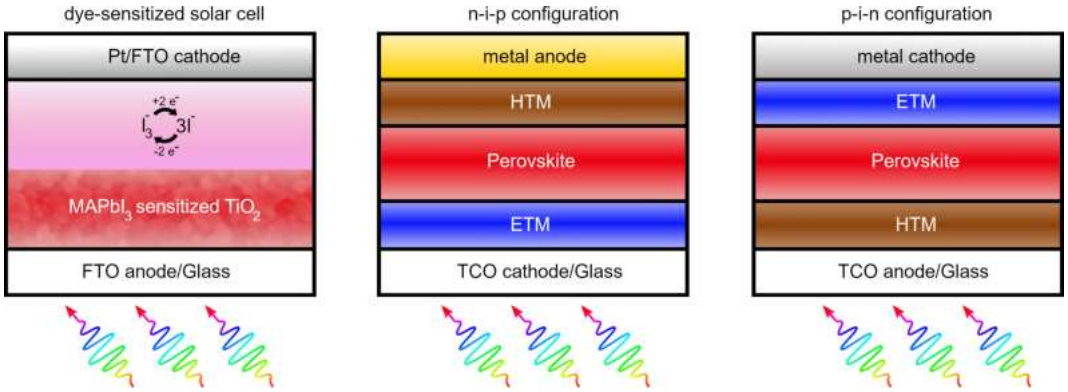

Figure 1.10: Archetypical dye sensitized solar cell based on $MAPbI_3$ (left). Perovskite solar cell in n-i-p configuration (middle), typically with Au as the metal anode. Perovskite solar cell in p-i-n configuration (right), typically with Ag as the metal cathode.[24]

The functional principle and architecture of the modern perovskite solar cell is not too different from the original dye sensitized solar cell, as shown in Fig. 1.10 (middle and right). Mainly, the perovskite absorber material is present as a distinct, crystalline layer between an electron transport material and a hole transport material. It can be constructed in a p-i-n type or an inverted n-i-p type configuration, with the transparent conductive oxide substrate being the cathode or anode material, respectively.

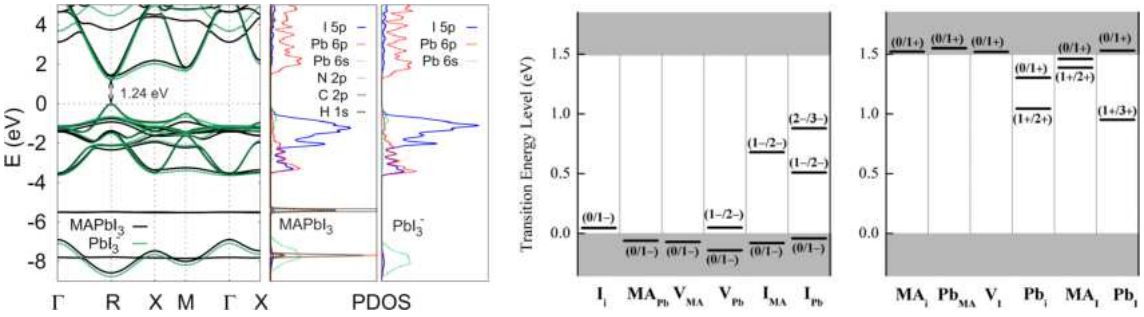

Figure 1.11: Band structures of $MAPbI_3$ and PbI_3^- with the density of states using the PBE functional without SOC effects (left). Reproduced with permission from APS.[25] Transition energy levels of intrinsic acceptor and donor type defects in $MAPbI_3$ (right). Reproduced with permission from AIP Publishing.[26]

The origin of the excellent performance of $MAPbI_3$ (and other lead halide perovskites) lies in its electronic structure, featuring a number of key properties. $MAPbI_3$, in its tetragonal phase, features a direct band gap of 1.24 eV (Figure 1.11 left), being close to the optimum of the Shockley-Queisser limit. The high crystalline symmetry and its direct band gap result in exceptionally high absorption coefficients, being the first precondition for efficient photoactive semiconductors. This also means that the perovskite layers require orders of magnitude smaller thicknesses compared to conventional Si layers in solar cells. The narrow bands at the VBM and CBM also result in small effective charge carrier masses, making them mobile and easily extracted.[27] Furthermore, lead halide perovskites are very tolerant towards electronic defect states, as shown in Figure 1.11 right. The dominant point defects have low formation energies and create shallow defect levels, being very close to the valence and conduction band. Defects at deep levels in the band gap have high formation energies and are thus unlikely to form.[26,28] $MAPbI_3$ further features low exciton binding energies, leading to a large number of free charge carriers at room temperature.[29] The reason for these qualities of $MAPbI_3$ and its electronic structure lies in the electronic configuration, with the Pb lone pair 6s-I 5p σ-antibonding orbital forming the valence band maximum and the Pb 6p-I 5s σ-antibonding and Pb 6p-I 5p π-antibonding orbitals forming the conduction band minimum.[27] All these properties combined provide the exceptional performance in solar cells and other optoelectronic devices.

Lead halide perovskites are almost perfect semiconductor materials, as their above explained qualities are attainable through incredibly simple synthesis techniques. They can be synthesized from solutions of their constituent halide salts in organic solvents, requiring only room temperature for dissolution and relatively low crystallization temperatures of 100 °C, to form functional, polycrystalline thin films on almost any substrate.

Two central challenges remain and are in the focus of contemporary research efforts: i) The toxicity of the central element Pb in its oxidation state Pb(II) and ii) the intrinsic

instability of lead halide perovskites. The stable Pb^{2+} state is cytotoxic, posing danger to plants, wildlife and humans altogether. This is due to its charge and ionic radius, allowing it to mimic many metal cofactors, inhibiting enzymatic processes. For humans, lead poisoning is another well-known danger, where Pb^{2+}, due to its similarity to Ca^{2+} and Mg^{2+}, can pass the blood brain barrier and cause great neurological damage, especially in the developing brains of children. PbI_2, a precursor and direct decomposition product of lead halide perovskites is a known carcinogenic compound.[30,31]

Unfortunately, these grave toxicity issues are only amplified when the instability of lead halide perovskites is considered. Due to the mobility of the organic cation and other ion migration phenomena, lead halide perovskites often exist in different crystalline phases. $MAPbI_3$ for example undergoes temperature dependent phase transitions from orthorombic (*Pnma*), to tetragonal (*I4/mcm*), to cubic (*Pm-3m*) between 150 and 180 K, 250 and 320 K and above 350 K.[32] Additionally, at elevated temperatures of only 358 K (85 °C), volatile components such as methylammonium or HI evaporate, degrading the perovskite and leaving PbI_2 behind.[33] Towards moisture, the instability is caused by the H_2O being able to form coordination complexes or directly dissolving the perovskite. This of course is especially concerning, as high water solubility directly affects the toxic potential and the bioavailablity of lead perovskites. Lastly, also photon-induced degradation mechanisms are prevalent, as either the photon energy can directly dismantle the perovskite into its constituents, or in an enhanced manner, under normal atmospheric conditions, with superoxide anions O_2^- forming, which deprotonate MA^+ of photo-excited $MA^\bullet$ and act as a degradation catalyst.[32–35]

In the context of lead halide perovskites being used in photovoltaic and other photoactive devices, these instabilities towards atmospheric conditions are a major barrier for commercialization. While some stability improvements have been achieved through a mixed formulation approach in a triple cation, mixed anion lead perovskite $Cs_x(MA_{0.17}FA_{0.83})_{1-x}Pb(I_{0.83}Br_{0.17})_3$ (FA = formamidinium),[36] or through encapsulation of the full devices,[37] other more fundamental possibilities to replicate the performance of lead perovskites, ideally completely removing the central but toxic element Pb, are a large area of current research.

Removing Pb means retaining the perovskite structure and replacing Pb with an element that is as close as possible to its electronic configuration, being the origin for the exceptional optoelectronic properties. The different routes are schematically depicted in Figure 1.12 and explained in the following. The most apparent choice is a homovalent substitution with other group 14 elements, such as Ge or Sn. Sn results in similar band gaps and electronic properties, whereas Ge results in larger band gaps, mostly due to its deeper 4s orbital energies and the structural distortion due to the small ionic radius

of Ge^{2+}. Ge perovskites display very poor performances, due to high defect densities, whereas Sn perovskites perform much better. Both elements however produce highly unstable perovskites, due to their easy oxidation to the Sn^{4+} and Ge^{4+} states.[38,39]

The second option is a heterovalent substitution with elements that only have similar electronic configuration to Pb^{2+} at different oxidation states. The most common choices are group 13 and 15 elements; In, Tl, Sb or Bi. Due to the scarcitiy of In and the toxicity of Tl, most alternative materials are based primarily on Bi and secondarily on Sb. To keep the electronic configuration and the s^2 lone pair, group 15 elements have to be in the oxidation state +3, requiring different charge balancing in the ABX_3 stoichiometry. To retain the perovskite structure, either ion-splitting or vacancy-formation has to be integrated. Ion-splitting refers to the distribution of charges on either the anion X position, with chalcogenides (Group 16) balancing different B-cation oxidation states, or the cation B position, with one B(I) and one B(III) metal cation replacing two Pb(II) cations, resulting in a double perovskite structure. Common B(I) cations are group 11 elements in their oxidation state +1, such as Cu or Ag. Mixed chalcogenide/halide perovskites have similar optoelectronic properties, but are mostly thermodynamically unstable.[40] Double perovskites are very stable and offer rich chemistry, providing a large number of new materials.[41] Their structure and properties will be explained in greater detail in the following chapter 1.1.4.

Heterovalent substitution through vacancy-formation either replaces two Pb(II) cations with one B(IV) cation and one vacancy, or three Pb(II) cations with two B(III) cations and one vacancy. While the former mostly retains the perovskite structure, referred to as vacancy-ordered perovskites, the latter strays quite far from the perovskite structural motif. These vacancy ordered nonperovskites can be divided into dimer and layered phases. In dimer phases with the chemical formula $A_3B(III)_2X_9$, the vacancy introduces isolated, face-shared $[B_2X_9]$ octahedral double layers, separated by one completely empty layer. In the layered phase with the chemical formula $A(B_{2/3}\square_{1/3})X_3$ ($\square$ = vacancy), the vacancy also removes one complete octahedral layer, but maintains the corner-shared octahedral double layer, similar to the polyhedral connectivity in perovskites.[42] While also being more stable than lead halide perovskites, their optoelectronic properties are not on par and they often exhibit deep defect states.[44–47]

Another group of emerging, perovskite-inspired, lead-free materials are pnictogen-based metal halides and rudorffites. Different compositions of the ternary phase space Ag-Bi-I have attracted a lot of attention recently, while others, including Cu or Sb are also gaining attraction. More generally, these materials follow the formula $A(I)_aB(III)_bX_{a+3b}$, comprised of interconnected $[A/B]X_6$ octahedra, being able to adopt a number of similar but slightly different structure types. Interestingly, the A- and B-site cations can occupy

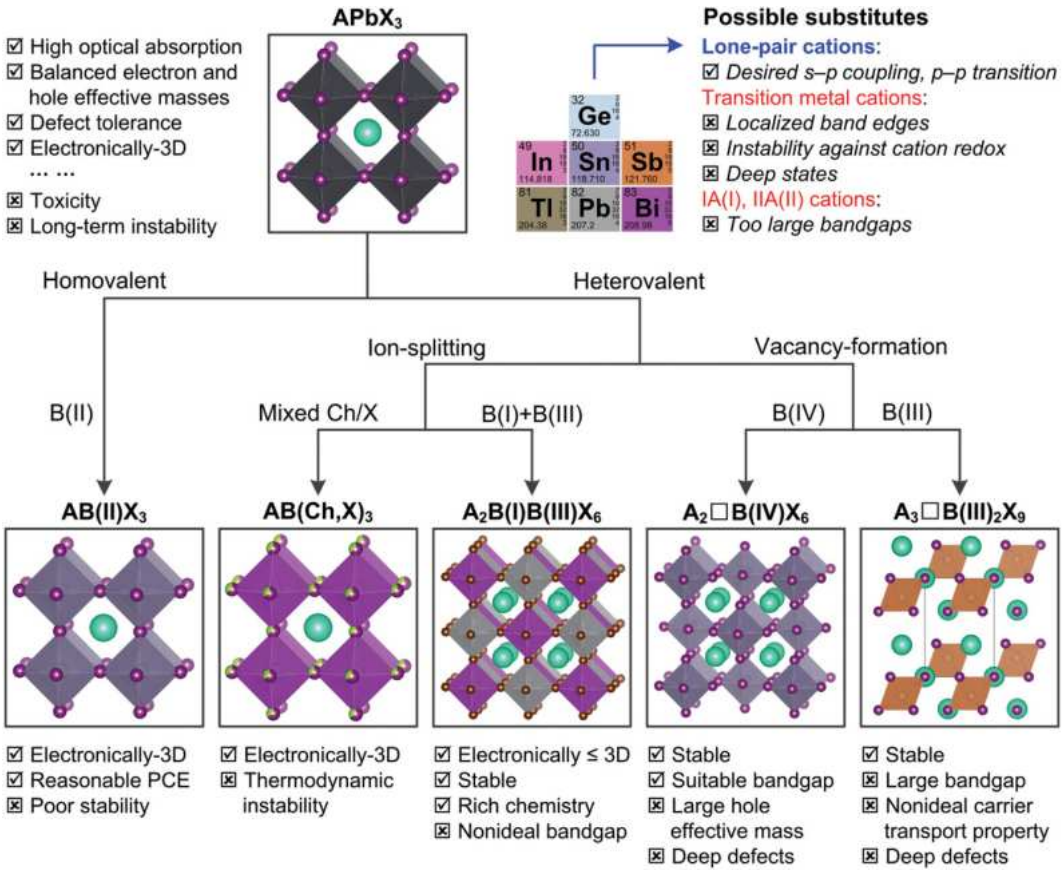

Figure 1.12: Schematic diagram of possible replacement strategies for $APbX_3$ perovskites and their structural and physical consequences, with A-site cations *A*, B-site cations with oxidation state in brackets *B*, Chalcogenides *Ch*, vacancies □ and halides *X*. Recently, antiperovskites are explored as a further alternative through ion type inversion and anion ordering in the perovskite lattice sites. Reproduced with permission from Wiley.[42,43]

the same lattice positions, leading to large stoichiometric freedom but also structural disorder. Most of these materials can be described through the $NaVO_2$ structure, identified by *Walter Rüdorff* and *Hans Becker* in 1954, with different A/B cation fractions and vacancies, and are referred to as rudorffites. As not all structures so far were proven by single crystal analysis to adopt this structure, they more generally are pnictogen-based metal halides, so far ranging from this $NaVO_2$-type to a three-dimensional (3D) defect-spinel type ($Fd\bar{3}m$) or a two-dimensional (2D) $CdCl_2$-type ($R\bar{3}m$). While research on these types of materials is still in its infancy, initial reports suggest that they are not very defect-tolerant, due to their disordered structural occupancies.[48–52]

1.1.4 Double Perovskites

In the search for lead-free perovskite alternatives, halide double perovskites are currently the most studied group of materials, only being surpassed by Sn-based perovskites. While oxide double perovskites have been well explored in the past for their unusual magnetic ground states, ferromagnetism and magnetoresistance,[53–55] halide double perovskites have only been put on the stage in 2016, due to the outstanding stability and promising optoelectronic properties of $Cs_2AgBiBr_6$.[56–58] Generally, they are based on the formula $A_2B(I)B(III)X_6$, where $[B(I)X_6]^{5-}$ and $[B(III)X_6]^{3-}$ octahedra adopt a rock salt type ordering, with the large A-site cation occupying the cuboctahedral cavities (Figure 1.13).

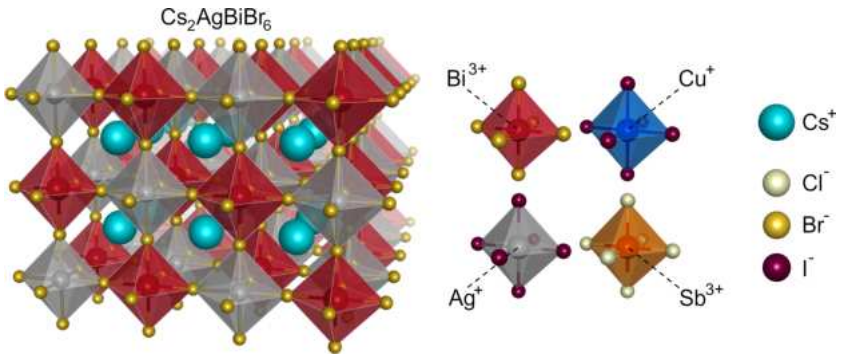

Figure 1.13: Crystal structure of the archetypal halide double perovskite $Cs_2AgBiBr_6$[56] and selected, widespread possibilities for the octahedral building blocks, the large A-site cation Cs and the halides Cl, Br and I.

Considering all possible elements, the Goldschmidt tolerance factor α (Eq. 1.10) and the octahedral factor μ (The ratio of atomic radii B to X, eq. 1.11), there are thousands of theoretically possible $A_2B(I)B(III)X_6$ double perovskites.

$$\mu = \frac{r_B}{r_X} \tag{1.11}$$

Narrowing this down by using only the following elements: A = Li, Na, K, Rb, and Cs; B(I) = Li, Na, K, Rb, Cs, Cu, and Ag; B(III) = Al, Ga, In, Sb, Bi, Sc, and Y; and X = F, Cl, Br, and I, still results in 980 possible double perovskites. High-throughput first-principles studies have shown, that when predicting their thermodynamic stability, 112 out of these 980 double perovskites are stable, demonstrating the rich chemistry this structure has to offer.[59,60]

The alternating structure of $[B(I)X_6]^{5-}$ and $[B(III)X_6]^{3-}$ octahedra gives rise to unique electronic structures, due to their asymmetric structural properties, when compared to the $[PbI_6]^{3-}$ octahedral network in lead perovskites. Since B(I) and B(III) cations have different ionic radii, metal-halide bond lengths can vary, resulting in octahedral volume vari-

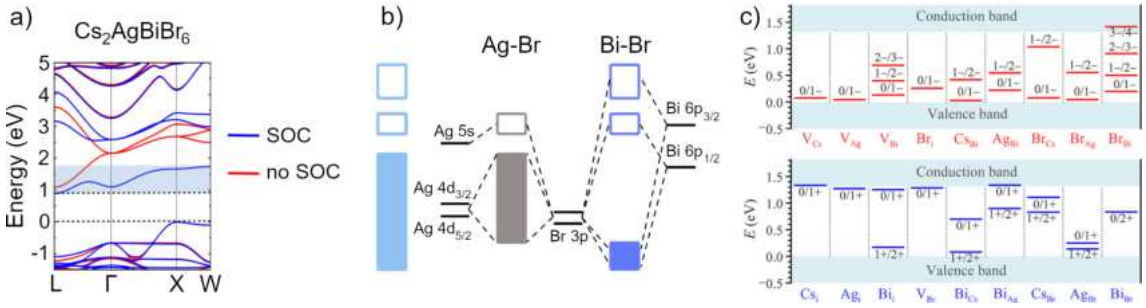

Figure 1.14: a) Electronic band structure of $Cs_2AgBiBr_6$ with (blue) and without (red) spin-orbit coupling, b) molecular orbital diagram of $Cs_2AgBiBr_6$ with atomic one electron energies as black lines, Ag-halide bands in grey, Bi-halide bands in dark blue, and the total bands in light blue, with occupied (valence) bands as filled rectangles and unoccupied (conduction) bands as empty rectangles.[61] Reproduced with permission from ACS. c) calculated defect type energies for intrinsic acceptors and donors in $Cs_2AgBiBr_6$. Reproduced with permission from Wiley.[63]

ations and distortions, which influences the orbital overlap and contributions to the band structure. Astonishingly, halide double perovskites still display a mostly cubic crystal structure with similar bond lengths and octahedral symmetries and structural distortions only start to play a role in lower dimensional substructures, which will be explained in detail in the next chapter 1.1.5. The atomic arrangement and order/disorder of B(I) and B(III) positions can further influence the band structure and the charge carrier properties.

The exemplary band structure of $Cs_2AgBiBr_6$ is shown in Figure 1.14, featuring an indirect band gap with experimental values of around 2 - 2.2 eV. For halide double perovskites and lead perovskites, spin-orbit coupling leads to a large splitting of the conduction band and is thus essential to correctly describe the band structure and the effective masses.[61] The highest valence band is predominantly made up of hybridized Ag 4d-Br 3p orbitals, while the isolated conduction band is predominantly made up of Bi 6p-Br 3p antibonding orbitals, with only a small contribution of Ag 5s-Br 3p orbitals. This hybridization between Ag and Bi orbitals is responsible for the indirect nature of the band gap. The relatively large band gap energy and indirect nature make $Cs_2AgBiBr_6$ not an ideal material for single-junction photovoltaic application. The large compositional freedom of double perovskites offers tunability though, where for example with In^+ or Tl^+ as the B(I)-site cation, a direct band gap can be achieved, which however, in light of the scarcity of In and the toxicity of Tl might not be the best option for further commercialization.[62]

Additionally, besides the octahedral disorder, $Cs_2AgBiBr_6$ has more deep defect types compared to the mostly shallow defects in $MAPbI_3$ (Fig. 1.14). Dominant defects based on formation enthalpies are Ag and Bi vacancies, Ag_{Bi} antisites and Br interstitials. While Ag vacancies are shallow and increase p-type conduction, Bi vacancies, Ag_{Bi} antisites and Br interstitials are deep and the dominant deteriorators of the photovoltaic performance.[63]

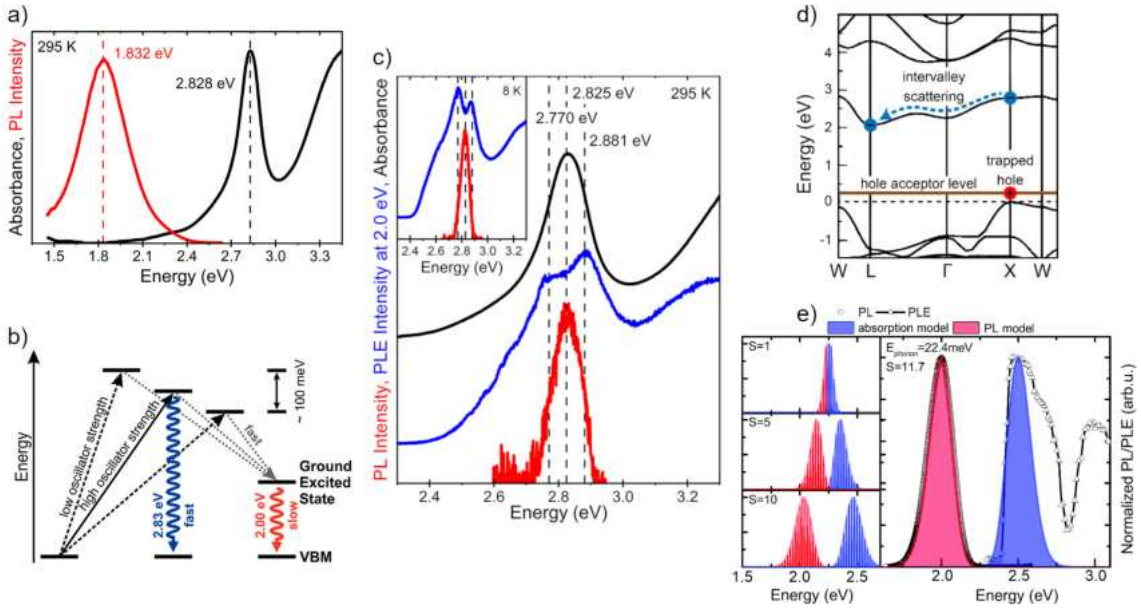

Figure 1.15: a) Absorbance and photoluminescence spectra of $Cs_2AgBiBr_6$. b) Schematic representation of the absorption, relaxation and emission processes in $Cs_2AgBiBr_6$,. c) Absorbance, photoluminescence and photoluminescence excitation spectra of $Cs_2AgBiBr_6$. Reproduced with permission from ACS.[65] d) Transition of the direct to indirect exciton through trapped hole states and intervalley scattering.[66] e) Evolution of absorption (blue) and emission spectra (red) as a function of the Huang-Rhys factor and the fitted results of this model to the PL and PLE spectra of $Cs_2AgBiBr_6$. Reproduced with permission from RSC.[67]

The initial observation of very long charge carrier recombination lifetimes (τ = 688 ns) and diffusion lengths (>1 µm) of $Cs_2AgBiBr_6$ held great promise for its photovoltaic application.[56,64] More detailed studies, though, unveiled a very complex picture of the underlying photophysical processes, requiring their elucidation for the search and optimization of functional halide double perovskites.

Starting with the absorption, $Cs_2AgBiBr_6$ has a moderate absorption coefficient between 1×10^3 cm^{-1} to 4×10^4 cm^{-1} above 2.2 eV. The absorption spectra display a shallow rise from the indirect absorption starting at 2.1 eV, followed by a characteristic, strong absorption peak at 2.83 eV and a sharp rise from the direct absorption from 3.15 eV and higher (Figure 1.15 (a)).

Photoluminescence excitation (PLE) measurements showed that this characteristic peak involves at least three individual transitions (Figure 1.15 (c)). Photoluminescence (PL) spectra display a broad, main emission, strongly red-shifted at 1.8 eV and a much weaker emission, resonantly at 2.83 eV ($I_{1.8\ eV}/I_{2.8\ eV} \approx 10^4$). The resonant absorption feature at 2.83 eV could be related to an optical transition from the $^1S_0$ ground state to the $^3P_1$ excited state, being allowed due to the strong spin–orbit coupling of the Bi ion, with possible contributions from charge-transfer states between Bi-s and Bi-p states and Ag-d and Bi/Br-p states. The involved transitions thus include one at 2.83 eV, with high os-

cillator strength, allowing for radiative recombination at 2.83 eV (Fig. 1.15 (c)), combined with two transitions, with low oscillator strength. All three compete with fast relaxation pathways down to the excited ground state, eventually emitting strongly at 1.83 eV (Figure 1.15 (b)).[65,68,69] Other explanations for the strong absorption peak and the broad, red-shifted PL emission are usually based on different types of excitons and giant electron-phonon coupling. Studies on nanocrystals could show the formation of an intitially, defect-bound direct exciton, formed through a defect-localized hole with a heavy electron in the valence band (Fig. 1.15 (d)). As the hole remains trapped, the electron can move to the conduction band minimun through intervalley scattering, transforming into an indirect exciton, leading to the observed red-shift of the PL emission.[66]

Due to the soft lattice, i.e. the highly mobile perovskite structure, $Cs_2AgBiBr_6$ exhibits substantial lattice dynamics and vibrational states, dominated by $[AgBr_6]^{5-}$ sublattice vibrations. This is another reason for the broad and strongly red-shifted PL, where longitudinal optical phonons couple to lattice interactions through Coulomb interactions, i.e. Fröhlich interactions or the formation of small polarons.[70,71] The strength of this electron-phonon coupling is characterized by the Huang-Rhys factor S, which is the average number of emitted phonons after photon absorption or emission. The evolution of the broadness and red-shift of the PL can be modelled according to this with increasing Huang-Rhys factor, and agrees well with the measured spectra with a Huang-Rhys factor $S = 11.7$ and a phonon energy of 22.4 meV (Fig. 1.15). This model is further based on the emission originating from a color center, rather than a band-to-band transition. Color centers are a type of crystallographic defect, where vacancies in the lattice are occupied by charge carriers, which can absorb photons, effectively from a defect state in the band gap. While its exact nature is unclear, it is caused by the strong deformation of the lattice after light absorption and carrier trapping through intrinsic, excitonic, defect-related or self-trapping events. Due to the soft lattice characteristics, lattice disorder and low formation energies for Ag vacancies and Ag_{Bi} antisites, it is suggestive that defects might be a likely explanation.[67]

Further studies on the charge-carrier dynamics revealed ultrafast localization of the initially highly mobile, delocalized states to self-trapped, small polaronic states, eventually diffusing to emissive color centers. This relaxation of the free carriers to localized states happens on a timescale of 1 ps, with initial delocalized state mobility $\approx 3\,cm^2\,V^{-1}\,s^{-1}$ and localized state mobility $\approx 1.3\,cm^2\,V^{-1}\,s^{-1}$ at 295 K (Fig. 1.16 a) and b)). While the self-trapping is not ideal for optoelectronic applications, the mobilities of delocalized and localized states are still respectable, especially in light of the temperature activation energy being present at room temperature, making photovoltaic application feasible.[72] With all the above explained phenomena, the carrier diffusion length in $Cs_2AgBiBr_6$ still

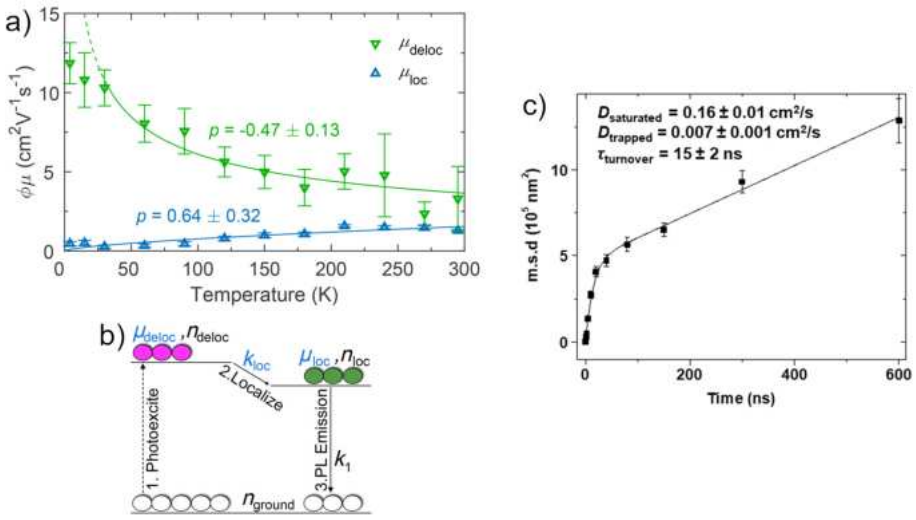

Figure 1.16: a) Temperature dependent, effective charge-carrier mobilities for the delocalized state (green) and localized state (blue) in $Cs_2AgBiBr_6$ from optical-pump terahertz-probe spectroscopy (OPTP), b) schematic of the two-level mobility model used to fit the OPTP decays with the intial delocalized state (pink) and the localized state (green)[72] and c) mean squared displacement of the expanding carrier distribution in $Cs_2AgBiBr_6$ with an initial trap-saturated charge diffusivity (D_{sat}) and a secondary trapping and thermally detrapping diffusivity from shallow traps (D_{trap}). Reproduced with permission from ACS.[64]

reaches ∼1.4 µm, due to long lifetimes of excited states, respectable mobilities of free and trapped states as well as predominance of shallow over deep trapping (Fig. 1.16 c)).[64]

Overall, the intrinsic charge-carrier properties and complex, underlying photophysics of $Cs_2AgBiBr_6$ have been explored in increasing detail throughout the recent years, as it is a flag bearer for the emerging field of halide double perovskites. While demonstrating limitations, this also offers opportunities for material optimization through fundamental understanding.

The partially promising intrinsic properties and the material being non-toxic and highly stable, quickly led to the incorporation of $Cs_2AgBiBr_6$ in photovoltaic devices, with the first report in 2017 delivering a PCE of 2.43%.[73] Considering the Shockley-Queisser limit and numerical simulations for optimized electron and hole extraction materials, $Cs_2AgBiBr_6$ could deliver a PCE of 18.18%, although under the more realistic spectroscopic limited maximum efficiency (SLME) metric, considering also the band gap nature and the strength of the optical absorption, the PCE is predicted to be 7.92%.[74,75] With reported values for the PCE struggling to exceed even 3%, much room for improvement is still left, as most solar cells are still based on the established electron and hole extraction materials being adopted from lead-based perovskite solar cell architectures.[76] These include mainly TiO_2 as the electron transport material and 2,2',7,7'-Tetrakis[N,N-di(4-methoxyphenyl)amino]-9,9'-spirobifluorene (Spiro-O-MeTAD) or poly(3-hexylthiophene-2,5-diyl) (P3HT) as the hole transport materials, while optimized simulations suggest ZnO as the electron transport material and Cu_2O or CuI as inorganic hole transport materials.[74,77]

Detailed studies confirmed the bottlenecks in $Cs_2AgBiBr_6$ solar cells to be the poor energy level alignment and charge carrier selectivity of the commonly used transport and contact materials, as well as large charge carrier recombination rates at the interfaces.[78,79] $Cs_2AgBiBr_6$ solar cells further suffer from a detrimental carrier mobility imbalance in the thin film material compared to the single crystal, with electron diffusion lengths of only 30 nm, due to a prevalence of energetic disorder and high density of electron trap states, compared to hole diffusion lengths greater than 150 nm.[80]

Ultimately, the present research directions for halide double perovskites focus on either finding more suitable areas of application, such as X-ray detection, where it is on par or even outperforming its lead based counterparts,[81,82] or moving towards material optimization to find more suitable double perovskites with direct band gaps, smaller band gap energies or otherwise improved charge carrier properties for photovoltaic application. While different B(I) and B(III) site combinations have already been explored, the obvious target of iodide double perovskites has so far largely eluded experimental realization. Following the elemental, periodic trend of the halides, the iodide compounds would lower the band gap energies significantly, bringing them closer to the optimum value for photovoltaic absorption. Unfortunately, due to the larger ionic size of I^-, the perovskite structure is mostly not able to support the interconnected octahedral coordination, required for its formation. Instead the formation of lower-dimensional, ternary $A_3B_2X_9$ phases is thermodynamically favored.[83] One alternative way to access the family of iodide double perovskites is the construction of two-dimensional double perovskites, which will be explained in the following chapter 1.1.5.

1.1.5 2D Perovskites

The research field of 2D halide perovskites and especially 2D halide double perovskites is rapidly growing. It has evolved from the exploration of 3D double perovskites, right after 3D lead perovskites were established in the scientific world of semiconductors. The motivation to synthesize 2D perovskites can be derived from a combination of principles and promises these materials possess. One one hand, the compositional limitation of 3D perovskites, due to the limited number of suitably small A-site cations (Cs^+, MA^+, FA^+), encourages the idea to include larger organic cations, which proved to stabilize octahedral distortions to a much larger extent than in the conventional 3D corner-sharing inorganic framework, giving access to otherwise metastable perovskite phases. On the other hand, this directly and extensively expands the compositional space, since the number of suitable organic molecules is very large. Including the compositional space for B(I)- and B(III)-site cations in double perovskites, the enormous number of materials to explore becomes evident.

The general formula of 2D perovskites, derived from the ABX_3 perovskite crystal lattice, can be expressed as $(A')_m(A)_{n-1}B_nX_{3n+1}$, where monovalent ($m = 2$) or divalent ($m = 1$) organic cations ($A'$) intercalate between the inorganic perovskite layers, with n being the number of inorganic layers, essentially forming a layered 2D perovskite structure.[84–86] In 2D double perovskites the formula is simply expanded to $(A')_{2m}(A)_{2n-2}B(I)_nB(III)_nX_{6n+2}$. Most reports consider 2D perovskites as such, if the intercalation of the organic layer is along the <100> or <001> direction, depending on the structure solution, with the classic corner-sharing octahedral motif. Other connectivity modes of the octahedra also exist, such as edge-sharing or face-sharing, as well as the intercalation being along the <110> or <111> directions, although these are more unconventional (Fig. 1.17 a).[84] The standard 2D perovskite crystal structure is shown as an evolution from the 3D perovskite structure down to 2D perovskites with decreasing inorganic layer thickness n in figure 1.17 b. In theory, this layer thickness n can be anywhere between 1 and ∞, although crystallographically defined structures only exist for $n < 7$, as structures with thicker inorganic layers have unfavorable enthalpies of formation and tend to form quasi 2D structures, leading to phase mixtures of 2D and 3D perovskites in reality.[87] Higher n phases are also more easily formed and observed for homovalent B(II) perovskites, than in the heterovalent B(I)+B(III) double perovskites, where the highest reported n value in a crystal structure is 2 in $(BA)_2CsAgBiBr_7$ (BA = butylammonium).[69,85,86]

Another classification for standard 2D perovskite structures is based on the connectivity of the organic layer, as the organic cations can be mono- or divalent, allowing them to either bind into one or two cuboctahedral cavities of the inorganic layers. For monovalent

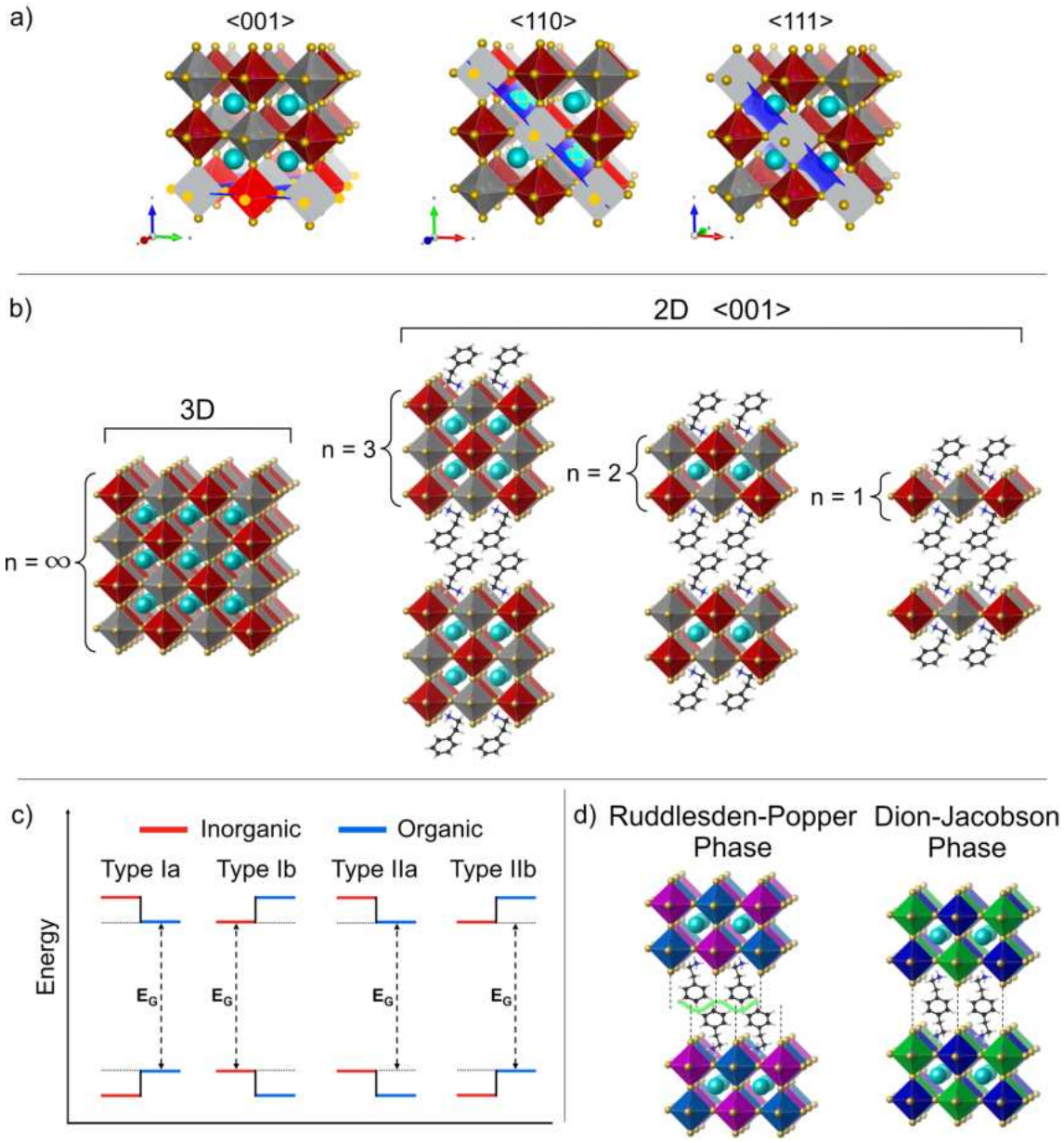

Figure 1.17: a) Three structural motifs for the formation of 2D perovskites when atomic layers along the <001>, <110> or <111> direction are removed and replaced by organic cations, with lattice planes in blue and removed layers highlighted. b) Structural evolution from the 3D to 2D double perovskite structures with decreasing inorganic layers n, c) Band structure alignment types between the inorganic and organic framework in 2D perovskites, with the inorganic frontier band contributions in red and the organic in blue and d) Ruddlesden-Popper phase on the left, with illustrated van der Waals gap in green in the organic layer and Dion-Jacobson phase on the right. Inorganic layer octahedral offsets depicted with dotted lines.

organic cations, the organic layer consists of a bilayer where the organic cations are interacting with each other via van der Waals, hydrogen bonding or dipole-dipole interactions. Borrowed from the nomenclature of oxide perovskites, they are known as Ruddlesden-Popper (RP) phases and are characterized by the van der Waals gap in the organic layer and also often feature an offset between inorganic octahedral layers (Fig. 1.17 d). For

divalent organic cations, the organic layer is a single molecule layer where the connection from one inorganic cuboctahedral binding site to the other extends through the covalent bonds of the organic cation. They are known as Dion-Jacobson (DJ) phases and mostly do not feature an offset between the inorganic octahedral layers.[84–86]

One key feature of 2D perovskites is the special electronic structure resulting from the spatial separation of the inorganic and organic layers. Since the combined electronic structure is derived from the inorganic band structure and the organic molecular orbitals, the resulting band structure can be described as a quantum well system. The frontier bands can be made up of different combinations of inorganic VBM, inorganic CBM, organic highest occupied molecular orbital (HOMO) and organic lowest unoccupied molecular orbital (LUMO) levels, being alternated in real space through the layered crystal structure. Depending on the alignment they are classified as type Ia, Ib, IIa, or IIb electronic heterojunctions (Figure 1.17 c). These special electronic structures offer interesting opportunities for materials design and are explored in growing detail in contemporary research. Since the organic cations play a major role in defining these properties, they will be explained in the following.

The options for organic cations are manifold, but should still be considered under the restrictions or limits for them to form a 2D perovskite. The first requirement is the anchoring moeity intended to bind into the cuboctahedral cavity. This needs to be a positively charged group, with a size that is not greater than the cuboctahedral cavity. Most commonly these are nitrogen-containing functional groups, i.e. amino or ammonium groups, although other heteroatom bonds with a strong dipole, for example terminal C – I bonds, are also possible.

Secondly, the organic cation must have at least one of these anchoring moeities, mostly they possess one or two, as described earlier for mono- and divalent cations. Theoretically, more than two anchoring moeities are also possible, but the geometric requirement for the organic cations, to still fit into the grid of cuboctahedral cavities to form the 2D perovskite gets increasingly challenging.

Thirdly, the organic cation has a spatial limitation to form the 2D perovskite phase. The main limitation therein is the width in the in-plane structural dimensions, as the organic cations must stack close enough to each other so that every cuboctahedral cavity will still be filled with an anchoring moeity. Considering this limitation, it is clear why in theory higher valent cations should be possible, reminiscent of coordination complex chemistry and molecules such as ethylenediaminetetraacetic acid (EDTA), but due to the geometric requirement mostly mono- and divalent cations have been reported in 2D perovskites. Interestingly, for the size limitation in the third dimension, i.e. the out-of-plane direction, there seems to be much flexibility, as 2D perovskites with interlayer spacings of up to

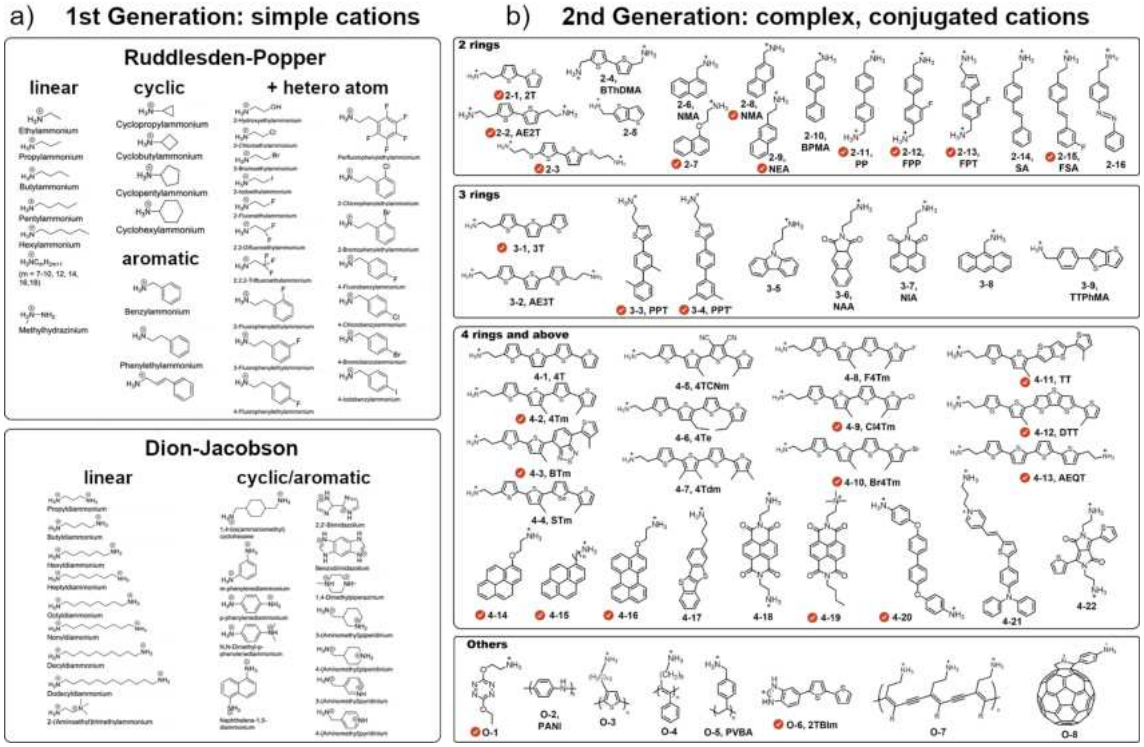

Figure 1.18: a) First generation organic cations based on simple, linear alkylic, cyclic or aromatic alkylic and hetero atom containing functional groups. Divided into monovalent cations, forming Ruddlesden-Popper phases and divalent cations, forming Dion-Jacobson phases. Reproduced with permission from ACS.[85] b) Second generation organic cations based on more complex and conjugated functional groups. Divided into groups according to the number of included ring systems (2, 3, 4 and above) and other, special mentions such as polymers and fullerenes. The red ticks indicate confirmed 2D perovskite crystal structures with the related cation. Reproduced with permission from ACS.[86]

31.4 Å, based on a monovalent, alkylic C_{18} chain cation have been reported.[88]

Following these limitations, the suitable organic cations can be categorized according to their central underlying functional groups. Based on historic increase in complexity of the cations, they can be divided into two main groups: The first generation, consisting of simple organic cations; and the second generation, consisting of more complex and most importantly, fully conjugated organic cations (Fig. 1.18). Next, first generation cations can be categorized by their functional group type and second generation cations by their number of molecular rings.

Simple, linear alkylic chain cations were explored very early, with butylammonium being incorporated into the homologous series of $(BA)_2(MA)_{n-1}Sn_nI_{3n+1}$ (n = 1-5) already in the year 1994.[89] Alkylic cations containing cyclic, non-aromatic groups can be seen as the next category of cations being able to form 2D perovskites. The third category are cations containing aromatic systems such as the widely used phenethylammonium (PEA), or other aromatic systems with varying alkylic chain lengths. They were also explored quite early with reports dating back to the year 1991 for 2D perovskites, such as

$(PEA)_2SnI_4$.[89–91] These three categories yield 2D perovskites with similar optoelectronic properties, mainly due to the small and simple organic cations being electrically insulating and producing mainly type Ib quantum well structures. Charge carriers are mainly generated and spatially limited in the inorganic part of the framework. A main factor influencing the band gap of these 2D perovskites results from the degree of octahedral tilting induced by the penetration depth of the anchoring group into the cuboctahedral cavities and the octahedral deformation through the cation size. Perfect 180° metal-halide-metal bond angles result in the largest orbital overlap and thus smallest band gaps, while distorted bond angles increase the band gap energy.[85] The promise of aromatic systems is that through π-π stacking the charge transport through the organic layer could be increased. While this favorable π-π stacking can be observed for even the smallest aromatic cations such as phenethylammonium, the insufficient orbital overlap in the intra-organic layer stacking (in Ruddlesden-Popper phases), as well as the large difference of the frontier band contributions between organic and inorganic layers in, i.e., type Ib quantum wells (in both Ruddlesden-Popper and Dion-Jacobson phases), still act as a barrier for charge carriers.

Increasing the size of the aromatic, conjugated systems can be used to modify the molecular orbitals and their energy alignment in the resulting 2D perovskites band structure. Consequently, large aromatic groups such as naphthalene, pyrene or perylene were shown to form different types of quantum wells and also increase the charge carrier transport through the organic layer in the out-of-plane lattice direction.[92] The downside of larger cations is the reduced solubility in the commonly used strong polar solvents, which can be alleviated by including methyl side chains, often employed for cations with three ring systems and above.

A subcategory or a combination of the aformentioned, three categories for organic cations can be considered as cations that include a heteroatom such as O, F, Cl, Br or I. The molecular dipole formed in the cation can influence the stacking between the organic cations themselves, as well as the penetration depth into the cuboctahedral inorganic cavities. The reasons for this are either increased dipole-dipole interactions or hydrogen bonding between the organic cation's functional groups and the heteroatoms, or between the inorganic halides and the heteroatoms.[85] Another interesting feature is the position of the heteroatoms on the organic cations, i.e. on the ortho-, meta-, or para-position of a phenyl ring, which can also influence the arrangement and stacking of the organic cations, influencing the structure and the resulting optoelectronic properties directly.[93,94]

The fourth category of organic cations is an extended case resulting from a combination of aromatic, heteroatom including cations. It represents organic cations that contain thiophene groups, enabling further modification of the molecular orbital energy levels and

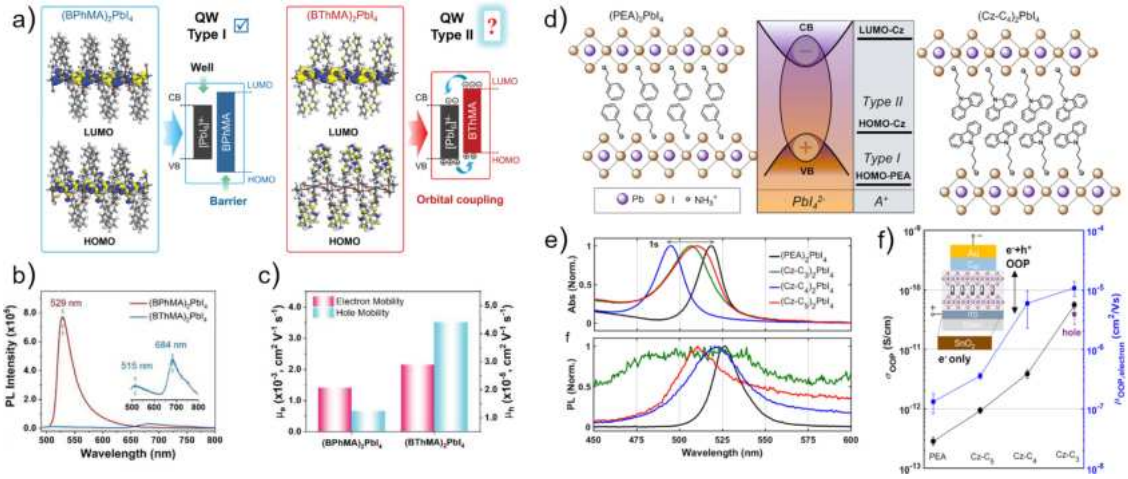

Figure 1.19: a) Density functional theory (DFT) calculated HOMO and LUMO and energy levels of organic and inorganic components of $(BPhMA)_2PbI_4$ and $(BThMA)_2PbI_4$, forming a type Ib and type IIb band alignment. b) PL spectra of $(BPhMA)_2PbI_4$ and $(BThMA)_2PbI_4$, displaying the quenched PL intensity for the type IIb band alignment of $(BThMA)_2PbI_4$. c) Charge carrier mobilities of $(BPhMA)_2PbI_4$ and $(BThMA)_2PbI_4$. Reproduced with permission from Wiley.[98] d) Schematic structures of $(PEA)_2PbI_4$ and $Cz-C_4)_2PbI_4$ with the schematic band diagram forming a type Ib and type IIb band alignment. e) Ultraviolet-visible light (UV-Vis) absorption and PL spectra of $(PEA)_2PbI_4$ and $Cz-C_i)_2PbI_4$ materials, displaying the quenched PL intensity for the type IIb band alignment of $Cz-C_4)_2PbI_4$. f) Out-of-plane charge carrier mobilities of $(PEA)_2PbI_4$ and $Cz-C_i)_2PbI_4$ devices.[99]

the band structure, similar to the use of large aromatic groups discussed among category three cations. This type of oligothiophene cations was explored initially in the year 1999, but the subject was picked up again recently.[95–97] These larger aromatic and thiophene containing cations offer the largest tunability and together with other exotic cases, such as polymers, form the second generation of cations that are now in the focus of current research (Fig. 1.18 b) to increase the out-of-plane conductivity and explore the photoactivity of the organic layer. Comparing a biphenylmethylammonium (BPhMA) cation with a bithiophenemethylammonium (BThMA) cation established the formation of a type Ib quantum well for $(BPhMA)_2PbI_4$ and a type IIb quantum well for $(BThMA)_2PbI_4$. In the type IIb case this leads to charge carrier separation, with electrons localizing in the inorganic layers and holes localizing in the organic layer (Fig. 1.19 a). Observable in the photoluminescence of such materials, the emission from the recombination in the inorganic layer in a type Ib structure will be strongly quenched in a type IIb structure, as here this radiative recombination is optically forbidden and competing with the lower energy radiative recombination as well as the non-radiative thermalization (Fig. 1.19 b). The charge carrier separation can be further confirmed by an increased electron and especially increased hole mobility (Fig. 1.19 c).[98]

More recently, a new group of electroactive carbazole-based organic cations (Cz-C_i) was explored, demonstrating their influence on the charge transfer dynamics in lead-based 2D perovskites. Compared to the electronically inactive PEA cation, leading to excitonic

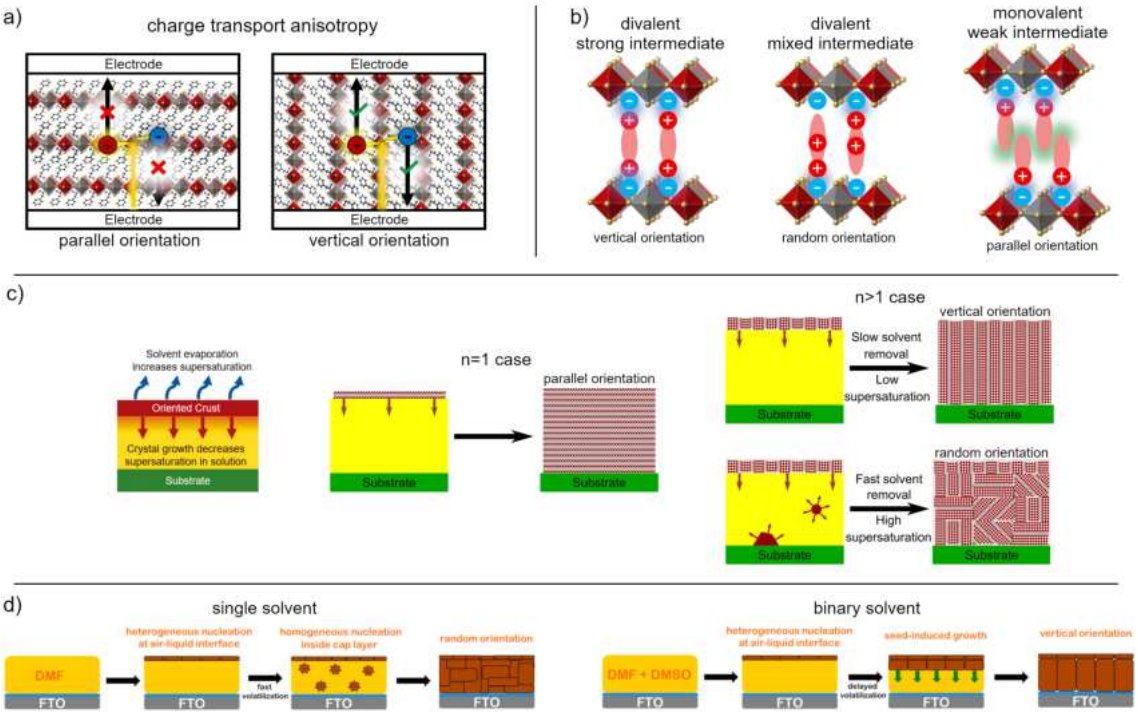

Figure 1.20: a) Charge transport anisotropy problem in 2D perovskites in a planar device architecture, common in photovoltaics or LEDs. b) Templating effect of mono- and divalent organic cations leading to the formation of different crystallization intermediates and orientations. Reproduced with permission from RSC.[102] c) Crystallization mechanism for solution based thin films, with different outcomes for the $n = 1$ and $n > 1$ case. Slow solvent evaporation can lead to a more preferential growth in $n > 1$ perovskites, here $(BA)_2(MA)_3Pb_4I_{13}$ ($n = 4$) compared to a fast solvent evaporation. Reproduced with permission from ACS.[103] d) Example of binary solvent engineering to affect the thin film crystal growth in $(BA)_2(MA)_3Pb_4I_{13}$ ($n = 4$). Reproduced with permission from ACS.[104]

charge carriers that are confined to the inorganic perovskite lattice, the Cz-C_i based 2D perovskites showed a photoinduced hole transfer from the inorganic to the organic layer, promoting the exciton separation and prolonging the charge carrier lifetimes (Fig. 1.19 d). The efficiency of this hole transfer was further found to depend on the distance between the inorganic layer and the carbazole core of the organic layer, also manifested in the increased out-of-plane conductivity for shorter inorganic-carbazole core distances. The same quenching behaviour of the PL as mentioned earlier for type IIb alignments can also be observed (Fig. 1.19 e-f).[99]

In the context of photovoltaics and other device applications, the improved structural stability of 2D perovskites is another advantage over their 3D counterparts. Due to the larger organic cations and their hydrophobicity, the stability towards moisture is greatly increased. Additionally, intrinsic degradation compared to MA- and FA-containing perovskites and the prevalent ion migration processes are also decreased due to the more stable cations and crystal structures.[100,101]

The anisotropic, layered crystal structures of 2D perovskites bring another important aspect of these materials into consideration, namely the crystal orientation, since in functional devices, the architectural component usually implicates a flow direction of electric current, either being extracted (photovoltaic, photodetection) or injected (LEDs). For photovoltaic devices, the generated charge carriers must be able to separate (typically) vertically to the substrate, towards the top and bottom electrodes of the device (for LEDs vice versa through injection), while for transistors they must separate parallel to the substrate towards the electrodes. These two orientational cases in a planar architecture are illustrated in figure 1.20 a. Synthetic control over the crystallographic growth direction is therefore crucial and still poses a challenge, as a complete, mechanistic understanding is still not established and as the growth depends strongly on the different perovskite system and the specific organic cations employed.[101,105]

Possible methods to influence the growth orientation of 2D perovskite thin films include the use of additives, solvent-intermediate interactions or the exploitation of substrate-nucleation effects. While for some 2D perovskites these approaches showed some success, the general tendency of 2D perovskites is to crystallize with the organic and inorganic layers being oriented parallel to the substrates surface. This is due to the fact that the crystallization generally starts at the substrate-solution or solution-atmosphere interfaces. Since the inorganic or organic constituents have favored binding situations and nucleation sites, for example organic cations will organize as a layer at the solution-atmosphere interface, forcing the subsequent layers to crystallize downward resulting in the substrate-parallel orientation (Fig. 1.20 c).[101] Solvent engineering and the formation of different solvent-intermediates, i.e. via coordination of dimethylsulfoxide (DMSO), dimethylformamide (DMF) or other solvents with the inorganic octahedral intermediates or colloids, combined with solvent annealing and post-annealing processes can influence and rearrange the orientation to be vertical to the substrate (Fig. 1.20 d). Understanding and finding the right organic cations with specific crystallization-inducing functional groups for chemical self-assembly and directed orientiational growth remains a major goal in 2D perovskite research.[101,105] This challenge is even greater for 2D double perovskites, as most findings were established with lead- or tin-based 2D perovskites and do not translate directly to 2D double perovskite crystallization kinetics. Additionally, since the formation of 2D double perovskites with $n > 2$ has not yet been realized, their properties remain unknown. The explored crystallization kinetics are mostly based on Ruddlesden-Popper phases, while the crystallization kinetics for Dion-Jacobson phases should be established. For $n = 1$ 2D double perovskites it could be shown that the valence, the shape and the charge distribution in the organic cation can all have a strong influence on the resulting film crystallization (Fig. 1.20 b). Since the different groups in the

organic cations have different bonding strengths and capabilities to each other and the inorganic network, different crystallization rates and preferences regarding different crystal facets dictate the crystallization. The positively charged ammonium or amine groups bind through strong electrostatic interactions into the cuboctahedral cavities, while the alkylic chains only bind to each other through weaker van der Waals interactions. Furthermore, the position of the positively charged groups in divalent cations also creates different bonding strengths. This leads to different solution intermediate formation and subsequent crystallization, where monovalent cations tend to bind primarily in-plane to each other and into the inorganic framework's cuboctahedral cavities, leading to the aforementioned solution-atmosphere interface crystallization and parallel orientations. Divalent cations on the other hand will (on both sides) primarily bind into the inorganic framework, leading to a vertical orientation. Divalent cations with differently positioned positive groups have imbalanced binding forces, leading to a random orientation.[102]

It is apparent that a significant exploration of 2D perovskites with various organic cations was already conducted almost 30 years ago, but these reports were mainly focused on the structural characterization of this newly established material class and their basic optoelectronic properties. Although incoroporation of 2D perovskites such as $(PEA)_2SnI_4$ in functioning devices such as a field-effect transistor was already demonstrated,[91] many concepts are now witnessing renewed consideration and extension, due to the success of lead halide perovskites in photovoltaics. These studies now focus in more detail on structure-function relationships and the control of the electronic structure and the charge carrier physics of these materials.

1.1.6 Scope of the Thesis

This thesis was conceived in view of the two major challenges in the search for lead-free perovskite materials. The first being the removal of the toxic Pb^{2+} as a constituent and the second being the synthesis of lead-free materials that are stable against atmospheric conditions.

With $Cs_2AgBiBr_6$ having these two key properties, it was the structural and material point of origin of this study. Accessing more suitable electronic structures and the double perovskite iodide phases formed the basis for the exploration of Ag-Bi based 2D double perovskites $(4\,FPEA)_4AgBiX_8$ (X = Cl, Br, I) in chapter 2, while also gaining a better understanding of the challenging charge-carrier dynamics of Ag-Bi based double perovskites.

As a consequence, the synergies of the 3D and 2D double perovskite phases were used to improve the performance and properties of $Cs_2AgBiBr_6$ solar cells in chapter 3, by constructing a 3D/2D heterojunction with $(PEA)_4AgBiBr_8$ towards the hole transport material and anode side of the solar cell.

Inspired by the controllable structure-function relationship of pure 2D perovskites, ultimately the intrinsic challenges and opportunities regarding 2D perovskites were addressed in chapter 4. Charge transport anisotropy and the electronic quantum well structure were explored and controlled through the use of conjugated organic cations based on naphthalene and pyrene moieties in $(X)_4AgBiI_8$ and $(X)_4CuBiI_8$ (X = NOE, NOP, POE, POP).

In chapter 5, the perovskite-inspired structure of rudorffites was explored as another possible lead-free photovoltaic material, demonstrating the synthesis of a $Cu_{1-x}Ag_xSbI_4$ phase, its feasibility as a solar cell absorber material and the challenges based on the structure's inherent degree of disorder.

1.2 References

[1] J.-J. Hublin, A. Ben-Ncer, S. E. Bailey, S. E. Freidline, S. Neubauer, M. M. Skinner, I. Bergmann, A. Le Cabec, S. Benazzi, K. Harvati, et al., *Nature* **2017**, *546*, 289–292.

[2] Z. Yin, K. Vargas, J. Cunningham, S. Bengtson, M. Zhu, F. Marone, P. Donoghue, *Current Biology* **2019**, *29*, 4307–4314.

[3] P. K. Strother, L. Battison, M. D. Brasier, C. H. Wellman, *Nature* **2011**, *473*, 505–509.

[4] B. Cavalazzi, L. Lemelle, A. Simionovici, S. L. Cady, M. J. Russell, E. Bailo, R. Canteri, E. Enrico, A. Manceau, A. Maris, et al., *Science Advances* **2021**, *7*, eabf3963.

[5] H. Ritchie, L. Rodés-Guirao, E. Mathieu, M. Gerber, E. Ortiz-Ospina, J. Hasell, M. Roser, Population Growth, https://ourworldindata.org/population-growth, Accessed: 10.09.2023.

[6] H. Ritchie, M. Roser, P. Rosado, Energy, https://ourworldindata.org/energy, Accessed: 10.09.2023.

[7] M. Grubb, C. Okereke, J. Arima, V. Bosetti, Y. Chen, J. Edmonds, S. Gupta, A. Köberle, S. Kverndokk, A. Malik, et al. in *IPCC, 2022: Climate Change 2022: Mitigation of Climate Change. Contribution of Working Group III to the Sixth Assessment Report of the Intergovernmental Panel on Climate Change*, Cambridge University Press, **2022**, pp. 150–213.

[8] S. Dhakal, J. Minx, F. Toth, Reisinger, W. F. Lamb, N. Döbbeling, T. Wiedmann, K. Hubacek, R. M. Andrew, M. Crippa, P. M. Forster, J. Olivier, G. P. Peters, J. Pongratz, M.Rigby, M. Saunois, S. J. Smith, E. Solazzo, H. Tian, K. Blok, H. Clark, A. Cowie, J. Fuglestvedt, O. Geden, V. Ginzburg, C. Guivarch, J. I. House, R. Mrabet, G. J. Nabuurs, K. Riahi, A. H. Strømman, R. Schaeffer, D. P. van Vuuren, A. A. Khourdajie, R. Slade in *IPCC, 2022: Climate Change 2022: Mitigation of Climate Change. Contribution of Working Group III to the Sixth Assessment Report of the Intergovernmental Panel on Climate Change*, Cambridge University Press, **2022**, pp. 215–275.

[9] I. P. O. C. Change, *Agenda* **2007**, *6*, 333.

[10] H. Ritchie, M. Roser, P. Rosado, CO2 and Greenhouse Gas Emissions, https://ourworldindata.org/co2-and-greenhouse-gas-emissions, Accessed: 10.09.2023.

[11] G. Pearson, W. H. Brattain, *Proceedings of the IRE* **1955**, *43*, 1794–1806.

[12] M. Grundmann, *Physics of semiconductors*, *Vol. 11*, Springer, **2010**.

[13] H. Ibach, H. Lüth, *Solid-state physics: an introduction to principles of materials science*, Springer Science & Business Media, **2009**.

[14] C. Kittel, P. McEuen, *Introduction to solid state physics*, John Wiley & Sons, **2018**.

[15] J. A. Nelson, *The physics of solar cells*, World Scientific Publishing Company, **2003**.

[16] P. Würfel, U. Würfel, *Physics of solar cells: from basic principles to advanced concepts*, John Wiley & Sons, **2016**.

[17] W. Shockley, H. Queisser in *Renewable Energy*, Routledge, **2018**, Vol2-35–Vol2-54.

[18] The Solar Spectrum, https://seos-project.eu/earthspectra/earthspectra-c02-p12.nl.html, Accessed: 10.09.2023.

[19] National renewable energy laboratory best research-cell efficiency chart, https://www.nrel.gov/pv/cell-efficiency.html, Accessed: 28.09.2023.

[20] V. M. Goldschmidt, *Naturwissenschaften* **1926**, *14*, 477–485.

[21] H. Kay, P. Bailey, *Acta Crystallographica* **1957**, *10*, 219–226.

[22] C. C. Stoumpos, C. D. Malliakas, M. G. Kanatzidis, *Inorganic chemistry* **2013**, *52*, 9019–9038.

[23] J. S. Manser, J. A. Christians, P. V. Kamat, *Chemical reviews* **2016**, *116*, 12956–13008.

[24] A. Kojima, K. Teshima, Y. Shirai, T. Miyasaka, *Journal of the american chemical society* **2009**, *131*, 6050–6051.

[25] W. Gao, X. Gao, T. A. Abtew, Y.-Y. Sun, S. Zhang, P. Zhang, *Physical Review B* **2016**, *93*, 085202.

[26] W.-J. Yin, T. Shi, Y. Yan, *Applied Physics Letters* **2014**, *104*.

[27] T. Umebayashi, K. Asai, T. Kondo, A. Nakao, *Physical Review B* **2003**, *67*, 155405.

[28] K. X. Steirer, P. Schulz, G. Teeter, V. Stevanovic, M. Yang, K. Zhu, J. J. Berry, *ACS Energy Letters* **2016**, *1*, 360–366.

[29] Y. Yang, D. P. Ostrowski, R. M. France, K. Zhu, J. Van De Lagemaat, J. M. Luther, M. C. Beard, *Nature Photonics* **2016**, *10*, 53–59.

[30] M. Lyu, J.-H. Yun, P. Chen, M. Hao, L. Wang, *Advanced Energy Materials* **2017**, *7*, 1602512.

[31] M. Ren, X. Qian, Y. Chen, T. Wang, Y. Zhao, *Journal of Hazardous Materials* **2022**, *426*, 127848.

[32] B.-w. Park, S. I. Seok, *Advanced Materials* **2019**, *31*, 1805337.

[33] B. Conings, J. Drijkoningen, N. Gauquelin, A. Babayigit, J. DHaen, L. DOlieslaeger, A. Ethirajan, J. Verbeeck, J. Manca, E. Mosconi, et al., *Advanced Energy Materials* **2015**, *5*, 1500477.

[34] A. H. Slavney, R. W. Smaha, I. C. Smith, A. Jaffe, D. Umeyama, H. I. Karunadasa, *Inorganic chemistry* **2017**, *56*, 46–55.

[35] S. Wang, A. Wang, F. Hao, *Iscience* **2022**, *25*.

[36] M. Saliba, T. Matsui, J.-Y. Seo, K. Domanski, J.-P. Correa-Baena, M. K. Nazeeruddin, S. M. Zakeeruddin, W. Tress, A. Abate, A. Hagfeldt, et al., *Energy & environmental science* **2016**, *9*, 1989–1997.

[37] S. Ma, G. Yuan, Y. Zhang, N. Yang, Y. Li, Q. Chen, *Energy & Environmental Science* **2022**, *15*, 13–55.

[38] I. Kopacic, B. Friesenbichler, S. F. Hoefler, B. Kunert, H. Plank, T. Rath, G. Trimmel, *ACS Applied Energy Materials* **2018**, *1*, 343–347.

[39] J. Cao, F. Yan, *Energy & Environmental Science* **2021**, *14*, 1286–1325.

[40] Y.-Y. Sun, M. L. Agiorgousis, P. Zhang, S. Zhang, *Nano letters* **2015**, *15*, 581–585.

[41] F. Igbari, Z.-K. Wang, L.-S. Liao, *Advanced Energy Materials* **2019**, *9*, 1803150.

[42] Z. Xiao, Z. Song, Y. Yan, *Advanced Materials* **2019**, *31*, 1803792.

[43] D. Han, C. Feng, M.-H. Du, T. Zhang, S. Wang, G. Tang, T. Bein, H. Ebert, *Journal of the American Chemical Society* **2021**, *143*, 12369–12379.

[44] B. Saparov, J.-P. Sun, W. Meng, Z. Xiao, H.-S. Duan, O. Gunawan, D. Shin, I. G. Hill, Y. Yan, D. B. Mitzi, *Chemistry of Materials* **2016**, *28*, 2315–2322.

[45] F. Bai, Y. Hu, Y. Hu, T. Qiu, X. Miao, S. Zhang, *Solar energy materials and solar cells* **2018**, *184*, 15–21.

[46] B. Saparov, F. Hong, J.-P. Sun, H.-S. Duan, W. Meng, S. Cameron, I. G. Hill, Y. Yan, D. B. Mitzi, *Chemistry of Materials* **2015**, *27*, 5622–5632.

[47] N. Giesbrecht, A. Weis, T. Bein, *Journal of Physics: Energy* **2020**, *2*, 024007.

[48] T. Oldag, T. Aussieker, H.-L. Keller, C. Preitschaft, A. Pfitzner, *Zeitschrift für anorganische und allgemeine Chemie* **2005**, *631*, 677–682.

[49] H. C. Sansom, G. F. Whitehead, M. S. Dyer, M. Zanella, T. D. Manning, M. J. Pitcher, T. J. Whittles, V. R. Dhanak, J. Alaria, J. B. Claridge, et al., *Chemistry of Materials* **2017**, *29*, 1538–1549.

[50] I. Turkevych, S. Kazaoui, E. Ito, T. Urano, K. Yamada, H. Tomiyasu, H. Yamagishi, M. Kondo, S. Aramaki, *ChemSusChem* **2017**, *10*, 3754–3759.

[51] H. C. Sansom, G. Longo, A. D. Wright, L. R. Buizza, S. Mahesh, B. Wenger, M. Zanella, M. Abdi-Jalebi, M. J. Pitcher, M. S. Dyer, et al., *Journal of the American Chemical Society* **2021**, *143*, 3983–3992.

[52] M. B. Gray, E. T. McClure, N. P. Holzapfel, F. P. Evaristo, W. Windl, P. M. Woodward, *Journal of Solid State Chemistry* **2021**, *297*, 121997.

[53] A. Ramirez, *Annual Review of Materials Science* **1994**, *24*, 453–480.

[54] O. Erten, O. N. Meetei, A. Mukherjee, M. Randeria, N. Trivedi, P. Woodward, *Physical review letters* **2011**, *107*, 257201.

[55] K.-I. Kobayashi, T. Kimura, H. Sawada, K. Terakura, Y. Tokura, *Nature* **1998**, *395*, 677–680.

[56] A. H. Slavney, T. Hu, A. M. Lindenberg, H. I. Karunadasa, *Journal of the American chemical society* **2016**, *138*, 2138–2141.

[57] E. T. McClure, M. R. Ball, W. Windl, P. M. Woodward, *Chemistry of Materials* **2016**, *28*, 1348–1354.

[58] G. Volonakis, M. R. Filip, A. A. Haghighirad, N. Sakai, B. Wenger, H. J. Snaith, F. Giustino, *The journal of physical chemistry letters* **2016**, *7*, 1254–1259.

[59] T. Zhang, Z. Cai, S. Chen, *ACS applied materials & interfaces* **2020**, *12*, 20680–20690.

[60] Z. Gao, H. Zhang, G. Mao, J. Ren, Z. Chen, C. Wu, I. D. Gates, W. Yang, X. Ding, J. Yao, *Applied Surface Science* **2021**, *568*, 150916.

[61] M. R. Filip, S. Hillman, A. A. Haghighirad, H. J. Snaith, F. Giustino, *The journal of physical chemistry letters* **2016**, *7*, 2579–2585.

[62] W. Meng, X. Wang, Z. Xiao, J. Wang, D. B. Mitzi, Y. Yan, *The journal of physical chemistry letters* **2017**, *8*, 2999–3007.

[63] Z. Xiao, W. Meng, J. Wang, Y. Yan, *ChemSusChem* **2016**, *9*, 2628–2633.

[64] M. Delor, A. H. Slavney, N. R. Wolf, M. R. Filip, J. B. Neaton, H. I. Karunadasa, N. S. Ginsberg, *ACS Energy Letters* **2020**, *5*, 1337–1345.

[65] A. Schmitz, L. L. Schaberg, S. Sirotinskaya, M. Pantaler, D. C. Lupascu, N. Benson, G. Bacher, *ACS Energy Letters* **2020**, *5*, 559–565.

[66] A. Dey, A. F. Richter, T. Debnath, H. Huang, L. Polavarapu, J. Feldmann, *ACS nano* **2020**, *14*, 5855–5861.

[67] S. Zelewski, J. M. Urban, A. Surrente, D. K. Maude, A. Kuc, L. Schade, R. Johnson, M. Dollmann, P. Nayak, H. Snaith, et al., *Journal of Materials Chemistry C* **2019**, *7*, 8350–8356.

[68] Y. Bekenstein, J. C. Dahl, J. Huang, W. T. Osowiecki, J. K. Swabeck, E. M. Chan, P. Yang, A. P. Alivisatos, *Nano letters* **2018**, *18*, 3502–3508.

[69] B. A. Connor, L. Leppert, M. D. Smith, J. B. Neaton, H. I. Karunadasa, *Journal of the American Chemical Society* **2018**, *140*, 5235–5240.

[70] J. A. Steele, P. Puech, M. Keshavarz, R. Yang, S. Banerjee, E. Debroye, C. W. Kim, H. Yuan, N. H. Heo, J. Vanacken, et al., *ACS nano* **2018**, *12*, 8081–8090.

[71] R. Kentsch, M. Scholz, J. Horn, D. Schlettwein, K. Oum, T. Lenzer, *The Journal of Physical Chemistry C* **2018**, *122*, 25940–25947.

[72] A. D. Wright, L. R. Buizza, K. J. Savill, G. Longo, H. J. Snaith, M. B. Johnston, L. M. Herz, *The journal of physical chemistry letters* **2021**, *12*, 3352–3360.

[73] E. Greul, M. L. Petrus, A. Binek, P. Docampo, T. Bein, *Journal of Materials Chemistry A* **2017**, *5*, 19972–19981.

[74] N. Singh, A. Agarwal, M. Agarwal, *Optical Materials* **2021**, *114*, 110964.

[75] C. N. Savory, A. Walsh, D. O. Scanlon, *ACS energy letters* **2016**, *1*, 949–955.

[76] H. Lei, D. Hardy, F. Gao, *Advanced Functional Materials* **2021**, *31*, 2105898.

[77] X. Li, J. Yang, Q. Jiang, W. Chu, D. Zhang, Z. Zhou, J. Xin, *ACS applied materials & interfaces* **2017**, *9*, 41354–41362.

[78] M. T. Sirtl, F. Ebadi, B. T. van Gorkom, P. Ganswindt, R. A. Janssen, T. Bein, W. Tress, *Advanced Optical Materials* **2021**, *9*, 2100202.

[79] W. Tress, M. T. Sirtl, *Solar RRL* **2022**, *6*, 2100770.

[80] G. Longo, S. Mahesh, L. R. Buizza, A. D. Wright, A. J. Ramadan, M. Abdi-Jalebi, P. K. Nayak, L. M. Herz, H. J. Snaith, *ACS Energy Letters* **2020**, *5*, 2200–2207.

[81] W. Pan, H. Wu, J. Luo, Z. Deng, C. Ge, C. Chen, X. Jiang, W.-J. Yin, G. Niu, L. Zhu, et al., *Nature photonics* **2017**, *11*, 726–732.

[82] J. A. Steele, W. Pan, C. Martin, M. Keshavarz, E. Debroye, H. Yuan, S. Banerjee, E. Fron, D. Jonckheere, C. W. Kim, et al., *Advanced Materials* **2018**, *30*, 1804450.

[83] P. Vishnoi, R. Seshadri, A. K. Cheetham, *The Journal of Physical Chemistry C* **2021**, *125*, 11756–11764.

[84] L. Mao, C. C. Stoumpos, M. G. Kanatzidis, *Journal of the American Chemical Society* **2018**, *141*, 1171–1190.

[85] X. Li, J. M. Hoffman, M. G. Kanatzidis, *Chemical reviews* **2021**, *121*, 2230–2291.

[86] J. Sun, K. Wang, K. Ma, J. Y. Park, Z.-Y. Lin, B. M. Savoie, L. Dou, *Journal of the American Chemical Society* **2023**.

[87] C. M. M. Soe, G. Nagabhushana, R. Shivaramaiah, H. Tsai, W. Nie, J.-C. Blancon, F. Melkonyan, D. H. Cao, B. Traoré, L. Pedesseau, et al., *Proceedings of the National Academy of Sciences* **2019**, *116*, 58–66.

[88] D. G. Billing, A. Lemmerer, *New Journal of Chemistry* **2008**, *32*, 1736–1746.

[89] D. B. Mitzi, C. Feild, W. Harrison, A. Guloy, *Nature* **1994**, *369*, 467–469.

[90] J. Calabrese, N. Jones, R. Harlow, N. Herron, D. Thorn, Y. Wang, *Journal of the American Chemical Society* **1991**, *113*, 2328–2330.

[91] C. R. Kagan, D. B. Mitzi, C. D. Dimitrakopoulos, *Science* **1999**, *286*, 945–947.

[92] J. V. Passarelli, D. J. Fairfield, N. A. Sather, M. P. Hendricks, H. Sai, C. L. Stern, S. I. Stupp, *Journal of the American Chemical Society* **2018**, *140*, 7313–7323.

[93] D. B. Mitzi, C. D. Dimitrakopoulos, L. L. Kosbar, *Chemistry of materials* **2001**, *13*, 3728–3740.

[94] J. Hu, I. W. Oswald, S. J. Stuard, M. M. Nahid, N. Zhou, O. F. Williams, Z. Guo, L. Yan, H. Hu, Z. Chen, et al., *Nature communications* **2019**, *10*, 1276.

[95] D. B. Mitzi, K. Chondroudis, C. R. Kagan, *Inorganic chemistry* **1999**, *38*, 6246–6256.

[96] Y. Gao, E. Shi, S. Deng, S. B. Shiring, J. M. Snaider, C. Liang, B. Yuan, R. Song, S. M. Janke, A. Liebman-Peláez, et al., *Nature chemistry* **2019**, *11*, 1151–1157.

[97] M. K. Jana, S. M. Janke, D. J. Dirkes, S. Dovletgeldi, C. Liu, X. Qin, K. Gundogdu, W. You, V. Blum, D. B. Mitzi, *Journal of the American Chemical Society* **2019**, *141*, 7955–7964.

[98] X. Dong, M. Chen, R. Wang, Q. Ling, Z. Hu, H. Liu, Y. Xin, Y. Yang, J. Wang, Y. Liu, *Advanced Energy Materials* **2023**, *13*, 2301006.

[99] Y. Boeije, W. T. Van Gompel, Y. Zhang, P. Ghosh, S. J. Zelewski, A. Maufort, B. Roose, Z. Y. Ooi, R. Chowdhury, I. Devroey, et al., *Journal of the American Chemical Society* **2023**.

[100] T. L. Leung, I. Ahmad, A. A. Syed, A. M. C. Ng, J. Popović, A. B. Djurišić, *Communications Materials* **2022**, *3*, 63.

[101] Y. Xu, M. Wang, Y. Lei, Z. Ci, Z. Jin, *Advanced Energy Materials* **2020**, *10*, 2002558.

[102] L.-Y. Bi, T.-L. Hu, M.-Q. Li, B.-K. Ling, M. S. Lassoued, Y.-Q. Hu, Z. Wu, G. Zhou, Y.-Z. Zheng, *Journal of materials chemistry A* **2020**, *8*, 7288–7296.

[103] A. Z. Chen, M. Shiu, X. Deng, M. Mahmoud, D. Zhang, B. J. Foley, S.-H. Lee, G. Giri, J. J. Choi, *Chemistry of Materials* **2019**, *31*, 1336–1343.

[104] J. Zhang, L. Zhang, X. Li, X. Zhu, J. Yu, K. Fan, *ACS Sustainable Chemistry & Engineering* **2019**, *7*, 3487–3495.

[105] J. Song, G. Zhou, W. Chen, Q. Zhang, J. Ali, Q. Hu, J. Wang, C. Wang, W. Feng, A. B. Djurišić, et al., *Advanced materials* **2020**, *32*, 2002784.

1.3 Characterization Techniques

1.3.1 X-ray Diffraction (XRD)

Diffraction is a process based on the interference of waves with an object or through an aperture. X-ray diffraction is thus based on light-matter interactions, which depending on the photon energy regime can be divided into three scattering processes, namely Rayleigh, Thomson and Compton scattering. Rayleigh scattering is an elastic scattering process in the low energy regime with particles where the size is much smaller than the photon wavelength. Thomson and Compton scattering can be grouped into the mid energy regime, where Thomson scattering can be described as the low energy regime of Compton scattering. Compton scattering occurs when the photon energy is large enough to interact with an atom's electrons through a transfer of energy, resulting in a change in photon wavelength and electron momentum after scattering, making it an inelastic scattering process. Thomson scattering occurs for the lower energy case, where the scattered photon does not change in energy. Hereby, the electromagnetic wave of a photon excites an electron to a coherent, harmonic oscillation which is reemitted with the same frequency, making it an elastic scattering process. It is the primary, underlying process used for X-ray diffraction in crystalline materials.

This phenomenon was described simultaneously in 1912 by *Max von Laue* and *William Lawrence Bragg* under different assumptions. While both are based on the periodic atomic crystal lattice, the Laue equations explain the diffraction through scattering on the single atom, where scattering occurs if the change of the wave vector $\Delta\vec{k}$, with the incoming and outgoing wave vectors $\vec{k}$ and $\vec{k'}$, respectively, is equivalent to a reciprocal lattice vector $\vec{G}$:[1]

$$\Delta\vec{k} = \vec{k'} - \vec{k} = \vec{G} \tag{1.12}$$

If the equation is satisfied, constructive interference can be measured and the basis of the reciprocal lattice of a crystal structure can be determined by using the primitive vectors a, b and c and the Miller indices (h, k, l) according to equation 1.13:

$$\begin{aligned} \Delta\vec{k} * a &= 2\pi h \\ \Delta\vec{k} * b &= 2\pi k \\ \Delta\vec{k} * c &= 2\pi l \end{aligned} \tag{1.13}$$

The Bragg condition is based on the diffraction at lattice planes, whose distance d is periodic and parallel, with an incident angle θ, leading to an interference pattern as shown in Figure 1.21[2,3]

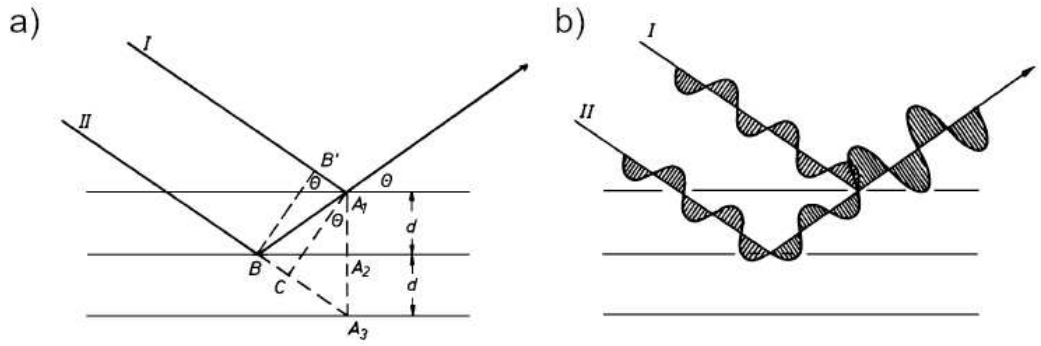

Figure 1.21: a) Diffraction of X-rays on lattice planes and b) constructive interference of the reflected X-rays. Reproduced with permission from Springer Nature.[2]

The diffraction condition is described in Bragg's law as follows:

$$n \cdot \lambda = 2d_{hkl} \sin(\theta) \tag{1.14}$$

With *n* being an integer, λ the wavelength, d_{hkl} the distance between lattice planes (with Miller indices hkl) and θ being the X-ray incident angle.

After irradiation of a powder sample, the scattering lattice planes form the tangent to the surface of a cone, with opening angle 4θ (Fig. 1.22). When the scattered radiation

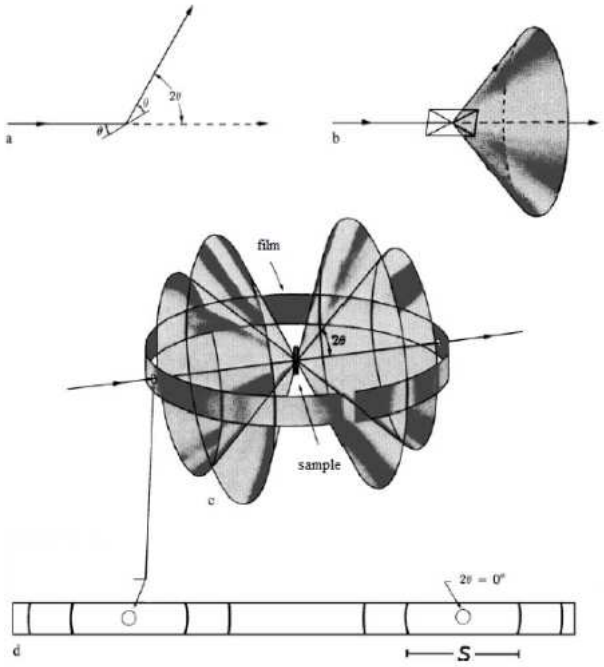

Figure 1.22: (a) Diffraction on lattice planes, (b) Cone of reflections produced by a statistically distributed, crystalline powder with an opening angle of 4θ, (c,d) Different, coaxial cones around the primary beam, surrounded by a cylindrical camera film resulting in the lines of a diffractogram. Reproduced with permission from Springer Nature.[2]

is collected on a flat plate detector, the rotational averaging leads to smooth diffraction

rings around the beam axis, rather than the discrete Laue spots observed in single crystal diffraction. Reducing the data to a line cut, a standard diffractogram with x-axis 2θ and y-axis intensity is obtained. By using the now known 2θ and λ, as well as Bragg's law and the Laue equations, one can calculate d and index the reflections to their lattice planes. The relation between Miller indices (hkl) and the lattice plane distance d is shown in equation 1.15 for the simplest case of a cubic crystal system ($\alpha = \beta = \gamma = 90°$ and $a_0 = b_0 = c_0$):

$$d_{hkl} = \frac{a_0}{\sqrt{h^2 + k^2 + l^2}} \tag{1.15}$$

Inserting this relation into Bragg's equation according to equation 1.16 yields information about the Miller indices of the crystal structure:

$$sin^2\theta = \frac{\lambda^2}{4a_0^2}(h^2 + k^2 + l^2) \tag{1.16}$$

As the access to this and other basic information from a powder diffraction measurement gets increasingly more difficult for more complex crystal structures, the more reliable method is the analysis of single crystals, which is explained in the following chapter 1.3.5.

Another information gathered is the intensity of the reflections, which corresponds to intensity of scattered X-rays, which depends both on the crystal structure, the elemental composition, crystal orientations and morphologies. In case of phase mixtures in a sample this is of special interest, as it also relates to the amount of each phase fraction.

The real strength of the diffraction analysis lies in the ability to identify crystalline materials in a rapid and non-destructive manner without any considerable sample requirements with regard to purity and preparation. Through the unique diffraction pattern and intensity profile for every crystal structure, phases and mixtures can be quickly identified by comparing them to large crystallographic databases such as the powder diffraction file database by the international centre for diffraction data (PDF), the Cambridge structural database (CSD) or the inorganic crystal structure database (ICSD).

The radiation source for X-rays in laboratory diffractometers is the X-ray tube. Through an electron source operated at high voltages, commonly between 10 and 150 kV, an electron beam is generated and accelerated onto an anode target material, generating characteristic X-rays. The working principle of electron sources and characteristic X-rays is explained in more detail in chapter 1.3.6. Common elements and corresponding wavelengths used are chromium (0.229 nm), iron (0.194 nm), cobalt (0.179 nm), copper (0.154 nm) or molybdenum (0.071 nm). After beam manipulation through X-ray optics systems including filters or monochromators, the focusing optics, mirror and slit systems a suitably monochromated, fine beam is focused on the sample and diffracted. For detection, the

most common types of detectors are scintillation detectors, gas-filled detectors or semiconductors. In principle, all detectors convert X-rays into electric current, which can then be transformed and analysed with regard to the diffraction angle 2θ and the intensity.[2–5]

1.3.2 Powder X-ray Diffraction (PXRD)

As explained in the previous chapter, the theory and physical principles behind X-ray diffraction analysis is the same for both powder and thin-film measurements. The differences in the measurement setup and diffractometer geometry and their consequences will be explained briefly in this and the following chapter.

Powder X-ray diffraction is conducted with a finely ground crystal powder, leading to a statistical number of crystals satisfying the diffraction conditions. The powders are either prepared in a cylindrical capillary or between two polymer sheets on a flat holder and mounted on a rotating sample holder to further provide statistical distribution of diffraction events. Transmission or reflection geometry is used with either a fixed position X-ray source and a moving detector, i.e. a $\theta - 2\theta$ scan, or with both moving X-ray source and detector, i.e. a $\theta - \theta$ scan. The resulting data are then commonly analyzed with regard to phase identification and mixture by comparison to crystallographic databases or analyzed in more detail through methods such as Rietveld refinement, which through the combination of sample and instrumental parameters is able to access information about the unit cell parameters, atomic parameters, crystallinity, disorder, defects, preferred orientation and crystallite size.[2–6]

1.3.3 Thin-film X-ray Diffraction (TFXRD)

Thin-film X-ray diffraction differs mostly from powder measurements in terms of the sample structure. As thin films are synthesized on a substrate, the diffractometer is operated in reflection geometry. The two major differences to the statistically distributed powder are i) a varying irradiation profile, with larger irradiation profiles under low angles 2θ and reduced profiles for large angles 2θ, and ii) the influence of crystal orientation, as through the crystallization process on a substrate the crystals can grow under anisotropic conditions or substrate interactions, leading to a preferential orientation. The first point can be alleviated depending on which source-detector setting is chosen, i.e. a $\theta - 2\theta$ or $\theta - \theta$ scan. The second point unavoidably leads to a different diffraction pattern and intensity profile, as due to the detector position being fixed along the measurement angle of the diffractometer certain reflections might be positioned outside the observable range. For a more detailed analysis of oriented thin film samples another, more specialized technique is explained in the following chapter 1.3.4.

1.3.4 Grazing-Incidence Wide-Angle X-ray Scattering (GIWAXS)

Grazing-incidence wide-angle X-ray scattering is a specialized technique to investigate the nanostructure of crystalline thin-film samples. The experimental setup involves a number of key differences to standard X-ray diffraction experiments discussed in the earlier chapters.

The refractive index for X-rays is typically close to 1 or even smaller and thus when travelling from a less dense medium, i.e. vacuum, to a denser medium, total external reflection can be achieved through sufficiently small incident angles. The X-ray beam is thus kept at very small incidence angles to the sample surface, typically below $\alpha_i < 1°$, to allow for reflection and diffraction of variable probing depths into the film. The depth of the probe hereby depends on the critical angle of the material, where for $\alpha_i < \alpha_c$ only the topmost nanometers can be investigated. For $\alpha_i > \alpha_c$ the probing depth Λ can be adjusted variably as a function of the incident angle according to equation 1.17, with the wavenumber k and the imaginary part of the index of refraction β:[7]

$$\Lambda = \frac{1}{\sqrt{2}k\sqrt{\sqrt{(\alpha_i^2 - \alpha_c^2) + 4\beta^2} - (\alpha_i^2 - \alpha_c^2)}} \tag{1.17}$$

Here, the complex refractive index, following Snell's law of refraction, can be calculated according to equation 1.18, with dispersive and absorptive factors δ and β, which can be calculated through the atomic scattering factor if the material's elements and density are

known:

$$n = 1 - \delta + i\beta \tag{1.18}$$

Due to the grazing incidence, the X-ray beam also travels through the complete length of a sample allowing for a large, macroscopic probe volume while retaining a microscopic depth resolution.

To measure the scattered X-rays and gather information about the three-dimensional nanostructure of the sample, a two-dimensional detector is used. Depending on the sample-detector distance, ordered structures of different scales can be resolved. According to Bragg's law (Eq. 1.14), the diffraction or scattering of X-rays on periodic structures at the atomic scale, i.e. on the order of Å, leads to diffraction angles on the order of 1° to 180° 2θ, requiring a close sample-detector distance, commonly between 100 mm to 300 mm. As this method is a more general scattering technique, the common notation is based on the momentum transfer of the scattering vector q in the reciprocal space. The resolution of this wide-angle X-ray scattering (WAXS) setup can thus commonly access angles from 1° to 40°, or q-values from 0.1 $Å^{-1}$ to 0.4 $Å^{-1}$. Due to the inverse nature of the reciprocal space, if larger structures are to be analyzed, scattering angles <1° or q-values <0.1 $Å^{-1}$ need to be resolved, requiring larger sample-detector distances >300 mm, known as small-angle X-ray scattering (SAXS). The size of the resolved structures is at the order of nm, thus typically investigating the size and shape of nanoparticles or nanostructures.

In grazing incidence experiments, due to the imaging of the 3D scattering on a 2D flat detector, not all scattering can be probed. Since scattering happens in accordance to the Laue equations and scattering vectors, as discussed in chapter 1.3.1, the reciprocal lattice is probed at its intersection with the Ewald sphere, a construction from the scattering vectors arising in the experiment. Under wide scattering angles, the curvature of this Ewald sphere leads to an inaccesible area in the scattering data if the flat 2D detector image is transformed in accordance to the reciprocal space. This is commonly referred to as the missing wedge, observable in figure 4.1.

A schematic representation of the measurement setup is shown in figure 1.23 (a), with cartesian coordinates x,y,z, the incident X-ray with its wave vector k_i and angle α_i. It is scattered at an angle α_f or $2\theta_f$ with the wave vector k_f resulting in scattering vectors $q_{y,z}$ and the 2D scattering image.

As mentioned, one strength of GIWAXS with crystalline thin film samples is the possibility to determine its texture or orientation. This is depicted in figure 1.23 (b), where the different orientation of lattice planes for individual grains is shown at the top, with each corresponding 2D scattering image at the bottom. For the first case of uniform, parallel oriented layers the scattering image forms as discrete dots along the 0 ° azimuthal angle χ shown in i), reminiscent of single-crystal diffraction. Perpendicular orientation results in

discrete dots along $\chi = 90\,°$, as seen in ii) for a mixed distribution of crystallites. If orientation is not completely uniform, for example in oriented domains, the dots smear out as in the case of iii), until for completely random oriented crystallites Debye-Scherrer-like rings are formed as shown in iv).[8,9]

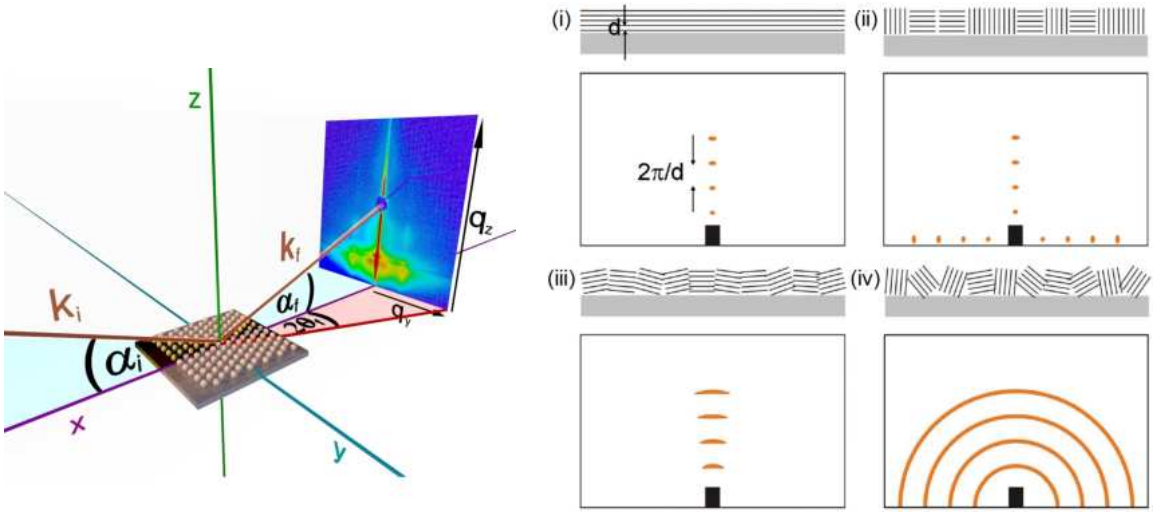

(a) (b)

Figure 1.23: (a) Schematic representation of the experimental GIWAXS setup with exemplary 2D detector data.[10] (b) Illustration of 2D detector patterns of different film orientations for and corresponding lattice plane distance d: (i) parallel layers (ii) vertical and parallel layers (iii) parallel oriented domains and (iv) completely random orientation. Reproduced with permission from Wiley.[9]

1.3.5 Single-Crystal X-ray Diffraction (SCXRD)

The most practical solution to solve a substance's structure is to measure the X-ray diffraction of a single crystal. Naturally, the first step in this process is creating and picking a suitable single crystal. Crystal growth is mainly controlled by the rate of crystal nucleation and its crystal growth rate. To succeed one should always aim for the latter to be bigger than the former, otherwise a polycrystalline conglomerate instead of a single or twin crystal will be formed. Since crystallisation behaviour of novel substances is mostly unknown, this is a task that requires chemical instinct as well as testing. For crystallisation growth, methods from solution, melt or gas phase are possible, depending on the substance. Common dimensions of edge length for single crystal measurements ranges from 0.1 mm to 0.5 mm, although this depends on factors like the absorption behaviour of the substance and the desire for a small crystal (better quality, less absorption and smaller beam divergence). Because of the different interaction of various compounds with X-rays choosing the right wavelength and X-ray source can also be of help. If the absorption coefficient μ is known the thickness D can be estimated by a rule of thumb following equation 1.19:

$$D = \frac{2}{\mu} \tag{1.19}$$

To evaluate a crystal's quality an optical assessment with a microscope and a polarisation filter is very useful. Most crystals are transparent and only cubic crystals are optically isotropic, other crystal classes with less symmetry are anisotropic. This behaviour is exploited as it rotates the plane of polarized light and it can be observed by using a rotational polarisation filter. Then the selected crystal gets prepared as described earlier. After mounting the crystal on the diffractometer's goniometer head, the measurement begins with the goal to measure a large number of reflections, usually in the range of 1,000 - 50,000. To get the reflections of every lattice plane (*hkl*) the crystal has to be rotated in all three dimensions. In theory this is attributed to the rotation of the reciprocal lattice until the scattering vector intersects with the Ewald sphere. The BRUKER D8 Quest uses fixed-κ-geometry and thus a two circle goniometer. For clarification of the angles see figure 1.24 with Φ, κ, ω_κ and 2θ. The ω angle, which rotates about an axis perpendicular to the beam; the κ angle, about an axis at roughly 50 ° to the ω axis; and, finally, the ϕ angle about the loop axis. One advantage of this geometry is the availability of the upper space above the sample in comparison to a setup in Euler geometry, which uses four circles. Cooling with nitrogen from above is easily accomplished that way. The charge-coupled device (CCD) detector is mounted on the goniometer as well. A CCD-chip has a fluorescing layer, for example gadolinium oxysulphide, making it sensitive for X-rays. They provide very good real time analysis, but come at the price of an electrically induced

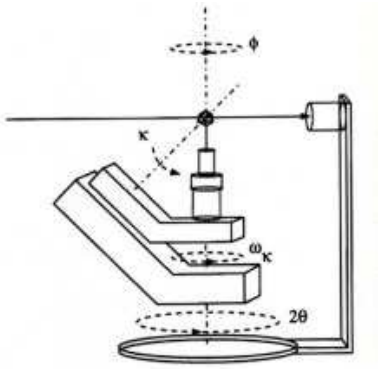

Figure 1.24: Scheme of a four circle goniometer with kappa geometry.[11]

background noise, which has to be taken care of by cooling it to around -40 °C with a Peltier-element.[4]

The next step after centring the crystal is defining the orientation matrix. The most common practice is to automatically measure and search for reflections which then can be used to calculate the basis and the elementary cell. The orientation matrix provides the information of the reciprocal cell parameters and its position relative to the goniometer coordinate system. With the matrice's help, points in the reciprocal space can be calculated and the desired reflection can be measured. The reflections intensity is dependent on many factors shown in the following equation 1.20:

$$I \sim I_0 \cdot V \cdot L \cdot P \cdot A \cdot \Theta \cdot E \cdot |F^2| \tag{1.20}$$

With the structure factor *F*, the intensity of the primary beam I_0, the crystal volume *V*, the polarisation factor *P* ($\frac{1}{2}(1 + \cos^2 2\theta)$), the Lorentz factor *L*, the absorption *A*, the temperature factor θ and the extinction *E*. To illustrate this, coming from the measured intensity I_{hkl}, the Structure factor F_{hkl} is introduced. It can be expressed in the following equation 1.21:

$$I_{hkl} = F_{hkl}^2 = \sum_{j=1}^{N} f_j e^{-2\pi i(hx_j + ky_j + lz_j)} \tag{1.21}$$

With the sum over all atoms j in the unit cell, x_j y_j z_j as the coordinates, Miller indices hkl and the atomic scattering factor f_j. The atomic scattering factor, or atomic form factor can be defined as follows (see equation 1.22):

$$f = \int_0^\infty U(r) \frac{\sin \mu r}{\mu r} dr \tag{1.22}$$

with

$$U(r) = 4r^2 \pi \rho(r) \tag{1.23}$$

and

$$\mu = \frac{4\pi}{\lambda} \sin \phi \tag{1.24}$$

The structure factor can be expressed as the Fourier transform of the electron density. To calculate the electron density, techniques like the self-consistent field method or the Thomas-Fermi method are used. To solve the actual crystal structure, one would have to measure the intensity as well as the phase of all scattered X-rays. Because the structure factor is proportional to the square of the intensity, the information of the phase is lost due to the cancellation of the imaginary part, by taking the root of the structure factor.[5,12]

To solve this phase problem means to solve the actual structure and its atomic positions, besides the already known information like the unit cell, space group and intensities. There are different theories available to solve this problem like Patterson- or direct methods. If solved there still are flaws in the used theories as well as in the dataset. To finalize the analysis a structure refinement can be done. Techniques like the least squares method, which is a weighing factoring method, based on different accuracies of the data, are commonly used. To see how good the structure model fits to the 'real' model, a calculation of the R- or residual-values can be done. The R-value gives an averaged, percentage deviation between observed and calculated structure amplitudes. To rate the quality of the measured data, R values are determined (see equation 1.25 and 1.26).

$$R_\sigma = \frac{\sum_i \sigma(F^2_{obs})}{\sum_i F^2_{obs}} \tag{1.25}$$

With R_σ being the data average standard deviation. This value should not be bigger than 0.3 and a good structural analysis has values smaller than 0.05.

$$R_{int} = \frac{\sum_i \sum_j |F^2_{obs_i} - F^2_{obs_j}|}{\sum_i F^2_{obs_i}} \tag{1.26}$$

If reflections have been measured more than once, a comparison can be done with R_{int} being the average deviation of a reflection to its averaged intensity. This value can be used to evaluate the space group symmetry, the crystal quality and also the quality of the absorption correction.

After collection and correction of the data the phase problem must be solved to determine the electron densities and thus the crystal structure. Due to the fact of fast processing power nowadays, most commonly used methods are direct methods and least-squares, assigning phases to strong reflections and calculating a refined fit by iteration of these. The basic equation for this is to calculate the electron density ρ_{xyz} for every point xyz in the

elementary cell over the Fourier summation (see equation 1.27).

$$\rho_{xyz} = \frac{1}{V} \sum_{hkl} F_{hkl} \cdot e^{-i2\pi(hx+ky+lz)} \tag{1.27}$$

To solve the phase information, all potential methods use a structural model with an approach for atom positions. There are iterative methods, the Patterson-method or heavy atom method, direct methods, the charge flipping method or direct measuring of the phases through twin-beam interference. Direct methods are based on the facts for elementary unit cells that firstly the electron density can never be negative and secondly that the electron density is concentrated at atom positions. An important theoretical breakthrough was made with *Sayres* equation:[13]

$$F_{hkl} = s \sum_{h'k'l'} F_{h'k'l'} \cdot F_{h-h',k-k',l-l'} \tag{1.28}$$

It states that the structure factor of a reflection can be calculated from the sum of the structure factors products of all reflection pairs, which fulfil the condition that their indices add up to the ones of the desired reflection. *Sayre* stated that for centrosymmetric structures the sum of big structure factors tend to have the same algebraic signs (S) as the structure factors. This can be expressed following equation 1.29.

$$S_{F_{h,k,l}} \approx S_{F_{h',k',l'}} \cdot S_{F_{h-h',k-k',l-l'}} \tag{1.29}$$

For the case of non-centrosymmetric structures the same principle applies albeit a little more complicated as seen in equation 1.30.

$$F_{hkl} = \sum c \cdot F_{hkl} \cdot F_{h-h',k-k',l-l'} \cdot e^{i\phi(hkl)} \cdot e^{i\phi(h-h',k-k',l-l')} \tag{1.30}$$

The charge flipping method provides an attempt already given by its name, an algorithm including a charge flipping operation. Hereby all negative electron densities are inverted. The iteration cycle begins with a random phase guess and the electron density ρ is calculated by inverse Fourier transform. Then all negative values are flipped to positive while other data points remain unchanged. Temporary structure factors are calculated with Fourier transform again and lastly the new structure factors are calculated by adding the experimental values to the calculated phases and setting all other not measured structure factors to zero. This process is repeated until there is convergence.

Finally, one is left with the last step of structure refinement, whereby remaining errors in the calculated model as well as in the dataset get minimized, in order that predicted reflection intensities and the ones measured coincide. The mathematical method of least

squares is the most used one and is always applicable when one physical quantity is linearly dependent on other variables that are of interest. This can be expressed as searching for the minimum following equation 1.31.

$$\sum w|F_{obs}^2 - F_{calc}^2| \tag{1.31}$$

The refinement procedure starts with the first step of refining the position of heavy atoms. Then the light atoms are found by use of difference Fourier transform. The refinement of the thermal displacement parameter follows. Now the weighing parameter *w* is adjusted and lastly the extinction parameter is refined.

To test the quality criteria of the solution and refinement R-values are calculated like described earlier (cf. equation 1.25 and 1.26). To include a more realistic solution, the R-values are then calculated using a weighted approach for R, namely wR_2 (see equation 1.32, with index 2 because calculation is done with squared F).

$$wR_2 = \sqrt{\frac{\sum_i w((F_{obs}^i)^2) - ((F_{calc}^i)^2)^2}{\sum_i w((F_{obs}^i)^2)^2}} \tag{1.32}$$

Another criterion of quality is the so called goodness of fit or GooF-value, which describes the discrepancy between observed and expected data in a statistical way. It can be expressed following equation 1.33.

$$GooF = \sqrt{\frac{\sum_{hkl} w|F_{obs}^2 - F_{calc}^2|^2}{m-n}} \tag{1.33}$$

With the number of reflections *m* and the number of parameters *n*. For a good structure solution the values of GooF should approach 1, but should not be smaller than that.[4,5,14]

1.3.6 Scanning Electron Microscopy (SEM) and Energy-dispersive X-ray Spectroscopy (EDX)

Microscopy is a powerful tool to investigate a sample on a magnified scale compared to what the human eye can naturally observe and resolve. By utilizing sample interactions of electromagnetic radiation or electrons in the form of diffraction, refraction or reflection, images can be created to receive information about the specimens existence in the three-dimensional space or any other visualisation of the sample's interaction with the probing particles. Since conventional visible-light microscopy is limited to the Abbe diffraction limit dependent on the wavelength of visible light as shown in equation 1.34, with the resolution d, the wavelength λ and the numerical aperture (NA) with the index of refraction n and the lens half-angle θ. Resolution on the submicro- to nanometer scale thus depends upon different techniques.

$$d = \frac{\lambda}{2n \sin\theta} = \frac{\lambda}{2\mathrm{NA}} \tag{1.34}$$

The scanning electron microscope permits this observation and analysis of organic and inorganic samples on the micrometer to nanometer scale through the use of electrons, whose wavelength is dependent on their acceleration voltage and thus very high spatial resolutions are possible. At the present day, a typical SEM can provide resolutions between 1 and 10 nm while also having a relatively large depth of focus (up to 1 µm to 5 µm). For the execution of this, a finely focused electron beam is emitted onto the sample in a rastered or static way, to provide various interactions for analysis. After interaction with the sample, the electron beam generates different signals such as secondary electrons (SEs), backscattered electrons (BSEs), Auger-electrons and characteristic X-rays. These can then be used to analyse properties such as surface topography, crystallography or composition.

The major components of an SEM are shown in Figure 1.25 and include the electron column and the control console. The column system is evacuated at a pressure of 10^{-6} Torr (i.e. one billionth of atmospheric pressure), where the electron beam is guided through a series of electromagnetic lens systems and apertures to be positioned and rastered on the sample by the scan coils. As the source or electron gun, nowadays often field emission guns are the standard choice as they produce an electron beam typically in an energy range of 0.1 keV to 30 keV, possessing a smaller diameter, better coherence and greater current density compared to older techniques such as thermionic emitters based on tungsten or lanthanum-hexaboride tipped filaments, which use high temperatures for the electrons to overcome the work function barrier of the materials. Field emission sources utilize a high applied electrical field to cause electrons to tunnel out of the tip, regardless of the temperature (cold field emitter). The conical beam emitted usually has a diameter of only a few nanometers and a few degrees divergence. Thermal field emitters use the same

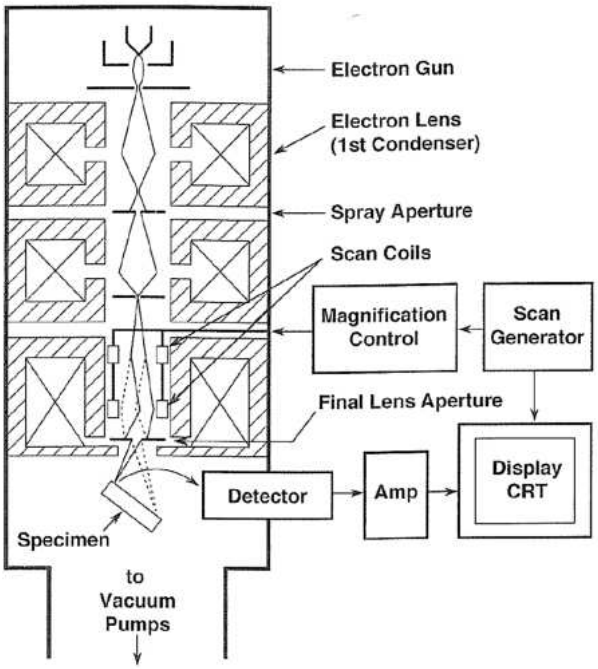

Figure 1.25: Schematic diagram of a scanning electron microscope including the electron gun, lenses and aperture systems and detection. Reproduced with permission from Springer Nature.[15]

principle, although at an elevated temperature to improve on properties such as better tip performance and stability. Lastly, an improved type of the thermal field emission source is the Schottky emitter, which utilizes an added tip deposition of ZrO_2 to reduce its work function and improve the performance to be comparable to cold emission sources.

After passing through the initial condensor system, consisting of spray apertures, i.e. simple bored metal disks with varying smaller diameters made from for example platinum or molybdenum, and electromagnetic condensing lenses, the now focussed electron beam passes through the deflection system made up of two pairs of scanning coils. The first pair of coils deflect the beam off the optical axis of the microscope while the second pair of coils deflects it back onto the pivot point of the scan. In this manner, the beam can be scanned or rastered across the sample, creating spot, line or area signals and imaging.

Second to the operation principles of the SEM itself are then the actual interactions of the electron beam with the sample. As negative particles, the electrons will interact dominantly with the electron shells of the atoms present in the sample. Electrons can be deflected through elastic scattering without the loss of kinetic energy and if redirected back to the surface, leave the sample again as back-scattered electrons. As this process is strongly dependent on the electron density and atomic number of the samples elements, it is a great way to determine elemental uniformity or distribution in a sample. Beam electrons can also scatter inelastically with the samples atoms, producing secondary electrons, Auger-electrons or X-rays. As electrons in the sample atoms shells are excited, they

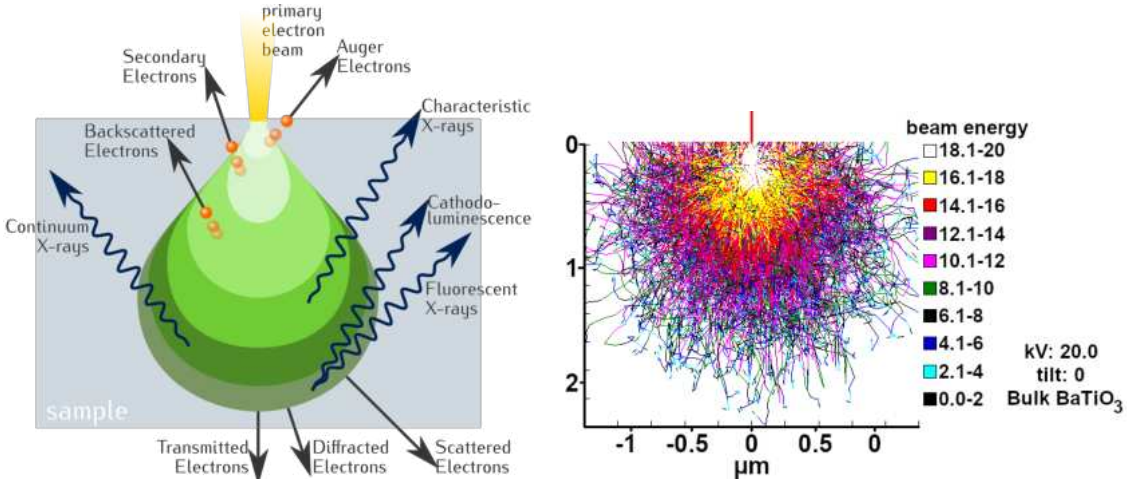

(a) (b)

Figure 1.26: a) Schematic diagram of electron-sample interaction and the various signals created. b) Electron interaction volume and path modelled using a Monte Carlo simulation with an initial beam energy of 20 kV on a bulk $BaTiO_3$ sample with electron energy drops shown with a color gradient.[16]

can relax back to lower energetic states and, depending on the initially absorbed kinetic energy, emit the three aforementioned types of electron or photon radiation. Since secondary electrons are mostly emitted closer to the surface, they are a great way to produce topographic images of the sample's surface and morphology. Due to the required energy to leave the sample again and the penetration depth, the beam-sample interaction volume and the possibility to detect these signals can be depicted schematically in a pear-shape, as shown in Figure 1.26 a), or as a more realistic model through Monte Carlo simulation in Figure 1.26 b). The created electron signals after sample interaction are collected and converted to an electric signal, explained based on the widely used Everhart-Thornley detector shown in Figure 1.27. A collector with a variable voltage applied is able to let through either both the secondary electrons and back-scattered electrons (positive voltage) or separate them (negative voltage), as the kinetic energy of BSEs is much larger than that of the SEs. After conversion through a scintillator, the light signal is photomultiplied through a series of dynodes and finally detected with a photocathode. After amplification, the signal can be analysed, where imaging mostly relies on the difference in contrast. Similarly, any other signals than SEs and BSEs can be collected in the same way to create an image.

The second most important feature of the SEM is its analytical capability based on the generation of characteristic X-ray radiation, called energy-dispersive X-ray spectroscopy (EDX or EDS). When an electron interacts with the coulombic field of atoms in a sample, its energy can be attenuated and the lost energy be emitted in form of a photon. These X-ray photons are called "Bremsstrahlung" and can possess any energy from zero up to the incident electron's full energy. As this is of no use for specific analysis it needs

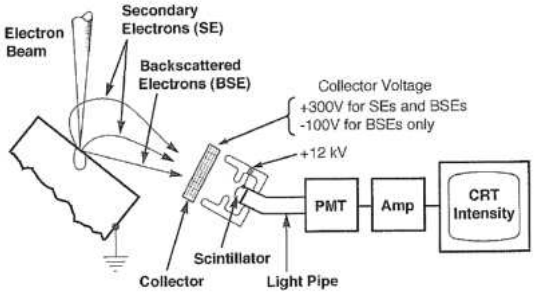

Figure 1.27: Collection of secondary- and back-scattered electrons with the Everhart-Thornley detector. Reproduced with permission from Springer Nature.[15]

to be kept in mind as the background radiation for the analysis of the characteristic X-ray radiation. More importantly, the beam electrons can also directly interact with the sample atom's electronic shell and excite one of its electrons, effectively ejecting it. On the timescale of picoseconds, the atom relaxes back to its ground state with outer shell electrons transitioning to fill the electron vacancy. Moving down, the electrons emit the surplus of energy either by transmitting it to another, outer shell electron ejecting it to form an Auger electron, or by emitting a characteristic X-ray photon. Both have characteristic energies corresponding to specific elemental transitions, making them useful for qualitative as well as quantitative analysis. As electron beam energies usually range from 0.1 keV to 30 keV, X-rays are dominantly produced from interactions with K and L shell electrons, in modern notation $1s$ and $2s, 2p$ orbitals, respectively. The process is shown in Figure 1.28 as an energy level diagram.

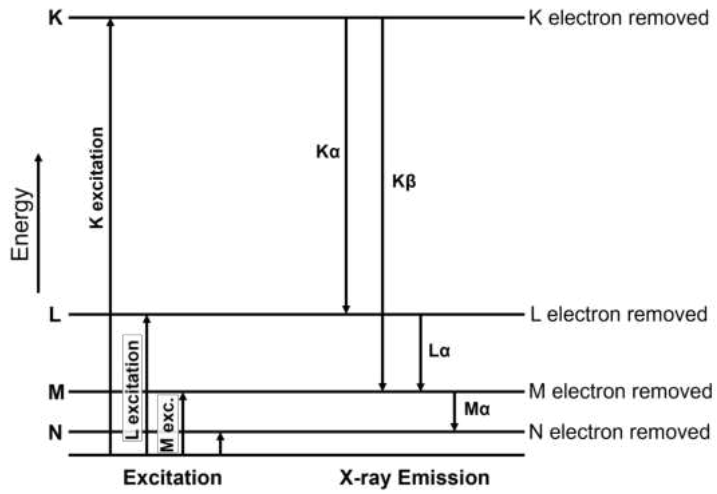

Figure 1.28: Energy level diagram for an atom with increasing energy upon ionization, i.e. excitation. When the energy is emitted again, $K\alpha$, $K\beta$, $L\alpha$ or $M\alpha$ X-rays are emitted.[15]

As every line or energetic state has a precisely defined energy, also known as the ionization energy to remove the respective electron from its atom, the differences between them

can also be precisely calculated as for example $E_{K\alpha} = E_K - E_L$. With every element having its specific atomic and electronic structure, its electromagnetic emission produces a characteristic spectrum of energy and intensity profiles making it useful for qualitative and quantitative analysis.

Considering the complex theoretical understanding behind electron-matter interactions and the technological accomplishements required to construct and operate the scanning electron microscope, most analysis and interpretation of the produced images is rather straight forward. In cases of more complex situations, discussions with the experienced electron microscopist are indispensable. In summary, the visualization of any topographic sample or the elemental analysis utilizing EDX is one of the most common and useful tools in the current field of, among many others, materials science.[15,17–20]

1.3.7 Atomic Force Microscopy (AFM)

Atomic force microscopy is a scanning probe microscopy technique that allows for resolution of surfaces on the nanometer, or for more specialized techniques even on the atomic scale. It originated from the scanning tunneling microscopy technique and is closely related. The principle relies on a cantilever with a sharp tip probing a samples surface, producing a feedback which in simple terms is similar to the deformation of a spring according to Hooke's law $F = kx$, where the force F scales with the spring's stiffness constant k and the distance x. The displacement of the tip can be measured through piezoelectric feedback or a laser deflection technique, both converting the displacement into an electric signal. This general setup is shown in figure 1.29, containing the following main components: 1) The sample stage which can be moved in all three dimensions x, y and z. 2) The AFM cantilever with an atomically sharp tip attached to its front. 3) the tip mount which optionally can be a piezoelectric element. 4) The displacement laser, focussed on the backside of the cantilever. 5) The detection system of the displaced laser beam, with a mirror and a position sensitive photodiode divided into quadrants. 6) The position feedback controller and the signal converter.[21,22]

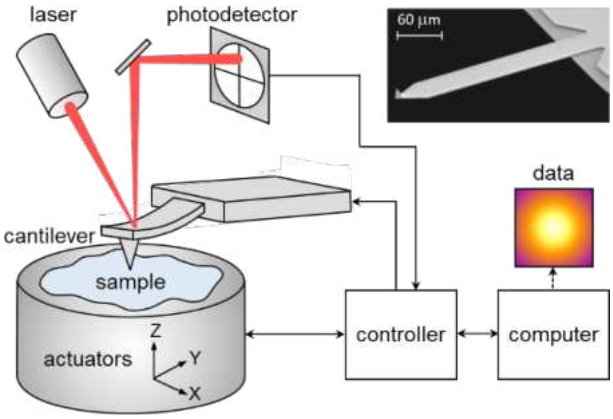

Figure 1.29: Measurement setup and main components of an atomic force microscope.[23]

The AFM tip is typically made of silicon or silicon nitride, with different coatings being optional, depending on the specific technique. Measurement modes are typically divided into contact, intermittent or non-contact modes, utilizing different types of tip-sample interactions such as mechanical contact, van der Waals forces, electrostatic forces or chemical bonding. In contact mode, the tip is touching the surface directly and being moved across the sample, producing direct feedback of the surface topology. In intermittent or tapping mode, the tip is oscillating through the piezo element in the cantilever or an alternating current magnetic field. Through this oscillation, either the distance to the sample is kept at a constant frequency and amplitude, or the change of those are measured directly. In non-contact mode, the tip is also operated under oscillation at either its

resonant frequency, i.e. frequency modulated, or slightly above that, i.e. amplitude modulated. Long-range interactions between the tip and the sample surface cause changes of the tip's oscillation, providing the signal used for imaging.[21,22]

Most commonly, topographic images are created using the height differences measured to create an image based on contrast or gradient coloration. There are many modifications to the AFM technique, allowing for a plethora of analysis possibilities. One example also used in this thesis is the conductive atomic force microscopy (cAFM). Here, the tip is coated with a conductive metal layer, commonly platinum, gold or other stable alloys such as Pt-Ir. The measurement is done in contact mode, with a direct contact between the tip and sample where a voltage is applied, enabling a current to be measured, flowing through the sample on a conductive substrate. Due to the small size of the tip and the corresponding small current, a low noise and high gain amplifier is needed to measure the current flow. Correlating the resulting current with the material' thickness can give valuable insights into the electrical conductivity of a sample, which is of great interest for optoelectronic thin film applications.[21,22]

1.3.8 Density Functional Theory (DFT)

Quantum mechanics is the fundamental physical theory to describe the properties of atomic and subatomic particles. Molecular quantum mechanics is a field of physical chemistry to describe chemical systems and in particular the electronic structure of materials. Density functional theory is a computational approach to model many-body systems based on the spatial dependence of electron densities. The calculations are based on the many-electron time-independent Schrödinger equation under the Born-Oppenheimer approximation shown in equation 1.35:[24,25]

$$\hat{H}\Psi = [\hat{T} + \hat{V} + \hat{U}]\Psi = \left[\sum_{i=1}^{N}(-\frac{\hbar^2}{2m_i}\nabla_i^2) + \sum_{i=1}^{N} V(r_i) + \sum_{i>j}^{N} U(r_i, r_j)\right]\Psi = E\Psi \quad (1.35)$$

Here, $\hat{H}$ is the Hamiltonian, Ψ the wavefunction, E the total energy, $\hat{T}$ the kinetic energy, $\hat{V}$ the potential energy, $\hat{U}$ the electron-electron interaction energy. Theoretically, DFT is based on the two Hohenberg-Kohn theorems. The first, stating that the ground state of a many-electron system is described by the electron density depending only on three spatial coordinates, instead of $3N$ spatial coordinates. The second, stating that the ground state energy can be obtained variationally, delivering the charge density which minimizes the total energy, i.e. the ground state energy. The reduced requirement for computational power of DFT compared to other methods, such as Hartree-Fock or Post-Hartree-Fock methods, makes it the most common approach to complex systems and materials science. One problem of DFT is that the exact exchange-correlation functionals are not known. Depending on the requirements of the calculation and the computing power, different approximations for these are used. The general gradient approximations (GGA) such as the PBE0 (Perdew–Burke-Ernzerhof), or hybrid functionals such as the B3LYP (Becke, 3-parameter, Lee–Yang–Parr), or HSE (Heyd–Scuseria–Ernzerhof) are the most commonly used ones.[24–28]

The electronic structure obtained from these calculations gives valuable insights into the nature of the band gap, its band dispersion, the density of states, etc., and is a standard method for the investigation of hybrid perovskites and other functional materials.

1.3.9 Ultraviolet-Visible (UV-Vis) Spectroscopy

According to the Lambert-Beer law, the absorbance is dependent on the sample's concentration, its absorption coefficient and the light's path length through the sample. This is expressed in equation 1.36, with the absorbance A, the incoming light intensity I_0, the transmitted light intensity I, the molar absorption coefficient ϵ, the concentration c and the light's path length. i.e. sample thickness d.[29]

$$A = \log\left(\frac{I_0}{I}\right) = \epsilon \cdot c \cdot d \tag{1.36}$$

Since this law is based on samples in solution, for solid state measurements of thin films a different dependence can be expressed following equation 1.37 and 1.38, with the absorbance A, the transmittance T and the reflectance R.

$$A = \log\left(\frac{I_0}{I}\right) = -log(1 - \%A) \tag{1.37}$$

$$\%A = 1 - \%T - \%R \tag{1.38}$$

To compensate measurement losses due to reflection and scattering, an integrating sphere is used, which is covered with a diffuse, white, reflecting material (Spectralon®) to ensure uniform scattering. The schematics of this in two measurement modes of thin films for transmittance and reflectance are shown in figure 1.30 (a).[30] To correct for the specular reflectance of the thin film samples, a corrected absorption can be obtained by use of equation 1.39, with the corrected absorption A, transmission T, and reflectance R. Differentiation between sample and substrate is given by subscripts.[30]

$$A_{corr}(\lambda) = -\log \frac{\frac{T_{sam}(\lambda)}{T_{sub}(\lambda)}}{1 - \frac{(R_{sam}(\lambda) - R_{sub}(\lambda))}{(T_{sub}(\lambda))^2}} \tag{1.39}$$

For solid state powder samples the diffuse reflectance R is measured and transformed to pseudo absorption with the Kubelka-Munk model following equation 1.40.[31] The beam path in the used Praying Mantis® diffuse reflection setup (HARRICK) is shown in figure 1.30 (b). The standard light path gets redirected through different mirrors and after interaction with the sample, the reflected light is directed back into the normal path, towards the detector.

$$A = \frac{(1 - R)^2}{2R} \tag{1.40}$$

An important information that can be extracted from UV-Vis spectra is the optical band gap by using the Tauc method.[34,35] By plotting $(\alpha h\nu)^x$ against $h\nu$, with $x = 1/2$ for indirect transitions and $x = 2$ for direct transitions, the band gap energy E_g is obtained

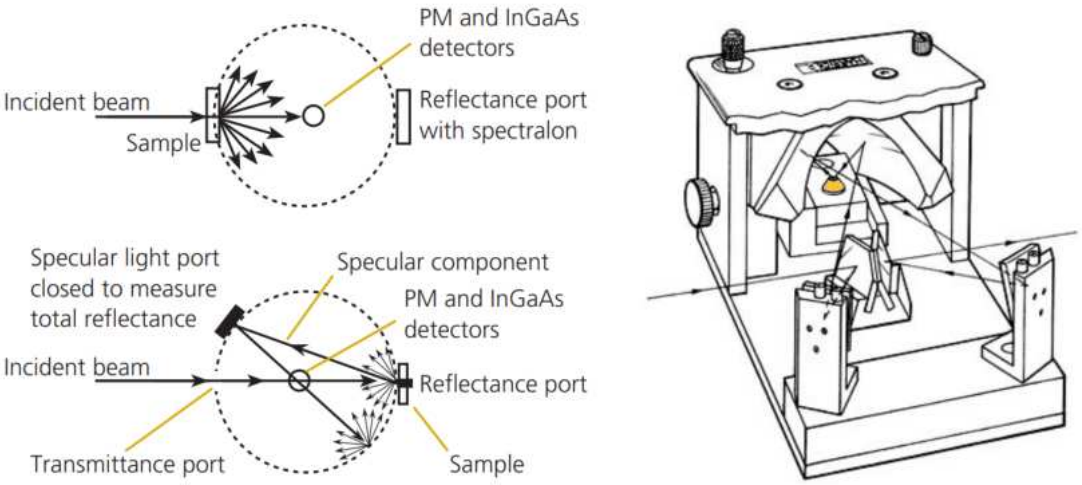

(a) (b)

Figure 1.30: (a) Schematic view of a UV-Vis measurement setup with an integrating sphere for transmittance (top) and reflectance (bottom) measurements.[32] (b) Schematic view of the Praying Mantis® setup with the beam path as a solid arrowed line and the sample holder highlighted in yellow.[33]

through extrapolation of the distinct, linear region at the x-axis intercept. Here, α is the optical absorption coefficient, ν the photon frequency and h Planck's constant.

1.3.10 Photoluminescence Spectroscopy (PL)

Luminescence is a process in which a material emits light through the relaxation of a preceding excited state back to its ground state. In case of photoluminescence, this preceding excited state is reached through the absorption of one or multiple photons. Luminescence is generally divided into two categories, fluorescence and phosphorescence, where the categorization is based on the mechanism and order of time in which the relaxation takes place. Fluorescence is based on a singlet excited state, where the return to the ground state is happening on the order of 10^{-9} s, i.e. nanoseconds. Phosphorescence on the other hand is based on a triplet excited state, where due to the forbidden transition back to the ground state the order of time is of 10^{-3} s to 1 s, i.e. milliseconds to seconds.

The involved processes of absorption and emission are commonly described by a Jablonski diagram shown in Figure 1.31, where the singlet ground, first and second electronic states are depicted by S_0, S_1 and S_2, respectively. The excited states can exist at multiple vibrational energy levels for each electronic energy level, depicted by further horizontal lines 1 and 2 above the associated thick lines 0. Electronic transitions between every state are depicted by solid arrows, where according to the Franck-Condon principle transitions occur on timescales of 10^{-15} s. After absorption of a photon, depending on its energy, an electron is excited to the matching vibrational level of the excited electronic state, where it will undergo rapid relaxation to the vibrational ground state on a timescale of 10^{-12} s. The reason for the timescale of fluorescence at 10^{-9} s thus lies in it being a probabilistic event, rather than being limited by the electronic and vibrational transitions themselves, which occur much faster. Excited states can also undergo a spin conversion from the S_1 state to a triplet state T_1, from where the emission occurs as phosphoresence. As the spin conversion from the T_1 state to the singlet ground state S_0 is forbidden, again for probabilistic reasons this process happens orders of magnitude slower than fluorescence.[36]

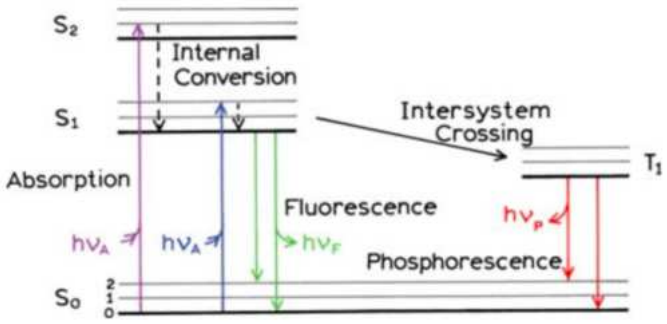

Figure 1.31: Simple Jablonski Diagram depicting the general processes of absorbtion, fluorescence and phosphorescence. Reproduced with permission from Springer Nature.[36]

Due to their close correlation, absorption and emission are thus processes that can give valuable insights into a material's electronic structure of radiative states. The emission energy can only reach a theoretical maximum value equal to that of the absorption and thus the absorption and emission spectra can be compared and are generally of similar shape. Due to the internal conversions, in reality the emission spectrum always has less energy, which is called the Stokes shift. Besides the mentioned vibrational and electronic transitions, other effects inducing a Stokes shift in the solid state can be excited-state reactions, energy transfer, or in a realistic approach as samples rarely behave as perfectly as simplified theory predicts, trap or sub-bandgap states of various kinds.

Next to the energetic spectrum of the emission, the quantum yield and emission lifetime are the other two main characteristics of photoluminescence. The quantum yield Q is simply the ratio between emitted and absorbed photons with the rate constants Γ for radiative decay and k_{nr} for the non-radiative decay following equation 1.41

$$Q = \frac{\Gamma}{\Gamma + k_{nr}} \tag{1.41}$$

For any radiative transition the lifetime τ is defined as the average time a system stays in the excited state before relaxing back to its ground state, simply expressed in equation 1.42:

$$\tau = \frac{1}{\Gamma + k_{nr}} \tag{1.42}$$

Considering theses three characteristics, their investigation is generally accomplished by either of the following two techniques: i) steady-state and ii) time-resolved photoluminescence. In steady-state measurements, the illumination and observation is constant, while in time-resolved measurements the illumination is pulsed. A steady-state measurement gives a time averaged intensity. To also extract the luminescence lifetime data, i.e the exact shape of the decay and to distinguish between the exact decay components and the weighted averages of multiple decays obtained, time-resolved measurements are indispensable, which can give valuable insights regarding the photophysical properties.

1.3.11 Optical-Pump Terahertz-Probe Spectroscopy (OPTP)

Charge carriers in semiconductors are the basis for the large variety of applications in optoelectronics. The charge carrier state and its properties are dependent on many factors such as the nanostructure of the material, external factors such as light or temperature, the crystal structure, the band gap, the dielectric function and electron-phonon coupling. The mobility differs largely depending on the charge carriers being free, in polaronic states or being bound as excitons. Terahertz spectroscopy provides a valuable method to investigate their properties, as charge carriers interact with electromagnetic waves in the low-frequency regime, i.e. frequencies around 1 THz (1×10^{12} Hz) or energies in the range of meV. Ultrafast lasers generating THz pulses on the femtosecond time scale allow for the investigation of mechanisms and time scales of carrier cooling, trapping, recombination, the dynamics of excitons and polarons, carrier density and mobility.[37]

Terahertz radiation can be produced through either i) photoconductivity or ii) the use of nonlinear optical processes. For i), a femtosecond optical pulse is absorbed by a semiconductor antenna, typically GaAs or silicon, producing charge carriers which are then accelerated in an applied electrical field. The produced, transient current will emit electromagnetic radiation in the THz regime which is used to probe the sample. In the second method ii), through optical rectification, a low-frequency polarization is generated by a second-order nonlinear process, when a laser pulse propagates through a non-centrosymmetric crystal, such as ZnTe, GaP, or GaSe. For either method, titanium:sapphire lasers with emission at 800 nm are commonly used, as they can provide ultrashort pulses down to 10 fs and emit in a suitable energy range. The detection of the THz transients is achieved similarly through either photoconductivity or a nonlinear optical method. A photoconductive detector antenna will interact as described above with the THz pulse to produce a current that can be detected. For the nonlinear optical variant the detection is based on a crystal with inversion symmetry which, under an applied electrical field, causes the rotation of the polarization of the probe pulse, which then can be measured. Thus, generation and detection methods are fundamentally similar and can be achieved with identical materials. To investigate a system's excited charge carriers, a laser pump pulse is used to simultaneously excite the material at its required excitation energy.[37]

To analyse a material, its properties need to be extracted from the obtained material complex dielectric function. The complex dielectric function $\epsilon(v)$ is related to the complex refractive index by $\epsilon(v) = n^2(v)$ and the optical conductivity by $\sigma(v) = -2\pi iv\epsilon_0(\epsilon_v - 1)$. Through Fourier transforms of the measured electric-field waveforms, which are obtained by measuring the intensity of the THz signal as a function of the time delay between the generation pulse (generation crystal/antenna) and the gate pulse (detection crystal/antenna). After the application of a transfer matrix analysis and a Taylor expansion the

following equation 1.43 results from which $\epsilon(v)$ can be obtained:[37]

$$\frac{E(v)}{E_{ref}(v)} = \frac{1+i\beta}{1+(i2\pi vd/c)(1+(\sqrt{\epsilon}-1)(\sqrt{\epsilon_{sub}}-\sqrt{\epsilon})/(1+\sqrt{\epsilon_{sub}}))'} \tag{1.43}$$

$E(v)$ and $E_{ref}(v)$ are the THz transmissions through the sample and the substrate, respectively, β is the phase delay due to propagation inside the material, d is the sample's thickness and c is the speed of light.[37]

To analyse the excited charge carriers through the pump-probe experiment, i.e. the photoinduced change of dielectric function $\Delta\epsilon(v)$, the THz waveform $E(t)$ is measured after passing through an unexcited sample and after passing through the pumped sample $\Delta E(t)$. The Fourier transform of both yields $\Delta\epsilon(v)$:[37]

$$\frac{\Delta E(v)}{E(v)} = \frac{t(\epsilon+\Delta\epsilon, v) - t(\epsilon, v)}{t(\epsilon, v)} \tag{1.44}$$

One key property of THz spectroscopy is the direct determination of conductivity parameters of free charge carriers and their evolution after photogeneration, enabling the analysis of ultrafast dynamics. Furthermore, the characterization of excitons is especially important as they are generally present in 2D and double perovskites and as they have significant consequences for solar cells. Within the range of normally used THz radiation (0.5 to 4 THz), excitons can only be observed indirectly. Exciton formation reduces the number of free charge-carriers, i.e. the measured signal decays. Free charge-carriers can interact with the THz radiation's electric field oscillation, due to the energy being resonant with their natural transitions. For excitons on the other hand, the energy required is usually higher due to the exciton binding energy making the THz pulse nonresonant with an excitons transitions. One common way to extract the material parameters such as mobility is the use of the Drude model. It assumes charge-carriers to behave as a dilute gas, interacting through scattering and collisions. They are accelerated by the electric field and their momentum is randomised through scattering events with a time interval τ between events. Accordingly, the mobility of the charge-carriers can be expressed as:[37]

$$\mu = \frac{e\tau}{m} \tag{1.45}$$

Here μ is the mobility, e is the electrons charge, τ is the lifetime mentioned above and m is the charge-carriers effective mass.

The non-contact measurement and sub-picosecond temporal resolution also enables the investigation of nanostructures, including for example quantum well structures. These are just a few examples why time-resolved optical-pump terahertz-probe spectroscopy is an extremely versatile, non-destructive technique to study charge carriers in semiconductors.[37]

1.3.12 Electrical Conductivity

The electrical conductivity or resistivity is a fundamental property for materials, defining how well it conducts or resists electrical current. For optoelectronic applications involving the flow of electrical current, such as solar cells, this is an important property. The resistance R in Ω is simply the ratio of voltage U to the current I following Ohm's law:

$$R = \frac{U}{I} \tag{1.46}$$

The conductance is simply the reciprocal of R in Siemens (S). As conductance and resistance also depend on the size of the material, more comparable values are given through the specific resistivity ρ, denoted as $\Omega \cdot m$ and the specific conductivity σ denoted as S/m, where A is the cross-section and l is the length of a uniform sample between to electrical contacts:

$$\rho = R\frac{A}{l} \tag{1.47}$$

$$\sigma = \frac{1}{\rho} \tag{1.48}$$

Since solar cell and other optoelectronic materials are semiconductors, their underlying principles for electrical conductivity are described through the band theory of electronic band structures. Charge carriers in semiconductors can move freely if they reside in bands with a suitable density of available states, and transitions induced through illumination can have a strong impact on conductivity. For solar cell characterization and most optoelectronic applications operating in the visible range of light, the illumination source is either a lamp with filters replicating the sun's spectrum, i.e. AM 1.5G (see chapter 1.3.13), or an LED-based spectrum of choice.

1.3.13 Solar Cell Characterisation

To describe the current-voltage characteristics of a photovoltaic device, a modified version of the diode current-voltage curve is used for a photodiode, shown in Fig. 1.32. Firstly, the conventional representation features the current density J instead of just the current I, as the extracted information is normalised in relation to the absorbing surface of the solar cell. Secondly, as solar cells are operated under illumination, there are two cases for the JV curve to consider: a) under dark conditions, where the situation is equal to the standard diode curve, and b) under light conditions, where the solar cell produces current through the absorbed light.

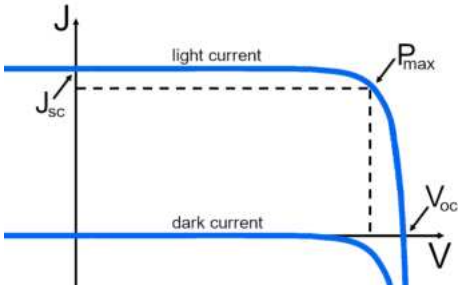

Figure 1.32: Schematic graph of current-voltage and power-voltage characteristics of a solar cell under normal conditions.

Under light conditions, the JV curve is shifted along the y-axis, proportional to the light induced current, as now there is a flow of current under zero bias voltage. This intersection point of the y-axis is denoted as the J_{sc}, the short-circuit current density, which in simple terms relates to the incident spectral photon flux b_s and the solar cell's quantum efficiency (QE), including the probability of an incident photon with energy E being converted to one electron to the external circuit and the electronic charge q:[38]

$$J_{sc} = q \int b_s(E) QE(E) dE \tag{1.49}$$

The quantum efficiency is a measure relating the system's number and energy per incident photon to the number and energy per extracted electron. This depends strongly on the absorption of the absorber material and the charge separation and collection of the full device. With the J_{sc}, the ideal diode equation modifies slightly to:

$$J = J_{sc} - J_0(e^{\frac{qV}{k_B T}} - 1) \tag{1.50}$$

The maximum voltage a solar cell can deliver is denoted as the V_{oc}, the open circuit voltage. It is the point at which dark and light current exactly cancel each other out and

can be expressed as:

$$V_{oc} = \frac{k_B T}{q} ln \frac{J_{sc}}{J_0} + 1 \tag{1.51}$$

As the output power of a solar cell does depend on both the current density and the voltage, the maximum power is reached at a point P_{max}, where the product of current density and voltage reaches its maximum. This characteristic is usually described through the fill factor FF:

$$FF = \frac{J_{Pmax} V_{Pmax}}{J_{sc} V_{oc}} \tag{1.52}$$

It is a ratio that can be visualized as the maximum rectangular area under the JV curve, as depicted by the dotted lines in fig. 1.6. Finally, the efficiency η of a solar cell can be expressed by using the above introduced figures of merit, either in dependence of the maximum power point, or the J_{sc}, V_{oc}, FF and P_{in}:[39–41]

$$\eta = \frac{P_{max}}{P_{in}} = \frac{J_{sc} V_{oc} FF}{P_{in}} \tag{1.53}$$

1.4 References

[1] M. Eckert, *Ann. Phys.* **2012**, *524*, A83–A85.

[2] W. Borchardt-Ott, *Kristallographie*, 7th ed., Springer, **2008**, pp. 281–294.

[3] D. Schwarzenbach, *Crystallography*, 1st ed., John Wiley & Sons, **1996**, pp. 89–128.

[4] W. Massa, *Kristallstrukturbestimmung*, 7th ed., Vieweg+Teubner, **2011**, pp. 49–55, 93–128, 131–148.

[5] C. Hoch, *Strukturanalyse - Teil II Beugungsmethoden - WS17/18*, LMU, **2017**.

[6] L. McCusker, R. Von Dreele, D. Cox, D. Louër, P. Scardi, *Journal of Applied Crystallography* **1999**, *32*, 36–50.

[7] B. L. Henke, E. M. Gullikson, J. C. Davis, *Atomic data and nuclear data tables* **1993**, *54*, 181–342.

[8] G. Renaud, R. Lazzari, F. Leroy, *Surface Science Reports* **2009**, *64*, 255–380.

[9] P. Müller-Buschbaum, *Advanced materials* **2014**, *26*, 7692–7709.

[10] A. Meyer, *www.gisaxs.de*, Institute of Physical Chemistry University of Hamburg, **2019**.

[11] Goniometer geometry, www.xtal.iqfr.csic.es/Cristalografia/parte_06-en.html, Accessed: 01.08.2018.

[12] R. Gross, A. Marx, *Festkörperphysik*, 1st ed., Oldenbourg Verlag München, **2012**, p. 1.

[13] D. Sayre, *Acta. Cryst.* **1952**, *5*, 60–65.

[14] C. Hoch, *Wochenkurs Röntgenstrukturanalyse an Einkristallen*, LMU, **2014**.

[15] J. I. Goldstein, D. E. Newbury, J. R. Michael, N. W. Ritchie, J. H. J. Scott, D. C. Joy, *Scanning electron microscopy and X-ray microanalysis*, Springer, **2017**.

[16] Electron beam interaction volume, https://intranet.stpaulsschool.org.uk/halley-research-community/scanning-electron-microscope-sem/interaction-volume, Accessed: 15.07.2023.

[17] A. Hartschuh, *Microscopy for Nanotechnology WS17/18*, LMU, **2017**.

[18] M. Döblinger, *Scanning Electron Microscopy and Analytical Techniques WS16/17*, LMU, **2016**.

[19] S. Amelinckx, D. van Dyck, J. van Landuyt, G. van Tendeloo, *Electron Microscopy: Principles and Fundamentals*, John Wiley & Sons, Hoboken, NJ, **1997**, pp. 305–328.

[20] R. F. Egerton, *Physical principles of electron microscopy: an introduction to TEM, SEM, and AEM*, 2nd ed., Springer, **2006**, pp. 15–16, 121–134.

[21] F. J. Giessibl, *Reviews of modern physics* **2003**, *75*, 949.

[22] H.-J. Butt, B. Cappella, M. Kappl, *Surface science reports* **2005**, *59*, 1–152.

[23] Atomic Force Microscope, https://afm.oxinst.com/assets/components/phpthumbof/cache/how-an-afm-works-970px.77f3b33ba3aa2c87b204d6ea0e1db99d.png, Accessed: 06.05.2024.

[24] K. Burke, *The Journal of chemical physics* **2012**, *136*.

[25] P. W. Atkins, R. S. Friedman, *Molecular quantum mechanics*, Oxford university press, **2011**.

[26] J. P. Perdew, K. Burke, M. Ernzerhof, *Physical review letters* **1996**, *77*, 3865.

[27] P. Hohenberg, W. Kohn, *Physical review* **1964**, *136*, B864.

[28] W. Kohn, L. J. Sham, *Physical review* **1965**, *140*, A1133.

[29] H.-H. Perkampus, *UV-VIS Spectroscopy and its Applications*, Springer Science & Business Media, **2013**.

[30] B. M. Klahr, T. W. Hamann, *The Journal of Physical Chemistry C* **2011**, *115*, 8393–8399.

[31] H. G. Hecht, **1976**, *466*, 57.

[32] C. Tams, N. Enjalbert, *Perkin Elmer Application Note* **2009**.

[33] *Harrick Scientific Products Data Sheet* **2019**.

[34] J. Tauc, R. Grigorovici, A. Vancu, *Physica Status Solidi (b)* **1966**, *15*, 627–637.

[35] B. D. Viezbicke, S. Patel, B. E. Davis, D. P. Birnie III, *Physica Status Solidi (b)* **2015**, *252*, 1700–1710.

[36] J. R. Lakowicz, *Principles of Fluorescence Spectroscopy*, 3rd ed., Springer Science & Business Media, **2006**.

[37] R. Ulbricht, E. Hendry, J. Shan, T. F. Heinz, M. Bonn, *Reviews of Modern Physics* **2011**, *83*, 543.

[38] J. A. Nelson, *The physics of solar cells*, World Scientific Publishing Company, **2003**.

[39] M. A. Green, *Solar cells: operating principles, technology, and system applications*, **1982**.

[40] P. Würfel, U. Würfel, *Physics of solar cells: from basic principles to advanced concepts*, John Wiley & Sons, **2016**.

[41] S. Rühle, *Solar Energy* **2016**, *130*, 139–147.

Chapter 2

Silver-Bismuth Based 2D Double Perovskites $(4\,FPEA)_4AgBiX_8$ (X = Cl, Br, I): Highly Oriented Thin Films with Large Domain Sizes and Ultrafast Charge-Carrier Localization

This chapter is based on the following publication:

R. Hooijer, A. Weis, A. Biewald, M. T. Sirtl, J. Malburg, R. Holfeuer, S. Thamm, A. A. Y. Amin, M. Righetto, A. Hartschuh, L. Herz, T. Bein, Advanced Optical Materials **2022**, 10, 2200354.

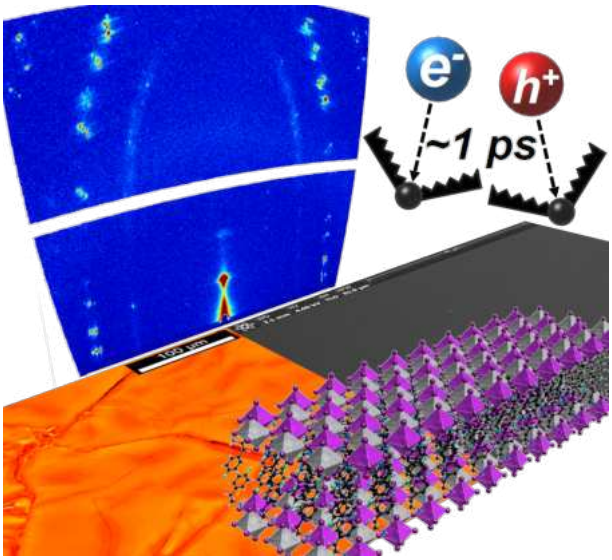

The following work was performed by R. Hooijer: conception, synthesis of single crystals, thin films and powder samples, device fabrication, XRD measurements and analysis, XRD profile refinements, GIWAXS measurements and analysis, light microscope measurements and analysis, SEM and EDX analysis, UV-Vis measurements and analysis, AFM measurements and analysis, complete data interpretation and writing the manuscript. A. Weis performed DFT calculations. A. Biewald performed PL measurements and analysis. M.T. Sirtl helped in the conception of the project. J. Malburg and S. Thamm worked on the project through internships. R. Holfeuer and A.A.Y. Amin performed photodetector measurements. M. Righetto performed OPTP measurements and analysis. All authors wrote and edited the manuscript for final submission.

2.1 Abstract

Two-dimensional (2D) hybrid double perovskites are a promising emerging class of materials featuring superior intrinsic and extrinsic stability over their 3D parent structures, while enabling additional structural diversity and tunability. Here, we expand the Ag–Bi-based double perovskite system, comparing structures obtained with the halides chloride, bromide, and iodide and the organic spacer cation 4-fluorophenethylammonium (4FPEA) to form the n = 1 Ruddlesden–Popper (RP) phases $(4\,\mathrm{FPEA})_4\mathrm{AgBiX}_8$ (X = Cl, Br, I). We demonstrate access to the iodide RP-phase through a simple organic spacer, analyze the different properties as a result of halide substitution and incor- porate the materials into photodetectors. Highly oriented thin films with very large domain sizes are fabricated and investigated with grazing incidence wide angle X-ray scattering, revealing a strong dependence of morphology on substrate choice and synthesis parameters. First-principles calculations confirm a direct band gap and show type Ib and IIb band alignment between organic and inorganic quantum wells. Optical characterization, temperature- dependent photoluminescence, and optical-pump terahertz-probe spectroscopy give insights into the absorption and emissive behavior of the materials as well as their charge-carrier dynamics. Overall, we further elucidate the possible reasons for the electronic and emissive properties of these intriguing materials, dominated by phonon-coupled and defect-mediated polaronic states.

2.2 Introduction

The exploration of 2D hybrid perovskites has gained increased attention, along with the success of their 3D analogs as optoelectronic materials for solar cells, laser diodes, and field-effect transistors, X-ray- and photodetectors or light-emitting diodes.[1–6] While a large number of 3D and 2D metal halide perovskites based on divalent metals such as Pb^{2+}, Sn^{2+}, Cu^{2+}, Mn^{2+}, Cr^{2+},and Cd^{2+} have been reported, a larger variety of materials based on the double perovskite structure $A^{I}{}_2B^{I}B^{III}X_6$ with A- and B-site cations and halides X remain comparatively uninvestigated. If not only the compositional variety of 3D double perovskites is considered, but also the dimensional reduction to 2D phases of such, the structural and compositional possibilities become phenomenally vast. By introducing mono- or multivalent organic A-site spacer cations, the materials' properties can be tuned by the variation of the spacer cation and also the thickness of the octahedral layers of the perovskite that are separated by the spacer cation.

Crystallographically speaking, a large number of double perovskites have been characterized or computed over the last 80 years, although the optoelectronic characterization and their potential for devices were only revisited recently.[7,8] Several halide double perovskites that are promising for optoelectronic application have been synthesized or computationally predicted, such as $Cs_2AgBiCl_6$,[9] $Cs_2AgBiBr_6$,[5] Cu_2AgBiI_6,[10] $(MA)_2TlBiBr_6$ (MA = methylammonium),[11] $Cs_2AgSbCl_6$,[12] $Cs_2AgInCl_6$,[13] $Cs_2AgTlBr_6$,[14] $ASbCuX_6$ (A = monovalent cation, X = Cl, Br, I),[15] and $(MA)_2KBiCl_6$.[16]

The currently most studied double perovskite is $Cs_2AgBiBr_6$, mostly owing to its promising charge-carrier properties and its stability, despite its relatively large band gap of 2.0–2.3 eV.[17–22] Following this interest, more recently the effects of the dimensional reduction from 3D to 2D phases of $Cs_2AgBiBr_6$ have been reported by several groups by elaborating the theme in the form of $(BA)_4AgBiBr_8$, $(BA)_2CsAgBiBr_7$ (BA = butylammonium),[23] $(PEA)_4AgBiBr_8$ (PEA = phenethylammonium),[24–26] $(iPA)_2CsAgBiBr_7$ (iPA = isopentylammonium),[27] $(PA)_2CsAgBiBr_7$ (PA = propylammonium), $(PA)_4AgBiBr_8$, $(OCA)_4AgBiBr_8$ (OCA = octylammonium), and $(BDA)_2AgBiBr_8$ (BDA = 1,4-butyldiammonium).[28]

As a way of tuning the band gap of halide perovskites, it is known that changing the halide anion decreases its size in the order of $Cl^- > Br^- > I^-$.[29] The desirable double perovskite Cs_2AgBiI_6 is unfortunately not easily synthesized because of its negative decomposition enthalpy resulting in $CsAg_2I_3$ and $Cs_3Bi_2I_9$.[30,31] Another beneficial effect of the dimensional reduction is that the 2D phases of this silver bismuth iodide system are thermodynamically stable and compounds of the Ruddlesden–Popper (RP) n = 1 structure $(OC^{I})_4AgBiI_8$ (OC^{I} = organic cation, monovalent; n = octahedral layer thickness)

or the Dion-Jacobson n = 1 structure $(OC^{II})_2AgBiI_8$ (OC^{II} = divalent) were successfully synthesized and reported, thus enabling access to iodide double perovskites. Besides the reduced band gap energies around 2.0 eV caused by the heavier halide, a change in nature from indirect to direct band gap was reported several times to accompany the dimensional reduction from 3D to 2D systems.[23,32]

While bromide analogs have been reported with simple, alkylic, and aromatic spacer cations such as butylammonium or phenethyl ammonium, the iodide analogs have only been reported recently with more strongly interacting organic spacer cations, as, for example, divalent molecules forming Dion- Jacobson phases or molecules with an increasing number of ring systems, thus increasing the strength of aromatic interactions. Organic spacer cations with atomic interactions through terminating atoms such as iodine, as demonstrated for $(3\,IPA)_4AgBiI_8$ (3IPA = 3-iodopropylammonium), or fluorine (our work) have also shown this ability to stabilize the lattice of thermodynamically unfavored iodide phases.[33] For these, a sufficient templating effect through either structural rigidity or stronger molecular interactions is required to discourage the formation of more stable 0D or 1D Bi-I lattices.[34] For the choice of the organic spacer cation, ammonium- terminated alkylic or aromatic molecules are most commonly used, optionally with chain/ring-incorporation of nitrogen or sulfur atoms or halogen substitution at various hydrogen positions.[35–38]

Here, we synthesized three new compounds of the $(OC)_4AgBiX_8$ (X = Cl, Br, I) RP n = 1 structure with 4-fluoro-phenethylammonium (4FPEA) serving as the organic cation. We present the first comparative halide study for 2D double perovskites. The compounds were structurally and optoelectronically characterized in powder and thin film form. We synthesized single crystals of $(4\,FPEA)_4AgBiBr_8$ and $(4\,FPEA)_4AgBiI_8$ while for $(4\,FPEA)_4AgBiCl_8$ possible unit cell parameters were indexed. We use density-functional theory (DFT) to obtain insight into the electronic structure and atomic contributions to the frontier orbitals. Furthermore, we synthesized high-quality thin films and thoroughly characterized them by employing grazing-incidence wide angle X-ray scattering (GIWAXS). Finally, we provide initial insights into the charge-carrier dynamics and emissive properties, employing optical-pump terahertz-probe spectroscopy (OPTP) and photoluminescence (PL) measurements of these materials and incorporate them into photodetectors.

2.3 Results and Discussion

2.3.1 Structural Characterization

The 3D halide perovskite structure is based on the general formula ABX_3 with corner-sharing BX_6 octahedra, divalent metal cations B^{2+} and halide anions X^-, where monovalent A^+ cations occupy the cuboctahedral cavities. For the 3D double perovskite, the general formula is expanded to $A_2B^IB^{III}X_6$, following the same occupational rules with the difference that the corner-sharing octahedra are now alternating between B^IX_6 and $B^{III}X_6$. RP double perovskites with an octahedral layer thickness of n = 1 adopt the general formula $(OC)_4B^IB^{III}X_8$, where the organic cation (OC) replaces the A^+ cation and is also monovalent. The organic cations separate the octahedral layers, with the positively-charged group (i.e. NH_3^+) terminating into the cuboctahedral cavities, while the uncharged part interacts via van der Waals (v.d.W.) forces and dipole–dipole interactions, leaving a van der Waals gap between the organic layers.[39]

Investigating the structural properties of (4 FPEA)$_4$AgBiCl$_8$, (4 FPEA)$_4$AgBiBr$_8$, and (4 FPEA)$_4$AgBiI$_8$ (synthesized from a simple solution approach explained in detail in the experimental part) we find very small changes, where the 4FPEA cation seems to have the dominant influence on the structural direction, enabling synthesis of the chloride and bromide structure but also stabilizing the iodide structure. In contrast, the unsubstituted phenethylammonium (PEA) cation can only yield the (PEA)$_4$AgBiCl$_8$ and (PEA)$_4$AgBiBr$_8$ compounds, but cannot stabilize the iodide structure (see XRD and EDX data in FigureSI 2.12, Supporting Information and TableSI 2.1, Supporting Information).

The structures of (4 FPEA)$_4$AgBiBr$_8$ and (4 FPEA)$_4$AgBiI$_8$ were determined through single-crystal X-ray diffraction, while for (4 FPEA)$_4$AgBiCl$_8$ the lattice parameters were determined through indexing of powder XRD data. We note that the crystal structure of (4 FPEA)$_4$AgBiI$_8$ was refined as a 2-component pseudomerohedral twin (pseudo-monoclinic cell) with a refined ratio of 0.75/0.25 for the two domains. The two equatorial iodides are slightly disordered with ratios of site occupation factors refined to 0.97/0.03 as seen in FigureSI 2.13, Supporting Information. This disorder of equatorial iodines was also observed for other 2D iodide double perovskites such as (AE2T)$_2$AgBiI$_8$.[34] For the following comparative discussion, only the iodine sites with an occupation of 97% will be considered. Furthermore, we limit the discussion to the comparison of the crystal structures to the bromide and iodide analogs as seen in Figure 2.1.

Unlike the octahedra in the cubic $Cs_2AgBiBr_6$ that exhibit equivalent bond lengths (Bi-Br = 2.814 Å, Ag-Br = 2.821 Å) and metal-halide-metal angles of 90°, the octahedra in (4 FPEA)$_4$AgBiX$_8$ are strongly distorted.[5] The angles in both structures in the Ag- and

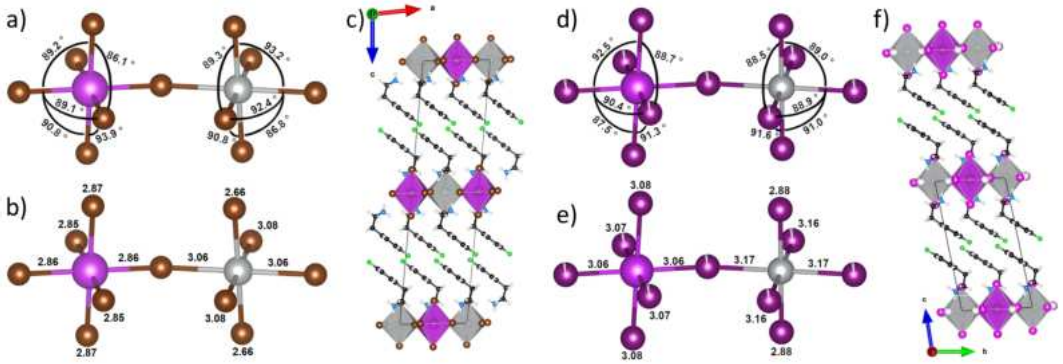

Figure 2.1: Single crystal structures of $(4\,FPEA)_4AgBiBr_8$ and $(4\,FPEA)_4AgBiI_8$ with a,d) octahedral angles in °, b,e) bond lengths in Å and c,f) comparative views of the unit cell of both structures. The bond angles shown are point symmetric with regard to their central metal atom and thus only shown once for clarity.

Bi-octahedra are equally distorted by up to 3.9° (Figure 2.1a,d). The bond lengths exhibit unequal distortion where the Ag-octahedra are strongly tetragonally contorted, resembling a Jahn–Teller effect with short axial bonds (Ag-Br = 2.66 Å, Ag-I = 2.88 Å) and long equatorial bonds (Ag-Br = 3.06/3.08 Å, Ag-I = 3.17/3.16 Å), while the Bi-octahedra are mostly symmetrically and only marginally distorted (Ag-Br = 2.85/2.86/2.87 Å, Ag-I = 3.06/3.07/3.08 Å) (Figure 2.1b,e). This tendency of monovalent Ag is also observed in compounds such as $Ag^{I}Ag^{III}O_2$, compounds with other similar d^{10} transition metals, e.g. Au^+ or Cu^+ or other recently reported, Ag-containing 2D hybrid double perovskites and is attributed to a mixing of filled transition-metal nd orbitals with empty (n + 1)s orbitals, stabilizing a linear coordination geometry.[8,23,33,34,40,41]

One factor required to form 2D hybrid double perovskite iodides is the templating influence of the organic spacer cations, a term coined by Mitzi in 2000.[42] Both the RP and DJ phases require an in-plane interaction of suitably sized organic spacers to stabilize the 2D lattice, for example, aromatic, v.d.W. or dipole–dipole interactions. Contrarily, while the DJ phases have an intrinsically stronger interlayer connectivity by binding one organic layer to two adjacent inorganic layers through the divalent character, RP phases also require a strong interaction between organic spacer molecules along the out-of-plane direction. As of now, this synthetic difficulty has only yielded a small, but growing number of published structures, namely $(CHD)_2AgBiI_8 \cdot H_2O$ (CHD = 1,4-cyclohexandiamine),[43] $(AE2T)_2AgBiI_8$ (AE2T = 5,5'-diylbis(aminoethyl)-[2,2'-bithiophene]),[34] $(3\,AMPY)_2AgBiI_8$ (3AMPY = 3-(aminomethyl) pyridinium),[44] $(4\,AMP)_2AgBiI_8$ (4AMP = (4-(aminomethyl) piperidinium),[45] $(3\,IPA)_4AgBiI_8$ (IPA = 3-iodopropylammonium),[33] $(4\,IBA)_4AgBiI_8$ (IBA = 4-iodobutylammonium),[46] $(4\,AMP)_4AgBiI_8$,[47] $(APP)_4AgBiI_8$ (APP = 4-aminopiperidinium) and (β-MPA)$_4$AgBiI$_8$ (β-MPA = β-methylphenethylammonium).[48] In our work, we used the simple modification of the

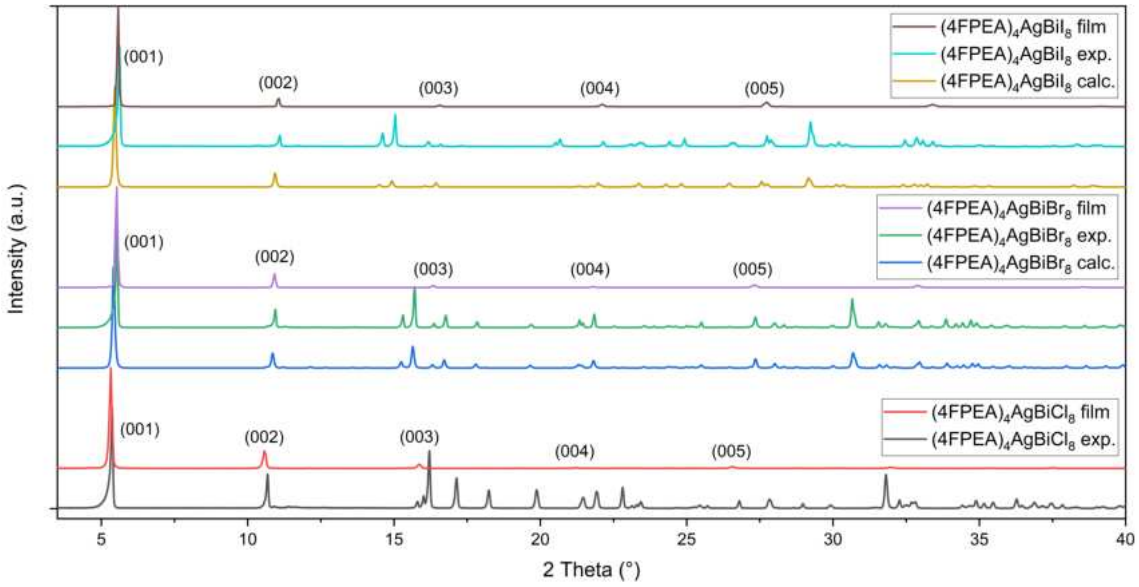

Figure 2.2: XRD patterns of thin films on ITO annealed at 140 °C and powdered crystals of (4 FPEA)$_4$AgBiX$_8$ (X = Cl, Br, and I) grown in solution along with calculated patterns for (4 FPEA)$_4$AgBiBr$_8$ and (4 FPEA)$_4$AgBiI$_8$ derived from single-crystal structures.

PEA$^+$ cation to the 4 FPEA$^+$ cation to achieve the stabilizing and templating effect. To emphasize this, the structural differences between (PEA)$_4$AgBiBr$_8$ and (4 FPEA)$_4$AgBiBr$_8$ are discussed in detail and shown in FigureSI 2.14, Supporting Information and FigureSI 2.15, Supporting Information.

Figure 2.2 shows the XRD patterns of polycrystalline powders and thin films of (4 FPEA)$_4$AgBiX$_8$ (X = Cl, Br, I) as well as theoretical patterns based on the single-crystal structures of (4 FPEA)$_4$AgBiBr$_8$ and (4 FPEA)$_4$AgBiI$_8$. For (4 FPEA)$_4$AgBiCl$_8$ a single crystal has not been obtained, but the indexed lattice parameters agree well with the powder XRD pattern and the lattice parameters of the bromide and iodide analog (TableSI 2.2, Supporting Information). For the bromide and iodide compounds, the experimental patterns also agree well with the simulated ones, without any detectable impurities, which we confirmed through a profile refinement (FigureSI 2.18, Supporting Information). Consistently, energy dispersive X-ray spectroscopy confirms the stoichiometric ratio for both crystals and thin films for all three compounds (TableSI 2.3, Supporting Information). A slight shift towards larger angles can be observed for both compounds from calculated to experimental diffractograms, indicating homogeneous lattice strain and thus a slightly compressed unit cell for experimental samples. From the thin film diffractograms, a strong orientation along the (00l) planes can already be observed, which is characterized more thoroughly with GIWAXS measurements (see below). If the three halide compounds are compared from Cl to Br to I, a shift toward smaller angles for the (hk0) planes can be observed, which is consistent with the increasing size of the unit cell in a and b directions, caused by the increase of ionic size of the halides and the increased

equatorial metal-halide bond lengths (TableSI 2.2, Supporting Information). In contrast, the (00l) planes are shifted toward larger angles from Cl to Br to I, also in agreement with the decrease of the unit cell size in the c direction. While the increase in bond distances and the ionic size is consistent for the axial octahedral bonds, the decrease in the c direction can be attributed to the slightly closer packing of the inorganic and organic layers.

2.3.2 Orientation and Thin Film Morphology

Thin films of $(4\,FPEA)_4AgBiCl_8$, $(4\,FPEA)_4AgBiBr_8$, and $(4\,FPEA)_4AgBiI_8$ were fabricated by spin coating from N-methyl-2-pyrrolidone (NMP) solutions onto different substrates with a subsequent annealing step. All three compounds in thin film form are strongly oriented along the (00l) planes, corresponding to a parallel orientation of inorganic and organic layers to the substrate surface. This horizontal orientation is typical for single-layered n = 1 2D double perovskite phases and so far, no other orientations have been prepared.[48,49] Furthermore, while for Pb- and Sn-based 2D perovskites higher n phases and vertical orientations have been reported, for Ag-Bi-based double perovskite systems $(BA)_2CsAgBiBr_7$, $(iPA)_2CsAgBiBr_7$ and $(PEA)_2CsAgBiBr_7$ remain the only known ones exhibiting the n = 2 thickness, though no thin films have been reported thus far.[23,26,27] While other studies have focused on initial thin film syntheses for n = 1 2D double perovskites,[33,34,43,47] here we have optimized the morphology of the thin films on different substrates and were able to observe structural differences depending on the choice of substrate roughness, the different halides, and annealing temperature.

To compare the influence of the substrate roughness we chose FTO-coated glass, ITO-coated glass, and Si-SiO_2 wafers as they are commonly used substrates for optoelectronic applications such as photovoltaics, photodetectors, light emitting diodes or field-effect transistors. The difference in surface roughness between these substrates is about one order of magnitude, with height differences (as RMS) of ±60 nm for FTO, ±5 nm for ITO, and ±1 nm for the polished SiO_2 wafer, see FigureSI 2.19, Supporting Information, for line profile scans and AFM images.

All thin film diffractograms exhibit the same general orientation along (00l) as shown in Figure 2.2 and Figure 2.3. We observe the same trends in crystallinity and an increasing quality from Cl > Br > I (a more detailed discussion of the diffractograms is given in the Supporting Information under FigureSI 2.20). One key feature is the splitting and broadening of reflections for the $(4\,FPEA)_4AgBiBr_8$ films, which we attribute to increased lattice parameters for higher annealing temperatures of 140 °C versus 100 °C, exerting tensile stress on the crystal lattice. To identify these different phases, a profile refinement revealed the slightly different lattice parameters for the concerned films, see

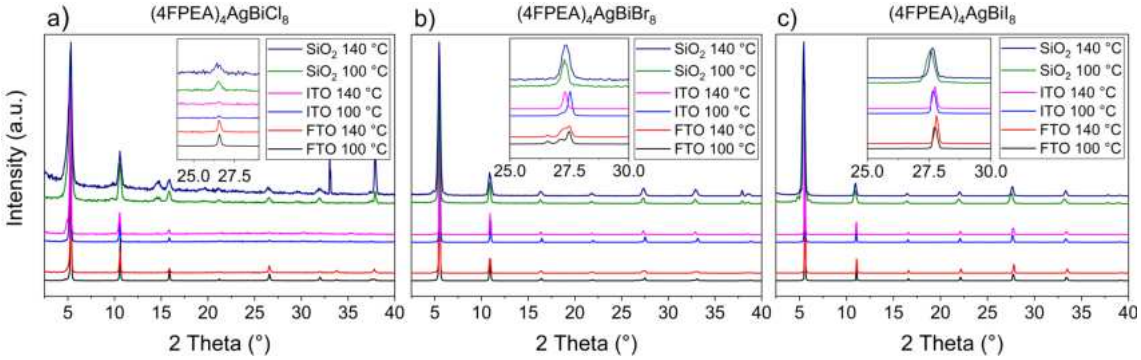

Figure 2.3: XRD patterns of thin films of a) (4 FPEA)$_4$AgBiCl$_8$, b) (4 FPEA)$_4$AgBiBr$_8$ and c) (4 FPEA)$_4$AgBiI$_8$ on substrates FTO, ITO, and SiO_2 from NMP solution with annealing at 100 °C or 140 °C. The different parameters are indicated in the legends, insets show a magnified view of the 005 reflections.

TableSI 2.4, Supporting Information. Interestingly, while the annealing temperatures for all three substrates were identical, there is an observable difference in the diffractograms. We attribute this to the varying thickness and heat conductivity of the substrates. While the silicon wafer already has a higher heat conductivity than ITO and FTO coated glass substrates, additionally the substrate thickness increases from 0.625 mm (Si-SiO_2 wafer) to 1 mm (ITO coated glass) and 3 mm (FTO coated glass), which leads to a faster heat transfer along FTO $<$ ITO $<$ SiO_2. This results in a decreasing rate of solvent evaporation and crystallization toward FTO substrates. We believe this to be a reason why for FTO samples a mixture of both phases is seen for both temperatures, while for ITO the two phases are formed much more distinctly and on SiO_2 the crystallization is basically too fast for a distinct phase to form, leading to a broad reflection profile that indicates a very small crystallite size and a largely strained crystal lattice. Thin films of (4 FPEA)$_4$AgBiI$_8$ show no additional reflections and no reflection splitting, as observed in (4 FPEA)$_4$AgBiBr$_8$. Interestingly, the influence of the annealing temperature is inverse to that of (4 FPEA)$_4$AgBiBr$_8$. With higher temperature the reflections shift toward higher angles compared to the diffractograms obtained with 100 °C annealing. This leads to the conclusion that while films of (4 FPEA)$_4$AgBiBr$_8$ at 140 °C display increased lattice parameters and tensile stress, films of (4 FPEA)$_4$AgBiI$_8$ show decreased lattice parameters and thus compressive stress. This trend is seen for all three substrates and while again the SiO_2-based films show broad reflections, they are also shifted toward higher angles.

To further analyze the influence of the substrate choice and annealing temperature, we performed GIWAXS measurements. The films prepared on FTO substrates, having the roughest surface of the three substrates, show the largest broadening of the reflections along the azimuthal angle χ compared to a smaller broadening for ITO substrates and sharp reflection dots for SiO_2 substrates (Figure 2.4). This orientational degree can be visualized quantitatively by plotting the intensity of the 001 reflection with χ as the ab-

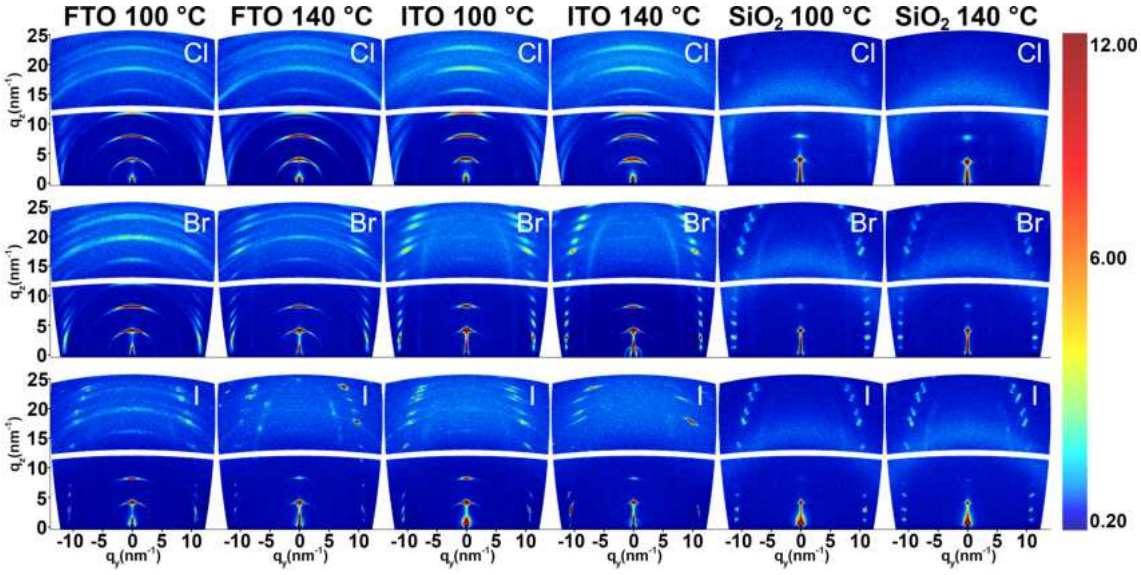

Figure 2.4: GIWAXS images of $(4\,\mathrm{FPEA})_4\mathrm{AgBiCl_8}$, $(4\,\mathrm{FPEA})_4\mathrm{AgBiBr_8}$, and $(4\,\mathrm{FPEA})_4\mathrm{AgBiI_8}$ on FTO, ITO, and SiO_2 annealed at 100 °C and 140 °C, measured with an incident angle $\alpha_i = 0.2°$.

scissa and is discussed in more detail under FigureSI 2.22, Supporting Information. The measurements shown in FigureSI 2.22, Supporting Information, reveal that for all films the orientation is present and of the same degree throughout the complete film. Only for $(4\,\mathrm{FPEA})_4\mathrm{AgBiCl_8}$ and $(4\,\mathrm{FPEA})_4\mathrm{AgBiBr_8}$ films on FTO the orientations show slightly larger FWHMs for the surface layers indicating a marginally smaller degree of horizontal orientation. Furthermore, if annealing temperatures are compared, 140 °C compared to 100 °C results in sharper reflection spots and thus a higher degree of orientation. The main difference of these annealing temperatures is the increase in vapor pressure of the solvent N-methyl-2-pyrrolidone (NMP). With a boiling point of 202 °C, the vapor pressure increases almost tenfold from 3 kPa at 100 °C to 27 kPa at 140 °C, at ambient pressure.[50] This results in a much faster crystallization of the films, resulting in larger domains and a higher degree of orientation (FigureSI 2.24, Supporting Information). Finally, the crystallinity and degree of orientation increases for Cl < Br < I (FigureSI 2.25, Supporting Information). This can be seen by the decreased azimuthal broadening of reflections for Cl, Br, and I, respectively, as well as the increasing sharpness and intensity of reflections that originate from different (11l) planes, located at scattering vectors q_y = $10\,\mathrm{nm^{-1}}$ and $-10\,\mathrm{nm^{-1}}$ (Figure 2.4). For the chloride perovskites these reflections are only visible as weak and very broad areas, while for the bromide perovskites they are more distinct with an increased sharpness from FTO < ITO < SiO_2 and are distinctly shown as diffraction spots for the iodide. In the same way, the reflections of the 00l planes are only visible on FTO, while on ITO for the bromide and iodide the relative intensity of the 001 and 002 reflection is too high for reflections of l > 2 to be observable, demonstrating the high crystallinity of the $(4\,\mathrm{FPEA})_4\mathrm{AgBiBr_8}$ and $(4\,\mathrm{FPEA})_4\mathrm{AgBiI_8}$ thin films.

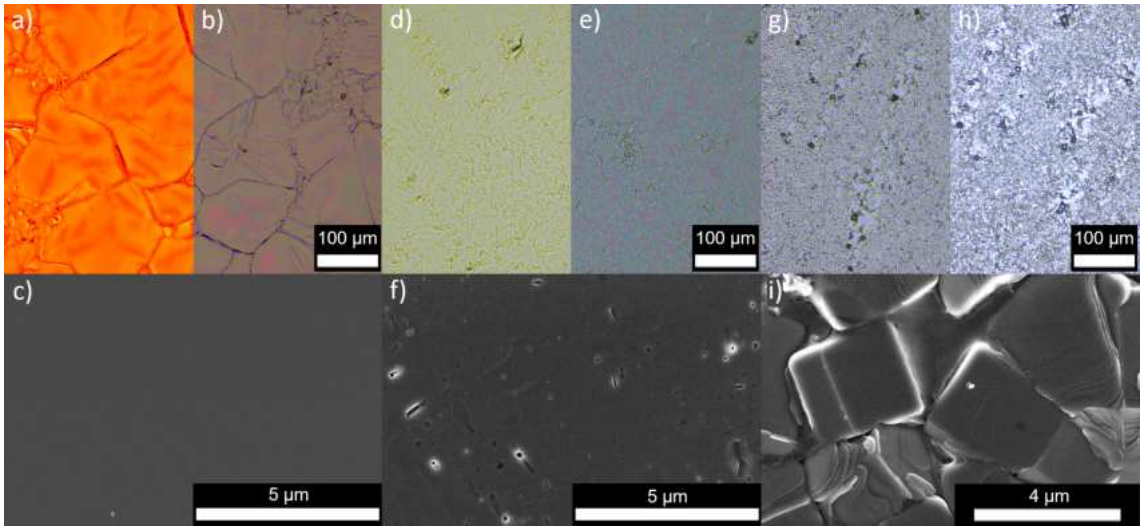

Figure 2.5: Optical microscopy (OM) images (top row) and SEM images (bottom row) for (4 FPEA)$_4$AgBiI$_8$ a–c), (4 FPEA)$_4$AgBiBr$_8$ d–f) and (4 FPEA)$_4$AgBiCl$_8$ g–i). OM images are shown in transmission lighting on the left and illumination lighting on the right (top) for the respective compound.

This relative increase is seen again for films on the SiO_2 substrates where only the 001 reflection is observable. To confirm the orientation and assignment of diffraction planes, indexed 2D GIWAXS images of thin films annealed at 100 °C are shown in FigureSI 2.25, Supporting Information, for all three compounds confirming the crystal phase of the thin films. While the diffraction positions of (00l) planes agree well with the calculated positions, the diffraction positions of planes including a and b lattice parameters exhibit a shift indicating a compressed unit cell in a and b. This almost single-crystalline, excellent orientation of the iodide thin films achieved by a simple-solution-based spin-coating process is remarkable. A similar high level of orientation and near single-crystalline growth has been achieved very recently by Zhao et al. with (R/S – β-MPA)$_4$AgBiI$_8$ utilizing a strongly crystallization-guiding capillary-bridge assembly technique.[48]

The surface morphology was probed with optical and scanning electron microscopy and both methods confirm the high quality of the films and their orientation. For example, here we show films fabricated on ITO substrates with the same experimental conditions for all three halides in Figure 2.5. The films of (4 FPEA)$_4$AgBiI$_8$ are homogeneous and form large domains with dimensions of up to 100 × 100 µm as shown in Figure 2.5a,b. The smooth surface morphology is of very high quality as seen in the SEM image in Figure 2.5c, where the contrast is homogeneous over the complete surface and grain boundaries inside a single domain cannot be observed. (4 FPEA)$_4$AgBiBr$_8$ also forms homogeneous films throughout the complete film surface (Figure 2.5d,e), yet does not form the large nearly perfect domains seen for the iodide perovskite. The domains seem bigger but rougher, which is also evident from the small holes in the SEM image in Figure 2.5f. Despite the small holes, the surface is still contrasted homogenously and grain bound-

aries cannot be observed. We note that for differently optimized parameters, an equally pristine surface can be obtained for $(4\,FPEA)_4AgBiBr_8$ films (FigureSI 2.26, Supporting Information). For $(4\,FPEA)_4AgBiCl_8$, the film quality is not as pristine as for the iodide or bromide structure. The OM images (Figure 2.5g,h) show a grained surface morphology and this is more clearly observable in the SEM image (Figure 2.5i) where single grains with dimensions in the range of several microns can be observed. Furthermore, the layered structure of the material can be clearly seen, as the individual layers stacking in the grains are evident for slightly tilted grains and with uneven surfaces.

2.3.3 First Principles Calculations

To get insight into the electronic structure, DFT calculations were conducted. Figure 2.6a–c shows the PBE-SOC-TS band structures of $(4\,FPEA)_4AgBiX_8$ (X = Cl, Br, I). All calculations were carried out with the unit cells obtained from experimental single crystal data, although the band structure for $(4\,FPEA)_4AgBiCl_8$ was simulated starting from the iodide single crystal unit cell with the Rietveld refined unit cell parameters from the powder XRD measurements. The treatment of Bi-based 2D hybrid organic-inorganic perovskites with spin-orbit coupling (SOC) and dispersion correction is necessary to accurately describe the electronic structure in these materials as shown extensively in previous works.[23] The inclusion of spin-orbit effects leads to a splitting of the conduction band (CB), mostly consisting of Bi 6p1/2 orbitals (Figure 2.6d–f) in the CB. This was also shown prominently for the 3D compounds $Cs_2AgBiBr_6$ and $Cs_2AgBiCl_6$.[51] Furthermore, this conduction band separation leads to a change in the nature of the bandgap, centering the CB minimum at the Γ point as opposed to the X point as shown in FigureSI 2.28, Supporting Information, for the non-SOC case, leading to a direct transition for all compounds. This was suggested to arise from band back-folding because of the structural distortion in 2D double perovskites as demonstrated by Connor et al. and is a common phenomenon described in multiple theoretical simulations.[23,34] Furthermore, the degeneracy from Γ to Z highlights the reduced electronic dimensionality. The bandgaps in all calculations are under 2 eV, a significant and expected underestimation in comparison to the experimental results, mostly caused by the notorious ineffectiveness of DFT-PBE to quantitatively describe the experimental absorption edge values.[52]

To obtain insight into the atomic character of the frontier orbitals, the projected density of states (DOS) was evaluated for every compound. As expected, the character of the valence band maximum (VBM) and conduction band minimum (CBM) is similar for every halide, where the valence band (VB) consists of mostly halide-p and some Ag-d orbitals and the CB is predominantly made up of Bi-p and a contribution of halide p orbitals (analogous to Pb-p and I-p for 2D Pb systems),[53] in agreement with previ-

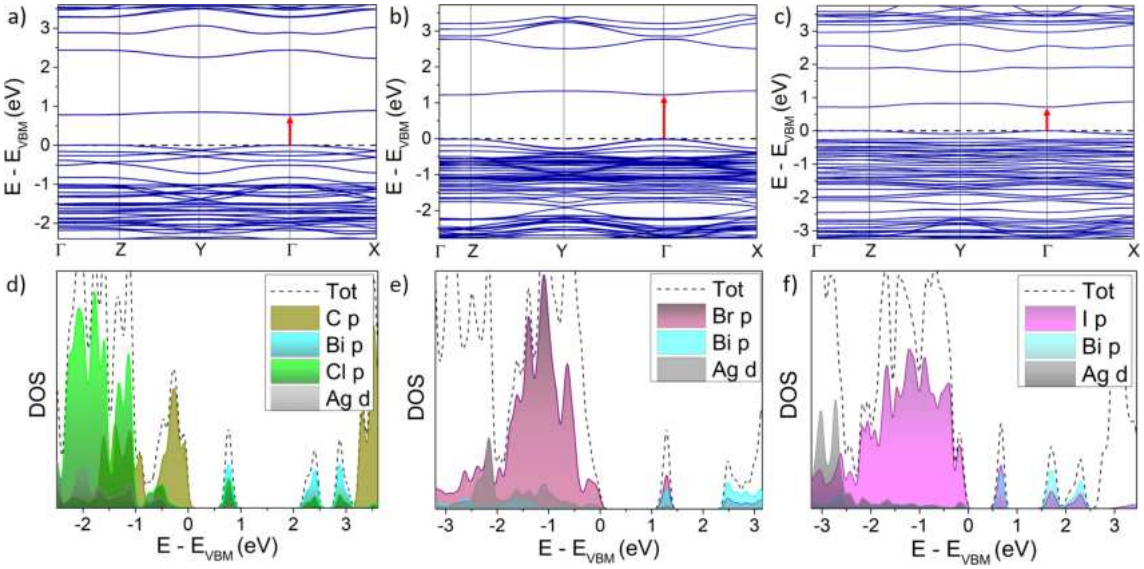

Figure 2.6: Band structures and projected density of states for a) and d) (4 FPEA)$_4$AgBiCl$_8$, b) and e) (4 FPEA)$_4$AgBiBr$_8$, and c) and f) (4 FPEA)$_4$AgBiI$_8$. The direct transition at the Γ point is indicated as a red arrow in a), b) and c).

ous publications.[23,34] However, the VB character of (4 FPEA)$_4$AgBiCl$_8$ seems to be of organic nature, with a dominant contribution of C-p states. Interestingly, the band dispersion appears to decrease from Cl to I, which we attribute to the growing degeneracy and separation of the organic HOMO and inorganic VB (FigureSI 2.29, Supporting Information), where the organic frontier orbital is almost isoenergetic to the inorganic component for I, further apart for Br and well separated for Cl. The compounds therefore mostly form type Ib heterojunctions between inorganic and organic quantum wells, except the chloride phase, which manifests type IIb behavior, but considering the limits of DFT simulations the iodide phase could also represent a IIb heterojunction as shown for (AE2T)$_2$AgBiI$_8$ by Jana et al.[34]

2.3.4 Optical Properties

Absorption

We employed UV–vis spectroscopy to determine the experimental values for the band gap energies for both powders and thin films. As the first principle calculations revealed the direct nature of the band gap, the Tauc plots for a direct allowed transition are shown as insets in Figure 2.7 for a, thin films and b, powders. For thin films, a corrected absorption was calculated by measurement of transmittance and reflectance spectra according to FigureSI 2.32, Supporting Information. For powders, diffuse reflectance spectra were measured and transformed according to the Kubelka–Munk function F(R).[54] The absorption and absorbance spectra show the typical blueshift for halide compounds with

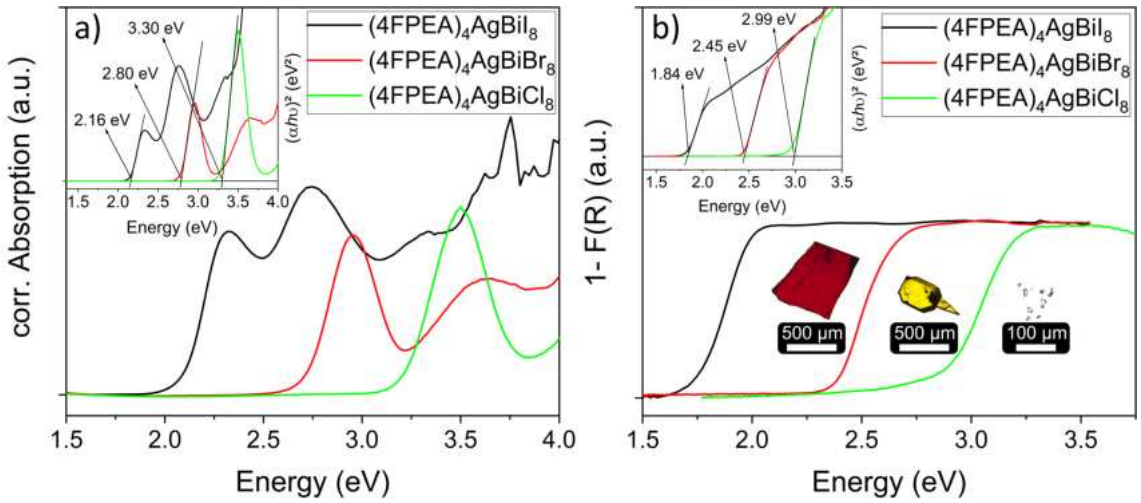

Figure 2.7: UV-vis absorption measurements with insets showing Tauc plots for a direct allowed transition for a) thin film and b) powder samples of $(4\,FPEA)_4AgBiI_8$, $(4\,FPEA)_4AgBiBr_8$, and $(4\,FPEA)_4AgBiCl_8$. Pictograms in b) show single crystals of the corresponding samples of (4FPEA)4AgBiI8 (left), $(4\,FPEA)_4AgBiBr_8$ (middle) and $(4\,FPEA)_4AgBiCl_8$ (right).

decreasing atomic number of the halide. The values for powders are 1.84, 2.45, and 2.99 eV and for thin films 2.16, 2.80, and 3.30 eV for $(4\,FPEA)_4AgBiI_8$, $(4\,FPEA)_4AgBiBr_8$ and $(4\,FPEA)_4AgBiCl_8$, respectively.

The lowest energy absorption in thin films is an isolated feature centered at 2.34 eV (iodide), 2.98 eV (bromide), and 3.53 eV (chloride). This feature is in line with other findings, as a strong isolated absorption maximum is also found for thin films of the 3D analog $Cs_2AgBiBr_6$ or 2D analogs like $(BA)_4AgBiBr_8$ or $(AE2T)_2AgBiI_8$.[23,49,56] The feature is rather broad, in line with the aforementioned analogs and in contrast to the observed sharp excitonic feature in lead-based 2D perovskites.[55] The broad character, the absence of a strong temperature dependence and the large exciton binding energy (EBE) attracted attention to the origin of this feature for $Cs_2AgBiBr_6$, and recently Wright et al. provided support for the theory that the absorption peak in the 3D compound arises from a direct exciton despite the mentioned anomalies.[56] A second isolated feature is visible at higher energies of 2.76 eV (iodide) and 3.66 eV (bromide) but overlapping with the UV absorption of the substrate and hence not measurable for the chloride. The second feature appears stronger for the iodide than for the bromide, being the absorption maximum at high energy blue light. This second feature is slightly less visible for the bromide and again not measurable for the chloride, due to the UV absorption overlap of glass. Furthermore, the simulated absorption from the dielectric response for the bromide reveals strikingly similar features, excluding excitonic effects (FigureSI 2.31, Supporting Information). Here, the two first absorption maxima are attributed to the inorganic contribution in the VBM and CBM, probably caused by the aforementioned Bi 6p band splitting.[57] Moreover, a similar mechanism as described by Jana et al. is suggested, where the ab-

sorption is traced back to the equatorial halide ion rather than a direct Ag to Bi transition, as the contributions of Bi p/Ag d in the VBM/CBM are negligible.[34] The intense lowest-energy absorption peak has also been demonstrated theoretically for inorganic and hybrid double perovskites A_2SbCuX_6, with the iodide compounds showing the highest maxima compared to lighter halide compounds. This absorption thus seems intrinsic to the double perovskite halide family.[15]

The powder absorption data display a redshift for all three compounds and do not show the distinct absorption features of the thin films as clearly, but still visible upon scaling (FigureSI 2.32, Supporting Information). The features, ordered from lower to higher energy, have their maxima for the iodide at 2.14, 2.39, 2.52, and 2.96 eV, for the bromide at 3.07 eV and for the chloride at 3.45 eV. The number of maxima match those of their respective thin film plots, although not as distinctly visible (for the iodide the feature at 2.14 eV appears very small, whereas the maxima at 2.39, 2.52, and 2.96 eV appear reminiscent of the observed pattern in the thin films, with the features at 2.39 eV and 2.52 eV either overlapping, which could be caused by the 2nd and 3rd CBM, or appearing due to low measurement resolution.) The shift of 0.32 eV (iodide), 0.35 eV (bromide), and 0.31 eV (chloride) relative to thin film data might be caused by anisotropic absorption, considering the rough surface of the powder and the resulting surface scattering, which is relevant to the variation in particle size of the powder, as well as the thickness dependence where indirect transitions in bulk powder measurements are statistically more relevant than for thin films of a few hundred nanometers.

Charge-Carrier Dynamics and Emission

In the following, we discuss the charge-carrier dynamics and emissive behavior of thin films of (4 FPEA)$_4$AgBiBr$_8$ and (4 FPEA)$_4$AgBiI$_8$. While these processes and the excitonic character of 3D $Cs_2AgBiBr_6$ are well established in the literature, they are yet to be fully explored for the 2D submembers of the double perovskite. Although substantial advances have been made recently by Schmitz et al. and Pantaler et al. elucidating the emissive features and charge-carrier dynamics of Ag–Bi– Br based 2D double perovskites, a comprehensive view is still lacking.[26,49,56–58] Here, we observe similarities owing to the related Ag-Bi double perovskite system, but also some differences between the perovskites with halides bromide and iodide.

Photoluminescence: Photoluminescence (PL) measurements on thin films show weak intensities and very broad emissions with a FWHM (full width half maximum) of 300 meV for the iodide and 320 meV for the bromide at room temperature (Figure 2.8a,b). The characteristic broad emission for these systems is also observed in other 2D silver-bismuth-halide, 2D lead-halide and 3D silver-bismuth-halide systems.[23,45,49,56,59]

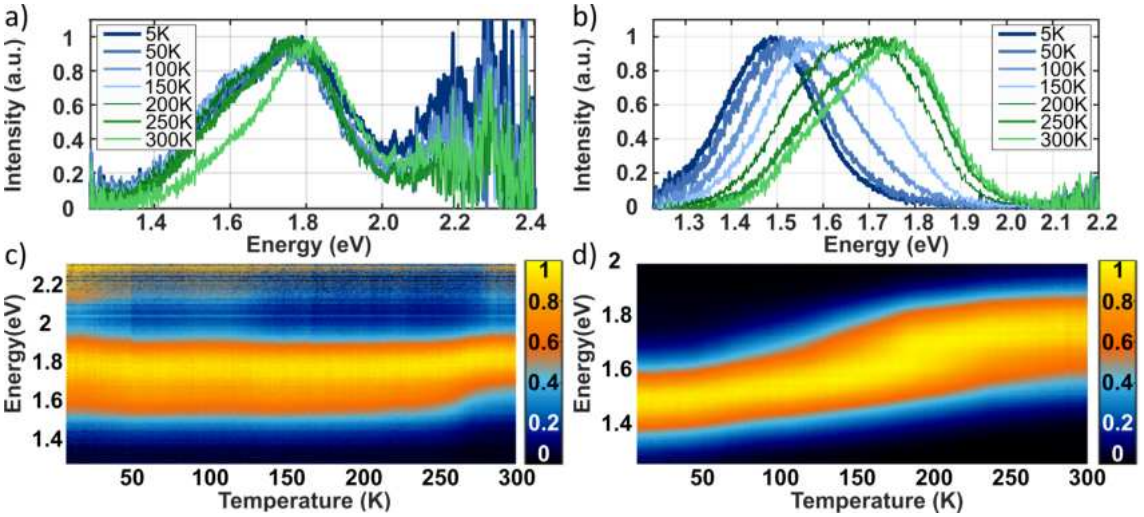

Figure 2.8: Temperature-dependent PL spectra and color plots of the normalized PL spectra at temperatures between 5 and 300 K for a) and c) $(4\,FPEA)_4AgBiBr_8$, and b) and d) $(4\,FPEA)_4AgBiI_8$.

In $Cs_2AgBiBr_6$, it is generally attributed to substantial electron-phonon coupling, leading to self-trapping or localization of the charge carriers or excitons. These self-trapped charge carriers subsequently diffuse to color centers and recombine, leading to the broad and strongly red-shifted PL.[26,56,60]

Intriguingly, for $(4\,FPEA)_4AgBiI_8$ a significant spectral shift of the emission with decreasing temperature is observed, with a redshift of the emission maximum from 1.7 eV at 300 K to 1.46 eV at 5 K (FigureSI 2.33, Supporting Information). This is remarkable as this large shift is not observed in $Cs_2AgBiBr_6$ or other 2D silver-bismuth-halide double perovskites for which the temperature-dependent PL data have been examined.[34,56] While initially often argued that the broadness of the emission and thus the absence of a narrow emission at low temperatures is counterintuitive of a dominant excitonic contribution, we find a moderate reduction of the FWHM by 120 meV, from 320 meV at 300 K down to 200 meV at 5 K (FigureSI 2.33, Supporting Information). One reason for the persistent broadness of the PL is attributed to defect-mediated charge-carrier recombination and thus a considerable defect population. Since an intrinsic defect population has been reported for single crystals of $Cs_2AgBiBr_6$, demonstrating a tendency towards disorder and/or crystallographic imperfections arising from B-site metal disorder between Ag and Bi, we would assume this tendency of double perovskites to also be present in their 2D subsets.[17,60] Adding the fact that we measured thin film samples, with a rapid crystallization mechanism compared to a single crystal synthesis, we can assume an even higher number of defects, potentially explaining the large temperature-independent inhomogeneous broadening parameter Γ_0 = 200 meV (ignoring scattering from ionized impurities).[60,61] Contrary to these two trends observed for the temperature-dependent emission of $(4\,FPEA)_4AgBiI_8$, the emission for $(4\,FPEA)_4AgBiBr_8$ peak shifts

only slightly, from 1.78 eV at 300 K to 1.68 eV at 5 K. On the other hand, the FWHM of the emission increases from 300 meV at 300 K up to 420 meV at 5 K. However, by inspecting more closely the PL temperature-dependent lineshape, we notice that the emergence of a lower energy feature (peaked at 1.6 eV) may conceal any spectral broadening and shifts of the peak observed at room temperature.

Interestingly, for (PEA)$_4$AgBiBr$_8$ a similar emission shape was observed for spectra recorded at 300 and 80 K, with a redshift or an emerging feature at lower energies 80 K.[26] We further notice a difference between the reported absorption with its maximum at 3.2 eV and our measurement with its absorption maximum at 3 eV. Such prominent Stokes shifts are also commonly reported for $Cs_2AgBiBr_6$, where exact values can depend on the measurement technique, as well as potentially on the morphology of the measured thin films (See FigureSI 2.27, Supporting Information, showing the flat and homogeneous surface morphology observed for the samples, compared to the dendritic or needle-shaped morphology of (PEA)$_4$AgBiBr$_8$ thin films reported in[26]).

In the following, we compare the PL data collected as part of our study of (4 FPEA)$_4$AgBiBr$_8$ and (4 FPEA)$_4$AgBiI$_8$ with the available data reported in the literature for (PEA)$_4$AgBiBr$_8$,[26] (BA)$_4$AgBiBr$_8$,[49] and (iBA)$_4$AgBiBr$_8$.[49] While the excitation energies and the reported PL ranges differ depending on the employed setup and the publication, they share similar overall features. Schmitz et al. proposed a sound explanation for the processes of the excited states,[49] which we confirmed and displayed schematically in Figure 2.9. Initially, at sufficient above band gap excitation free charge carriers are generated. Owing to the strong excitonic interactions in these materials, a fraction of the free carriers (depending on the EBE, usually in the hundreds of meVs for these materials) will rapidly form a free exciton state. Furthermore, because of the strong carrier-phonon interactions prevalent in these systems, these free charge carriers or free excitons subsequently undergo an ultrafast localization process or self-trapping forming a small polaron state. Moreover, these polarons will diffuse to color centers where recombination occurs.

To further complement these interpretations, we draw attention to the DFT studies reported by Schmitz et al.[49] These first-principle calculations on (PEA)$_4$AgBiBr$_8$ suggest that the PL emission energies of the differently trapped excited states vary substantially, in good agreement with their experimental observations. Namely, for the Ag–Bi–Br based materials, which feature the main absorption around 3 eV, they predicted the first, higher-energy emission at around 2.6 eV to be caused by either band-to-band exciton recombination or self-trapped hole recombination. The second, lower-energy emission at around 1.8 eV could be assigned to self-trapped electron or defect-mediated recombinations. Owing to our excitation energy of 3.06 eV for the PL measurements, being barely resonant with the main band gap absorption of (4 FPEA)$_4$AgBiBr$_8$ at room temperature, as well as our

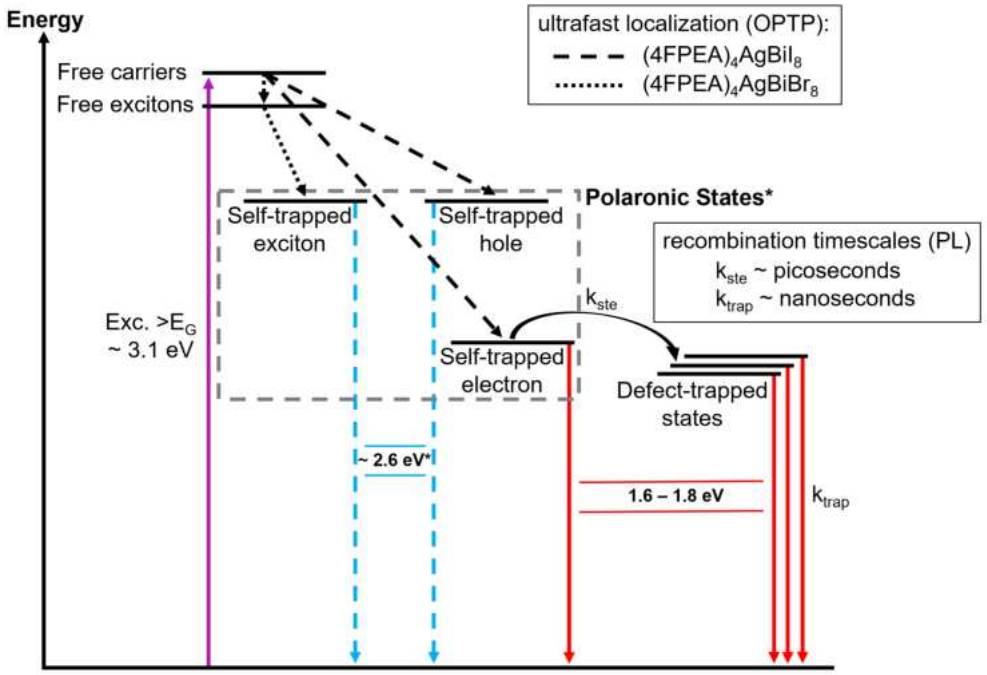

Figure 2.9: Schematic mechanism of the charge-carrier dynamics and emission for Ag-Bi based 2D double perovskites with exemplary energy values from our experiments, i.e. excitation energy of 3.1 eV and observed photoluminescence at around 1.6 eV. * The asterisk indicates the part of the model which was combined from previous findings in the literature on Ag-Bi-Br based 2D double perovskites and the reported energy ranges, i.e. emission at 2.6 eV from self-trapped excitons and self-trapped holes (not observable here due to the experimental setup) and emission at 1.6 – 1.8 eV from self-trapped electrons and defect-trapped states. The PL data for $(4\,FPEA)_4AgBiI_8$ suggest that emission is dominated by intrinsic recombination, while for $(4\,FPEA)_4AgBiBr_8$ the emission is dominated by defect-mediated recombination (see amplitude ratios in FigureSI 2.34, Supporting Information).

detection limit at 2.1 eV, such high-energy emission was not observable. Nonetheless, the observed low-energy emission at 1.8 eV agrees well with the findings for the other Ag–Bi–Br systems. To explain the small redshift and the possible appearance of a second emissive feature at 1.6 eV with decreasing temperatures further research is still needed. Although the excitation energy of 3.06 eV should be sufficiently above the band gap absorption for $(4\,FPEA)_4AgBiI_8$, we are still limited with a detection limit at 2.1 eV, but the observed emission with its maximum at 1.7 eV is in line with the expected energies for self-trapped electron or defect-mediated recombination. The origin of the seemingly single feature with its much larger redshift with decreasing temperature could be due to the more dominant intrinsic recombination of the polaronic states, compared to the more defect-dominated recombination of the bromide.

We measured similar PL transients for both materials and fitted them with a biexponential decay function, which helped us identify two recombination processes occurring on different timescales. For $(4\,FPEA)_4AgBiI_8$ we report a first very short-lived component with lifetimes in the range of 20 ps at 300 K increasing to 100 ps at 5 K. The second, longer-lived component showed lifetimes of 1 ns at 300 K increasing to 50 ns at 5 K. The

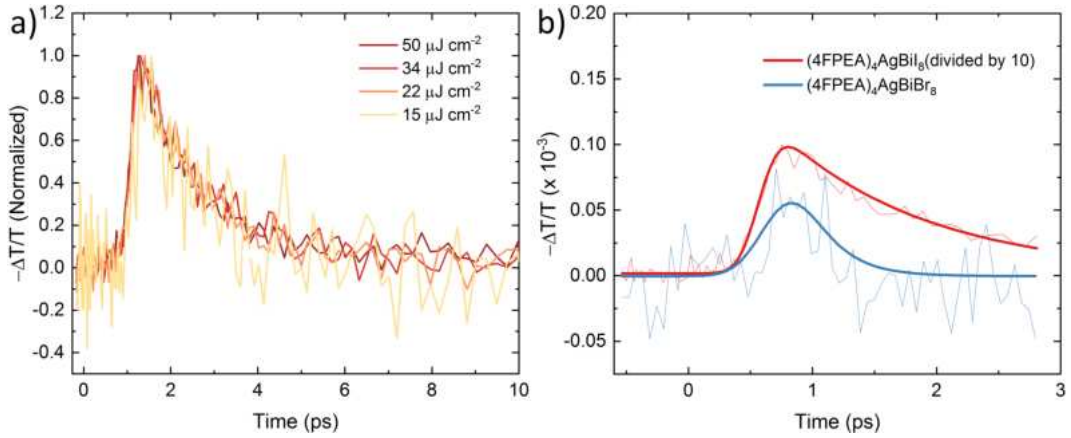

Figure 2.10: (a) Early time fluence-dependent optical pump terahertz probe (OPTP) signal measured for (4 FPEA)$_4$AgBiI$_8$ after 3.1 eV pulsed excitation and fitted with a two-level mobility model, with the fits shown as colored solid lines. The two-level mobility model is explained in detail in the Supporting Information section (see FigureSI 28, Supporting Information). (b) Comparison between early time OPTP signal measured for (4 FPEA)$_4$AgBiI$_8$ and (4 FPEA)$_4$AgBiBr$_8$ after 3.1 eV pulsed excitation at a fluence of 50 µJ cm^{-2}. The signal for (4 FPEA)$_4$AgBiI$_8$ is divided by a factor of 10 to facilitate the comparison. Solid lines represent experimental data and dashed lines represent fits to the two-level mobility model, described in the Supporting Information section (see FigureSI 28, Supporting Information).

transients for both compounds are shown in FigureSI 2.34, Supporting Information. In the given model, we would assign the first, short lifetime to a charge hopping process of the self-trapped electrons from a slightly higher energy level before they fall into defect trap states, which can be confirmed by time- and spectral-dependent measurements, as shown in FigureSI 2.35, Supporting Information. For the energetically higher-lying spectral part above 1.7 eV, we find a higher amplitude ratio for the short-lived component compared to the energetically lower lying contribution below 1.3 eV. As the thermal barrier relatively increases at lower temperatures, this trap-mediation becomes less likely, self-trapped electrons live longer and thus the lifetime of the emission of self-trapped electrons increases. Additionally, we used an Arrhenius plot to extract an activation energy of 126 meV for (4 FPEA)$_4$AgBiBr$_8$ and 20 meV for (4 FPEA)$_4$AgBiI$_8$ as the energy barrier of said hopping process (FigureSI 2.36, Supporting Information). The second, longer-lived lifetime component is assigned to defect-mediated recombination, which freezes out below temperatures of 100 K.

Optical-Pump Terahertz-Probe Spectroscopy: To further support the photophysical picture presented in Figure 2.9, we measured the early-time dynamics of photoexcited charge carriers for (4 FPEA)$_4$AgBiI$_8$ and (4 FPEA)$_4$AgBiBr$_8$ thin films by using optical-pump terahertz-probe (OPTP) spectroscopy. This technique monitors the dynamics of free charge carriers by measuring the change in transmitted THz electric-field amplitude (expressed here as -ΔT/T) upon photoexcitation of the material using a 3.1 eV femtosecond laser pulse.

OPTP measurements for $(4\,FPEA)_4AgBiI_8$ (Figure 2.10a) reveal an ultrafast and almost complete decay of the photoconductivity within 10 ps after photoexcitation. Crucially, the observed photoconductivity signal is proportional to three factors: the photon- to-charge branching ratio ϕ (i.e., the fraction of free carrier density generated per absorbed photon density), the number of photogenerated charge carriers n and the electron-hole sum-mobility μ.[62] Therefore, in principle, the observed ultrafast decay can be caused by variations in each of these quantities, in processes such as exciton formation, charge carrier localization and defect-mediated recombination. The reported EBEs for 2D and 3D silver-bismuth halide perovskites are in the hundreds of meVs (250 meV for $(OC)_4AgBiI_8$ and $\approx$300 meV for $Cs_2AgBiBr_6$),[26,56] thus we expect strong excitonic interactions for thermally equilibrated charge carriers. However, we note that: i) at the typical excitation densities of OPTP experiments ($\approx 1013\,cm^{-2}$), the Saha equation predicts a nonnegligible fraction of free carriers for EBEs $\geq$ 200 meV;[63] and ii) the excess energy provided by 3.1 eV pump pulses implies the transient generation of free carriers rather than excitons.

Recent studies on $Cs_2AgBiBr_6$ and Cu_2AgBiI_6 reported a similar ultrafast decay of the photoconductivity and attributed this to the strong carrier-phonon coupling and the formation of small polarons, i.e., to an ultrafast localization of the charge carriers caused by a significant distortion of the lattice.[56,64] To test this hypothesis, we fitted the fluence-dependent OPTP data with a two-level mobility model developed by Wright and coworkers (explained in details in the SI, Supporting Information).[56] The excellent agreement between experimental data and fits supports the hypothesis of ultrafast carrier localization as a major cause in the ultrafast decay of photoconductivity. Furthermore, the fluence-independent nature of the OPTP signal (FigureSI 2.39, Supporting Information) rules out exciton formation as a possible cause.

The average initial mobility value for $(4\,FPEA)_4AgBiI_8$ extracted across the range of fluences is $\phi\mu_{del} = (0.6 \pm 0.1)\,cm^2\,V^{-1}\,s^{-1}$, almost five times lower than what was reported for $Cs_2AgBiBr_6$,[56] and the observed localization rate is $k_{loc} = (0.7 \pm 0.1)\,ps^{-1}$. Interestingly, the mobility after localization is below our detection limit and is set to zero in the fitting procedure. We note here that the OPTP sensitivity is in the range of $\mu = 0.1\,cm^2\,V^{-1}\,s^{-1}$. Therefore, our measurements reveal that the mobility after localization is $\leq 0.1\,cm^2\,V^{-1}\,s^{-1}$.[65] The observation of this low mobility supports the predictions of low electronic dimensionality for silver-bismuth halide elpasolites, which extended to bi-dimensional layers implies the complete electronic de-coupling of $[AgX_6]^{5-}$ and $[BiX_6]^{3-}$ octahedra (i.e., holes are localized on $[AgX_6]^{5-}$ octahedra, which are surrounded by $[BiX_6]^{3-}$ octahedra, thus hindering the charge-carrier hopping - and vice-versa for electrons).[66,67]

As shown in Figure 2.10b, the comparison between $(4\,FPEA)_4AgBiI_8$ and

(4 FPEA)$_4$AgBiBr$_8$ reveals a significantly reduced photoconductivity for the bromide counterpart. The estimated carrier mobility for (4 FPEA)$_4$AgBiBr$_8$ is $\phi\mu$ = 0.06 cm^2 V^{-1} s^{-1} and the observed signal decay is almost limited by the time resolution of our setup (290 fs). Here, the lower branching ratio-times-mobility factor could be, in principle, caused by either a lower mobility or by a more prominent role played by excitons. We note that a comparatively lower excess energy is provided by the pump pulse (i.e., at 3.1 eV, (4 FPEA)$_4$AgBiBr$_8$ is excited almost directly on its absorption peak). Furthermore, we also note that no substantial change of mobility or carrier-phonon coupling has been observed for 3D Cs$_2$AgBiBr$_6$ and Cu$_2$AgBiI$_6$ (i.e., different halides).[56,64]

Therefore, we hypothesize that the lower OPTP signal and the observed ultrafast decay of the signal could imply ultrafast exciton formation rather than charge localization. These findings suggest that, while a significant fraction of free charge carriers contribute to the (4 FPEA)$_4$AgBiI$_8$ excited state dynamics, the formation of excitons could rule the charge-carrier dynamics for (4 FPEA)$_4$AgBiBr$_8$ when excited at 3.1 eV. However, we envision that further studies are needed to further investigate the difference between different halides.

Overall, our findings agree with the current interpretation of the charge-carrier dynamics, displaying much more complicated, underlying photophysical processes compared to 3D lead perovskites, because charge carriers are almost exclusively present as excitonic pairs, subsequently forming polarons as a result of the inherent spatial localization on the Ag-Bi based octahedra in the double perovskite structure, as well as structural reorganization following excitation which supports small-polaron formation.

2.3.5 Photodetectors

2D hybrid perovskites have been implemented successfully in various optoelectronic applications such as solar cells, field-effect transistors, X-ray- and photodetectors or light-emitting diodes.[24,32,36,68,69] Specifically, 2D Pb- and Sn-based perovskite photodetectors display excellent performance in terms of photoresponsivity and detectivity. However, their toxicity and environmental instability may limit their practical applications.[6] Some of the emerging lead-free 2D double perovskites have been demonstrated as phototransistors and polarized-light detectors.[24,48,68,70] Recently an Ag-Bi-based 2D double perovskite crystal (iPA)$_2$CsAgBiBr$_7$ has been demonstrated as an electronic device with a polarized light sensitivity application.[27] Another recent work demonstrated the high performance of a photodetector based on single-crystalline microwire arrays of (R/S – β-MPA)$_4$AgBiI$_8$ after employing a capillary-bridge assembly technique. While photodetectors based on bulk single crystal (R/S – β-MPA)$_4$AgBiI$_8$ achieved detectivities of 1.2 $\times$ 10^7 Jones, the incorporation into the microwire arrays achieved an increase of

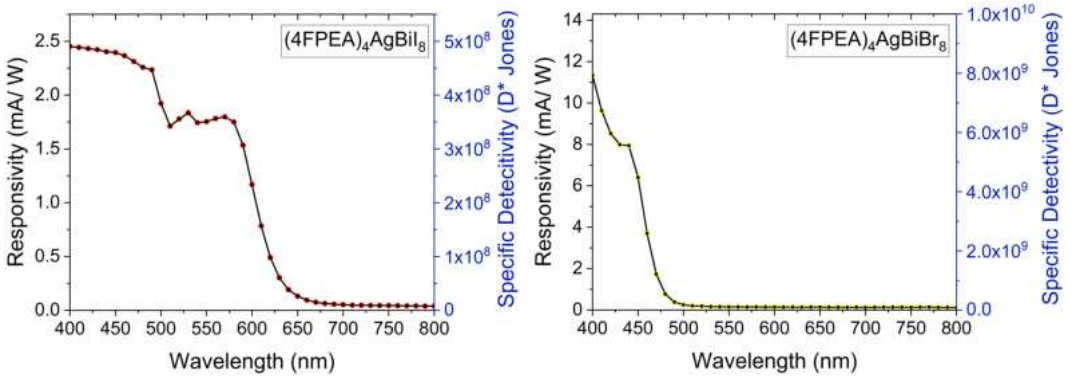

Figure 2.11: Responsivity and specific detectivity of photodetectors of a) $(4\,\mathrm{FPEA})_4\mathrm{AgBiI}_8$ and b) $(4\,\mathrm{FPEA})_4\mathrm{AgBiBr}_8$.

detectivity of up to 3.98×10^{11} Jones, demonstrating the importance of crystal quality, crystal orientation with regard to the electrode as well as the distance of the electrodes (single crystal channel area of $0.32\,\mathrm{mm}^2$ compared to microwire channel width of $2\,\mu\mathrm{m} \times$ height of $0.225\,\mu\mathrm{m}$).[48,71]

Here, we demonstrate the first thin film, solution-processed Ag-Bi-based 2D double perovskite photodetectors fabricated via a one-step processing method. The air-stable solutions of $(4\,\mathrm{FPEA})_4\mathrm{AgBiBr}_8$ and $(4\,\mathrm{FPEA})_4\mathrm{AgBiI}_8$ are compatible with deposition protocols such as spin coating, doctor-blading, and drop casting, showing promise regarding scalable methods such as printing. The solutions for the devices can be prepared by directly dissolving the perovskite material, or dissolving the halide salts, as explained in the experimental section. The solutions were deposited on interdigitated gold electrodes (channel width of $10\,\mu\mathrm{m}$) either by doctor blading or drop casting and were annealed at 80 °C for 5 min directly afterward. Since the photoconductivity setup was operated with a halogen lamp operating from 400 nm which is not sufficient for the excitation of the large band gap perovskite $(4\,\mathrm{FPEA})_4\mathrm{AgBiCl}_8$, only the responsivity and specific detectivity of $(4\,\mathrm{FPEA})_4\mathrm{AgBiBr}_8$ and $(4\,\mathrm{FPEA})_4\mathrm{AgBiI}_8$ were characterized (Figure 2.11). A current-voltage measurement applied between 0 and 1 V provided a linear dependence for both materials, corresponding to an ohmic behavior with high resistance. At constant bias illumination with white light and an intensity of $100\,\mathrm{mW\,cm^{-2}}$ the current increased by a factor of three. The photodetectors based on $(4\,\mathrm{FPEA})_4\mathrm{AgBiI}_8$ show responsivities of over $2\,\mathrm{mA\,W^{-1}}$ with a bias voltage of 1 V with a low noise level ($110\,\mathrm{pA\,Hz^{-1}}$), which results in a specific detectivity of up to 5×10^8 Jones (see TableSI 2.6, Supporting Information). Photodetectors based on $(4\,\mathrm{FPEA})_4\mathrm{AgBiBr}_8$ show higher responsivities of up to $10\,\mathrm{mA\,W^{-1}}$, with a similar noise level and a specific detectivity of up to 6×10^9 Jones. A comparison with state-of-the-art lead-free perovskite photodetectors is given in TableSI 2.6, Supporting Information (see TableSI 2.6, Supporting Information). Our devices based on $(4\,\mathrm{FPEA})_4\mathrm{AgBiI}_8$ demonstrate a detectivity one order of magnitude higher

than that based on bulk single crystal (R/S – β-MPA)$_4$AgBiI$_8$, but 3 orders of magnitude lower than those based on single crystalline microwire array (R/S – β-MPA)$_4$AgBiI$_8$.[48,71] We assume that the lower performance of the single-crystal-based device is caused by the top evaporated contacts, which should limit the out-of-plane charge transport and thus throughout the crystal, owing to the layered 2D structure and the insulating organic layers. This is partially overcome by using interdigitated contacts (i.e. microwire arrays). The crystallization method of a functionalized morphology to control the capillary spread employed in the microwire arrays further increases the contact quality over the simple synthesis technique we employed here. Lastly, smaller channel widths or electrode distances seem to contribute to a better charge transport, because of the ultra-short lifetimes and large binding energies of the generated charge carriers in these materials. Although the 2D double perovskites show some intrinsic deficits compared to 3D Sn- and Ag-Bi-based perovskites, their incipient performance is already comparable, demonstrating the potential of controlled crystallization and orientational freedom intrinsic to 2D structures. Lastly, both devices have shown stable performance for more than two weeks with measurements and storage under ambient conditions.

2.4 Conclusion

We demonstrate the synthesis of three new 2D hybrid silver-bismuth double perovskites (4 FPEA)$_4$AgBiX$_8$ (X = Cl, Br, I) and prove the ability of a simple, fluorinated organic spacer to stabilize the silver-bismuth-iodide double perovskite lattice. The simple solution-based synthesis yields highly crystalline materials in both bulk and thin-film form. The thin films crystallize as highly oriented structures in which organic and inorganic layers are oriented exclusively horizontally to the substrate surface. The crystalline thin-film quality can be tuned through choice of substrate and synthesis parameters to form domains of up to hundreds of microns with single-crystalline-grade morphology and orientation. DFT calculations reveal key properties such as the direct band gap caused by dimensional reduction. Moreover, we show how the band dispersion is influenced by the halides and attribute this to the growing degeneracy of the organic HOMO and inorganic VB from Cl to Br and I. Our temperature-dependent PL measurements show extremely broad and strongly Stokes shifted emission for all three materials. OPTP measurements point toward photoexcitation being followed by an initial, ultrafast charge-carrier localization and the formation of small-polaron states. We are thus able to account for the observed charge-carrier dynamics and emissive behavior through a mechanism based on inherent exciton formation, small-polaron formation (or "self-trapping") and defect-mediated recombination. Finally, we demonstrate the incorporation of (4 FPEA)$_4$AgBiBr$_8$

and $(4\,FPEA)_4AgBiI_8$ into photodetector devices showing promising performance, if the interplay of intrinsic 2D double perovskite properties and morphological control for device fabrication is considered. Our work provides detailed insights into the emerging structural class of lead-free 2D hybrid double perovskites and their distinct properties in comparison to 3D double perovskite structures.

2.5 Experimental Section

Bulk and Single Crystals: 4-Fluorophenethylammonium salts (4FPEAX, X = Cl, Br, I) were synthesized by dissolving 1 eq. 4-fluorophenethylamine (Sigma-Aldrich 99%) in 150 mL ethanol (Fischer Scientific absolute, >99%) at 0 °C. Then, 1.1 eq. conc. HX acid (X = Cl, Br, I) (Sigma-Aldrich hydrochloric acid 37 wt% in H_2O, 99.999% trace metals basis; Sigma-Aldrich hydrobromic acid, 48 wt% in H_2O, $\geq$ 99.99%, 48%; Sigma-Aldrich hydroiodic acid 57 wt% in H_2O, distilled, stabilized, 99.95%) was slowly added and the mixture was stirred at 0 °C for 2 h. Afterward, the solution was allowed to warm up to room temperature and the solvent was removed under vacuum. The product was washed three times with adequate amounts of diethyl ether (Sigma-Aldrich contains 1 ppm BHT as inhibitor, anhydrous, $\geq$ 99.7%) and dried under medium vacuum.

Powders of $(4\,FPEA)_4AgBiX_8$ (X = Cl, Br, and I) were synthesized by slowly adding an excess of aq. conc. HX acid (X = Cl, Br, and I) (Sigma-Aldrich hydrochloric acid 37 wt% in H_2O, 99.999% trace metals basis; Sigma-Aldrich hydrobromic acid, 48 wt% in H_2O, $\geq$99.99%; Sigma-Aldrich hydroiodic acid 57 wt% in H_2O, distilled, stabilized, 99.95%) to 0.5 eq. Ag_2O (Fluka 99%), 0.5 eq. Bi_2O_3 (Alfa-Aesar 99,975% metals basis) and 4 eq. 4-fluorophenethylamine (Sigma-Aldrich 99%) under stirring at room temperature for 1 h. The solutions were filtered and the products were washed three times with adequate amounts of diethyl ether (Sigma-Aldrich contains 1 ppm BHT as an inhibitor, anhydrous, $\geq$99.7%) and then dried under medium vacuum.

Single crystals of $(4\,FPEA)_4AgBiBr_8$ were grown by dissolving the synthesized powder (as described above) in 1 mL GBL (γ-butyrolactone; Sigma-Aldrich ReagentPlus, $\geq$99%) in a small vial (V = 1.5 ml) which was placed in a bigger vial (V = 25 mL) filled with 2 ml dIPE (di-isopropylether; Sigma-Aldrich anhydrous, 99%). By vapor diffusion of the antisolvent dIPE into the GBL perovskite solution, single crystals were obtained and washed three times with adequate amounts of diethyl ether and dried under a medium vacuum.

Single crystals of $(4\,FPEA)_4AgBiI_8$ were grown by cooling a saturated aqueous HI solution with 1 eq. AgI (Sigma-Aldrich 99%), 1 eq. BiI_3 (TCI anhydrous) and 4 eq. 4FPEAI at 3° C h^{-1} from 110 to 30 °C. The solution was filtered and the obtained single

crystals were washed three times with adequate amounts of diethyl ether and dried under medium vacuum.

Thin Films: The substrates FTO-coated glass, ITO-coated glass and Si–SiO_2 (polished with 300 nm thermally grown SiO_2) wafers were cleaned by ultrasonication for 15 min in a solution of acetone, isopropanol, and ethanol (1:1:1). Afterward, the substrates were cleaned for 10 min under nitrogen plasma. Stoichiometric amounts of AgX, BiX_3, and 4FPEAX (X = Cl, Br, I) (AgCl Sigma-Aldrich 99%; $BiCl_3$ Sigma-Aldrich > 98%; AgBr Alfa-Aesar 99,5%; $BiBr_3$ Sigma-Aldrich > 98%; AgI Sigma-Aldrich 99%; BiI_3 (TCI anhydrous > 98%) were dissolved in 1-methyl-2-pyrrolidinone (NMP Sigma-Aldrich anhydrous, 99.5%). Thin films on FTO and ITO were spin-coated in a glove box with N_2 atmosphere from a 0.5 M solution, thin films on Si-SiO_2 wafers were spin-coated from a 0.06 M solution. Thin films were spin-coated at an initial step of 3000 rpm for 10 s with a second step of 6000 rpm (FTO, ITO) or 8000 rpm (Si-SiO_2) for 50 s. The films were annealed at 100 °C for 3 min or 140 °C for 1 min with a subsequent annealing at 70 °C for 5 min to afford a slow cool down to room temperature.

Photodetectors: Gold contacts were prepared on glass substrates by optical lithography and thermal evaporation followed by a lift-off process. The electrodes are films of Au/Ti with 40/10 nm thickness. The size of the gap between electrodes was 10 µm and the total length was 8 mm, giving an 8×10^{-8} m^2 active area. The noise characterization was done with a larger active area of 0.1 cm^2. Photodetectors were fabricated by doctor blading or drop casting (4 FPEA)$_4$AgBiX$_8$ (X = Br & I) solution in NMP onto prepatterned finger-structured gold contacts. The devices were then dried at 80 °C for 5 min at ambient conditions.

Characterization Techniques: Powder X-Ray Diffraction (P-XRD): P-XRD measurements were carried out on a Stoe Stadi P diffractometer in Debye-Scherrer geometry, operating at 40 kV and 40 mA, using monochromated (Ge(111) single crystal monochromator) Cu-$K_{\alpha 1}$ radiation (λ = 1.5406 Å) and a Dectris Mythen 1k detector.

Thin Film X-Ray Diffraction (TF-XRD): TF-XRD measurements were carried out on a Bruker D8 Discover diffractometer in Bragg–Brentano geometry, with Ni-filtered Cu-$K_{\alpha 1}$ radiation (λ = 1.5406 Å) and a positionsensitive LynxEye detector.

Single-Crystal X-Ray Diffraction (SC-XRD): SC-XRD measurements were carried out on a Bruker D8 Venture Txs system equipped with a multilayer mirror monochromator and a Mo-$K_{\alpha 1}$ rotating anode X-ray tube (λ = 0.71073 Å). The frames were integrated with the Bruker SAINT software package. Data were corrected for absorption effects using the Multi-Scan method (SADABS). The structure was solved and refined using the Bruker Shelxtl Software Package.

Grazing-Incidence Wide Angle X-Ray Scattering (GIWAXS): GIWAXS measurements

were carried out on an Anton-Paar Saxspoint 2.0 with a Primux 100 microfocus source with Cu-$K_{\alpha 1}$ radiation (λ = 1.5406 Å) and a Dectris Eiger R 1M 2D Detector.

Scanning Electron Microscopy (SEM) and Energy Dispersive X-Ray Spectroscopy (EDX): SEM and EDX measurements were carried out on a FEI Helios NanoLab G3 UC Dual Beam microscope.

Atomic Force Microscopy (AFM): AFM measurements were performed under ambient conditions using a Nanoink atomic force microscope with Si n-type tip with a radius of <10 nm in tapping mode with a scan rate of 0.2 Hz.

First-Principles Calculations Density-Functional Theory (DFT): First-principles DFT calculations were based on a plane wave basis set and pseudopotentials as implemented in the Quantum Espresso package.[72] Furthermore, the PBE exchange-correlation functional and the Tkatchenko-Scheffler (TS) dispersion scheme were used.[73,74] The latter is necessary to accurately describe the structural properties in low-dimensional perovskite materials.[75] The structures were optimized until all residual forces on the nuclei were below 1.0×10^{-3} a.u. Hereby, the following equilibrium unit cell parameters were obtained, all within less than 1% deviation from experimental data:

$(4\,\mathrm{FPEA})_4\mathrm{AgBiI}_8$: a = 8.62, b = 8.75, c = 16.37, α = 98.97, β = 90.12, γ = 90.01

$(4\,\mathrm{FPEA})_4\mathrm{AgBiBr}_8$: a = 7.83, b = 7.62, c = 30.22, α = 90.00, β = 91.87, γ = 90.00

$(4\,\mathrm{FPEA})_4\mathrm{AgBiCl}_8$: a = 8.16, b = 7.78, c = 16.77, α = 90.01, β = 97.38, γ = 90.12

A kinetic energy cutoff of 50 Ry for the wavefunctions and 400 Ry for the charge density was used. For the bromide structure, a minimal, suitably converged $2 \times 2 \times 1$ k-point grid was utilized for SCF and relaxation calculations because of the large dimension of the system. The iodide and chloride compounds were calculated by using a larger $4 \times 4 \times 1$ grid. Furthermore, larger $12 \times 12 \times 3$ grids were used for NSCF calculations to accurately describe the projected DOS.

UV-Vis Absorption (UV-Vis): UV-Vis spectra were taken on a Perkin-Elmer Lambda 1050 spectrometer equipped with a 150 mm integration sphere. Thin films were measured in transmittance and reflectance mode. Powder measurements were measured in reflection mode with a Praying Mantis diffuse reflection setup.

Photoluminescence (PL): Photoluminescence spectra were measured with a self-built confocal microscope system. The used objective was a Nikon 100×0.75 NA DIC with a working distance of 4 mm. Furthermore, a closed cycle cryostat system (Atto Dry 800, Attocube) with an ultrashort-working-distance option (3 mm from sample to outside) was installed, which allows one to control the sample temperature from 5 to 300 K. As laser-source for excitation a 405 nm pulsed laser diode (Pico Quant P-C-405) was used, which has an adjustable repetition rate and a pulse length of 50 to 300 ps, depending on the applied diode voltage. Besides, a Short Pass Filter 450 (Fesh 450 Thorlabs) in

the excitation path was installed to clean the laser spectrum and a Long Pass Filter 490 (Chroma) was used for the detection side. In the detection path, an Avalanche Photo Diode (APD, model MPD PDM, 50 µm detector size) was built in for confocal images and was combined with a Time Correlated Single Photon Counting (TCSPC)-Card (Becker & Hickel) measuring time-dependent PL-decays. In addition, a second optical path was implemented with an Andor Shamrock spectrometer SR303i combined with a charged coupled device (CCD) camera (Andor Newton DU920 open electrode) to record spectra.

Photoconductivity (PC): Photoconductivity was measured by illumination with a tungsten lamp monochromatized through an Acton SP2150 (Princeton Instruments) spectrograph/monochromator. PC spectra were recorded for light modulated by a mechanical chopper with a frequency of 13 Hz. Bias was applied by a Keithley 236 SMU at 2 V, chosen according to the stability of the dark current. The signal was recorded by a Signal Recovery 7265 DSP lock-in amplifier, which provides as a standard output also the noise voltage or current per bandwidth. The setup was controlled by home-written software in LabView IV.

Optical-Pump Terahertz-Probe Spectroscopy: Our optical pump terahertz probe (OPTP) setup has been described in detail previously.[64] Briefly, the OPTP setup used an amplified Ti:sapphire laser system (Spitfire), providing 800-nm emission with 35 fs pulse duration and 5 kHz repetition rate. The fundamental output was used to generate single-cycle THz radiation pulses via the inverse spin Hall effect.[76] THz transmission was measured by using free-space electro-optic (EO) sampling with a 1 mm thick ZnTe (110) crystal, a Wollaston prism and a pair of balanced photodiodes. Samples for OPTP were deposited onto 2 mm thick z-cut quartz. In the setup, samples were excited by frequency-doubled 400 nm pulses, obtained by second-harmonic generation in a beta-barium-borate (BBO) crystal. During the OPTP measurements, the THz emitter, EO crystal, and samples were kept under vacuum at pressures below 0.1 mbar.

Crystal Structure Data: [CCDC 2151233–2151234 contains the supplementary crystallographic data for this paper. These data can be obtained free of charge from The Cambridge Crystallographic Data Centre via www.ccdc.cam.ac.uk/data_request/cif.]

2.6 Acknowledgements

The authors thank Dr. Steffen Schmidt for the SEM and EDX measurements. The authors thank Dr. Peter Mayer for the SC-XRD measurements and structure solutions. Furthermore, the authors thank the Bavarian research network Solar Technologies go Hybrid, the Deutsche Forschungsgemeinschaft (DFG) Excellence Cluster e-conversion (EXC 2089/1 - 390776260) and the DFG focus program SPP 2196 for funding. L.M.H. acknowledges support through a Hans Fischer Senior Fellowship from the Technical University of Munich's Institute for Advanced Study, funded by the German Excellence Strategy. Open access funding enabled and organized by Projekt DEAL.

2.7 Supporting Information

Silver-Bismuth based 2D Double Perovskites (4 FPEA)$_4$AgBiX$_8$ (X=Cl, Br, I): Highly Oriented Thin Films with Large Domain Sizes and Ultrafast Charge-Carrier Localization

Rik Hooijer, Andreas Weis, Alexander Biewald, Maximilian T. Sirtl, Julian Malburg, Rico Holfeuer, Simon Thamm, Amir Abbas Yousefi Amin, Marcello Righetto, Achim Hartschuh, Laura M. Herz, Thomas Bein

S1

Our attempts to synthesize (PEA)$_4$AgBiI$_8$, (2 FPEA)$_4$AgBiI$_8$ and (3 FPEA)$_4$AgBiI$_8$ in the same way as for (4 FPEA)$_4$AgBiI$_8$ yielded only hybrid bismuth iodides. The resulting crystalline powder is of orange color compared to the red colored (4 FPEA)$_4$AgBiI$_8$ and the resulting diffractogram differs greatly from the expected diffractogram that should be close to the standard n = 1 double perovskite patterns, this is shown in FigureSI 2.12. Furthermore, we performed EDX measurements on said powder and confirm the absence of any Ag, only showing the presence of Bi and I as seen in TableSI 2.1.

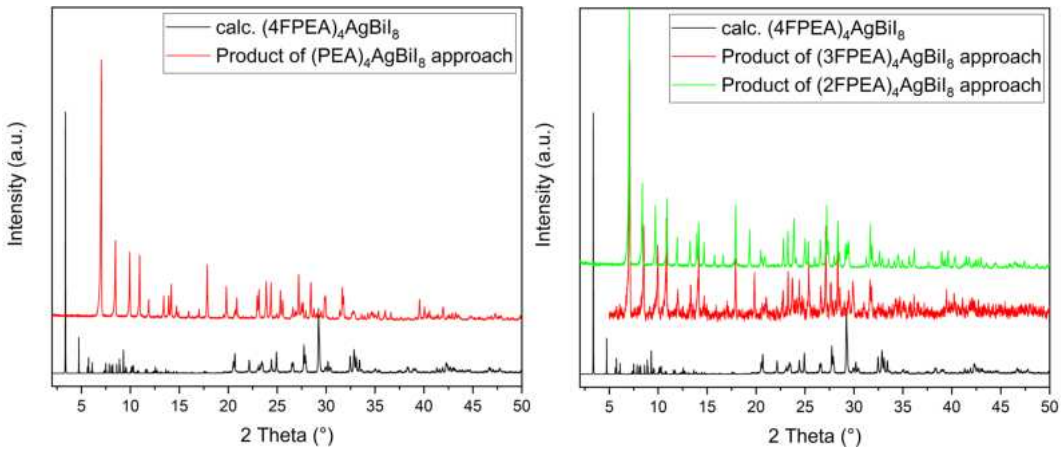

Figure 2.12: Diffractogram of the products of the synthesis approaches for a) (PEA)$_4$AgBiI$_8$ and (2 FPEA)$_4$AgBiI$_8$ compared to the calculated diffractogram of (4 FPEA)$_4$AgBiI$_8$.

Table 2.1: EDX data for the crystalline products of the synthesis approach for $(PEA)_4AgBiI_8$.

Measurement	Ag (at%)	Bi (at%)	I (at%)	Ratio(Bi:I)
1	-	13.51	86.49	1:6.40
2	-	12.23	87.77	1:7.18
3	-	13.66	86.32	1:6.32
4	-	15.36	84.64	1:5.51
5	-	15.05	84.95	1:5.65
6	-	15.26	84.74	1:5.55

S2

The structure of $(4\,FPEA)_4AgBiI_8$ has been refined as a 2-component pseudomerohedral twin (pseudo-monoclinic cell). The twin volume ratio of the two domains refined to 0.75/0.25. Two iodides are slightly disordered, the ratio of site occupation factors refined to 0.97/0.03.

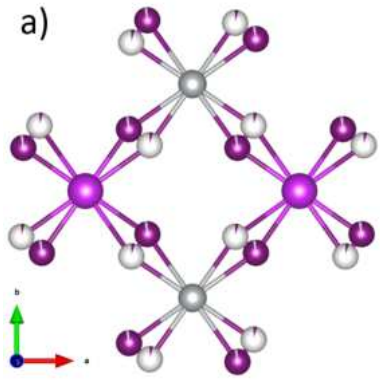

Figure 2.13: Iodide Disorder in the single crystal structure of $(4\,FPEA)_4AgBiI_8$.

S3 and S4

The structures $(4\,FPEA)_4AgBiBr_8$ and $(PEA)_4AgBiBr_8$ display different levels of organic interlayer stacking effects. We note that the structures of $(4\,FPEA)_4AgBiBr_8$ and $(4\,FPEA)_4AgBiI_8$ are sufficiently similar (as seen in Figure 2.1) to explain why $(PEA)_4AgBiBr_8$ cannot be obtained without additional control of the interactions between layers. By simple comparison of the organic layers in the four shown directions (FigureSI 2.15), the increased order of the $4FPEA^+$ cations vs. the PEA^+ cations can be observed. When viewed along a, the ring-to-ring stacking for both seems similar, but when viewed along b the twisting of the PEA^+ moiety can be seen distinctly. In FigureSI 2.15 this is visualized by red lines connecting equal carbon atom positions in $4FPEA^+$ and PEA^+ and a yellow dot/lines displaying the channel formed by the arranged

phenyl rings. The aromatic rings of 4FPEA$^+$ are stacked in-plane of the organic layer along ab as well as out-of-plane along c, while PEA$^+$ is only stacked in-plane of the organic layer along ab and not also out-of-plane along c, which is a reason for the stabilizing binding effect between the organic layers. Furthermore, while in-plane stacking of 4FPEA$^+$ cations is present in only one direction, as seen when viewed along b (FigureSI 2.15 b)), PEA$^+$ cations in-plane stacking is present in two directions in an alternating fashion (FigureSI 2.15 b) and d)). This increased out-of-plane stacking effect of the 4FPEA$^+$ moieties could be caused by the increased dipole moment of the molecule and/or the fluorine-fluorine attraction, leading to the observed point-symmetric anti stacking of the phenyl-rings (FigureSI 2.15 b) and d)).[49,77] The calculated dipole moment for PEA$^+$ is 13.47 Debye, whereas for 4FPEA$^+$ the value increases to 17.50 Debye, visualized in FigureSI 2.16. We further note that the substitution position of the fluorine atom seems crucial for the stabilizing effect for the 2D hybrid double perovskite iodide. While for lead- and tin-based 2D hybrid perovskites the ortho, meta and para position of the fluorine all yield the desired n = 1 2D hybrid double perovskite phase, our attempts with 2FPEA$^+$ and 3FPEA$^+$ only yielded hybrid bismuth iodides (FigureSI 2.12), confirming that not only sufficient binding effects but also specific geometric requirements of the organic cation are needed to stabilize the silver bismuth iodide system.[78,79] This is best seen in FigureSI 2.14, where the in-plane stacking of the phenyl rings is observable for both structures in b) and d), but the out of plane organic layer stacking is only seen in (4 FPEA)$_4$AgBiBr$_8$ in a) compared to (PEA)$_4$AgBiBr$_8$ in c). This difference is displayed more in detail in FigureSI 2.15, where only the organic part of the structures is shown. Red dotted lines illustrate the stacking positions of layer-to-layer stacking of adjacent phenyl rings and yellow dotted lines illustrate the in-plane stacking of adjacent phenyl rings. It is apparent that the 4FPEA molecules are arranged orderly in- and out-of-plane, while the PEA molecules are only ordered in-plane. The in-plane stacking is further worse for the PEA molecules, as they stack in an alternating manner, best seen in FigureSI 2.15 b) and d).

S5

The dipole moment of the cations was calculated by using the Gaussian 16W suite, using DFT and the B3LYP functional in a 6-31G* basis set.[80] The value for PEA$^+$ is 13.4646 Debye, whereas for 4FPEA$^+$ the value increased to 17.4947 Debye. The direction of the dipole moment is visualized in FigureSI 2.16 as a blue arrow, with the arrow head indicating the positive charged side and the arrow tail indicating the negative charged side. The difference in charge is visualized through an increased length of the arrow in 4FPEA. The increased dipole moment is one of the reasons for the increase in ordered stacking effect for 4FPEA vs PEA, alongside other effects like π-π stacking and fluorine-

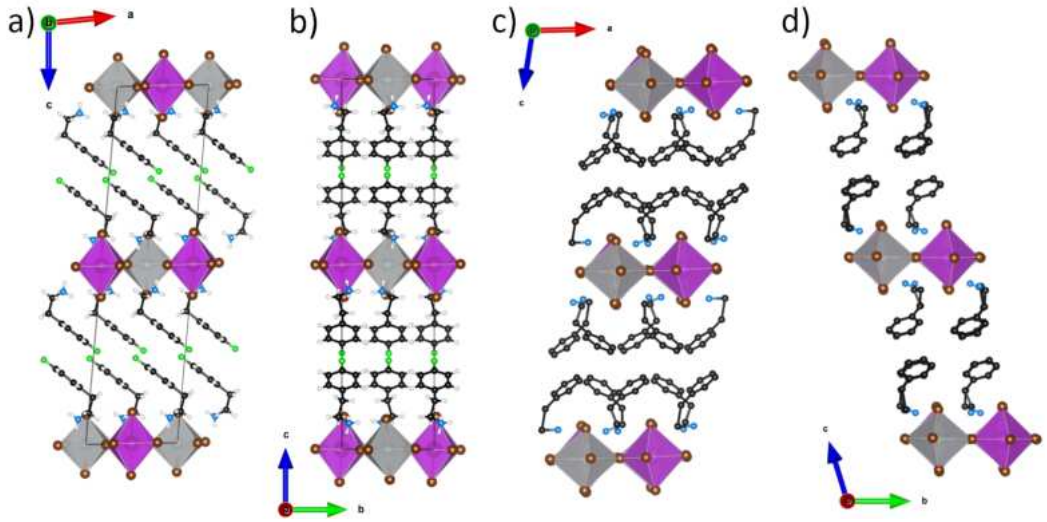

Figure 2.14: Comparison between the crystal structures of a) and b) $(4\,FPEA)_4AgBiBr_8$ and c) and d) $(PEA)_4AgBiBr_8$ along the b- and a-axis.

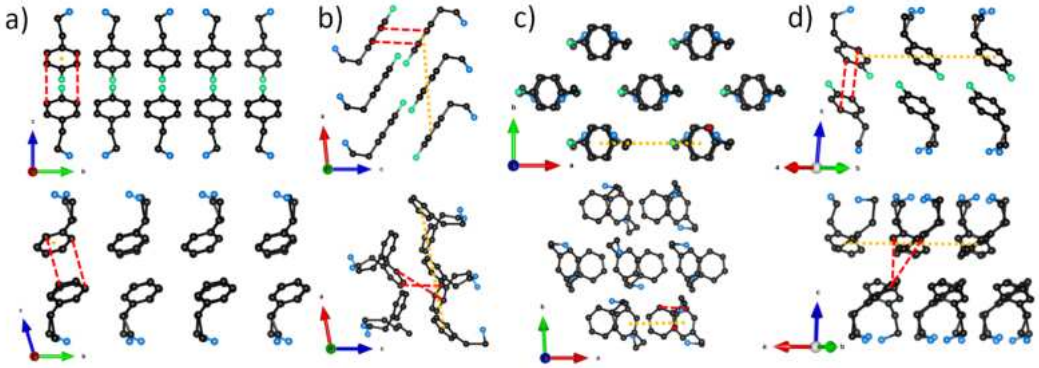

Figure 2.15: Comparison between the organic layers of $(4\,FPEA)_4AgBiBr_8$ on the top and $(4\,FPEA)_4AgBiBr_8$ on the bottom, along different crystallographic axis in a) b) c) and d).

fluorine interactions.[77]

TableSI 2.2

The lattice parameters for $(4\,FPEA)_4AgBiBr_8$ and $(4\,FPEA)_4AgBiI_8$ were determined through the single crystal structure solution. For $(4\,FPEA)_4AgBiCl_8$ we performed indexing in EXPO 2014 using the indexing program N-TREOR09 and compared the given solutions with the two solved structures to choose the most plausible parameters.[81] The lattice parameters are given in TableSI 2.2 and agree well with the powder patterns.

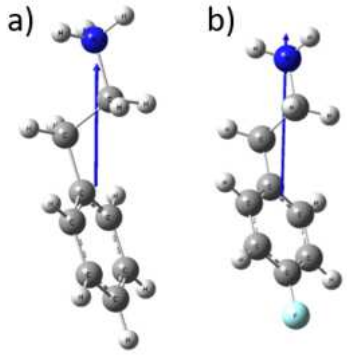

Figure 2.16: Dipole moments of a) PEA^+ and b) $4FPEA^+$ visualized as blue arrows.

Compound	a (Å)	b (Å)	c (Å)	α (°)	β (°)	γ (°)	V (Å^3)	Space Group
(4 FPEA)$_4$AgBiCl$_8$	8.1741	7.8068	16.7934	90	97.60	90	1062.2	P 1 21 1
(4 FPEA)$_4$AgBiBr$_8$	8.3833	8.1395	32.7693	90	96.120	90	2223.3	P12/n1
(4 FPEA)$_4$AgBiI$_8$	8.6236	8.7470	16.3676	98.973	90.119	90.013	1219.5	P-1

Table 2.2: Lattice parameters for (4 FPEA)$_4$AgBiX$_8$ (X=Cl, Br, I). Parameters for (4 FPEA)$_4$AgBiBr$_8$ and (4 FPEA)$_4$AgBiI$_8$ are obtained from the single crystal structure solution, while parameters for (4 FPEA)$_4$AgBiCl$_8$ were obtained from indexing powder XRD data.

S6

Cross section of (4 FPEA)$_4$AgBiI$_8$ on SiO_2 showing a homogeneous coverage, with (4 FPEA)$_4$AgBiI$_8$ lightest contrast on top, 500 nm thick darker contrast SiO_2 below and a lighter contrast Si on the bottom.

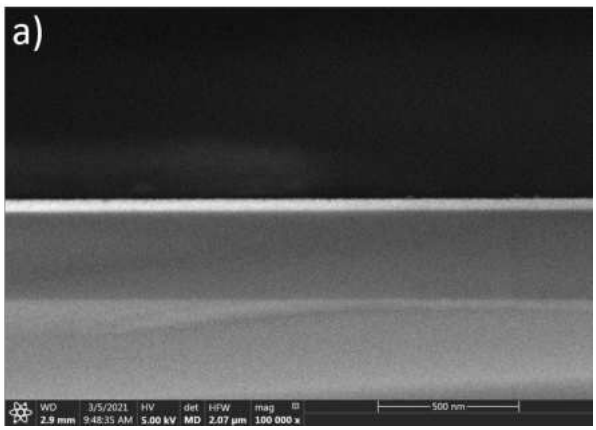

Figure 2.17: Cross section of (4 FPEA)$_4$AgBiI$_8$ on SiO_2.

S7

To confirm the bulk powder products of (4 FPEA)$_4$AgBiBr$_8$ and (4 FPEA)$_4$AgBiI$_8$ we performed a profile refinement in EXPO 2014 employing a Pearson VII profile shape function, background modelling by a Chebyshev polynomial of degree 16 and a refine-

ment of non-structural parameters with the LeBail method.[81] The refinement values R_p and R_{wp} are in good agreement and the biggest deviations can be seen in the difference plots coming from the main reflex between 5-6 ° 2 θ, showing a large asymmetric peak shape which is caused by the small angle area and the resulting inaccuracy of the diffractometer. As there are no additional reflexes present in the difference plots or any reflexes missing we conclude the product to be phase pure.

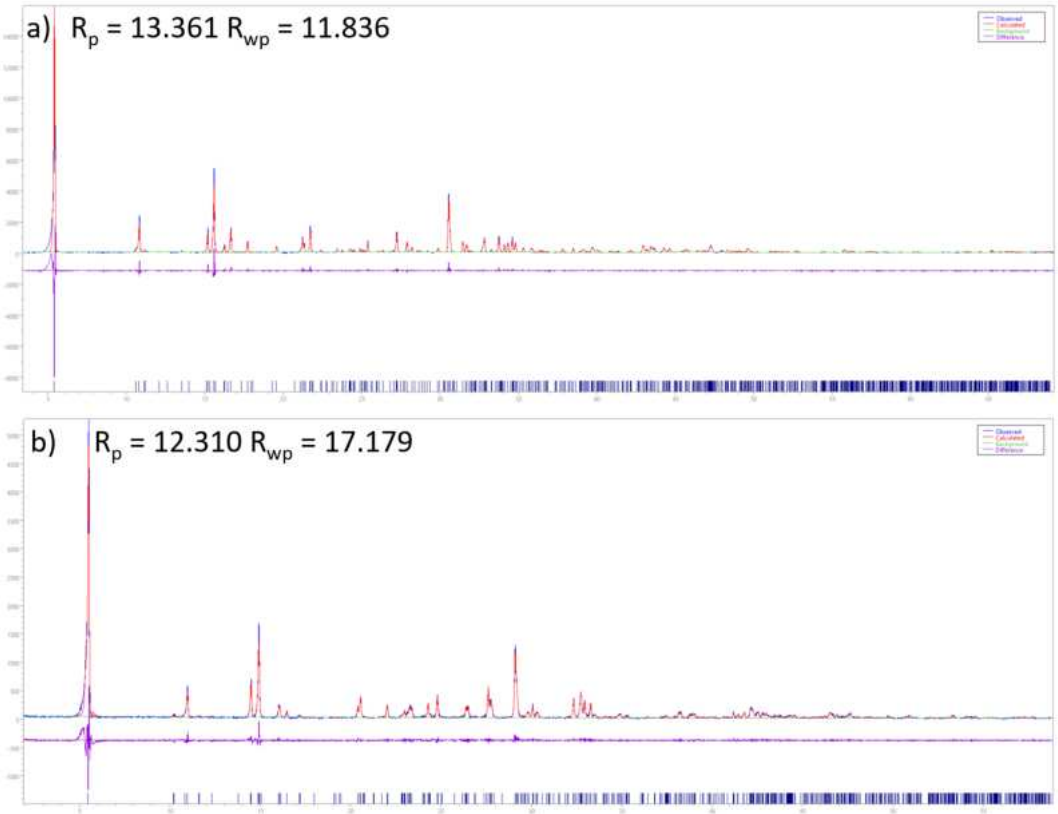

Figure 2.18: Profile Refinements for powder samples of a) $(4\,FPEA)_4AgBiBr_8$ and b) $(4\,FPEA)_4AgBiI_8$.

TableSI 2.3

To confirm the elemental composition and purity of the powder and thin films samples, we performed EDX measurements on crystalline powder samples and thin film samples shown in TableSI 2.3. Since the thin film samples on their respective substrates show an influence of the substrates on the measured signals causing an underestimation of the Ag, we scraped off the thin films from the substrates and measured them separately as powders. All samples agree well with the theoretic stoichiometry and the deviations are in the standard precision limits of the EDX method.

Sample	Ag (at%)	Bi (at%)	Cl (at%)	Ratio (Ag:Bi:X)
Crystal (avg.)	11.94	11.81	76.25	1.01:1:6.46
Thin Film (avg.)	5.86	10.24	83.90	0.57:1:8.19
Powdered Film (avg.)	9.69	12.00	78.32	0.81:1:6.53
	Ag (at%)	Bi (at%)	Br (at%)	
Crystal (avg.)	11.46	10.69	77.84	1.07:1:7.28
Thin Film (avg.)	5.73	9.02	85.26	0.63:1:9.45
Powdered Film (avg.)	12.43	11.14	76.42	1.12:1:6.86
	Ag (at%)	Bi (at%)	I (at%)	
Crystal (avg.)	10.59	10.02	79.40	1.06:1:7.92
Thin Film (avg.)	5.83	9.58	84.58	0.61:1:8.83
Powdered Film (avg.)	11.73	10.14	78.13	1.16:1:7.71

Table 2.3: EDX data for all (4 FPEA)$_4$AgBiX$_8$ (X = Cl, Br, I) in atom% from crystalline samples, thin film samples on ITO substrates and the same thin film samples scraped off and measured in powder form.

S8

AFM images of the substrates show the difference in surface roughness of a) Si-SiO_2 wafer, b) ITO coated-glass and c) FTO-coated glass, which is plotted in FigureSI 2.19 d) as a line cut across the full length of the substrate. The y-axis zero point was chosen to represent the average height value from the AFM measurement.

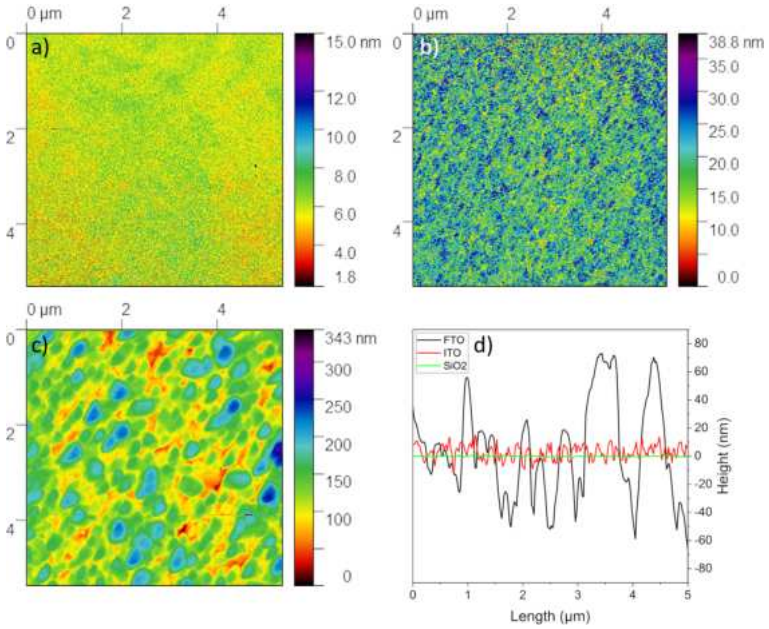

Figure 2.19: AFM images of substrates a) SiO_2, b) ITO, c) FTO and a line cut of each sample in d).

S9

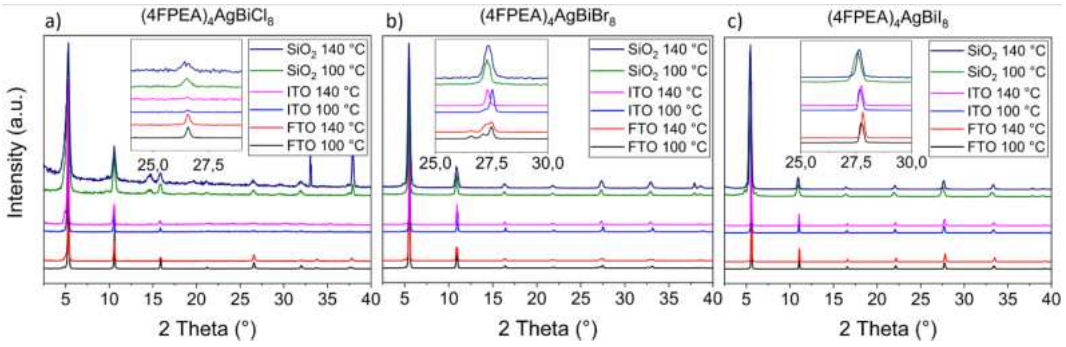

Figure 2.20: XRD patterns of thin films of a) $(4\,FPEA)_4AgBiCl_8$, b) $(4\,FPEA)_4AgBiBr_8$ and c) $(4\,FPEA)_4AgBiI_8$ on substrates FTO, ITO and SiO_2 from NMP solution with annealing at 100 °C or 140 °C. The different parameters are indicated in the legends, insets show a magnified view of the 005 reflection.

$(4\,FPEA)_4AgBiCl_8$: The films of $(4\,FPEA)_4AgBiCl_8$ on FTO and ITO exhibit similar patterns, albeit with smaller intensities and slightly worse signal-to-noise ratio (S/N) on ITO. The S/N is further worsened on SiO_2, which can mainly be attributed to the film being thinner compared to the ones on FTO and ITO due to the reduced concentration of the spin coating solution. Additionally, films on SiO_2 show small, additional reflections and the film annealed at 140 °C shows the distinct reflection of the Si substrate at 33° 2θ. A broadening of the reflections can be observed for films on SiO_2 compared to the ones on FTO and ITO.

$(4\,FPEA)_4AgBiBr_8$: Thin films of $(4\,FPEA)_4AgBiBr_8$ follow the same trends, with two differences. Firstly, the crystallinity, i.e. the S/N under consistent scanning conditions, for all three substrates is better than for the chloride films. Secondly, the thin films on FTO display small additional reflections, best observed in the range from 15 to 35° 2θ. The increased annealing temperature of 140 °C vs. 100 °C for FTO films shows a shift of intensity, increasing the relative intensities of the lower angle reflections, yet the same general reflection positions are seen for both temperatures. This shift is more clearly observed in the thin films on ITO, where for both temperatures distinct, singular reflections are observed. For films annealed at 140 °C the reflections are shifted more clearly towards the lower angle region, while the films annealed at 100 °C have the reflections shifted towards higher angles but also show a remnant of the lower angle reflections (inset of FigureSI 2.20 b). The films on SiO_2 substrates display the same large broadening, compared to their respective FTO or ITO analogs. For clarity, a magnification of the reflections from 15 to 35 ° 2θ with the calculated diffractogram of $(4\,FPEA)_4AgBiBr_8$ is given in FigureSI 2.21, which shows that the reflection profile is not caused by neighboring reflections, but shows splitting characteristics.

$(4\,FPEA)_4AgBiI_8$: Thin films of $(4\,FPEA)_4AgBiI_8$ have the highest S/N and hence presumably the highest degree of crystallinity of the three materials. There are no ad-

ditional reflections and no reflection splitting, as observed in (4 FPEA)$_4$AgBiCl$_8$ and (4 FPEA)$_4$AgBiBr$_8$. Interestingly, the influence of the annealing temperature is opposite to that of (4 FPEA)$_4$AgBiBr$_8$. With higher temperature the reflections shift towards higher angles compared to the diffractograms of samples annealed at 100 °C. This leads to the conclusion that while films of (4 FPEA)$_4$AgBiBr$_8$ at 140 °C display increased lattice parameters and tensile stress, films of (4 FPEA)$_4$AgBiI$_8$ show decreased lattice parameters and thus compressive stress. This trend is seen for all three substrates and while again the SiO_2 films show broad reflections, they are also shifted towards higher angles.

S10

Zoom in on the splitting features of (4 FPEA)$_4$AgBiBr$_8$ thin film diffractograms with the calculated diffractogram from the single crystal structure.

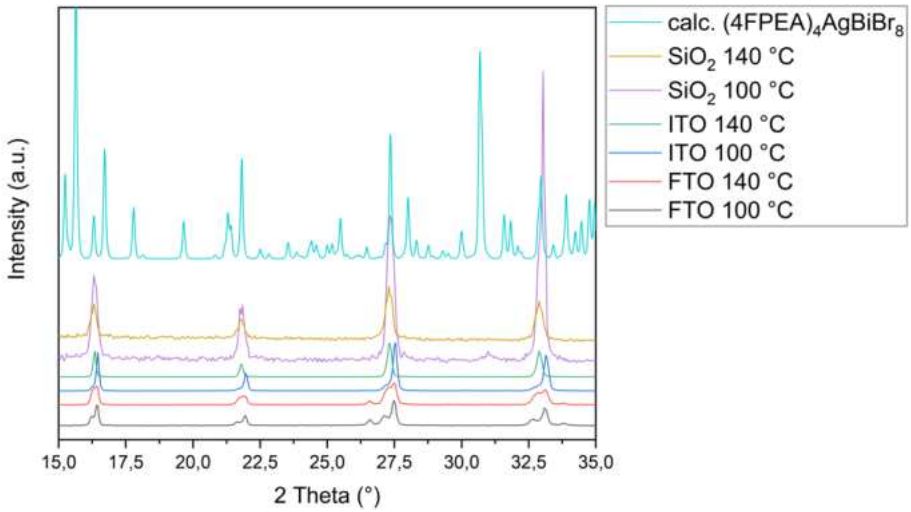

Figure 2.21: XRD zoom in from 15-35° 2θ of the thin films of (4 FPEA)$_4$AgBiBr$_8$ on all three substrates FTO, ITO and SiO_2 for both annealing temperatures 100 °C and 140 °C.

TableSI 2.4

Compound	a (Å)	b (Å)	c (Å)	α (°)	β (°)	γ (°)
(4 FPEA)$_4$AgBiBr$_8$	8.3833	8.1395	32.7693	90	96.120	90
(4 FPEA)$_4$AgBiBr$_8$ - ITO 100 °C	8.3797	8.1441	32.8066	90	96.016	90
(4 FPEA)$_4$AgBiBr$_8$ - ITO 140 °C	8.3407	8.1666	32.9159	90	96.021	90
(4 FPEA)$_4$AgBiI$_8$	8.6236	8.7470	16.3676	98.973	90.119	90.013
(4 FPEA)$_4$AgBiI$_8$ - ITO 100 °C	8.6938	8.7752	16.3885	98.839	90.587	89.684
(4 FPEA)$_4$AgBiI$_8$ - ITO 140 °C	8.7153	8.8009	16.3610	98.992	91.025	89.778

Table 2.4: Profile refinements for thin films of (4 FPEA)$_4$AgBiBr$_8$ and (4 FPEA)$_4$AgBiI$_8$ identifying the two phases.

S11 and S12

The thin film samples have been probed under varying incident angles from 0.04° - 1.00° to evaluate the degree of orientation throughout the complete depths of the films. The penetration depth of the incident X-ray beam can be estimated by using the relation of refractive properties of the material and the incident angle, as shown in equation 1. The index of refraction was calculated in dependence of the X-ray beam energy and the density of the probed material.[82] All three materials have decreasing FHWMs of

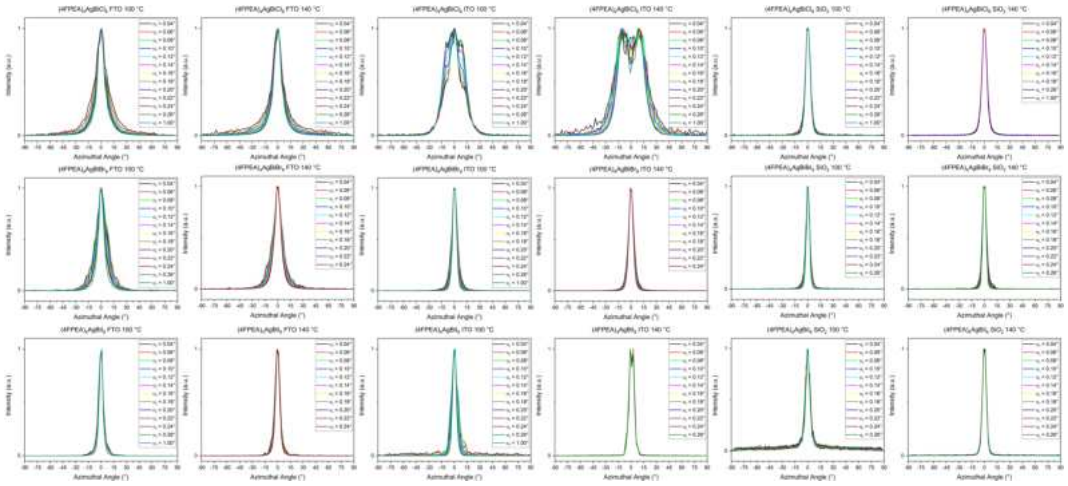

Figure 2.22: Azimuthal cuts of the 001 reflex for all thin films of $(4\,FPEA)_4AgBiCl_8$, $(4\,FPEA)_4AgBiBr_8$ and $(4\,FPEA)_4AgBiI_8$ on FTO, ITO and SiO_2 annealed at 100 °C and 140 °C, measured with incident angles from α_i = 0.04° to 1.00° (parameter in the panels).

χ going from FTO to ITO to SiO_2. Interestingly, while all samples have their maxima at χ = 0°, corresponding to an exclusively horizontal orientation relative the substrate, $(4\,FPEA)_4AgBiCl_8$ samples on ITO have a slightly tilted horizontal orientation with peak shouldering for 100 °C and peak splitting with maxima for 140 °C, both at χ = 10° and -10°. This small tilting can also be observed in $(4\,FPEA)_4AgBiI_8$ on ITO at 140 °C, albeit with minimally off-centered maxima at χ = 1° and -1°. To further probe the degree of orientation, we examined the films at varying incident angles from α_i = 0.04° to 1.00°, to distinguish the surface layers (i.e. several nm) from the complete film depth (i.e. several tens to hundreds nm. The impact of incident angle on penetration depth is further explained in S12).

S12

Equation 1 shows the dependence of the penetration depth Λ on the wavenumber k, the X-ray incident angle α_i, the critical angle α_c and the imaginary part of the index of refraction β.

$$\Lambda = \left[\sqrt{2}k \cdot \sqrt{\sqrt{(\alpha_i^2 - \alpha_c^2)^2 + 4\beta^2} - (\alpha_i^2 - \alpha_c^2)}\right]^{-1} \tag{2.1}$$

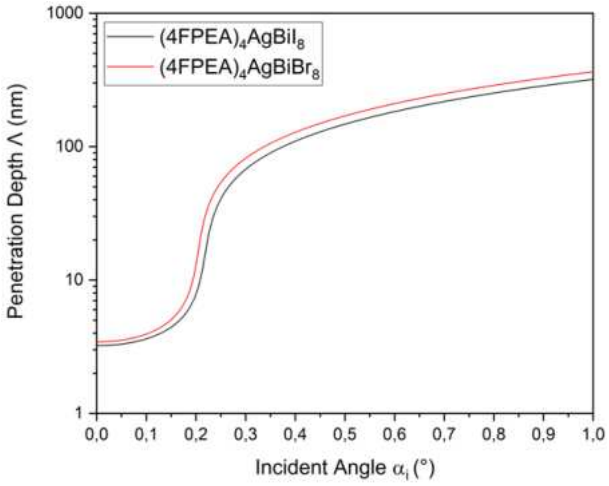

Figure 2.23: Penetration depth of the X-ray beam under grazing incidence as a function of the incident angle for (4 FPEA)$_4$AgBiBr$_8$ and (4 FPEA)$_4$AgBiI$_8$ according to equation (1).

S13

Optical and scanning electron microscope images in FigureSI 2.24 demonstrating the effect of the increased annealing temperature on the domain size on thin films of $(4\,FPEA)_4AgBiI_8$ a)+b), $(4\,FPEA)_4AgBiBr_8$ c)+d) and $(4\,FPEA)_4AgBiCl_8$ e)+f). **S14**

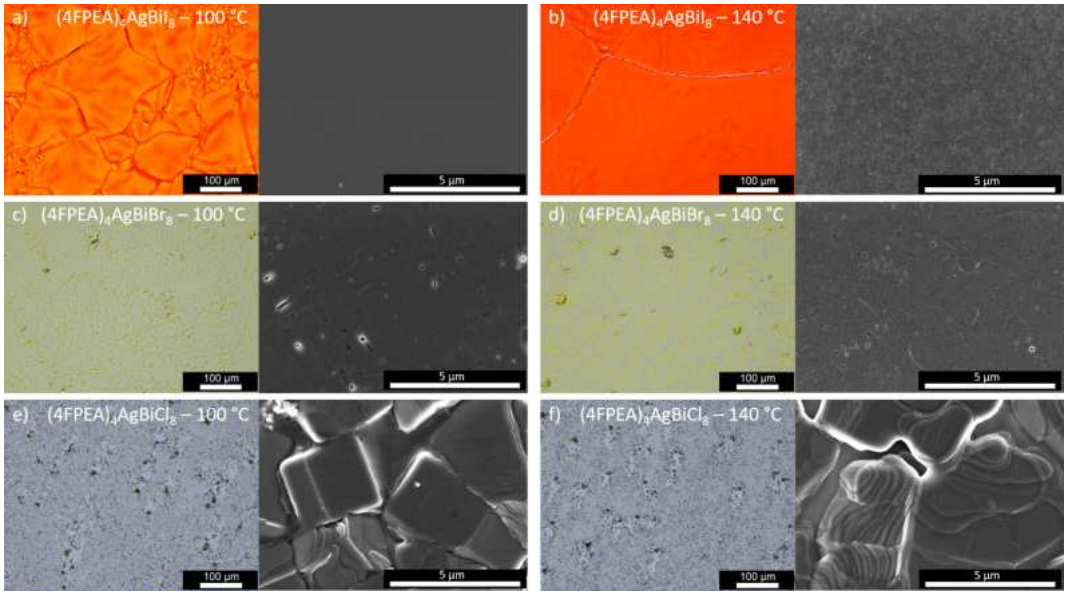

Figure 2.24: Microscope images of thin films spin coated from NMP solution on ITO of $(4\,FPEA)_4AgBiI_8$ annealed at 100 °C a) and 140 °C b), $(4\,FPEA)_4AgBiBr_8$ annealed at 100 °C c) and 140 °C d) and $(4\,FPEA)_4AgBiCl_8$ annealed at 100 °C e) and 140 °C f).

To confirm the crystal phase of our thin films we indexed 2D images of GIWAXS measurements at a sample detector distance of 155.7865 mm and an incident angle of 0.25 °. Representatively, we measured thin film samples on ITO substrates annealed at 140 °C for a) $(4\,FPEA)_4AgBiCl_8$, b) $(4\,FPEA)_4AgBiI_8$ and c) $(4\,FPEA)_4AgBiI_8$ with the lattice parameters shown in TableSI 2.1 and the indexed 2D images shown in FigureSI 2.25. Indexing of the GIWAXS data was carried out with the program GIXSGUI.[9] While the diffraction positions of (00l) planes agree well with the calculated positions, the diffraction positions of planes including a and b lattice parameters exhibit a shift indicating a compressed unit cell in a and b. This agrees with the observed lattice compression between thin films and calculated diffractograms in main text Figure 2.2.

S15 and S16

The optimized synthesis parameters for thin films of $(4\,FPEA)_4AgBiBr_8$ to yield the same pristine surface morphology as the in the main text shown $(4\,FPEA)_4AgBiI_8$ thin film, were different by that the spin coating took place under ambient conditions and the initial spin coating step was at 1000 rpm and the second step was at 6000 rpm.

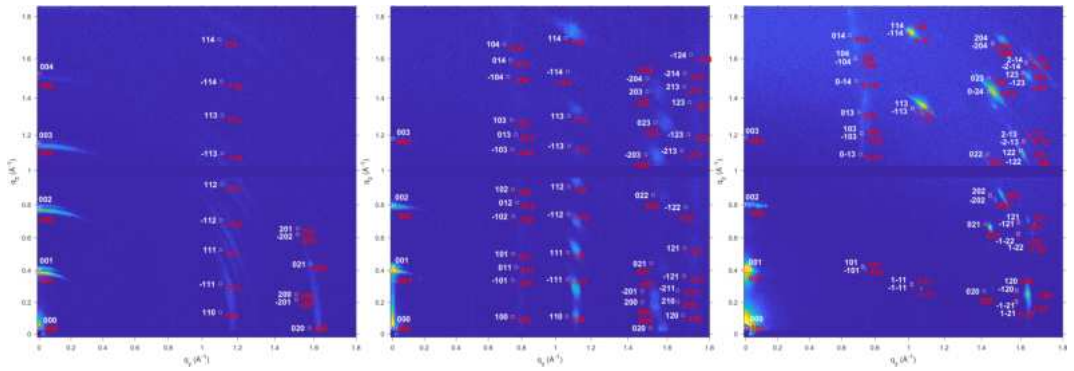

Figure 2.25: GIWAXS 2D images with indexed diffraction positions for a) (4 FPEA)$_4$AgBiCl$_8$, b) (4 FPEA)$_4$AgBiI$_8$ and c) (4 FPEA)$_4$AgBiI$_8$ thin films on FTO substrates annealed at 140 °C.

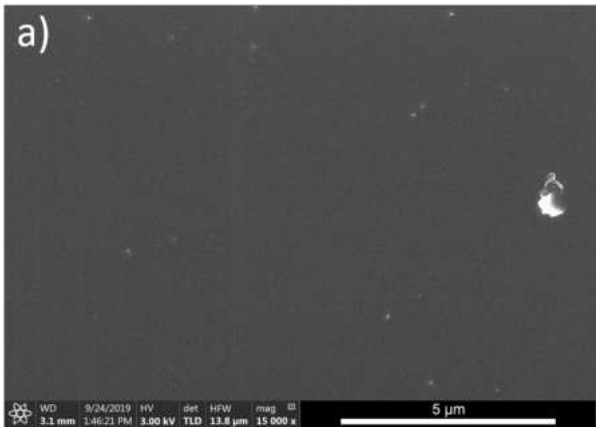

Figure 2.26: Pristine surface morphology from optimized synthesis parameters for (4 FPEA)$_4$AgBiBr$_8$ films on FTO.

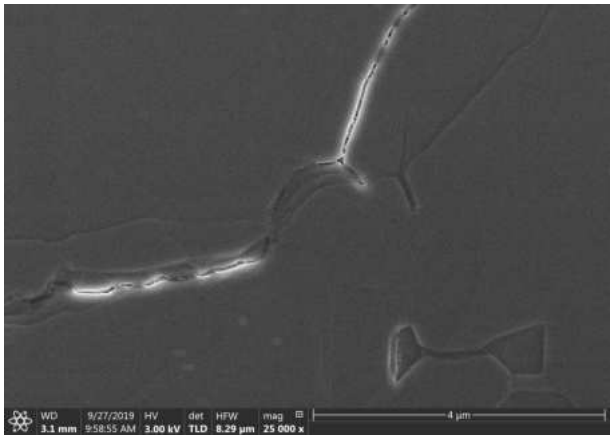

Figure 2.27: Surface morphology of (PEA)$_4$AgBiBr$_8$ thin films on FTO.

S17, S18 and S19

FigureSI 2.28 shows the indirect nature of the band gap for $(4\,\mathrm{FPEA})_4\mathrm{AgBiBr}_8$ and $(4\,\mathrm{FPEA})_4\mathrm{AgBiI}_8$ if spin-orbit coupling is not considered. To gather more understanding

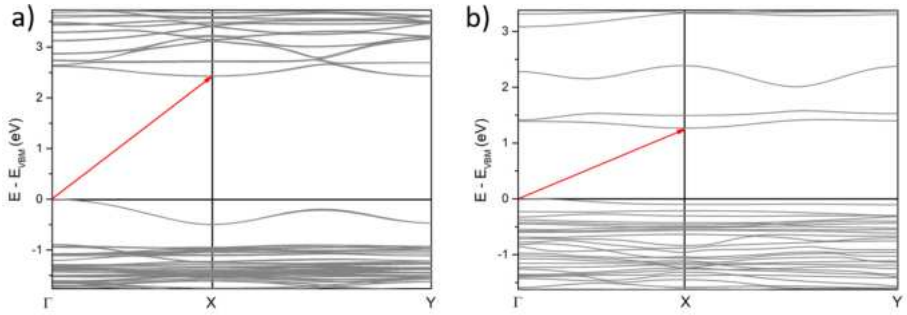

Figure 2.28: Band structures of a) $(4\,\mathrm{FPEA})_4\mathrm{AgBiBr}_8$ and b) $(4\,\mathrm{FPEA})_4\mathrm{AgBiI}_8$ without SOC.

into the type of quantum well band alignment in these hybrid materials, the partial density of states for organic and inorganic components is depicted in FigureSI 2.29. To approx-

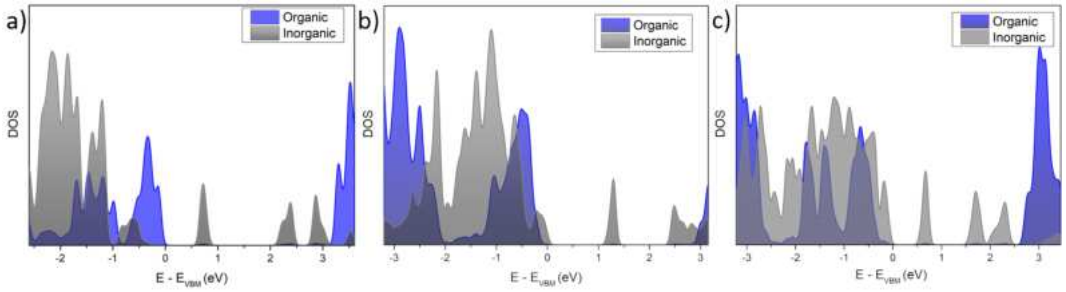

Figure 2.29: Partial DOS for organic and inorganic components for a) $(4\,\mathrm{FPEA})_4\mathrm{AgBiCl}_8$, b) $(4\,\mathrm{FPEA})_4\mathrm{AgBiBr}_8$ and c) $(4\,\mathrm{FPEA})_4\mathrm{AgBiI}_8$.

imate the values for the effective masses at the high symmetry point Γ in the calculated band diagrams for the bromide and iodide compounds, a simple parabolic fit function was employed. The curvature values were used to calculate the effective masses as shown in the following equation:

$$m^* = \hbar \left(\frac{\delta^2 E}{\delta k^2} \right)^{-1} \tag{2.2}$$

Where $m*(k)$, $\hbar$, $E(k)$, and k are the effective mass, reduced Planck's constant, energy, and wave vector, respectively. The obtained values are depicted in TableSI 2.5:

	Bromide	Iodide
Effective masses of electrons $[m_e^*/m_0]$ $(\Gamma - X/\Gamma - Y)$	0.136	0.122
Effective masses of holes $[m_h^*/m_0]$ $(\Gamma - X/\Gamma - Y)$	0.123	0.242

Table 2.5: Effective masses of electrons and holes.

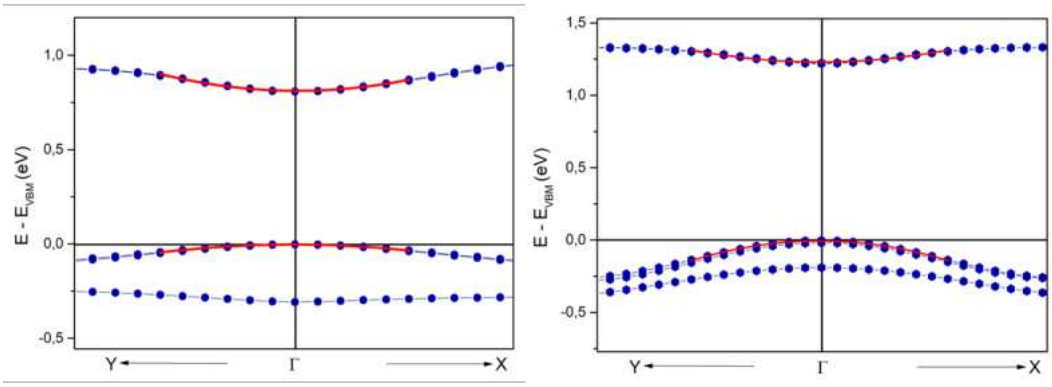

Figure 2.30: E(k) diagrams for (4 FPEA)$_4$AgBiBr$_8$ (left) and (4 FPEA)$_4$AgBiI$_8$ (right).

As expected from the dispersion in the E(k) diagrams, the value for the effective hole mass is much larger for 4FPEAI than for 4FPEABr. The effective electron masses differ by a small amount, also apparent in the band structure plot, with the conduction band being slightly less dispersed for 4FPEABr. We note that the exact prediction of effective mass values requires higher levels of theory, which were not accessible because of the prohibitive system dimensions, but PBE-SOC was also shown to provide satisfactory experimental agreement.[83]

S20

The theoretical absorption spectra were simulated by calculating frequency-dependent complex dielectric functions as implemented in the Quantum espresso epsilon package according to equation 2.3.[72]

$$\alpha(\omega) = \frac{4\pi\omega}{hc}\left[\frac{\sqrt{Re\varepsilon(\omega)^2 + Im\varepsilon(\omega)^2} - Re\varepsilon(\omega)}{2}\right]^{0.5} \tag{2.3}$$

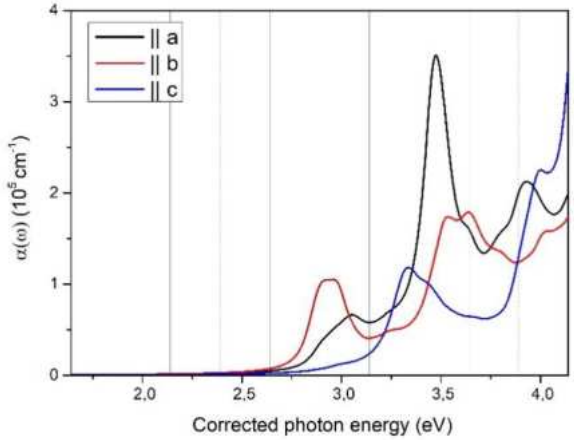

Figure 2.31: Simulated absorption for (4 FPEA)$_4$AgBiBr$_8$ from dielectric response employing the random phase approximation excluding excitonic effects and subtracting the experimental absorption edge.

S21

Employed spectral corrections in equation 2.4, which takes into account the absorption of light reflected from all interfaces, derived by Klahr and Hamann.[84] Here, A_{corr} represents the corrected absorption, while T_{sub}, T_{sam}, R_{sub}, R_{sam} represent the spectral transmittance and reflectance of the substrate and the coated substrate, respectively.

$$A_{corr}(\lambda) = -\log \frac{\frac{T_{sam}(\lambda)}{T_{sub}(\lambda)}}{1 - \frac{R_{sam}(\lambda) - R_{sub}(\lambda)}{T_{sub}(\lambda)^2}} \tag{2.4}$$

Powder samples were measured as diffuse reflectance spectra with a white standard ($BaSO_4$) background.

Zoom in on the powder absorption spectra displaying similar features as the thin film absorption spectra:

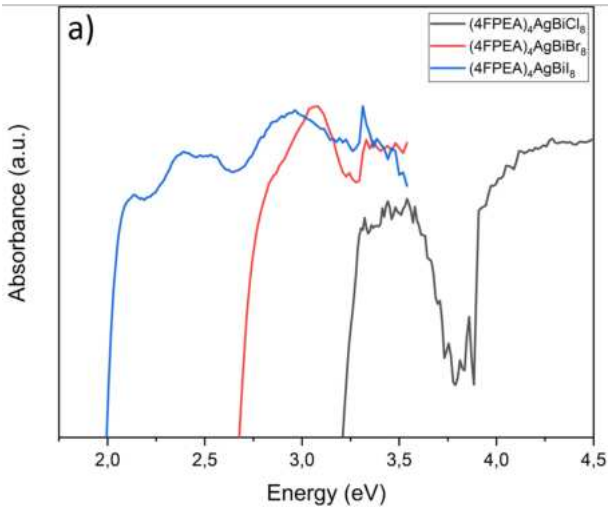

Figure 2.32: Magnification of the absorption features of powder UV-Vis absorbance data for $(4\,FPEA)_4AgBiCl_8$, $(4\,FPEA)_4AgBiBr_8$ and $(4\,FPEA)_4AgBiI_8$.

S22

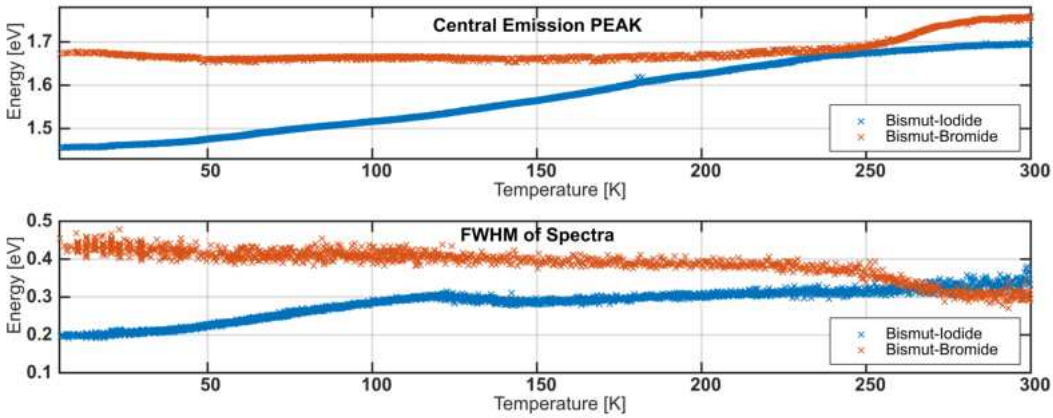

Figure 2.33: Temperature dependent spectral shift of the central emission peak and FWHM of the PL spectra for (4 FPEA)$_4$AgBiBr$_8$ and (4 FPEA)$_4$AgBiI$_8$.

S23, S24, S25, S26

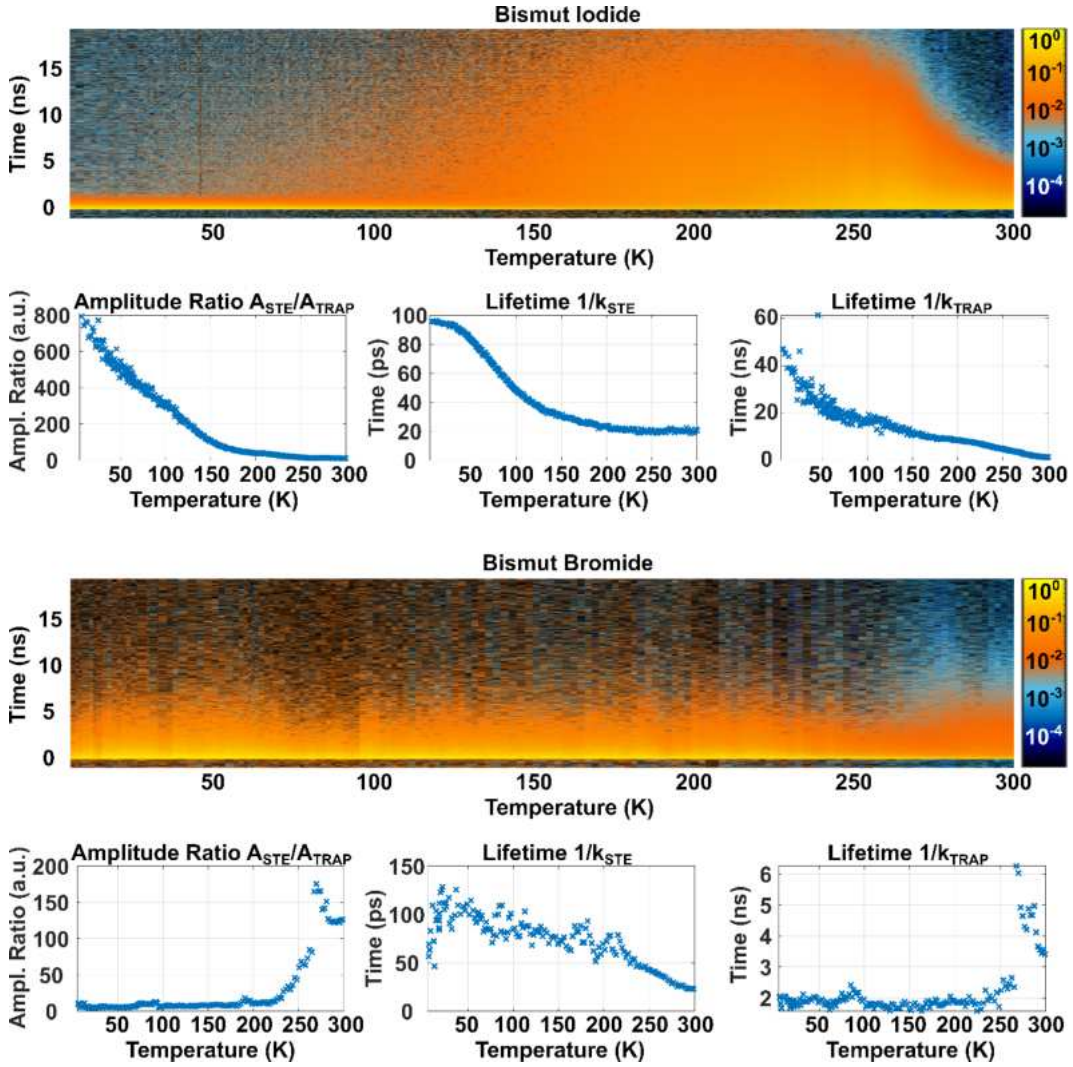

Figure 2.34: Temperature dependent transients and extracted lifetime plots for the short- and long-lived component from a biexponential fitting for $(4\,FPEA)_4AgBiBr_8$ and $(4\,FPEA)_4AgBiI_8$.

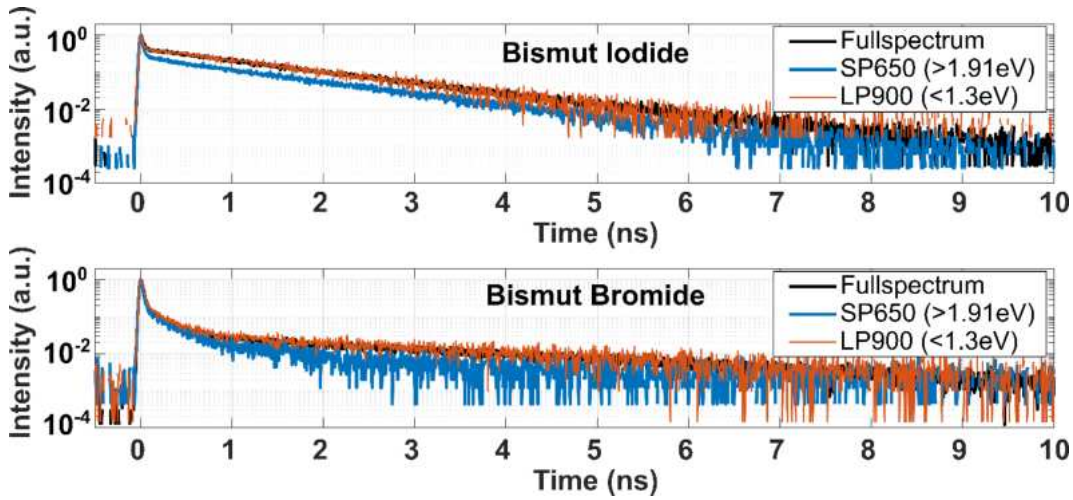

Figure 2.35: PL transients at room temperature with full spectrum (black), short-pass filter 700/650 nm (blue) and long-pass filter 900 nm (red) for $(4\,FPEA)_4AgBiBr_8$ and $(4\,FPEA)_4AgBiI_8$.

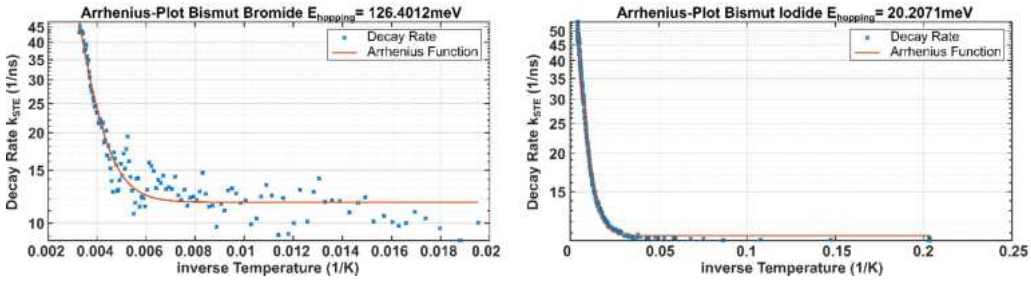

Figure 2.36: Arrhenius plots to extract the activation energy of the proposed hopping barrier for (4 FPEA)$_4$AgBiBr$_8$ (left) and (4 FPEA)$_4$AgBiI$_8$ (right).

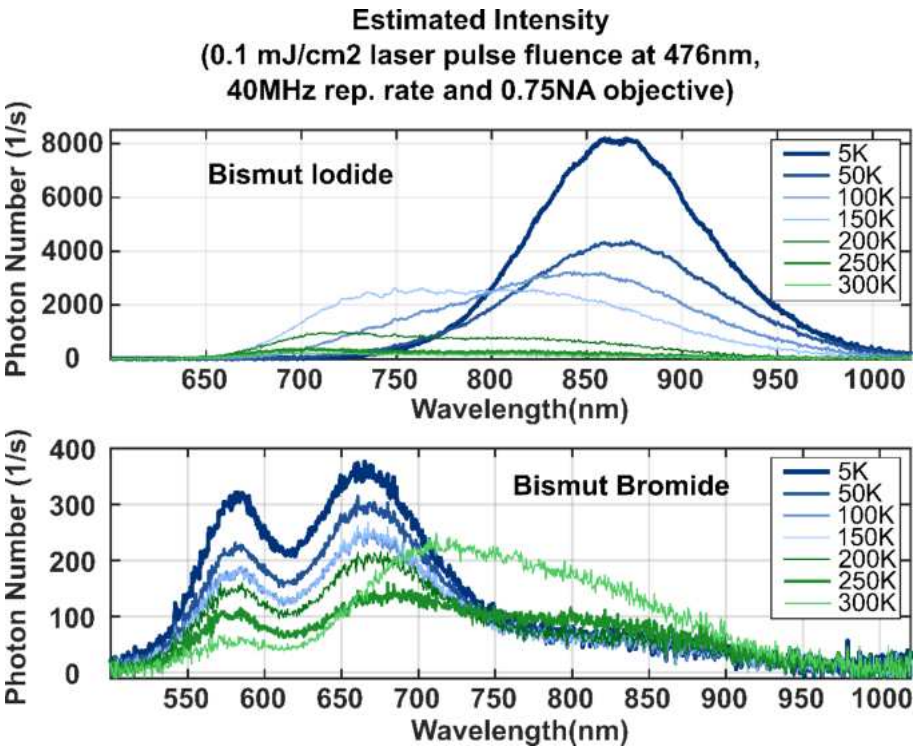

Figure 2.37: Estimated intensities of the temperature dependent emission for (4 FPEA)$_4$AgBiI$_8$ at the top and (4 FPEA)$_4$AgBiBr$_8$ at the bottom.

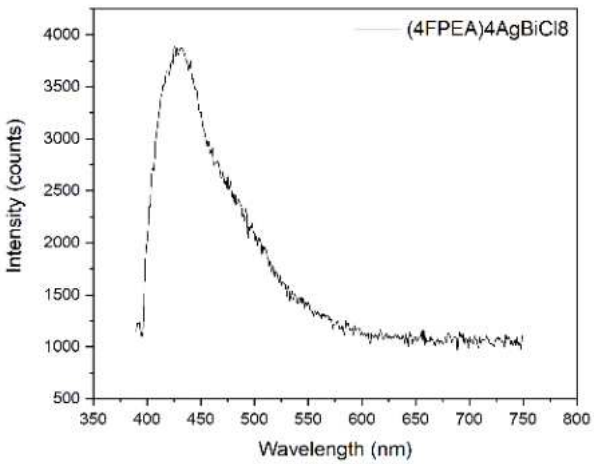

Figure 2.38: Room temperature PL spectrum of $(4\,\mathrm{FPEA})_4\mathrm{AgBiCl}_8$ with excitation wavelength of 375 nm, displaying the same characteristic broad emission as for the bromide and iodide thin films.

S27

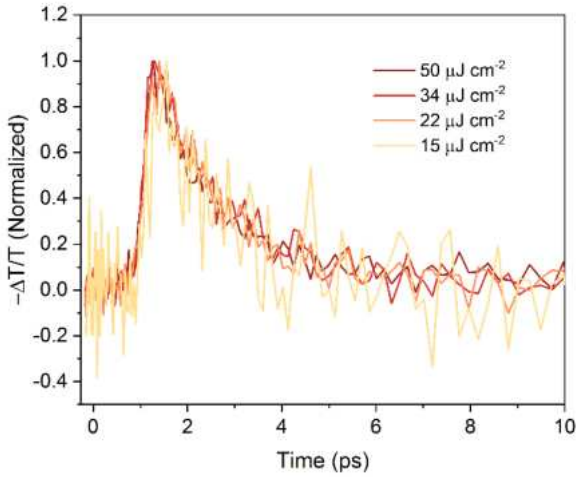

Figure 2.39: Comparison between normalized fluence-dependent OPTP transients for (4 FPEA)$_4$AgBiI$_8$ after 3.1 eV pulsed excitation. Different coloured lines represent different fluences in the range 15 to 50 μJ cm^{-2}.

S28

Derivation of charge-carrier mobility from OPTP measurements

The charge-carrier mobility was determined using the approach developed by Wehrenfennig et al..[85] Furthermore, we fitted the OPTP transient with a two-level mobility model developed by Wright et al. and Buizza et al..[56,64] In the adopted method, we converted the (ΔT/T) traces to a photoconductivity signal $\delta\sigma$, which is proportional to the charge-carrier mobility μ and to the charge carrier density n via the equation $\Lambda\sigma = en\mu$. For our experimental geometry (i.e., transmission geometry for thin film on a z-cut quartz substrate), the sheet photoconductivity can be approximated to

$$\Delta\sigma = -\frac{\epsilon_0 c(n_q + n_v)}{d_{film}} \frac{\Delta T}{T} \tag{2.5}$$

where d_{film} is the thickness of the studied thin film and n_q = 2.13 and n_v = 1 are the refractive indexes of quartz and vacuum, respectively.[86] Therefore, in order to derive the charge-carrier mobility from the sheet photoconductivity, the photogenerated carrier number N needs to be determined as

$$N = \phi \frac{E\lambda}{hc}(1 - R_{pump} - T_{pump}) \tag{2.6}$$

Where ϕ is the photon-to-charge branching ratio (i.e., the fraction of generated charges per photons absorbed), E is the excitation energy per pulse, $\epsilon = hc/\lambda$ is the energy of a photon with wavelength λ, and R_{pump} and T_{pump} are the reflectance and transmittance of the sample at the excitation wavelength. This is converted to the photogenerated charge

carrier density n_0 by dividing the film thickness d_{film} and the effective overlap area between THz and pump beam A_{eff}.

The resulting effective mobility can be then expressed as:

$$\phi\mu = -\epsilon_0 c\,(n_q + n_v)\,\frac{A_{eff} hc}{eE\lambda\,(1 - R_{\text{pump}} - T_{\text{pump}})}\left(\frac{\Delta T}{T}\right) \tag{2.7}$$

To better capture the photoconductivity dynamics in silver-bismuth halides, Wright and Buizza developed a two-level mobility model, which describes the charge carrier localization process.[56,64] In this model, the photoconductivity of the material can be described as the sum photoconductivity for two different states with a definite population and mobility: a delocalized state (n_{del},μ_{del}) and a localized state (n_{loc},μ_{loc}). The resulting photoconductivity can be expressed as $\Delta\sigma = e(n_{del}\mu_{del} + n_{loc}\mu_{loc})$. In the low excitation fluence regime, where the recombination from the localized state is predominantly monomolecular, the carrier population is described by the set of coupled rate equations:

$$\begin{cases} \frac{dn_{del}}{dt} = -k_{loc} n_{del}(t) \\ \frac{dn_{loc}}{dt} = k_{loc} n_{del}(t) - k_1 n_{loc}(t) \end{cases} \tag{2.8}$$

Here, k_{loc} and k_1 are the localization and monomolecular recombination rates, respectively. As reported in Refs[64] and,[56] the resulting $\Delta T/T$ signal can be described as:

$$\frac{\Delta T}{T} = -\frac{e n_0 d_{\text{film}}}{\epsilon_0 c\,(n_q + n_v)}\left(\left(\mu_{\text{del}} - \frac{\mu_{\text{loc}}\,k_{\text{loc}}}{k_{\text{loc}} - k_1}\right)e^{-k_{\text{loc}}\,t} + \frac{\mu_{\text{loc}}\,k_{\text{loc}}}{k_{\text{loc}} - k_1}e^{-k_1 t}\right) \tag{2.9}$$

Furthermore, to fit the experimental data reported in Figure 2.10, we convoluted the resulting decay function with a Gaussian function with broadening σ = 290 fs (representing the instrumental response function) as described in Reference.[64]

S29

Although the responsivity of a photodetector gives a measure of the output signal of the detector for a given optical input signal, it does not give any information about the sensitivity of the device. The sensitivity of the detector can be defined as the minimum detectable optical input power that can be sensed with a signal-to-noise ratio of unity. This power is called the noise-equivalent-power (NEP) of the detector and the detectivity of a detector is the inverse of this noise-equivalent-power. The specific detectivity is denoted D* and is the detectivity of a photodetector with an area of 1 cm^2 and an electrical bandwidth of 1 Hz, where A is the area of the detector in cm^2. D* is expressed in units of cm $Hz^{0.5}$ W^{-1}.

$$D^* = D\sqrt{A\Delta f} = \sqrt{A\Delta f}\frac{1}{P_{NEP}} \tag{2.10}$$

S30

Active layer		Responsivity A W^{-1}	Specific Detectivity $(Jones)$	Reference
2D Sn(II) based perovskites	$(PEA)_2SnI_4$	16	1.92e11	17
	graphene/$(PEA)_2SnI_4$/MoS_2/graphene	121	8.09e9	18
	$(PEA)_2SnI_4$	329	2.06e11	19
3D Ag – Bi based double perovskites	$Cs_2AgBiBr_6$	7.01	5.66e11	20
	$Cs_2AgBiBr_6$/SnO_2 heterojunctions	0.11	2.1e10	21
	$Cs_2AgBiBr_6$	0.14	3.29e12	22
2D Ag – Bi based double perovskites	$(4\,FPEA)_4AgBiBr_8$	0.010	6e9	This work
	$(4\,FPEA)_4AgBiI_8$	0.002	5e8	This work
	((R/S-β-MPA)$_4$AgBiI$_8$ - microwire array	0.052	3.9e11	23
	((R/S-β-MPA)$_4$AgBiI$_8$ - single crystal	0.000022	1.2e7	24

Table 2.6: Summary of related photoconductors.

net formula	C32H44AgBiBr8F4N4
Mr/g mol-1	1516.84
crystal size/mm	0.050 × 0.050 × 0.020
T/K	297.(2)
radiation	MoK$_\alpha$
diffractometer	'Bruker D8 Venture TXS'
crystal system	monoclinic
space group	'P 1 2/n 1'
a/Å	8.3833(2)
b/Å	8.1395(2)
c/Å	32.7693(7)
α/°	90
β/°	96.1200(10)
γ/°	90
V/Å^3	2223.30(9)
Z	2
calc. density/g cm-3	2.266
μ/mm-1	11.626
absorption correction	Multi-Scan
transmission factor range	0.53–0.80
refls. measured	32609
Rint	0.0451
mean σ(I)/I	0.0439
θ range	2.579–29.129
observed refls.	5392
x, y (weighting scheme)	0, 24.9411
hydrogen refinement	mixed

refls in refinement	5973
parameters	233
restraints	0
R(Fobs)	0.0489
Rw(F2)	0.1302
S	1.239
shift/errormax	0.001
max electron density/e Å-3	1.446
min electron density/e Å-3	-1.333

Table 2.7: Crystallographic data (4 FPEA)$_4$AgBiBr$_8$

net formula	C32H44AgBiF4I8N4
Mr/g mol-1	1892.76
crystal size/mm	0.100 × 0.080 × 0.010
T/K	298.(2)
radiation	MoK$_\alpha$
diffractometer	'Bruker D8 Venture TXS'
crystal system	triclinic
space group	'P -1'
a/Å	8.6236(6)
b/Å	8.7470(5)
c/Å	16.3676(11)
α/°	98.973(2)
β/°	90.119(2)
γ/°	90.013(2)
V/Å^3	1219.51(14)
Z	1
calc. density/g cm-3	2.577
μ/mm-1	9.109
absorption correction	Multi-Scan
transmission factor range	0.77–0.91
refls. measured	31455
Rint	0.0424
mean σ(I)/I	0.0428
θ range	3.171–30.507
observed refls.	6516
x, y (weighting scheme)	0.0412, 7.1338
hydrogen refinement	mixed

refls in refinement	7455
parameters	241
restraints	0
R(Fobs)	0.0435
Rw(F2)	0.1040
S	1.037
shift/errormax	0.001
max electron density/e Å-3	2.231
min electron density/e Å-3	-1.350

Table 2.8: Crystallographic data (4 FPEA)$_4$AgBiI$_8$

2.8 References

[1] S. D. Stranks, H. J. Snaith, *Nature nanotechnology* **2015**, *10*, 391–402.

[2] W. Yu, F. Li, L. Yu, M. R. Niazi, Y. Zou, D. Corzo, A. Basu, C. Ma, S. Dey, M. L. Tietze, et al., *Nature communications* **2018**, *9*, 5354.

[3] L. Yin, H. Wu, W. Pan, B. Yang, P. Li, J. Luo, G. Niu, J. Tang, *Advanced Optical Materials* **2019**, *7*, 1900491.

[4] A. Sadhanala, S. Ahmad, B. Zhao, N. Giesbrecht, P. M. Pearce, F. Deschler, R. L. Hoye, K. C. Gödel, T. Bein, P. Docampo, et al., *Nano letters* **2015**, *15*, 6095–6101.

[5] A. H. Slavney, T. Hu, A. M. Lindenberg, H. I. Karunadasa, *Journal of the American Chemical Society* **2016**, *138*, 2138–2141.

[6] Y. Zhang, Y. Ma, Y. Wang, X. Zhang, C. Zuo, L. Shen, L. Ding, *Advanced Materials* **2021**, *33*, 2006691.

[7] G. Meyer, *Progress in Solid State Chemistry* **1982**, *14*, 141–219.

[8] N. Elliott, L. Pauling, *Journal of the American Chemical Society* **1938**, *60*, 1846–1851.

[9] E. T. McClure, M. R. Ball, W. Windl, P. M. Woodward, *Chemistry of Materials* **2016**, *28*, 1348–1354.

[10] H. C. Sansom, G. Longo, A. D. Wright, L. R. Buizza, S. Mahesh, B. Wenger, M. Zanella, M. Abdi-Jalebi, M. J. Pitcher, M. S. Dyer, et al., *Journal of the American Chemical Society* **2021**, *143*, 3983–3992.

[11] Z. Deng, F. Wei, S. Sun, G. Kieslich, A. K. Cheetham, P. D. Bristowe, *Journal of Materials Chemistry A* **2016**, *4*, 12025–12029.

[12] T. T. Tran, J. R. Panella, J. R. Chamorro, J. R. Morey, T. M. McQueen, *Materials Horizons* **2017**, *4*, 688–693.

[13] G. Volonakis, A. A. Haghighirad, R. L. Milot, W. H. Sio, M. R. Filip, B. Wenger, M. B. Johnston, L. M. Herz, H. J. Snaith, F. Giustino, *The journal of physical chemistry letters* **2017**, *8*, 772–778.

[14] B. A. Connor, R.-I. Biega, L. Leppert, H. I. Karunadasa, *Chemical science* **2020**, *11*, 7708–7715.

[15] M. Roknuzzaman, J. A. Alarco, H. Wang, K. K. Ostrikov, *Computational Materials Science* **2021**, *186*, 110009.

[16] F. Wei, Z. Deng, S. Sun, F. Xie, G. Kieslich, D. M. Evans, M. A. Carpenter, P. D. Bristowe, A. K. Cheetham, *Materials Horizons* **2016**, *3*, 328–332.

[17] W. Pan, H. Wu, J. Luo, Z. Deng, C. Ge, C. Chen, X. Jiang, W.-J. Yin, G. Niu, L. Zhu, et al., *Nature photonics* **2017**, *11*, 726–732.

[18] O. Lozhkina, A. Murashkina, M. Elizarov, V. Shilovskikh, A. Zolotarev, Y. V. Kapitonov, R. Kevorkyants, A. Emeline, T. Miyasaka, *Chemical Physics Letters* **2018**, *694*, 18–22.

[19] D. Bartesaghi, A. H. Slavney, M. C. Gélvez-Rueda, B. A. Connor, F. C. Grozema, H. I. Karunadasa, T. J. Savenije, *The Journal of Physical Chemistry C* **2018**, *122*, 4809–4816.

[20] E. Greul, M. L. Petrus, A. Binek, P. Docampo, T. Bein, *Journal of Materials Chemistry A* **2017**, *5*, 19972–19981.

[21] M. T. Sirtl, F. Ebadi, B. T. van Gorkom, P. Ganswindt, R. A. Janssen, T. Bein, W. Tress, *Advanced Optical Materials* **2021**, *9*, 2100202.

[22] M. T. Sirtl, M. Armer, L. K. Reb, R. Hooijer, P. Dörflinger, M. A. Scheel, K. Tvingstedt, P. Rieder, N. Glück, P. Pandit, et al., *ACS applied energy materials* **2020**, *3*, 11597–11609.

[23] B. A. Connor, L. Leppert, M. D. Smith, J. B. Neaton, H. I. Karunadasa, *Journal of the American Chemical Society* **2018**, *140*, 5235–5240.

[24] X. Wang, K. Li, H. Xu, N. Ali, Y. Wang, Q. Shen, H. Wu, *Chemical Communications* **2020**, *56*, 7917–7920.

[25] M. T. Sirtl, R. Hooijer, M. Armer, F. G. Ebadi, M. Mohammadi, C. Maheu, A. Weis, B. T. van Gorkom, S. Häringer, R. A. Janssen, et al., *Advanced Energy Materials* **2022**, *12*, 2103215.

[26] M. Pantaler, V. Diez-Cabanes, V. I. Queloz, A. Sutanto, P. A. Schouwink, M. Pastore, I. García-Benito, M. K. Nazeeruddin, D. Beljonne, D. C. Lupascu, et al., *Jacs Au* **2021**, *2*, 136–149.

[27] Y. Li, T. Yang, Z. Xu, X. Liu, X. Huang, S. Han, Y. Liu, M. Li, J. Luo, Z. Sun, *Angewandte Chemie International Edition* **2020**, *59*, 3429–3433.

[28] L. Mao, S. M. Teicher, C. C. Stoumpos, R. M. Kennard, R. A. DeCrescent, G. Wu, J. A. Schuller, M. L. Chabinyc, A. K. Cheetham, R. Seshadri, *Journal of the American Chemical Society* **2019**, *141*, 19099–19109.

[29] A. Walsh, *The Journal of Physical Chemistry C* **2015**, *119*, 5755–5760.

[30] Z. Xiao, W. Meng, J. Wang, Y. Yan, *ChemSusChem* **2016**, *9*, 2628–2633.

[31] P. Vishnoi, R. Seshadri, A. K. Cheetham, *The Journal of Physical Chemistry C* **2021**, *125*, 11756–11764.

[32] Z. Xu, X. Liu, Y. Li, X. Liu, T. Yang, C. Ji, S. Han, Y. Xu, J. Luo, Z. Sun, *Angewandte Chemie International Edition* **2019**, *58*, 15757–15761.

[33] Y. Yao, B. Kou, Y. Peng, Z. Wu, L. Li, S. Wang, X. Zhang, X. Liu, J. Luo, *Chemical Communications* **2020**, *56*, 3206–3209.

[34] M. K. Jana, S. M. Janke, D. J. Dirkes, S. Dovletgeldi, C. Liu, X. Qin, K. Gundogdu, W. You, V. Blum, D. B. Mitzi, *Journal of the American Chemical Society* **2019**, *141*, 7955–7964.

[35] F. Zhang, D. H. Kim, H. Lu, J.-S. Park, B. W. Larson, J. Hu, L. Gao, C. Xiao, O. G. Reid, X. Chen, et al., *Journal of the American Chemical Society* **2019**, *141*, 5972–5979.

[36] J. Shi, Y. Gao, X. Gao, Y. Zhang, J. Zhang, X. Jing, M. Shao, *Advanced Materials* **2019**, *31*, 1901673.

[37] W. Fu, H. Liu, X. Shi, L. Zuo, X. Li, A. K.-Y. Jen, *Advanced Functional Materials* **2019**, *29*, 1900221.

[38] D. B. Straus, S. Hurtado Parra, N. Iotov, Q. Zhao, M. R. Gau, P. J. Carroll, J. M. Kikkawa, C. R. Kagan, *ACS nano* **2020**, *14*, 3621–3629.

[39] Y. Chen, Y. Sun, J. Peng, J. Tang, K. Zheng, Z. Liang, *Advanced Materials* **2018**, *30*, 1703487.

[40] R. G. Pearson, *Journal of the American Chemical Society* **1969**, *91*, 4947–4955.

[41] J. A. McMillan, *Journal of Inorganic and Nuclear Chemistry* **1960**, *13*, 28–31.

[42] D. B. Mitzi, *Inorganic chemistry* **2000**, *39*, 6107–6113.

[43] L.-Y. Bi, Y.-Q. Hu, M.-Q. Li, T.-L. Hu, H.-L. Zhang, X.-T. Yin, W.-X. Que, M. S. Lassoued, Y.-Z. Zheng, *Journal of Materials Chemistry A* **2019**, *7*, 19662–19667.

[44] D. Fu, S. Wu, Y. Liu, Y. Yao, Y. He, X.-M. Zhang, *Inorganic Chemistry Frontiers* **2021**, *8*, 3576–3580.

[45] X. Li, B. Traore, M. Kepenekian, L. Li, C. C. Stoumpos, P. Guo, J. Even, C. Katan, M. G. Kanatzidis, *Chemistry of Materials* **2021**, *33*, 6206–6216.

[46] Z. Xu, H. Wu, D. Li, W. Wu, L. Li, J. Luo, *Journal of Materials Chemistry C* **2021**, *9*, 13157–13161.

[47] M. S. Lassoued, L.-Y. Bi, Z. Wu, G. Zhou, Y.-Z. Zheng, *Journal of Materials Chemistry C* **2020**, *8*, 5349–5354.

[48] Y. Zhao, M. Dong, J. Feng, J. Zhao, Y. Guo, Y. Fu, H. Gao, J. Yang, L. Jiang, Y. Wu, *Advanced Optical Materials* **2022**, *10*, 2102227.

[49] F. Schmitz, J. Horn, N. Dengo, A. E. Sedykh, J. Becker, E. Maiworm, P. Bélteky, A. Kukovecz, S. Gross, F. Lamberti, et al., *Chemistry of Materials* **2021**, *33*, 4688–4700.

[50] E. Brandes, W. Möller, M. Molnárné, T. Schendler, V. Schröder, *Sicherheitstechnische Kenngrößen. 1. Brennbare Flüssigkeiten und Gase*, Wirtschaftsverlag NW, Verlag für neue Wissenschaft, **2003**.

[51] J. Su, T. Mou, J. Wen, B. Wang, *The Journal of Physical Chemistry C* **2020**, *124*, 5371–5377.

[52] P. J. Hasnip, K. Refson, M. I. Probert, J. R. Yates, S. J. Clark, C. J. Pickard, *Philosophical Transactions of the Royal Society A: Mathematical Physical and Engineering Sciences* **2014**, *372*, 20130270.

[53] C. Liu, W. Huhn, K.-Z. Du, A. Vazquez-Mayagoitia, D. Dirkes, W. You, Y. Kanai, D. B. Mitzi, V. Blum, *Physical Review Letters* **2018**, *121*, 146401.

[54] P. Kubelka, F. Munk, *Z. Tech. Phys* **1931**, *12*, 259–274.

[55] J.-C. Blancon, A. V. Stier, H. Tsai, W. Nie, C. C. Stoumpos, B. Traore, L. Pedesseau, M. Kepenekian, F. Katsutani, G. Noe, et al., *Nature communications* **2018**, *9*, 2254.

[56] A. D. Wright, L. R. Buizza, K. J. Savill, G. Longo, H. J. Snaith, M. B. Johnston, L. M. Herz, *The Journal of Physical Chemistry Letters* **2021**, *12*, 3352–3360.

[57] R.-I. Biega, M. R. Filip, L. Leppert, J. B. Neaton, *The journal of physical chemistry letters* **2021**, *12*, 2057–2063.

[58] R. Kentsch, M. Scholz, J. Horn, D. Schlettwein, K. Oum, T. Lenzer, *The Journal of Physical Chemistry C* **2018**, *122*, 25940–25947.

[59] T. Hu, M. D. Smith, E. R. Dohner, M.-J. Sher, X. Wu, M. T. Trinh, A. Fisher, J. Corbett, X.-Y. Zhu, H. I. Karunadasa, et al., *The journal of physical chemistry letters* **2016**, *7*, 2258–2263.

[60] J. A. Steele, P. Puech, M. Keshavarz, R. Yang, S. Banerjee, E. Debroye, C. W. Kim, H. Yuan, N. H. Heo, J. Vanacken, et al., *ACS nano* **2018**, *12*, 8081–8090.

[61] A. D. Wright, C. Verdi, R. L. Milot, G. E. Eperon, M. A. Pérez-Osorio, H. J. Snaith, F. Giustino, M. B. Johnston, L. M. Herz, *Nature communications* **2016**, *7*, 11755.

[62] N. K. Noel, S. D. Stranks, A. Abate, C. Wehrenfennig, S. Guarnera, A.-A. Haghighirad, A. Sadhanala, G. E. Eperon, S. K. Pathak, M. B. Johnston, et al., *Energy & Environmental Science* **2014**, *7*, 3061–3068.

[63] M. Righetto, D. Giovanni, S. S. Lim, T. C. Sum, *Applied Physics Reviews* **2021**, *8*.

[64] L. R. Buizza, A. D. Wright, G. Longo, H. C. Sansom, C. Q. Xia, M. J. Rosseinsky, M. B. Johnston, H. J. Snaith, L. M. Herz, *ACS Energy Letters* **2021**, *6*, 1729–1739.

[65] H. Hempel, T. J. Savenjie, M. Stolterfoht, J. Neu, M. Failla, V. C. Paingad, P. Kužel, E. J. Heilweil, J. A. Spies, M. Schleuning, et al., *Advanced Energy Materials* **2022**, *12*, 2102776.

[66] D. H. Fabini, R. Seshadri, M. G. Kanatzidis, *MRS Bulletin* **2020**, *45*, 467–477.

[67] Z. Xiao, W. Meng, J. Wang, D. B. Mitzi, Y. Yan, *Materials Horizons* **2017**, *4*, 206–216.

[68] M. Li, S. Han, B. Teng, Y. Li, Y. Liu, X. Liu, J. Luo, M. Hong, Z. Sun, *Advanced Optical Materials* **2020**, *8*, 2000149.

[69] L. Zhu, D. Liu, J. Wang, N. Wang, *The Journal of Physical Chemistry Letters* **2020**, *11*, 8502–8510.

[70] C. Chen, L. Gao, W. Gao, C. Ge, X. Du, Z. Li, Y. Yang, G. Niu, J. Tang, *Nature communications* **2019**, *10*, 1927.

[71] D. Li, X. Liu, W. Wu, Y. Peng, S. Zhao, L. Li, M. Hong, J. Luo, *Angewandte Chemie* **2021**, *133*, 8496–8499.

[72] P. Giannozzi, S. Baroni, N. Bonini, M. Calandra, R. Car, C. Cavazzoni, D. Ceresoli, G. L. Chiarotti, M. Cococcioni, I. Dabo, et al., *Journal of physics: Condensed matter* **2009**, *21*, 395502.

[73] J. P. Perdew, K. Burke, M. Ernzerhof, *Physical review letters* **1996**, *77*, 3865.

[74] A. Tkatchenko, M. Scheffler, *Physical review letters* **2009**, *102*, 073005.

[75] R. L. Hoye, P. Schulz, L. T. Schelhas, A. M. Holder, K. H. Stone, J. D. Perkins, D. Vigil-Fowler, S. Siol, D. O. Scanlon, A. Zakutayev, et al., *Chemistry of Materials* **2017**, *29*, 1964–1988.

[76] T. Seifert, S. Jaiswal, U. Martens, J. Hannegan, L. Braun, P. Maldonado, F. Freimuth, A. Kronenberg, J. Henrizi, I. Radu, et al., *Nature photonics* **2016**, *10*, 483–488.

[77] R. J. Baker, P. E. Colavita, D. M. Murphy, J. A. Platts, J. D. Wallis, *The Journal of Physical Chemistry A* **2012**, *116*, 1435–1444.

[78] K. Kikuchi, Y. Takeoka, M. Rikukawa, K. Sanui, *Current Applied Physics* **2004**, *4*, 599–602.

[79] J. Hu, I. W. Oswald, S. J. Stuard, M. M. Nahid, N. Zhou, O. F. Williams, Z. Guo, L. Yan, H. Hu, Z. Chen, et al., *Nature communications* **2019**, *10*, 1276.

[80] M. Frisch, G. Trucks, H. Schlegel, G. Scuseria, M. Robb, J. Cheeseman, G. Scalmani, V. Barone, G. Petersson, H. Nakatsuji, et al., *Wallingford CT* **2016**, *421*.

[81] A. Altomare, C. Cuocci, C. Giacovazzo, A. Moliterni, R. Rizzi, N. Corriero, A. Falcicchio, *Journal of Applied Crystallography* **2013**, *46*, 1231–1235.

[82] B. L. Henke, E. M. Gullikson, J. C. Davis, *Atomic data and nuclear data tables* **1993**, *54*, 181–342.

[83] J.-P. Yang, M. Meissner, T. Yamaguchi, X.-Y. Zhang, T. Ueba, L.-W. Cheng, S. Ideta, K. Tanaka, X.-H. Zeng, N. Ueno, et al., *Solar RRL* **2018**, *2*, 1800132.

[84] B. M. Klahr, T. W. Hamann, *The Journal of Physical Chemistry C* **2011**, *115*, 8393–8399.

[85] C. Wehrenfennig, G. E. Eperon, M. B. Johnston, H. J. Snaith, L. M. Herz, *Advanced materials* **2014**, *26*, 1584–1589.

[86] H. J. Joyce, J. L. Boland, C. L. Davies, S. A. Baig, M. B. Johnston, *Semiconductor Science and Technology* **2016**, *31*, 103003.

Chapter 3

2D/3D Hybrid $Cs_2AgBiBr_6$ Double Perovskite Solar Cells: Improved Energy Level Alignment for Higher Contact-Selectivity and Large Open Circuit Voltage

This chapter is based on the following publication:

M. T. Sirtl, R. Hooijer, M. Armer, F. G. Ebadi, M. Mohammadi, C. Maheu, A. Weis, B. T. van Gorkom, S. Häringer, R. A. J. Janssen, T. Mayer, V. Dyakonov, W. Tress, and T. Bein, Advanced Energy Materials **2022**, 12, 2103215.

The following work was performed by R. Hooijer: conception (with M.T. Sirtl), synthesis of 2D and 2D/3D perovskite samples, XRD and GIWAXS measurents and analysis, writing and editing the manuscript for final submission.

3.1 Abstract

Since their introduction in 2017, the efficiency of lead-free halide perovskite solar cells based on $Cs_2AgBiBr_6$ has not exceeded 3%. The limiting bottlenecks are attributed to a low electron diffusion length, self-trapping events and poor selectivity of the contacts, leading to large non-radiative V_{oc} losses. Here, 2D/3D hybrid double perovskites are introduced for the first time, using phenethyl ammonium as the constituting cation. The resulting solar cells show an increased efficiency of up to 2.5% for the champion cells and 2.03% on average, marking an improvement by 10% compared to the 3D reference on mesoporous TiO_2. The effect is mainly due to a V_{oc} improvement by up to 70 mV on average, yielding a maximum V_{oc} of 1.18 V using different concentrations of phenethylammonium bromide. While these are among the highest reported V_{oc} values for $Cs_2AgBiBr_6$ solar cells, the effect is attributed to a change in recombination behavior within the full device and a better selectivity at the interface toward the hole transporting material (HTM). This explanation is supported by voltage-dependent external quantum efficiency, as well as photoelectron spectroscopy, revealing a better energy level alignment and thus a better hole-extraction and improved electron blocking at the HTM interface.

3.2 Introduction

Halide double perovskites have recently attracted much interest in the photovoltaic community as they are seen as a possibility to solve several issues arising from their lead-based cousins featuring excellent optoelectronic properties.[1] Changing the simple perovskite ABX_3 structure to a $2 \times 2 \times 2$ supercell, halide double perovskites have the general formula $A_2B^IB^{III}X_6$ where two bivalent cations B^{2+} are exchanged by a combination of one monovalent cation B^+ (e.g., Cu^+, Ag^+, Au^+, In^+) and one trivalent cation B^{3+} (e.g., Bi^{3+}, Sb^{3+}).[2] Several theoretical calculations have been performed on this structural motif, providing a large variety of proposed thermodynamically stable compounds of which $Cs_2AgBiBr_6$ proved to be the most promising material so far.[3–7] $Cs_2AgBiBr_6$ was characterized first by McClure et al.[8] and, being long-term stable at ambient conditions and providing alternative element combinations that exclude toxic elements,[2] this material was moved into the focus of research, especially due to promising optoelectronic properties of single crystals (for instance a charge carrier lifetime of >500 ns)[9,10] and the

possibility to solution-process the material for thin films synthesis.[11]

After the first report on solar cells using $Cs_2AgBiBr_6$ as an active layer in 2017,[11] several groups reported solar cells implementing different architectures and contact layers. In order to optimize the optoelectronic properties and charge extraction behavior, the stoichiometric precursor ratio,[12,13] organic interface layers,[14] charge transport layers[15–18] and n-i-p, as well as p-i-n[19] structures have been investigated. Ultimately, these efforts led to power conversion efficiencies (PCE) that did not exceed 3.11% (or 4.23% using additional organic dyes) within several years of research.[16,20] Hence, present research activities aim at the investigation of the intrinsic bottlenecks of this material to find ways to overcome them and to push the solar cell efficiency further. While the energy level alignment between the valence band maximum (VBM) of the double perovskite and the highest occupied molecular orbital (HOMO) energy level of the commonly used hole-transport materials (HTM) is non-optimal for solar cell functions,[15] the position of the conduction band minimum (CBM) leads to a low selectivity of the contacts within the full solar cell.[17] Moreover, a short electron diffusion length in deposited thin film structures,[21] ultra-fast self-trapping of free charge carriers[22] and large non-radiative V_{oc} losses have been found,[17] while it remains unclear whether a large exciton binding energy is hampering the solar cell efficiency[23,24] and how the PL signal of the thin films can be explained.[13,17,25]

Another challenge is the rather large and indirect bandgap of 1.9-2.3 eV,[13,26–28] especially since the stabilization of the related double perovskite Cs_2AgBiI_6 has not yet been realized due to the low thermodynamic stability of this compound.[29] While tuning of the absorption onset is pursued by using additives and alloying,[30–34] as well as high pressure modification,[35] a promising pathway to stabilize iodine based Ag-Bi double perovskites is the introduction of a large A-site cation in order to form 2D double perovskites, as first introduced by Connor et al. in 2018 using bromide.[36] Following this procedure, Jana et al. synthesized the first iodine based Ag-Bi double perovskite by using an oligothiophene based double cation 5,5'-diylbis(aminoethyl)-[2,2'-bithiophene]) to stabilize $(AE2T)_2AgBiI_8$, which expressed a reduced and direct bandgap of 2 eV.[37] Going further, several other groups managed to stabilize the iodide phase using different spacer cations.[38,39] Due to the insulating properties of large organic cations, however, experience with lead-based perovskites shows a reduced efficiency of the pure 2D structures compared with their pure 3D counterpart.[40,41] To overcome this issue, either the formation of a quasi 2D perovskite ($n \geq 2$) can be achieved by using small amounts of a small A^+ cation to partially substitute the large cation, or the formation of a hybrid perovskite can be pursued, using a 3D layer and combining it with a very thin 2D layer on top.[40,42–45]

In this work, we introduce the first 2D/3D hybrid double perovskite to date. By us-

ing the simple aromatic phenethyl ammonium bromide (PEABr) salt in 2-propanol, we show the formation of a $(PEA)_4AgBiBr_8$ layer on top of a 3D $Cs_2AgBiBr_6$ thin film. Moreover, we achieved the formation of a pure 2D $(PEA)_4AgBiBr_8$ thin film that shows excellent coverage and uniformity to determine the optical properties where we calculated the bandgap to be direct. Using an ultra-thin $(PEA)_4AgBiBr_8$ layer on top of the 3D film, we show that the efficiency of the resulting solar cell is boosted from 2.1% to 2.5%, which we assigned to a large increase of the V_{oc} and J_{sc} both for the champion cells and the cells showing average performance. Especially the V_{oc} values are the highest so far reported for this material, reaching up to 1.18 V. We assign these changes to an increase in the selectivity of the contacts, while the recombination behavior seems to remain the same, and support these findings with voltage dependent external quantum efficiency (EQE) measurements, as well as ultraviolet photoelectron spectroscopy (UPS), X-ray photoelectron spectroscopy (XPS) and photoluminescence measurements (PL). Overall, we show that utilizing 2D/3D hybrid double perovskites offers opportunities to address the issues regarding poor energy level alignment towards the HTM side and to easily fine-tune the contact-selectivity, ultimately boosting the overall solar cell efficiency.

3.3 Results and Discussion

3.3.1 Formation of the Hybrid Phase

In the field of 2D/3D hybrid perovskites, one approach to form such a layer is the deposition of the spacer cation on top of the already formed 3D film. This leads to the formation of a very thin 2D or 2D/3D hybrid top layer.[40,46] In our work, we adapted this approach and prepared the 3D layer first by spincoating the preheated $Cs_2AgBiBr_6$ stock solution on top of preheated glass substrates. This was followed by high temperature annealing (Figure 3.1). After the formation of the 3D film, we introduced the spacer cation by spincoating phenethyl ammonium bromide (PEABr) on top, which is well known to form a 2D silver-bismuth perovskite phase.[47–49] We tested the hybrid perovskite formation with different PEABr concentrations in isopropylalcohol/2-propanol (IPA) ranging from 0.01 mol L^{-1} (0.01 M) to 0.1 M.

The insertion of long cations into a 3D perovskite leads to the formation of 2D phases with an increased lattice constant, which can be observed by the emergence of small angle XRD reflections.[36] To investigate the formation of a 2D layer on top of our 3D films, we performed both X-ray diffraction (XRD) in Bragg-Brentano geometry and grazing incidence wide angle X-ray scattering (GIWAXS) and compared the obtained patterns of the hybrid films (c(PEABr) = 0.1, 0.06, and 0.01 M) with the results for pure 3D

films and the theoretical XRD pattern of the n = 1 $(PEA)_4AgBiBr_8$ structure (obtained from ref.[47]) as shown in Figure 3.2 for the small angle region between 2 and 12° 2Θ. Figure 3.2a confirms the formation of the $(PEA)_4AgBiBr_8$ 2D-phase upon spincoating

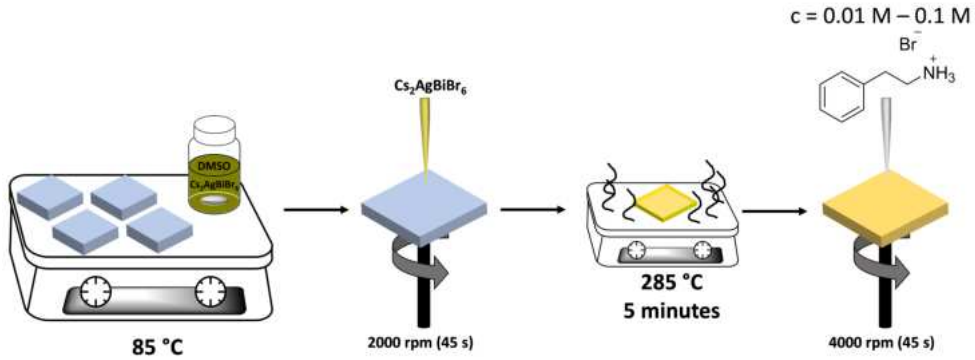

Figure 3.1: Schematic synthesis scheme for the 2D/3D hybrid double perovskite thin films. In a first step, we deposited the 3D double perovskite thin film by spincoating a preheated solution (85 °C) on a preheated substrate (85 °C) at 2000 rpm. After thermal annealing at 285 °C for 5 min, the spacer cation was spincoated on top of the 3D film at various concentrations (in IPA at 4000 rpm) to form a 2D/3D hybrid double perovskite film on top of the pure 3D layer. After addition of the spacer cation, no further annealing was applied.

the spacer cation on top of the pure 3D films for PEABr concentrations $\geq$0.06 M. The comparison of the XRD pattern of the hybrid film with the calculated pattern of the pure 2D $(PEA)_4AgBiBr_8$ shows the formation of the characteristic reflection at low angles of 5.5° 2θ. However, the formation of this reflection cannot be observed using the lowest PEABr concentrations of 0.01 M. This suggests the formation of a rather thin 2D layer for low PEABr concentrations, which we confirmed through further GIWAXS measurements. Interestingly, one can see the formation of a second phase of the 2D perovskite at even smaller angles ($\approx$4.5° 2θ). This can be related to the formation of 2D layers with n values bigger than one, which leads to a further increase of one unit cell dimension and hence to a shift of the reflection toward smaller angles. The full patterns in FigureSI 3.7, Supporting Information show that all films are phase-pure with respect to undesired side phases such as AgBr, CsBr, or $BiBr_3$, as well as $Cs_3Bi_2Br_9$ and $(PEA)_3Bi_2Br_9$. The only additional reflections visible are gold-related peaks, which is expected as the XRD patterns were recorded on full solar cells.[50] The GIWAXS measurements confirm the findings from the XRD measurements. Thin films treated with higher concentrated PEABr solutions (Figure 3.2b,c) show the formation of two peaks at low scattering vectors q compared to the 3D reference (Figure 3.2e), proving the presence of a low-dimensional phase. Using the same integration time, these reflections cannot be found for thin films treated with very low concentrated PEABr solutions (0.01 M, Figure 3.2d). However, by increasing the integration time by the factor 6, reflections at very small scattering vectors appear as shown in Figure 3.8, Supporting Information, demonstrating the formation of different

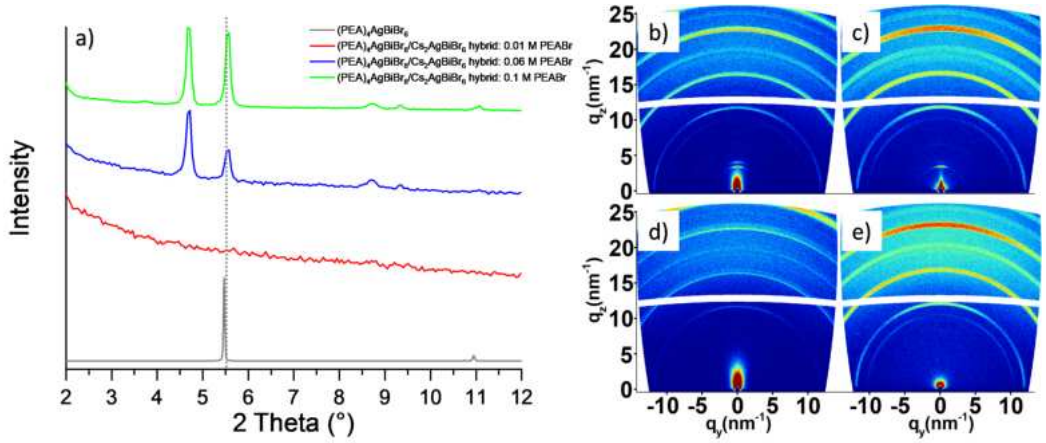

Figure 3.2: XRD pattern and GIWAXS data of the investigated thin films. a) Bragg-Brentano XRD patterns of modified thin films between 2 and 12° 2θ. Green (0.1 m PEABr), blue (0.06 m PEABr) and red lines (0.01 m PEABr) show the hybrid thin films while the grey line shows the theoretical pattern of the pure 2D $(PEA)_4AgBiBr_8$ double perovskite. The dashed grey line was added as a guide for the eye to emphasize the low-angle reflection. Panels (b)–(e) show the GIWAXS detector images of the b) 0.1 m, c) 0.06 m, and d) 0.01 m hybrid, as well as the e) 3D reference. The films were generated by spincoating the precursor solution on top of an FTO/c-TiO_2/mp-TiO_2 scaffold to simulate the same crystallization behavior utilized for the construction of solar cells.

2D phases. To further investigate the ultrathin 2D layers, SEM top-view images were recorded using the through-lens (TLD) and circular backscatter detector (CBS) as shown in the Supporting Information and Figure 3.3. The images compare the morphology of the above-discussed thin films with the 3D reference and the films obtained by spincoating PEABr solutions with the concentrations 0.1 and 0.01 M.

Figure 3.3 shows a zoom of the images shown in the Supporting Information. The morphology suggests the formation of rather big perovskite crystallites (>1 µm) that stick out from the mp-TiO_2 scaffold, which leads to rather large voids between the respective perovskite crystallites. However, this morphology has been proven to work well in solar cells[11] and the images clearly indicate the formation of a new layer for both PEABr concentrations. While the new layer forms big slabs within the voids of the 3D layer, the formation of this film can be seen from the back-scatter images in Figure 3.3f) also for very low PEABr concentrations. Hence, we were able to confirm the formation of an additional low-dimensional double perovskite layer by spincoating a spacer cation on top of the 3D layer. We will now discuss the solar cells comprising this material as an active layer.

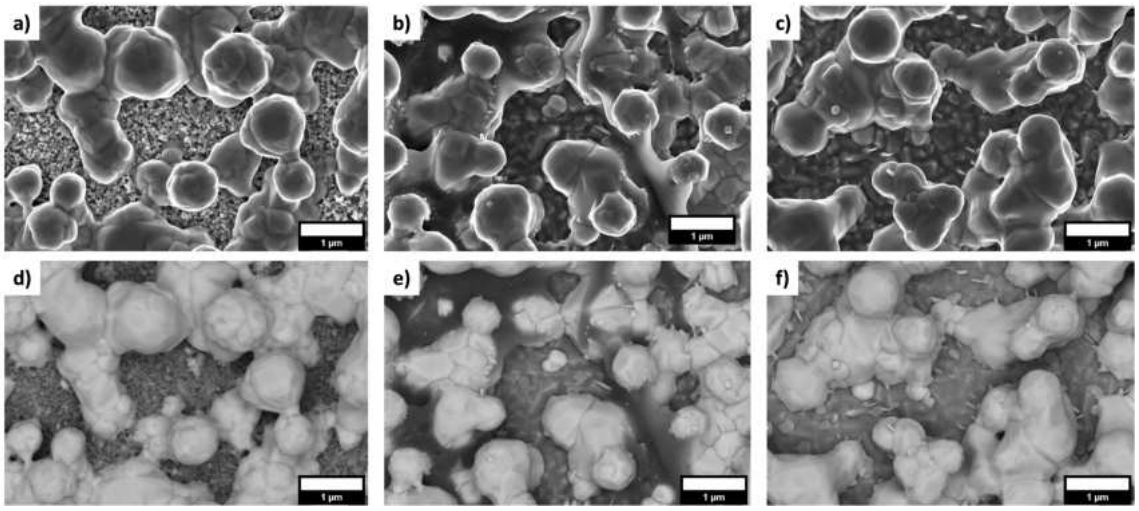

Figure 3.3: SEM top view images of the a,d) 3D reference, b,e) the 0.1 M hybrid, and c,f) the 0.01 M hybrid perovskite materials. The images (a)–(c) show the SEM top views obtained with a through-lens (TLD) and the images (d)–(f) show the images obtained with a circular backscatter detector (CBS). A smaller magnification can be found in the Supporting Information.

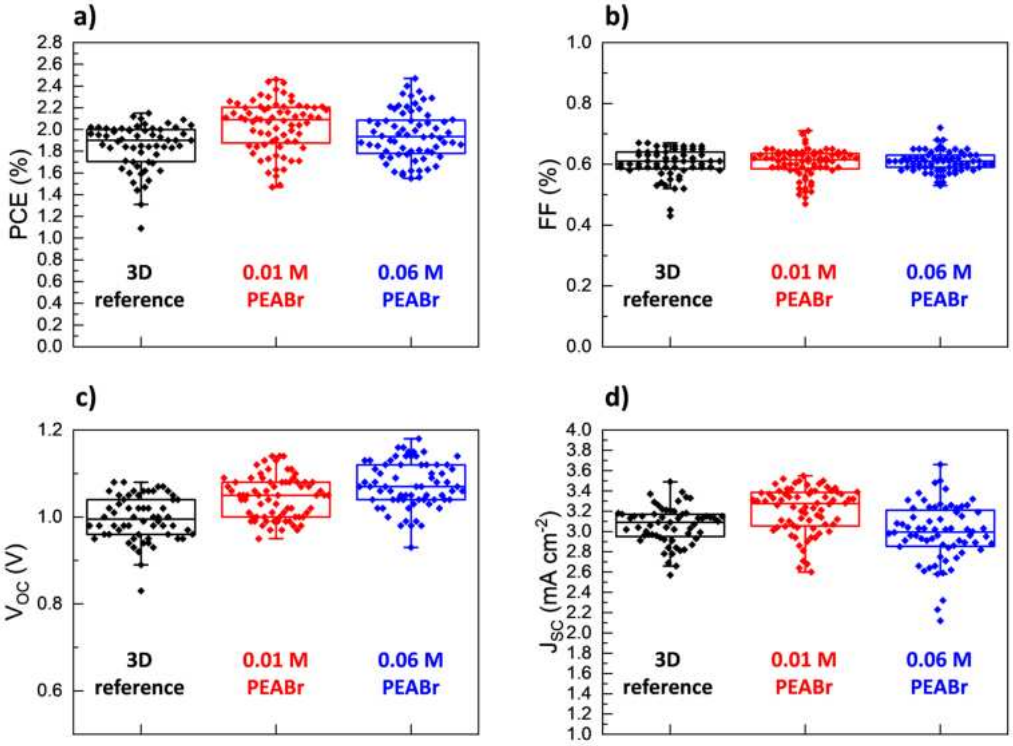

Figure 3.4: Box plots of the solar cell parameters of the investigated cells: black: 3D reference, red: 0.01 M hybrid, blue: 0.06 M hybrid. Panel (a) shows the power conversion efficiency (PCE) of the solar cells in %, panel (b) shows the fill factor (FF) of the solar cells, panel (c) shows the open circuit voltage (V_{oc}) in V and panel (d) shows the short circuit current (J_{sc}) in mA cm^{-2}. In panel (c), dashed horizontal lines were added as a guide to the eye to show the maximum achieved V_{oc} values in this work (color coded accordingly, the numbers show the actual values).

3.3.2 Solar Cell Performance

In the lead-halide perovskite community, it is well known that the hybridization of 3D films towards a 2D/3D structure can lead to an improvement of the photovoltaic performance of the resulting solar cells. This improvement has been attributed to better interfaces within the solar cells as well as trap passivation, resulting in a significant increase in V_{oc}.[42,45]

$Cs_2AgBiBr_6$ double perovskite solar cells, however, are known to suffer from a rather small electron diffusion length, a fast localization and self-trapping of charge carriers and, more importantly, from rather large non-radiative V_{oc} losses and non-selective contacts.[17,21,22] To investigate the impact of the above discussed lead-free 2D/3D hybrid perovskite, we employed the thin films in solar cells with the architecture FTO/c-TiO_2/mp-TiO_2/$Cs_2AgBiBr_6$/$(PEA)_4AgBiBr_8$/Spiro-OMeTAD/Au. The results are shown in Figure 3.4. Please note that the PEABr concen- trations of 0.01 and 0.06 M were chosen after a screening process, during which the thin films comprising these parameters

were shown to improve the solar cells in comparison to other concentrations and the 3D reference. An exemplary J/V-curve of a 0.1 M device is shown in FigureSI 3.10, Supporting Information, where it is clearly seen that the PCE suffers from large J_{sc} losses as expected with a thicker 2D layer within the solar cell, hampering the charge transfer towards the back electrode. SEM cross-sections can be found in FigureSI 3.11, Supporting Information, together with sketches of the layer-stacks of the investigated solar cells.

The values show a clear improvement of the solar cell efficiency by using 2D/3D hybrid perovskite active layers in the solar cells. The average results show an optimum cation concentration of 0.01 mol L^{-1} PEABr in IPA, as solar cells with this cation-concentration achieve the highest efficiencies, both in the champion and the average values. Solar cells made with 0.06 M PEABr do show a champion cell with 2.5% PCE as well, the average values though are lower compared to the 0.01 M cells.

For both 2D/3D hybrid double perovskite solar cells, maximum PCEs of up to 2.46% (0.01 M PEABr) and 2.47% (0.06 M PEABr) were achieved, which is an improvement of 13% compared to the 3D reference where the champion cell reached up to 2.15% PCE. J/V-curves of high-performance solar cells are shown in FigureSI 3.10, Supporting Information. While the high PCE of almost 2.5% is highly reproducible for the low concentrated (0.01 M PEABr, in the following called 0.01 M hybrid) hybrid, this value was only achieved once for the higher concentrated (0.06 M PEABr, in the following called 0.06 M hybrid) hybrid. This can be seen in the average values where the 3D reference results in 1.84% with 60 solar cells, while the 0.06 M hybrid shows an improvement to 1.95% with 68 devices. The 0.01 M hybrid double perovskite achieves also on average the highest PCE with 2.03%, which is almost 10% better compared to the 3D reference.

To find the reasons for the increase in efficiency, the different PV parameters need to be investigated. Figure 3.4 shows the different boxplots of the solar cells investigated in this work. While the fill factor only changes for the respective champion cells, it does not have an influence on the average improvement of the solar cells as it has values of 60% for both the 3D reference and the 0.01 M hybrid and only improves to 61% for the 0.06 M hybrid solar cells. The biggest changes in the photovoltaic (PV) parameters can be found in the open circuit voltage (V_{oc}) and the short circuit current (J_{sc}). For both parameters, an improvement is observed for the 0.01 M hybrid compared to the 3D reference, both for the champion device and the average of all devices. On average, the 0.01 M hybrid solar cells express an improvement in their V_{oc} by 60 mV from 0.99 to 1.05 V, which translates to 6%. For the 0.06 M hybrid, the V_{oc} improvement is even larger with 80 mV, leading to an average value of 1.07 V. For the J_{sc}, an improvement can only be found for the 0.01 M hybrid. Here, the average value increases by 5% from 3.06 mA cm^{-2} for the 3D reference to 3.21 mA cm^{-2} for the hybrid cell. For the 0.06 M hybrid, the average J_{sc} is

reduced compared to the 3D reference with a value of 2.99 mA cm^{-2}. These effects are well within expectation and can be explained with the nature of the 2D perovskite. The addition of a 2D layer on top of a 3D layer is beneficial for the V_{oc} of the perovskite solar cells as already reported for lead-based perovskites.[40,42,45] Yet, a 2D layer is defined by its large organic cation, here a phenethyl ammonium cation. This leads to an insulating barrier on top of the 3D layer. While a thick 2D layer leads to a large improvement of the V_{oc}, it hampers charge transport from the 3D layer towards the back electrode. The thinner this layer becomes, the more charge carriers can travel through this layer, hence the J_{sc} is improved. Another reason for the improvement of the J_{sc} can be found in the structure of the formed 2D perovskite: While for the 0.06 M hybrid, two phases with different n-values are formed, the only reflection found for the hybrids with concentrations of 0.01 M is for a phase with an n value >1. This translates to thicker octahedral layers in between the insulating PEA-layers and thus only a few insulating layers.

To further understand the improvement of the solar cells, additional measurements were performed.

3.3.3 Photoluminescence and Light Intensity Dependent V_{oc}

For lead-based 2D/3D hybrid perovskites, the corresponding reports discuss the improvement in the PCE and especially the V_{oc} with an increase in the signal of steady state photoluminescence, as well as an increase in the charge carrier lifetime obtained using time-resolved photoluminescence (TRPL).[40,42,45] Hence, we performed the same set of experiments as shown in Figure 3.5.

In contrast to lead-based perovskites, we did not observe any significant changes in the charge carrier behavior, both in the steady state and time resolved photoluminescence. This behavior is counter-intuitive, as we would expect a change in the recombination behavior of our thin films, especially the hybrids, following the V_{oc} trend from the solar cells. First, we measured the photoluminescence quantum yield (PLQY) of our thin films.

A small increase of the photoluminescence (PL) signal can be found (Figure 3.5a) for the 0.01 M hybrid, while the PL signal of the 0.06 M hybrid is almost double in intensity compared to the 3D film. To exclude measurement artifacts, every film was measured several times at several different spots. PLQY values show an improvement of the thin films from ≈0.36% for the 3D reference up to 0.61% for the 0.06 M hybrid, while the 0.01 M hybrid lies at around 0.44%. While all of these values are the highest so far reported for this material, they match well with the observed trend of the V_{oc} values of the solar cells.[21] Yet, the PLQY values are only sufficient to explain an increase of the V_{oc} by 20 mV in case of the 0.06 M hybrid films.[51] This shows that the dominant recombination regime might not change significantly, as no significant change in the radiative

recombination yield was observed (as from the changes of V_{oc}, we would expect an increase of the signal by around two orders of magnitude). However, we do not claim that no passivation effect occurs at all. To investigate this further, we additionally measured fluence dependent steady state PL (Figure 3.5c) of the thin films on glass, comparing the 0.06 M hybrid with the 3D reference (as only for the 0.06 M hybrid, bigger changes are visible so far). While the slopes in the fluence-dependent PL do change going from lower to higher laser intensity, this is expected from our previous work and can be explained as a shift from trap-assisted recombination towards excitonic recombination as at higher laser intensity, the ratio of free charge carriers to excitons is smaller compared to lower light intensity.[13,52] Among the different architectures, however, the data points do not show different values. This suggests that the dominating recombination behavior of the 2D/3D hybrid films is the same as for the 3D reference,[53] while all films have a change of the recombination regime going from low to high laser intensities (Figure 3.5b), which again indicates the formation of a hybrid phase instead of a simple passivation effect. Time resolved measurements (Figure 3.5c) do not show significant changes either, detecting a charge carrier lifetime of 331 ns for the 3D reference up to 352 ns for the 0.01 M hybrid and 356 ns for the 0.06 M hybrid, respectively. Hence, we can conclude that the lifetime of the charge carriers does not contribute significantly to the observed changes of the V_{oc}. As an increased V_{oc} not only indicates changed recombination behavior in the pristine film, but can also be linked to better contact selectivity leading to a reduction of charge carrier recombination rates at the interface,[54,55] light intensity dependent V_{oc} measurements were performed as they are a valuable tool to determine the ideality factor of the diode that represents a solar cell. While fluence dependent steady state PL gives information about the recombination regime within the pristine film, the ideality factor does the same within the full device where n = 1 should indicate a perfect bimolecular recombination and n = 2 indicates a perfect trap assisted recombination. The ideality factor can be deduced using the following Equation (3.1):[56]

$$V_{oc} \approx n \times \frac{kT}{e} \times ln(I) \tag{3.1}$$

where kT/e has a value of 0.02527 V at room temperature.

However, if the recombination behavior is dominated by interfacial recombination, the ideality factor may be equal to 1 as well and eventually reach values below 1.[56,57] In this case, the initial V_{oc} of the respective solar cell should be <1 V, which is not the case in this work.

Figure 3.5d shows the graphs obtained from measuring the three different solar cells, the values of the ideality factors obtained from the linear fit of the values in a ln plot (FigureSI 3.12, Supporting Information) are written in the figure. Contrary to the fluence-

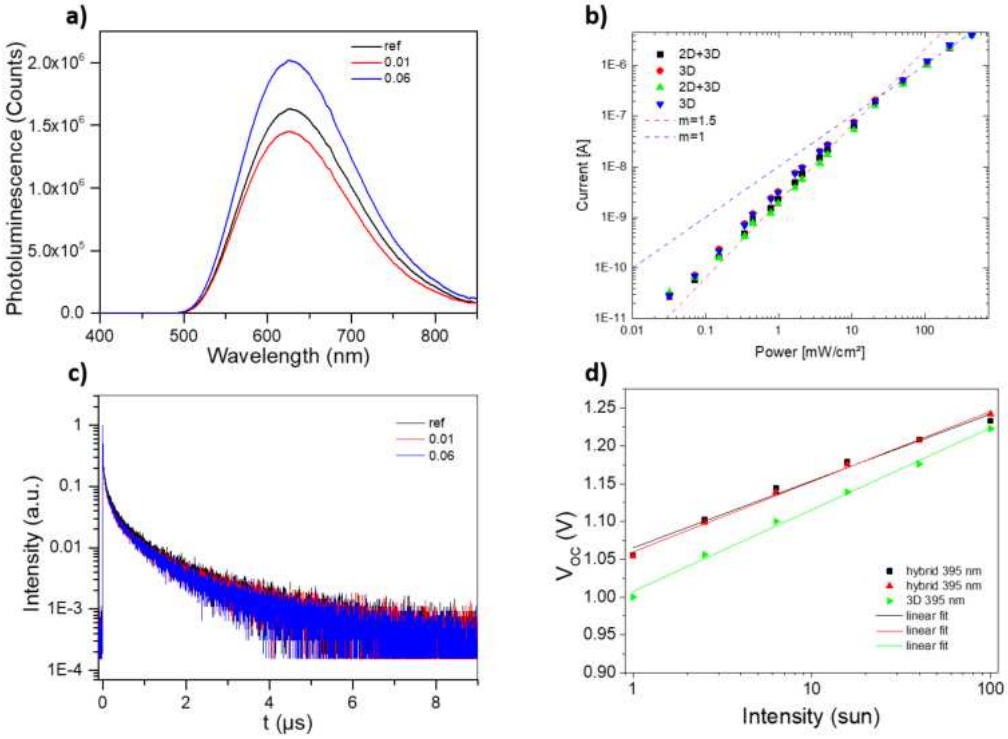

Figure 3.5: a) Steady state PL of the different films spincoated on glass, b) the fluence-dependent PL with m giving the slopes at different incident laser power, c) the PL decay of the different films. d) Shows the light intensity dependent VOC measurements with the respective ideality factor given as n-value. All panels have the same color-coding: black: 3D reference, red: 0.01 m hybrid, blue: 0.06 m hybrid.

dependent PL measurements, the devices show in fact a change in the recombination behavior. While the 3D reference expresses an ideality factor of 1.86 at 395 nm excitation, indicating a mere trap assisted recombination behavior, the hybrid solar cells show values of 1.52 (0.01 M) and 1.59 (0.06 M), respectively. This could indicate a change of the recombination behavior towards both perfect bimolecular, or interfacial recombination.[56,57] As discussed above, however, a dominant interfacial recombination process would be associated with a rather low V_{oc} below 1 V. This is not the case in this work with average values of 1.07 and 1.05 V for 0.06 and 0.01 M cells respectively. Hence, the results indicate that for the 2D/3D hybrids, the recombination behavior is less dominated by interfacial and trap assisted recombination than com- pared to the 3D reference. This indicates a large improvement of the selectivity of the contacts, which we recently determined as one of the major bottlenecks.[17] The improvement of the charge carrier recombination in the full devices is further evidenced by EL EQE measurements that we performed using cells comprising the 3D reference and the 0.01 M hybrid solar cells. Here, an improvement of the EL EQE from 4×10^{-8} to 10^{-7} at the start of the measurement and from 1.5×10^{-8} to 10^{-7} after 170 s does show an increase of almost one order of magnitude for the 2D/3D hybrid solar cell (FigureSI 3.13, Supporting Informa-

tion). While the value of the 3D reference is comparable to that from ref.,[17] the 0.01 M cell indicates a significant improvement of the recombination behavior and thus explains a reduction of non-radiative V_{oc} losses (difference between radiative V_{oc} limit ($V_{oc,rad}$) and the V_{oc}) by up to 50 mV according to Equation (3.2):[17,27,28,58]

$$\Delta V_{oc} = V_{oc,rad} - V_{oc} = -\frac{kT}{q} ln(EQE_{EL}) \tag{3.2}$$

where kT/q is the thermal voltage.

Moreover, the measurement shows an improvement of the stability of the hybrid compared to the 3D reference. This is also evidenced by MPP tracking performed over a time-span of 3600 s. While both solar cells show a rather high stability of over 90%, the 0.01 M cell has an improved value of maintaining 99.6% of the initial PCE compared to the 3D reference (98.5%, FigureSI 3.13, Supporting Information).

To further investigate the origin of the higher selectivity and the improved J_{sc}, we proceeded with quantum efficiency measurements and band-energy determination.

3.3.4 PV Quantum Efficiency and Energy Level Alignment

The 0.06 M hybrid and the 0.01 M hybrid show very comparable behavior regarding the optoelectronic measurements, especially the light intensity dependent V_{oc} data. The 0.01 M films, however, show superior efficiency in solar cells, resulting from an improvement in both the J_{sc} and the V_{oc}. Hence, we will continue to discuss only the 0.01 M hybrid in the remainder of this paper.

Solar cells comprising the 0.01 M hybrid show an improved J_{sc} compared to the 3D reference (from 3.06 to 3.21 mA cm^{-2} on average). This can also be seen in the EQE spectra in Figure 3.6a. Here, the cells measured with the 0.01 M hybrid show a higher EQE compared to the 3D reference. Please note that we chose pixels (solar cell devices) for this measurement with a PCE well within the average of the solar cells described above. The biggest difference in the EQE is observable for the peak at ≈450 nm, where the absorption is the highest (dashed lines in Figure 3.6c,d). Here, the EQE is at 50% for the 2D/3D hybrid, while the EQE of the 3D reference only reaches 40%. Overall, an average increase of 10% in the EQE can be observed for the 2D/3D hybrid perovskite solar cells, which directly leads to an increased integrated photocurrent by almost 25% (2.3 to ≈2.9 mA cm^{-2}) which matches well with the obtained J_{sc} values from the solar cells (2.6 mA cm^{-2} for the 3D reference and 2.8 mA cm^{-2} for the hybrid). It confirms the trend visible from average values of all measured devices as shown in the section above. To further investigate the trap density and recombination behavior of the solar cells, subgap-EQE measurements were performed (Figure 3.6b). The spectra show no

significant change in the trap density, observable by the signal in the spectral region below 2 eV. In fact, a slight increase in signal is observed for the 2D/3D hybrid double perovskite solar cells. This indicates that the hybrid cells express a slightly higher amount of gap-states and deep tails and confirms that no trap passivation occurred by hybridizing the 3D perovskite. It supports the finding that the boost in V_{oc} does not come from simple trap passivation.

In our recent publication, we observed a change of sign of the EQE by measuring the spectra as a function of the applied voltage, which was indicated by a large drop of the EQE at voltages >0.9 V.[17] While the bias causing this effect is much higher compared to our last work, we do see a very similar effect with the 3D solar cells: At voltages >1.00 V, we observe a drop in the EQE before it rises again strongly up to 80% (at 1.05 V external bias). The higher external voltage required compared to our recent report is well within the increase in the V_{oc} (0.9 V on average in ref.[17] compared to 0.99 V on average in the present work) and indicates either a larger built-in potential of 1 V that could be caused by the choice of Spiro-OMeTAD as HTM instead of P3HT. The first has a higher LUMO level compared to the latter, allowing for a better electron blocking and therefore a better overall selectivity.[59] In the present work, we again observe not only an increase of the absolute EQE values, but also a change in the shape. While the shape of the EQE spectra below 1 V external bias exactly follows the absorption peaks of the UV-vis spectrum (grey dashed line in Figure 3.6c), this shape is inverted after applying voltages above 1.00 V. Now, the EQE maxima are located at the spectral range of the absorption minima, which indicates that the charge carriers created more homogeneously in the perovskite layer result in a higher photocurrent. The high EQE value can only be explained by a photomultiplication effect due to a photoenhanced forward current. Given the well-aligned conduction band of TiO_2 and perovskites, this current is most likely carried by electrons, which recombine with holes on the HTM. This further confirms the findings of our recent work that we indeed have rather non-selective contacts and thus reduce the charge carrier collection.[17]

For the 2D/3D hybrid perovskite, no such change in the EQE is observed, at least for voltages up to 1.20 V. Here, the values of the EQE steadily decrease, as also observed for the 3D reference. Upon reaching voltages >1.25 V, the solar cell rapidly degrades and the measured values are not reliable. To make sure that the trend below 1.25 V is reproducible, we remeasured the EQE at 0 and 1.1 V and observed only slight changes in the EQE. The absence of the photocurrent inversion for the 2D/3D hybrid double perovskite solar cells indicates a large improvement of the selectivity within the solar cell, as not only the V_{oc} of the solar cell is increased (indicating an even larger internal voltage, as well as built-in potential), but also the photocurrent direction shows no change at all, indicating a higher

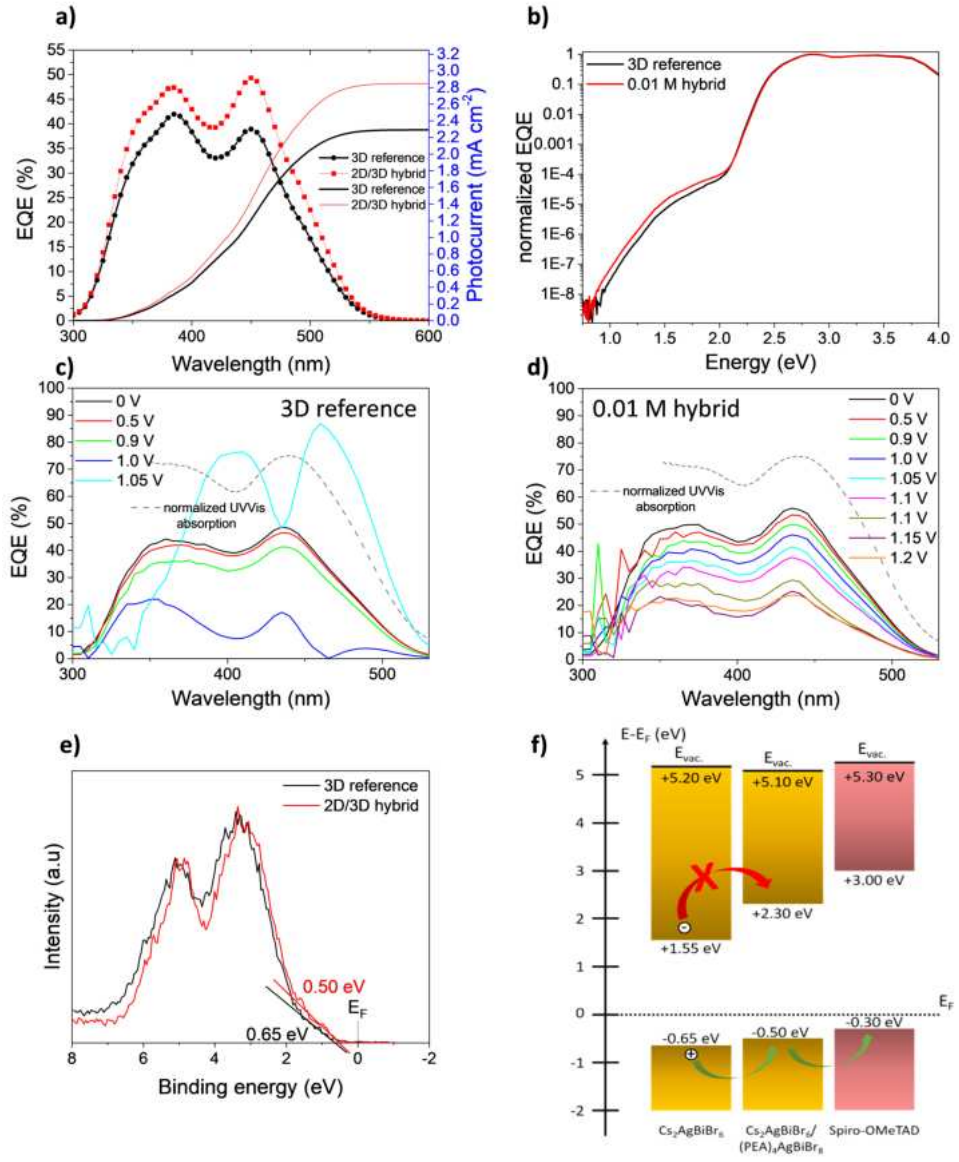

Figure 3.6: EQE and XPS spectra measured in this work. a) The EQE spectra obtained from the 3D reference (red line) and the 0.01 m hybrid (black line), plotted together with the integrated photocurrent. Panel (b) shows the subgap EQE spectra of the 3D reference (red line) and the 0.01 m hybrid (black line). Panels (c) and (d) show the voltage-dependent EQE measurements of the 3D reference and the 0.01 m hybrid, respectively. Different applied voltages are shown in the legend. The dashed grey line shows the respective UV–Vis absorption spectrum to guide the eye. Panel (e) shows the XPS spectra of the valence shell energies of the hybrid double perovskite (red line) with respect to the 3D reference (black line). Panel (f) shows a schematic energy level diagram obtained from the XPS values of the VBM and the optical bandgap obtained from the Tauc plots in the Supporting Information.

selectivity of the contacts. These results, together with the absence of trap passivation, support the indications of an increased contact selectivity, as well as reduced interface recombination leading to the significant improvement of the V_{oc} values of the resulting solar cells as observed with light intensity-dependent V_{oc} measurements.

To investigate the energy levels, photoelectron spectroscopy measurements were per-

formed on the perovskites deposited on FTO substrates as shown in Figure 3.6e, FiguresSI 3.13 and 3.14, Supporting Information.

Since the films were deposited at ambient conditions in air, contamination with oxygen could not be excluded. Hence, not UV irradiation but X-rays were used to determine the valence band maxima of the two different films. To confirm the presence of the spacer cation for the 2D/3D hybrid thin films, we determined the core-level energies of the different samples. FigureSI 3.15, Supporting Information exhibits the survey and the core level XPS spectra for the 3D reference and a 2D/3D hybrid. Binding energy positions of each element agree with a previous report.[12] The presence of nitrogen in the 2D/3D hybrid thin film confirms the presence of the spacer cation. A narrowing of the core level emission lines is also observed when the spacer cation is added. On average, the FWHM decreases to 100 meV and for the Br 3d spectra, it leads to more defined emission lines. This is in agreement with an ordering of the perovskite after a 3D to 2D transition[47,48] and confirms the presence of a 2D/3D hybrid phase. The nitrogen spectrum (N1s) can only be found for the 2D/3D hybrid material. However, the Cs 3d emission lines are visible as well, indicating that the contribution of the 3D phase to the PES spectra cannot be dismissed. This can be linked to the morphology of the investigated thin films as shown in Figure 3.3 and FigureSI 3.9, Supporting Information, showing the μm-sized 3D perovskite crystallite penetration out of the 2D layer.

Figure 3.6e shows a shift of the VBM after the addition of a spacer cation. It establishes that the VBM of the 2D material is 150 meV closer to the Fermi level, compared to the 3D reference. This is supported by the similar shifts of 100 meV (Bi4f, Ag3d) or 150 meV (Br3d, Cs3d) that are observed on the core level emission lines (FigureSI 3.15, Supporting Information). As all measurements are performed relative to the Fermi level of the sample, such global shift toward lower energy indicates a change in the Fermi level position of the perovskite absorber.

To determine the energy of the conduction band minimum, we measured the optical bandgap of a pure 2D $(PEA)_4AgBiBr_8$ thin film (FigureSI 3.17, Supporting Information). The thin film was deposited on an FTO substrate to simulate the same environment as for the 3D thin films, resulting in fully covered, smooth thin films (inset in FigureSI 3.17, Supporting Information). To determine the nature of the optical bandgap of the material, we calculated the band structure using first principle DFT calculations (FigureSI 3.18, Supporting Information). The PBE-SOC-TS band structure of $(PEA)_4AgBiBr_8$ shows a drastic change in the nature of the band gap compared to the 3D reference perovskite with the lowest band transition being centered at the Γ point in the Brillouin zone.[36] We note that although the bandgap is significantly underestimated, we can assume that the DFT-PBE method provides accurate predictions about the electronic nature of the

calculated structure.[60,61] Hence, a direct bandgap with an energy of 2.8 eV was obtained (FigureSI 3.17, Supporting Information), increasing the energy by 0.6 eV compared to the 3D $Cs_2AgBiBr_6$.[17]

Combining the optical bandgap, the VBM and the work function measured by UPS (FigureSI 3.16, Supporting Information), the full band diagram can be constructed (Figure 3.6f). To provide more insight on the charge carrier collection of our device, the energy levels of the HTM, a LiTFSI-doped Spiro-OMeTAD, were determined and added to the diagram. The corresponding VBM and the work function were measured with UPS (FigureSI 3.17, Supporting Information) and the band gap was assumed to be 3.3 eV, although the absorption energy of the oxidized species is slightly lower.[62] The 2D perovskite has a CBM of +2.3 eV (relatively to the Fermi level) which is 750 meV above the one of the 3D counterpart and 700 meV below the LUMO of the HTM. As the electrons are photogenerated inside the 3D material, the presence of the 2D layer enhances the electron blocking behavior of the resulting hybrid thin films. In addition, the VBM of the 2D/3D hybrid double perovskite is 150 meV closer to the HOMO energy level of the HTM compared to the 3D reference. It optimizes the holes extraction and therefore, it reduces the amount of interfacial recombination. This altogether confirms the findings of the EQE measurements that indicate a significant change in the selectivity of the contacts in the solar cell. It leads to the observed boost in the V_{oc} of the solar cells and addresses one of the major issues of solar cells based on Pb-free perovskites.

3.4 Conclusion

In this work, we successfully synthesized an Ag-Bi based 2D/3D hybrid double perovskite for the first time, using phenethyl ammonium bromide as large cation salt to form $Cs_2AgBiBr_6$/$(PEA)_4AgBiBr_8$ thin films. After confirmation of the film formation, we implemented this material in perovskite solar cells, obtaining a significant increase in the PCE from 1.84% on average for the 3D reference to 2.03% for the 2D/3D hybrid. The champion cells comprising the 2D/3D hybrid thin film even reach efficiencies of up to 2.5%. While the J_{sc} shows an improvement of 10% on average, the V_{oc} is improved on average by 70 mV to reach values of up to 1.14 and 1.18 V, which are among the highest values reported for $Cs_2AgBiBr_6$ solar cells. This boost in the V_{oc} is attributed to a large enhancement of the selectivity of the contacts in the solar cell, which was shown by comprehensive EQE and PL studies. Photoelectron spectroscopy reveals a shift in the valence band maximum of the 2D/3D hybrid perovskite thin film of 150 meV toward the Fermi level energy. This improves the energy level alignment and allows for a better hole-extraction towards the doped Spiro-OMeTAD layer. In combination with an increased bandgap of the 2D material, which was calculated to be direct, the XPS results predict an energy barrier of 750 meV between the 2D and the 3D perovskite, improving the contact selectivity in the solar cell. In this work, we show a way to easily tune the perovskite/HTM energy level alignment, as well as to improve the charge carrier selectivity of the contacts in the solar cell. Hence, this work offers a toolbox to efficiently address some of the bottlenecks that have been identified for the behavior of lead-free double perovskite solar cells.

3.5 Experimental Section

Materials and Thin Film synthesis: The stock solution was prepared by dissolving CsBr (Alpha Aesar, 99.999% metals basis), $BiBr_3$ (Alpha Aesar, 99.9% metals basis) and AgBr (Alpha Aesar, 99.998% metals basis) in 1 mL DMSO (Sigma Aldrich, anhydrous, $\geq$99.9%) by vigorous stirring at 130 °C for 60 min to obtain a 0.5 M solution. Weighing the precursors was performed in a nitrogen-filled glovebox, while all other steps, including the DMSO addition to the precursors, were done at ambient conditions in air.

Prior to the spincoating step, the substrates and the solution were placed on a hotplate (Heidolph with internal temperature sensor) at 85 °C to be preheated. The stock solution was constantly stirred. The thin films were fabricated by spincoating the warm solution dynamically (2000 rpm for 45 s) onto the preheated substrates (100 µL of the stock solution). After the spincoating, the thin films were annealed at 285 °C for 5 min at ambient

conditions in air.

Solar Cell Fabrication: Fluorine-doped tin oxide coated glass sheets (7 Ω cm^{-2}) were patterned by etching with zinc-powder and 3 m HCl, cleaned with a detergent followed by washing with acetone and ethanol and dried under an air stream. Directly before applying the hole-blocking layer, the substrates were oxygen plasma cleaned for 5 min.

Compact TiO_2 (c-TiO_2): A compact TiO_2 layer was prepared from a sol-gel precursor solution by spin-coating 100 µL onto the 3 cm × 3 cm substrates for 45 s at 2000 rpm and calcination afterwards at 500 °C for 30 min in air, resulting in a 50 nm thick layer. For the sol-gel solution, 2 m HCl (35 µL) in 2.53 mL dry 2-propanol was added dropwise to a solution of 370 µL of titanium-isopropoxide in 2.53 mL dry 2-propanol under vigorous stirring. After cooling down, the substrates were again plasma cleaned for 5 min and transferred to a nitrogen-filled glovebox.

Mesoporous TiO_2 (mp-TiO_2): After the deposition of the layer of compact TiO_2, 100 µL of a dispersion of mp-TiO_2 nanoparticles (DyeSol, 3:1 EtOH:TiO_2-paste) was spincoated on top of the c-TiO_2 layer without plasma-cleaning. Afterward, the substrates were calcined at 500 °C for 30 min in air resulting in a 500 nm thick layer. After cooling down, the active layer was deposited on top of the TiO_2 layer as described above.

Deposition of Hole Transporting Materials (HTM): 73 mg of 2,2',7,7'-tetrakis-(N,N-di-4-methoxyphenylamino)-9,9'-spirobifluorene (Spiro-OMeTAD, Borun Chemicals, 99.5% purity) were dissolved in 1 mL of chlorobenzene. To this solution, 10 µL of 4-tert-butylpyridine and 30 µL of a bis(trifluoromethane)sulfonamide lithium salt solution (LiTFSI, 170 mg in 1 mL acetonitrile) were added. The resulting HTM solution was deposited via dynamic spincoating (1500 rpm, 45 s) in a nitrogen-filled glovebox. Afterward, the samples were stored overnight in air at <30% relative humidity (R.H.) to allow the hole transporting material to oxidize.

The top electrode with a thickness of 40 nm was deposited by thermally evaporating gold under vacuum (at $\approx 10^{-7}$ mbar).

DFT Calculations: First-principle DFT calculations were based on a plane wave basis set and norm-conserving Vanderbilt pseudopotentials as implemented in the Quantum Espresso package.[63,64] Furthermore, the PBE exchange-correlation functional and the Tkatchenko-Scheffler (TS) dispersion scheme were used.[65,66] The latter is necessary to accurately describe the structural properties in low-dimensional perovskite materials.[67] Additionally, spin-orbit coupling was included to treat the heavy Bi atom. The structure, starting from the single crystal data of Schmitz et al.,[49] was optimized until all residual forces on the nuclei were below 1×10^{-3} a.u. Thereby, the following equilibrium unit cell parameters were obtained:

a = 11.4661 Å, b = 11.5138 Å, c = 17.0237 Å, α = 106.6141°, β = 99.6955°, γ =

90.7676°

A kinetic energy cutoff of 50 Ry for the wavefunctions and 400 Ry for the charge density was used. A 4 × 4 × 1 k-point grid was utilized.

Materials Characterization: Powder X-Ray Diffraction (PXRD) Measurements: The patterns were recorded using a Bruker D8 Discover Diffractometer with Ni-filtered Cu-K_α radiation and a LynxEye position-sensitive detector.

2D Grazing-incidence wide angle X-ray scattering (GIWAXS): GIWAXS measurements were carried out on a Anton-Paar Saxspoint 2.0 with a Primux 100 microfocus source with Cu-K_α radiation (λ = 1.5406 Å) and a Dectris Eiger R 1M 2D Detector.

Scanning Electron Microscopy (SEM): SEM data were taken with a FEI Helios NanoLab G3 UC field emission scanning electron microscope equipped with an additional concentric backscattered electron detector.

Photoelectron Spectroscopy (PES): Even though the samples were prepared under ambient conditions in air, to minimize contaminations, samples were shipped under nitrogen. They were opened in a glovebox and transferred to the ultra high vacuum system.

PES measurements were performed with a Thermo Fisher VG Escalab 250 spectrometer. It was equipped with a monochromatic X-ray source (Al-K_α = 1486.6 eV) set at 13 mA and 15 kV. The pressure inside the analytical chamber was monitored below 5×10^{-9} mbar. Measurements were performed in "dark conditions" as discussed in ref.[68] to avoid undesired photovoltage and misinterpretation of the energy levels.

Survey spectra were acquired with a pass energy of 50 eV, a step size of 0.1 eV and a dwell time of 50 ms per measurement point. The detailed scans were acquired with a lower pass energy (10 eV) and a lower step size (0.05 eV). UPS measurements were performed with the same spectrometer; He I (21.2 eV) discharge was used.

XPS spectra were calibrated using the Fermi level of silver (0 eV) measured by XPS as well as the binding energy of the Au $4f_{7/2}$ emission line (84.0 eV), the Ag $3d_{5/2}$ emission line (368.26 eV - FWHM at a pass energy of 10 eV was equal to 0.52 eV), and the Cu $2p_{3/2}$ emission line (932.67 eV). The Fermi level of silver was also measured with UPS to calibrate the corresponding spectra. The Fermi level value was determined with a sigmoid fit and taking the position where the intensity is at 50%. All calibration samples were cleaned with Ar sputtering prior to the measurement (3 kV, for 180 s). The Fermi level of the cleaned silver was also used to determine the instrumental resolution: 0.35 eV for XPS (pass energy of 10 eV) and 0.24 eV for UPS (pass energy of 2.5 eV).

Semi quantitative analysis was performed using the Thermo Avantage software. Core levels were fitted using modified Shirley background subtraction and Gauss-Lorentz convolution. Quantification was made with the machine-corrected atomic sensitivity factors based on Scofield's calculations.

Photoluminescence Quantum Yield (PLQY), Fluence Dependent Steady State PL and Time-correlated Single Photon Counting (TCSPC): The PLQY was measured using a laser with 405 nm wavelength, a power of 71.0 mW cm^{-2} and an integrating sphere. The spot size was 0.0152 cm^2.

The TRPL was recorded using a 375 nm laser with a repetition rate of 10 µs, an energy density of 8.3 nJ cm^{-2} and a spot size of 290 µm.

All spectra were measured using an Edinburgh Instruments FLS 980 spectrometer in reflection using a Si diode for detection.

Fluence-dependent steady state PL was measured using a 415 nm LED (Solis-415C, Thorlabs). The sample was placed at a 45° angle toward the excitation beam, so that measurements were performed in a reflection configuration. A silicon diode was placed in the emission pathway in order to monitor the resulting integrated photoluminescence.

EQE Measurements for Figure 3.6: Measurements were performed on a homemade system with a halogen lamp, a monochromator and a silicon reference diode. The light was chopped at 330 Hz and the signal was detected through a lock-in amplifier. The setup was calibrated with a silicon solar cell and no bias light was applied.

Sensitive EQE Measurements: Sensitive EQE measurements to characterize the sub-bandgap region were conducted using a halogen lamp (Osram 64 655 HLX 250 W) as illumination source. The light was chopped using an Oriel 3502 chopper at 330 Hz and subsequently passed through a double-grating monochromator (Oriel, Cornerstone 260). Several long-pass filters were used to filter out stray light. The samples were mounted in an air tight holder filled with nitrogen to prevent air exposure. The response was recorded from a pre-amplifier (Stanford Research, SR 570) using a lock-in amplifier (Stanford Research, SR 830) and calibrated using two Si and InGaAs reference cells.

Absorption Measurements: The absorption spectra of the films were taken on a Lambda 1050 (Perkin Elmer) instrument with an integrating sphere.

Solar Cell characterization: Current–voltage (J–V) characteristics of the perovskite solar cells were measured using a Newport OrielSol 2A solar simulator with a Keithley 2401 source meter. The devices were illuminated through a shadow mask, yielding an active area of 0.0831 cm^2. The J–V curves were recorded under standard AM 1.5G illumination from a Xenon lamp, and calibrated to a light intensity of 100 mW cm^{-2} with a Fraunhofer ISE certified silicon diode. The input bias voltage was scanned from -1.5 to 0 V in 0.01 V steps with a rate of 0.1 V s^{-1} for the standard PCE measurements. For the experiments with different scan-speeds, bigger voltage steps varying from 0.01 to 1 V were chosen. All prepared devices show a comparable degree of hysteresis between the forward and the reverse scan.

3.6 Acknowledgements

The authors acknowledge funding from the German Federal Ministry of Education and Research (BMBF) under the agreement number 03SF0516B, the Bavarian Ministry of the Environment and Consumer Protection, the Bavarian Network "Solar Technologies Go Hybrid", the German Science Foundation (DFG) focus program SPP 2196 and the DFG Excellence Cluster e-conversion (EXC 2089/1-390776260). The authors thank Dr. Steffen Schmidt for performing the SEM measurements. Open access funding enabled and organized by Projekt DEAL.

3.7 Supporting Information

2D/3D Hybrid $Cs_2AgBiBr_6$ Double Perovskite Solar Cells: Improved Energy Level Alignment for Higher Contact-Selectivity and Large Open Circuit Voltage

M. T. Sirtl, R. Hooijer, M. Armer, F. G. Ebadi, M. Mohammadi, C. Maheu, A. Weis, B. T. van Gorkom, S. Häringer, R. A. J. Janssen, T. Mayer, V. Dyakonov, W. Tress, and T. Bein

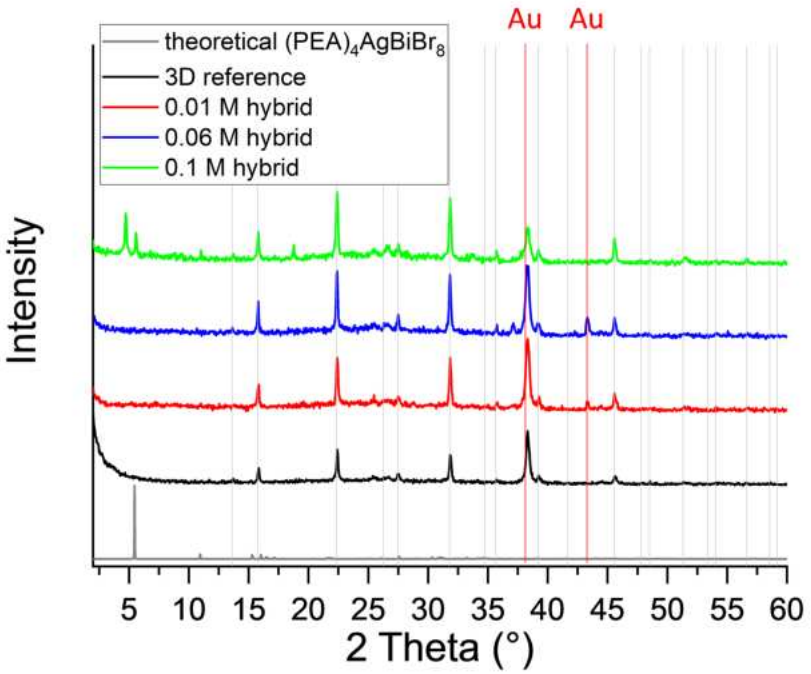

Figure 3.7: Full XRD patterns of the different thin films recorded in Bragg Brentano Geometry. The grey line shows the theoretical pattern of $(PEA)_4AgBiBr_8$ perovskite. The grey drop lines indicate the theoretical pattern of the 3D double perovskite $Cs_2AgBiBr_6$. The black line is the obtained pattern from the pure 3D solar cell, the red line shows the experimental pattern of the solar cell with the 0.01 M hybrid as active layer, the blue and green line show the experimental patterns of solar cells comprising the 0.06 M and 0.1 M hybrid respectively. The red drop line indicates the reflections arising from the gold electrode.

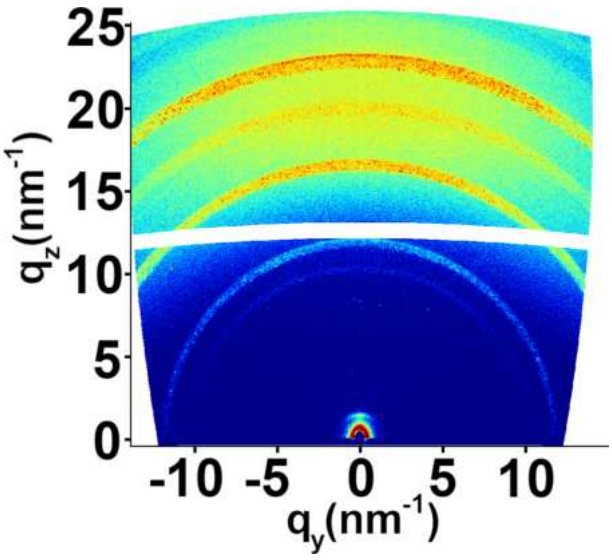

Figure 3.8: Detector-image of GIWAXS measurement performed on thin films treated with 0.01 M PEABr and measured with an increased integration time.

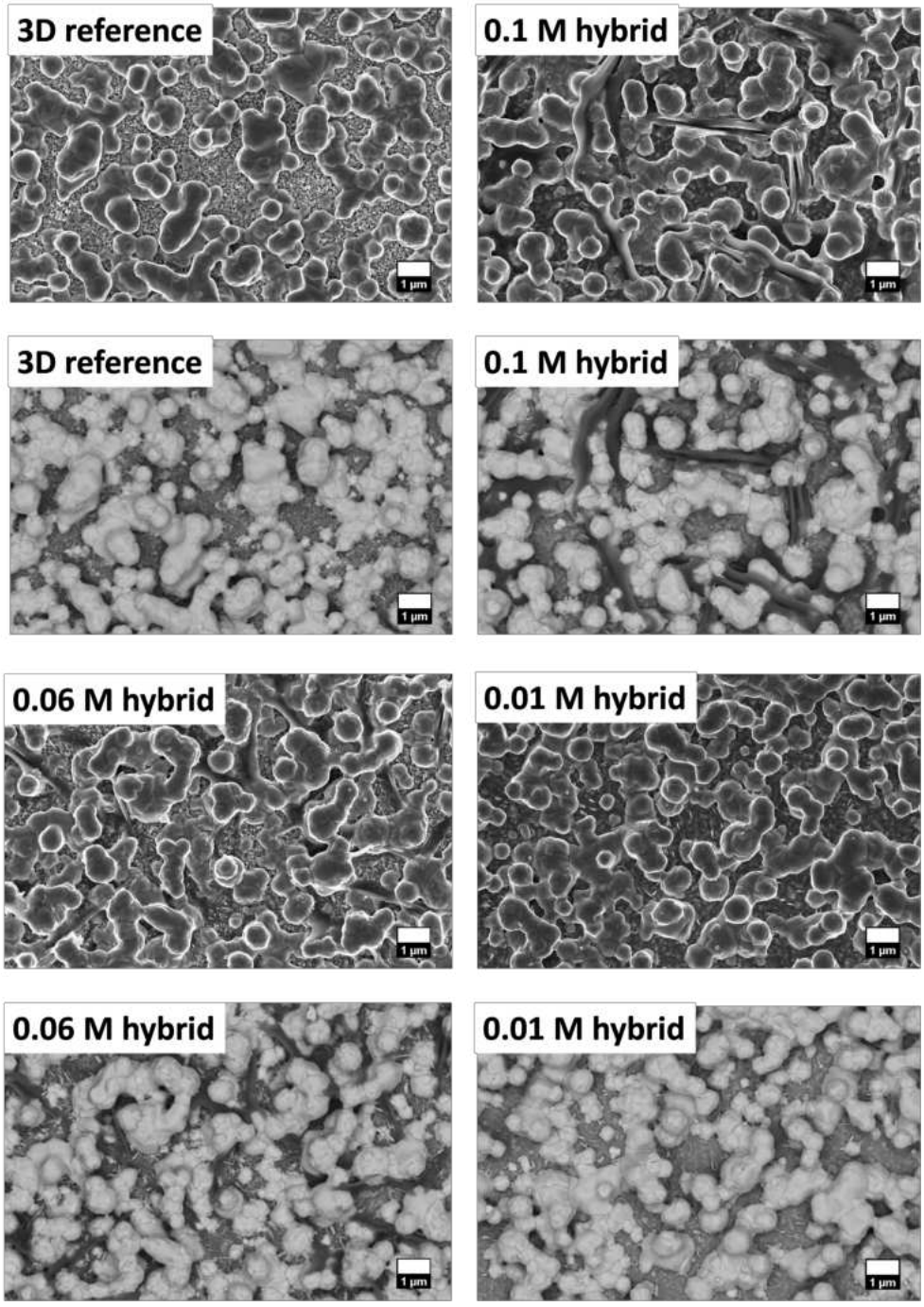

Figure 3.9: SEM topview images of the investigated thin films. Top line shows the through-the-lens detector (TLD) images. Lower line shows the images obtained with a circular backscatter detector (CBS). The 3D reference is shown on the left upper side, the 0.1 M hybrid in the right upper and the 0.06 M hybrid on the left lower side and the 0.01 M on the right lower side.

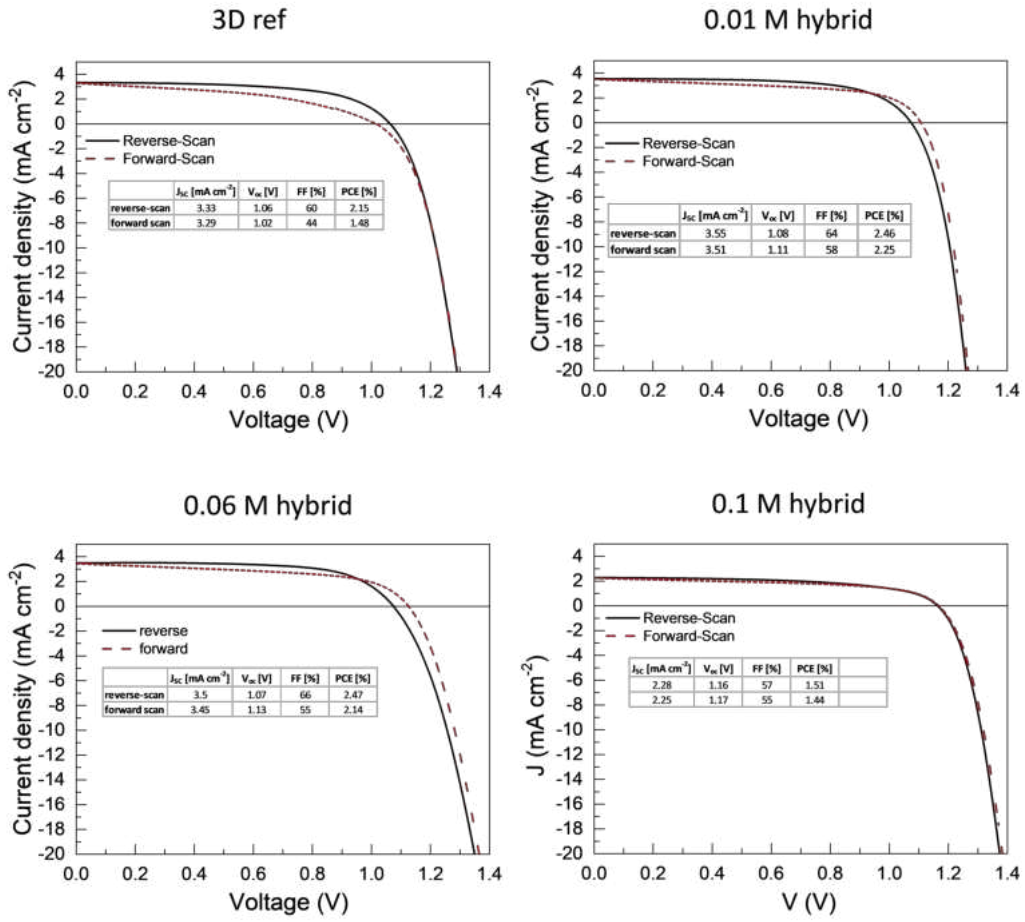

Figure 3.10: JV curves of the solar cells investigated in this paper. The curves show rather low hysteresis between the forward and the reverse scan.

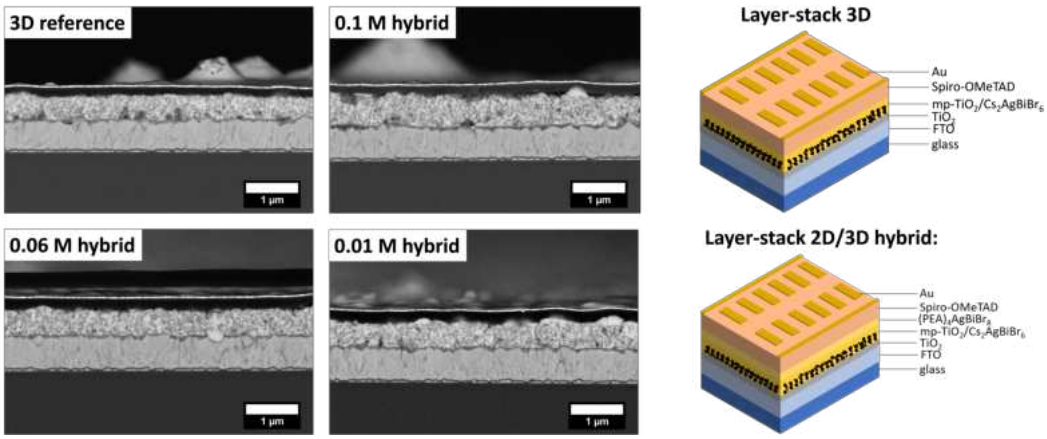

Figure 3.11: SEM cross-sections of the investigated solar cells. On the right, the layer-stacks of the 3D perovskite and the 2D/3D hybrid perovskite solar cells are shown.

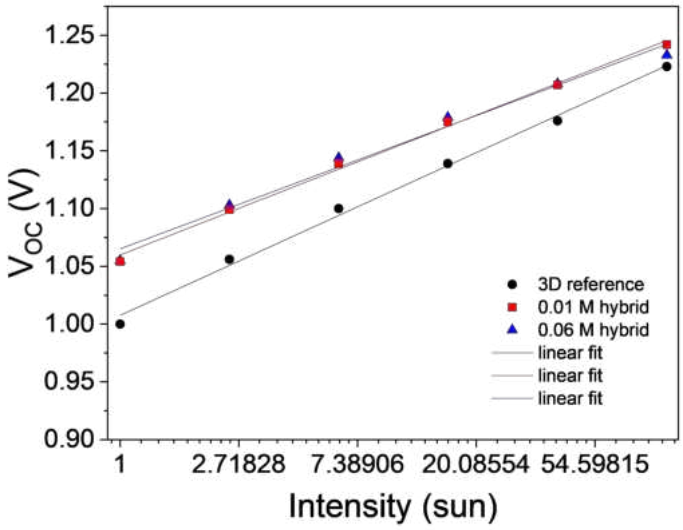

Figure 3.12: Semi-ln plots of the light intensity dependent V_{oc} measurements. The parameters are shown as indicated in the legend.

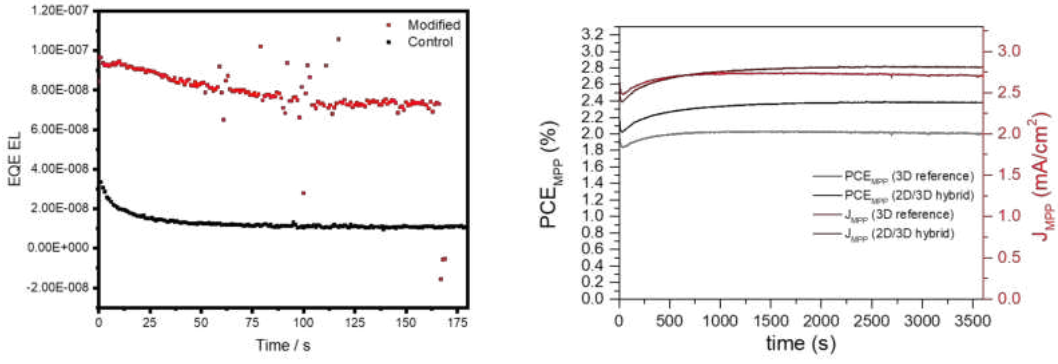

Figure 3.13: EQE EL and MPP measurements of the 0.01 M (red line) and the 3D reference (black line) solar cells.

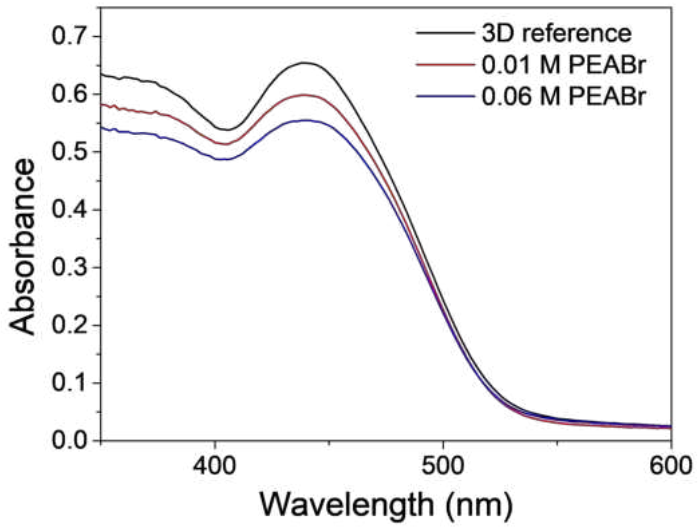

Figure 3.14: UV-Vis absorption spectra obtained from thin films on FTO substrates. Color coding as indicated in the legend.

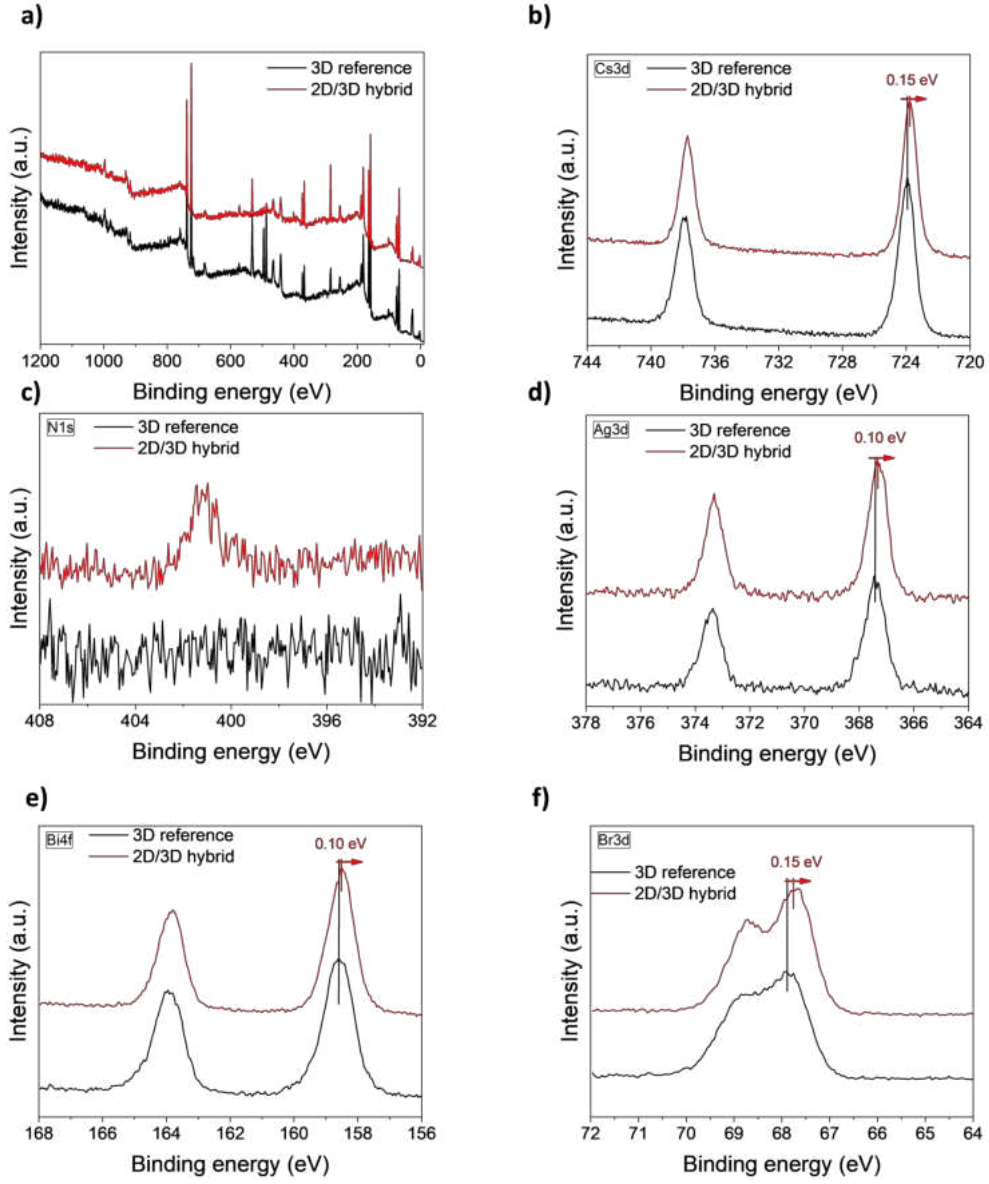

Figure 3.15: XPS spectra of the 2D/3D hybrid (red lines) and 3D reference (black line) thin films. a) Survey, b) Cs3d, c) N1s, d) Ag3d, e) Bi4f and f) Br3d, all expressing shifts of 100 or 150 meV.

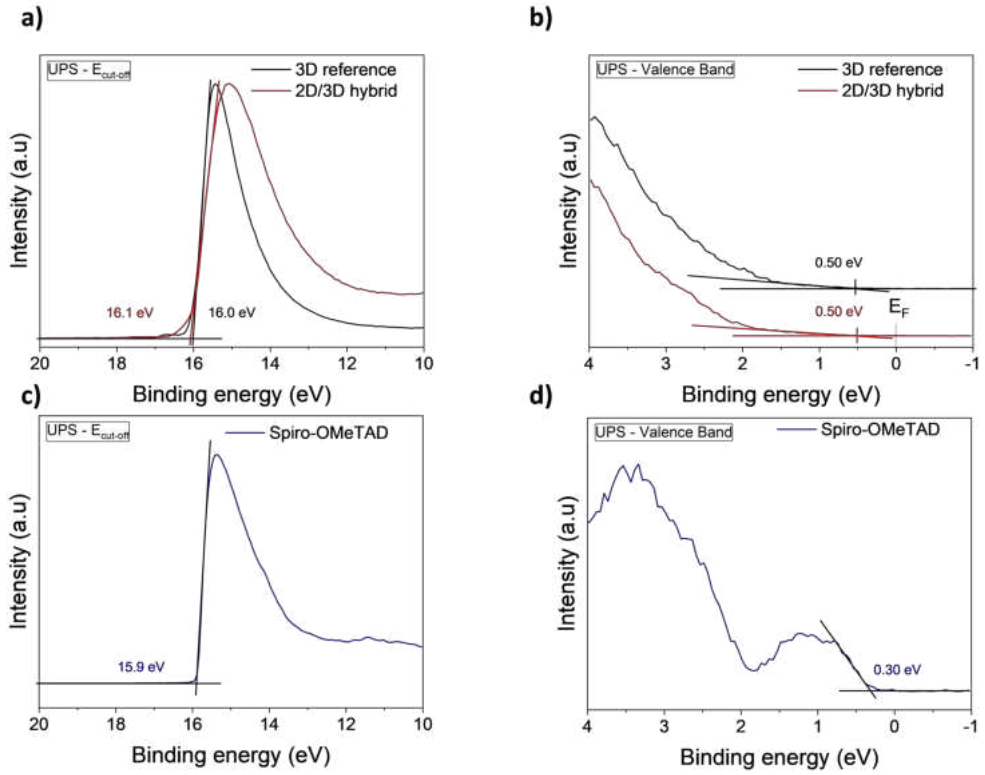

Figure 3.16: UPS spectra of the 2D/3D hybrid (red lines) and 3D reference (black line) thin films. a) Cut-off measured by applying a 6 V bias, b) valence band edge. UPS spectra of doped Spiro-OMeTAD with LiTFSI thin film. c) Cut-off measured by applying a 6 V bias, d) valence band edge.

The Cut-off ($E_{cut-off}$) provides the work function (W_f) of the material (the distance between the vacuum level and the Fermi level) through this equation: $W_f = hv - E_{cut-off}$, with hv the excitation energy, i.e. the He I discharge (21.2 eV).

The doped Spiro-OMeTAD thin film was prepared inside the ultra-high vacuum system and directly transferred to the analytic chamber for UPS analysis. It was prepared by the coevaporation of LiTSFI and Spiro-OMeTAD. The base pressure of the deposition chamber was 6×10^{-8} mbar and it increased to 2.5×10^{-7} mbar during the deposition process. A current of 625 mA and of 434 mA was applied to the Al_2O_3 crucibles containing, respectively, SpiroOMeTAD and LiTFSI. Co-evaporation lasted 2 hours.

The VBM of the 3D reference and the 2D/3D hybrid perovskite were measured similarly with UPS. We believe that the preparation or the transfer of the samples to Darmstadt might have induced some surface contaminations. The escape depth of the photoelectrons is higher for XPS than for UPS. Therefore, XPS measurements are less influenced by theses contaminations and are more reliable. However, it should be pointed out that the main conclusion of this section remains unchanged if we take the VBM difference obtained with XPS or with UPS. Because of the optical band gap difference a 0.15 eV (XPS) difference or a 0 eV (UPS) difference still induce an additional electron blocking layer at the 2D/3D interface.

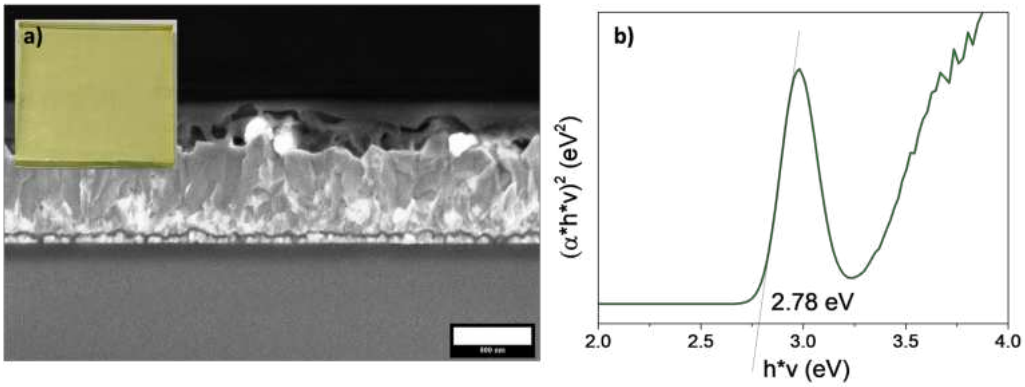

Figure 3.17: a) SEM cross-sectional image of the measured $(PEA)_4AgBiBr_8$ thin films with a photograph in the inset. b) Direct Tauc plot of pure $(PEA)_4AgBiBr_8$ thin films on FTO.

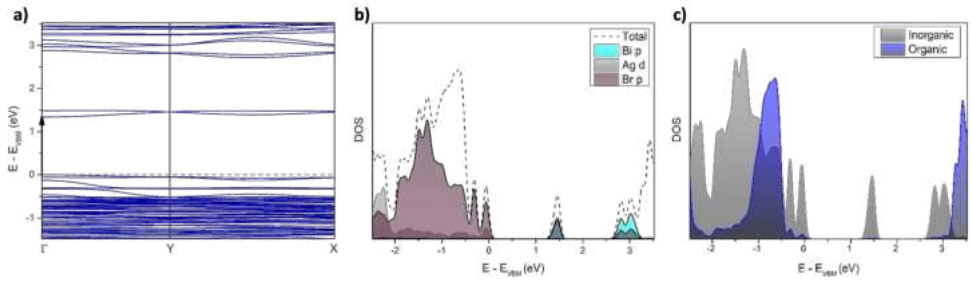

Figure 3.18: Band structure calculations. a) Shows the PBE-SOC-TS band structure of $(PEA)_4AgBiBr_8$, showcasing the characteristic conduction band splitting of the Bi 6p orbitals (b), already well described for $Cs_2AgBiBr_6$.[6] Furthermore, the band gap nature changes drastically, with the lowest band transition being centered at the Γ point in the Brillouin zone.[36] The absolute band gap is underestimated significantly (1.3 "eV), a known deficiency of the DFT-PBE method, whereas other characteristics like the electronic nature are expected to be predicted accurately.[60] The atomic contribution to the frontier orbitals is also identical to other previously published 2D Ag-Bi phases, consisting of mostly halide p and Ag d orbitals in the valence band, with the conduction band predominantly made up of Bi p and a contribution of halide p orbitals.[36,37]

3.8 References

[1] M. Green, E. Dunlop, J. Hohl-Ebinger, M. Yoshita, N. Kopidakis, X. Hao, Prog Photovoltaics Res Appl, vol. 29, **2021**.

[2] X.-G. Zhao, J.-H. Yang, Y. Fu, D. Yang, Q. Xu, L. Yu, S.-H. Wei, L. Zhang, *Journal of the American Chemical Society* **2017**, *139*, 2630–2638.

[3] Z. Xiao, W. Meng, J. Wang, Y. Yan, *ChemSusChem* **2016**, *9*, 2628–2633.

[4] M. R. Filip, X. Liu, A. Miglio, G. Hautier, F. Giustino, *The Journal of Physical Chemistry C* **2018**, *122*, 158–170.

[5] G. Volonakis, M. R. Filip, A. A. Haghighirad, N. Sakai, B. Wenger, H. J. Snaith, F. Giustino, *The journal of physical chemistry letters* **2016**, *7*, 1254–1259.

[6] M. R. Filip, S. Hillman, A. A. Haghighirad, H. J. Snaith, F. Giustino, *The journal of physical chemistry letters* **2016**, *7*, 2579–2585.

[7] G. Volonakis, A. A. Haghighirad, H. J. Snaith, F. Giustino, *The journal of physical chemistry letters* **2017**, *8*, 3917–3924.

[8] E. T. McClure, M. R. Ball, W. Windl, P. M. Woodward, *Chemistry of Materials* **2016**, *28*, 1348–1354.

[9] A. H. Slavney, T. Hu, A. M. Lindenberg, H. I. Karunadasa, *Journal of the American chemical society* **2016**, *138*, 2138–2141.

[10] R. L. Hoye, L. Eyre, F. Wei, F. Brivio, A. Sadhanala, S. Sun, W. Li, K. H. Zhang, J. L. MacManus-Driscoll, P. D. Bristowe, et al., *Advanced Materials Interfaces* **2018**, *5*, 1800464.

[11] E. Greul, M. L. Petrus, A. Binek, P. Docampo, T. Bein, *Journal of Materials Chemistry A* **2017**, *5*, 19972–19981.

[12] F. Igbari, R. Wang, Z.-K. Wang, X.-J. Ma, Q. Wang, K.-L. Wang, Y. Zhang, L.-S. Liao, Y. Yang, *Nano letters* **2019**, *19*, 2066–2073.

[13] M. T. Sirtl, M. Armer, L. K. Reb, R. Hooijer, P. Dörflinger, M. A. Scheel, K. Tvingstedt, P. Rieder, N. Glück, P. Pandit, et al., *ACS applied energy materials* **2020**, *3*, 11597–11609.

[14] X. Yang, Y. Chen, P. Liu, H. Xiang, W. Wang, R. Ran, W. Zhou, Z. Shao, *Advanced Functional Materials* **2020**, *30*, 2001557.

[15] B. Wang, L. Yang, C. Dall'Agnese, A. K. Jena, S.-i. Sasaki, T. Miyasaka, H. Tamiaki, X.-F. Wang, *Solar RRL* **2020**, *4*, 2000166.

[16] B. Wang, N. Li, L. Yang, C. Dall'Agnese, A. K. Jena, S.-i. Sasaki, T. Miyasaka, H. Tamiaki, X.-F. Wang, *Journal of the American Chemical Society* **2021**, *143*, 2207–2211.

[17] M. T. Sirtl, F. Ebadi, B. T. van Gorkom, P. Ganswindt, R. A. Janssen, T. Bein, W. Tress, *Advanced Optical Materials* **2021**, *9*, 2100202.

[18] C. Wu, Q. Zhang, Y. Liu, W. Luo, X. Guo, Z. Huang, H. Ting, W. Sun, X. Zhong, S. Wei, et al., *Advanced Science* **2018**, *5*, 1700759.

[19] W. Gao, C. Ran, J. Xi, B. Jiao, W. Zhang, M. Wu, X. Hou, Z. Wu, *ChemPhysChem* **2018**, *19*, 1696–1700.

[20] B. Wang, N. Li, L. Yang, C. Dall'Agnese, A. K. Jena, T. Miyasaka, X.-F. Wang, *Journal of the American Chemical Society* **2021**, *143*, 14877–14883.

[21] G. Longo, S. Mahesh, L. R. Buizza, A. D. Wright, A. J. Ramadan, M. Abdi-Jalebi, P. K. Nayak, L. M. Herz, H. J. Snaith, *ACS Energy Letters* **2020**, *5*, 2200–2207.

[22] A. D. Wright, L. R. Buizza, K. J. Savill, G. Longo, H. J. Snaith, M. B. Johnston, L. M. Herz, *The Journal of Physical Chemistry Letters* **2021**, *12*, 3352–3360.

[23] D. Bartesaghi, A. H. Slavney, M. C. Gélvez-Rueda, B. A. Connor, F. C. Grozema, H. I. Karunadasa, T. J. Savenije, *The Journal of Physical Chemistry C* **2018**, *122*, 4809–4816.

[24] R. Kentsch, M. Scholz, J. Horn, D. Schlettwein, K. Oum, T. Lenzer, *The Journal of Physical Chemistry C* **2018**, *122*, 25940–25947.

[25] S. Zelewski, J. Urban, A. Surrente, D. K. Maude, A. Kuc, L. Schade, R. Johnson, M. Dollmann, P. Nayak, H. Snaith, et al., *Journal of Materials Chemistry C* **2019**, *7*, 8350–8356.

[26] M. Armer, J. Höcker, C. Büchner, S. Häfele, P. Dörflinger, M. T. Sirtl, K. Tvingstedt, T. Bein, V. Dyakonov, *CrystEngComm* **2021**, *23*, 6848–6854.

[27] H. Lei, D. Hardy, F. Gao, *Advanced Functional Materials* **2021**, *31*, 2105898.

[28] W. Tress, M. T. Sirtl, *Solar RRL* **2022**, *6*, 2100770.

[29] P. Vishnoi, R. Seshadri, A. K. Cheetham, *The Journal of Physical Chemistry C* **2021**, *125*, 11756–11764.

[30] N. Pai, J. Lu, M. Wang, A. S. Chesman, A. Seeber, P. V. Cherepanov, D. C. Senevirathna, T. R. Gengenbach, N. V. Medhekar, P. C. Andrews, et al., *Journal of Materials Chemistry A* **2020**, *8*, 2008–2020.

[31] Z. Li, S. R. Kavanagh, M. Napari, R. G. Palgrave, M. Abdi-Jalebi, Z. Andaji-Garmaroudi, D. W. Davies, M. Laitinen, J. Julin, M. A. Isaacs, et al., *Journal of Materials Chemistry A* **2020**, *8*, 21780–21788.

[32] F. Ji, J. Klarbring, F. Wang, W. Ning, L. Wang, C. Yin, J. S. M. Figueroa, C. K. Christensen, M. Etter, T. Ederth, et al., *Angewandte Chemie* **2020**, *132*, 15303–15306.

[33] E. M. Hutter, M. C. Gélvez-Rueda, D. Bartesaghi, F. C. Grozema, T. J. Savenije, *ACS omega* **2018**, *3*, 11655–11662.

[34] A. Karmakar, M. S. Dodd, S. Agnihotri, E. Ravera, V. K. Michaelis, *Chemistry of Materials* **2018**, *30*, 8280–8290.

[35] Q. Li, Y. Wang, W. Pan, W. Yang, B. Zou, J. Tang, Z. Quan, *Angewandte Chemie International Edition* **2017**, *56*, 15969–15973.

[36] B. A. Connor, L. Leppert, M. D. Smith, J. B. Neaton, H. I. Karunadasa, *Journal of the American Chemical Society* **2018**, *140*, 5235–5240.

[37] M. K. Jana, S. M. Janke, D. J. Dirkes, S. Dovletgeldi, C. Liu, X. Qin, K. Gundogdu, W. You, V. Blum, D. B. Mitzi, *Journal of the American Chemical Society* **2019**, *141*, 7955–7964.

[38] L.-Y. Bi, Y.-Q. Hu, M.-Q. Li, T.-L. Hu, H.-L. Zhang, X.-T. Yin, W.-X. Que, M. S. Lassoued, Y.-Z. Zheng, *Journal of Materials Chemistry A* **2019**, *7*, 19662–19667.

[39] Y. Yao, B. Kou, Y. Peng, Z. Wu, L. Li, S. Wang, X. Zhang, X. Liu, J. Luo, *Chemical Communications* **2020**, *56*, 3206–3209.

[40] Y. Hu, J. Schlipf, M. Wussler, M. L. Petrus, W. Jaegermann, T. Bein, P. Müller-Buschbaum, P. Docampo, *ACS nano* **2016**, *10*, 5999–6007.

[41] J. Schlipf, Y. Hu, S. Pratap, L. Bießmann, N. Hohn, L. Porcar, T. Bein, P. Docampo, P. Müller-Buschbaum, *ACS Applied Energy Materials* **2019**, *2*, 1011–1018.

[42] Y. Liu, S. Akin, L. Pan, R. Uchida, N. Arora, J. V. Milić, A. Hinderhofer, F. Schreiber, A. R. Uhl, S. M. Zakeeruddin, et al., *Science advances* **2019**, *5*, eaaw2543.

[43] D. Liang, C. Dong, L. Cai, Z. Su, J. Zang, C. Wang, X. Wang, Y. Zou, Y. Li, L. Chen, et al., *Small* **2021**, *17*, 2100972.

[44] R. Yang, R. Li, Y. Cao, Y. Wei, Y. Miao, W. L. Tan, X. Jiao, H. Chen, L. Zhang, Q. Chen, et al., *Advanced Materials* **2018**, *30*, 1804771.

[45] T. Liu, J. Guo, D. Lu, Z. Xu, Q. Fu, N. Zheng, Z. Xie, X. Wan, X. Zhang, Y. Liu, et al., *ACS nano* **2021**, *15*, 7811–7820.

[46] Y. Hu, L. M. Spies, D. Alonso-Álvarez, P. Mocherla, H. Jones, J. Hanisch, T. Bein, P. R. Barnes, P. Docampo, *Journal of Materials Chemistry A* **2018**, *6*, 22215–22225.

[47] W. Yuan, G. Niu, Y. Xian, H. Wu, H. Wang, H. Yin, P. Liu, W. Li, J. Fan, *Advanced Functional Materials* **2019**, *29*, 1900234.

[48] X. Wang, K. Li, H. Xu, N. Ali, Y. Wang, Q. Shen, H. Wu, *Chemical Communications* **2020**, *56*, 7917–7920.

[49] F. Schmitz, J. Horn, N. Dengo, A. E. Sedykh, J. Becker, E. Maiworm, P. Bélteky, A. Kukovecz, S. Gross, F. Lamberti, et al., *Chemistry of Materials* **2021**, *33*, 4688–4700.

[50] E. R. Jette, F. Foote, *The Journal of Chemical Physics* **1935**, *3*, 605–616.

[51] K. Tvingstedt, O. Malinkiewicz, A. Baumann, C. Deibel, H. J. Snaith, V. Dyakonov, H. J. Bolink, *Scientific reports* **2014**, *4*, 6071.

[52] V. D'innocenzo, G. Grancini, M. J. Alcocer, A. R. S. Kandada, S. D. Stranks, M. M. Lee, G. Lanzani, H. J. Snaith, A. Petrozza, *Nature communications* **2014**, *5*, 3586.

[53] V. Sarritzu, N. Sestu, D. Marongiu, X. Chang, S. Masi, A. Rizzo, S. Colella, F. Quochi, M. Saba, A. Mura, et al., *Scientific reports* **2017**, *7*, 44629.

[54] E. J. Juarez-Perez, M. Wuβler, F. Fabregat-Santiago, K. Lakus-Wollny, E. Mankel, T. Mayer, W. Jaegermann, I. Mora-Sero, *The journal of physical chemistry letters* **2014**, *5*, 680–685.

[55] Y. Zhang, M. Liu, G. E. Eperon, T. C. Leijtens, D. McMeekin, M. Saliba, W. Zhang, M. de Bastiani, A. Petrozza, L. M. Herz, et al., *Materials Horizons* **2015**, *2*, 315–322.

[56] W. Tress, M. Yavari, K. Domanski, P. Yadav, B. Niesen, J. P. C. Baena, A. Hagfeldt, M. Graetzel, *Energy & Environmental Science* **2018**, *11*, 151–165.

[57] P. Caprioglio, C. M. Wolff, O. J. Sandberg, A. Armin, B. Rech, S. Albrecht, D. Neher, M. Stolterfoht, *Advanced Energy Materials* **2020**, *10*, 2000502.

[58] W. Tress, N. Marinova, O. Inganäs, M. K. Nazeeruddin, S. M. Zakeeruddin, M. Graetzel, *Advanced Energy Materials* **2015**, *5*, 1400812.

[59] J. Jiménez-López, W. Cambarau, L. Cabau, E. Palomares, *Scientific reports* **2017**, *7*, 6101.

[60] P. J. Hasnip, K. Refson, M. I. Probert, J. R. Yates, S. J. Clark, C. J. Pickard, *Philosophical Transactions of the Royal Society A: Mathematical Physical and Engineering Sciences* **2014**, *372*, 20130270.

[61] N. Giesbrecht, A. Weis, T. Bein, *Journal of Physics: Energy* **2020**, *2*, 024007.

[62] M. L. Petrus, K. Schutt, M. T. Sirtl, E. M. Hutter, A. C. Closs, J. M. Ball, J. C. Bijleveld, A. Petrozza, T. Bein, T. J. Dingemans, et al., *Advanced Energy Materials* **2018**, *8*, 1801605.

[63] P. Giannozzi, *J. Phys.: Condens. Matter* **2009**, *21*, 395502.

[64] D. Hamann, *Physical Review B* **2013**, *88*, 085117.

[65] J. P. Perdew, K. Burke, M. Ernzerhof, *Physical review letters* **1996**, *77*, 3865.

[66] A. Tkatchenko, M. Scheffler, *Physical review letters* **2009**, *102*, 073005.

[67] R. L. Hoye, P. Schulz, L. T. Schelhas, A. M. Holder, K. H. Stone, J. D. Perkins, D. Vigil-Fowler, S. Siol, D. O. Scanlon, A. Zakutayev, et al., *Chemistry of Materials* **2017**, *29*, 1964–1988.

[68] T. Hellmann, C. Das, T. Abzieher, J. A. Schwenzer, M. Wussler, R. Dachauer, U. W. Paetzold, W. Jaegermann, T. Mayer, *Advanced Energy Materials* **2020**, *10*, 2002129.

Chapter 4

Overcoming Intrinsic Quantum Confinement and Ultrafast Self-Trapping in Ag-Bi-I and Cu-Bi-I Based 2D Double Perovskites through Electroactive Cations

This chapter is based on the following publication:

R. Hooijer†, S. Wang†, A. Biewald, C. Eckel, M. Righetto, M. Chen, Z. Xu, D. Blätte, D. Han, H. Ebert, L. M. Herz, R. T. Weitz, A. Hartschuh, T. Bein, submitted.

†R.H. and S.W. contributed equally to this work.

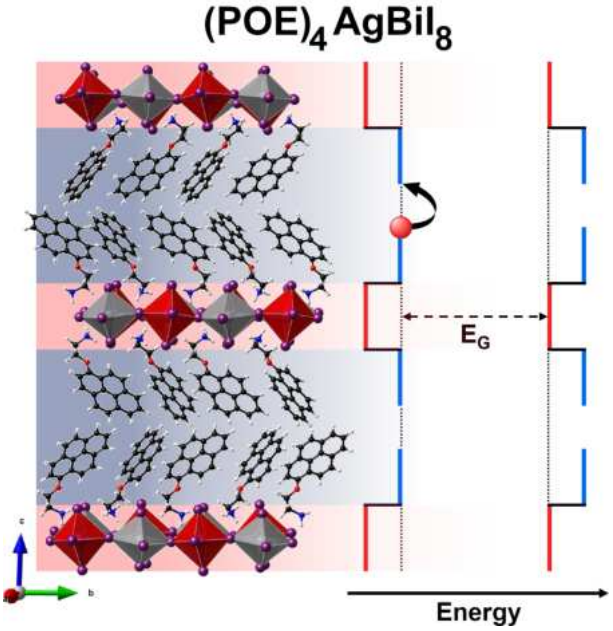

The work was conceived by R. Hooijer and S. Wang. S. Wang synthesized the organic cations. R. Hooijer and S. Wang contributed to the synthesis of single crystals, thin-film fabrication and characterization, as well as optoelectronic device fabrication and characterization. R. Hooijer performed XRD and GIWAXS measurements and analysis. R. Hooijer coordinated all cooperations. S. Wang coordinated the DFT cooperation. A. Biewald performed PL measurements and analysis. C. Eckel performed conductive AFM measurements and analysis. M. Righetto performed OPTP measurements and analysis. M. Chen work on the project through her Master's Thesis. Z. Xu performed crystal exfoliations. D. Blätte performed EQE measurements. D. Han performed DFT calculations. R. Hooijer performed complete data interpretation and writing the manuscript. All authors wrote and edited the manuscript for final submission.

4.1 Abstract

The possibility to combine organic semiconducting materials with inorganic halide perovskites opens exciting pathways towards tuning optoelectronic properties. Exploring stable and non-toxic, double perovskites as a host for electroactive organic cations to form two-dimensional hybrid materials is an emerging opportunity to create both functional and lead-free materials for optoelectronic applications. By introducing naphthalene and pyrene moieties into Ag-Bi-I and Cu-Bi-I double perovskite lattices, intrinsic electronic challenges of double perovskites are addressed and the electronic anisotropy of two-dimensional perovskites can be modulated. $(POE)_4AgBiI_8$ containing pyrene moieties in the 2D layers was selected from a total of eight new 2D double perovskites, exhibiting a favorable electronic band structure with a type IIb multiple quantum well system based on a layer architecture suitable for out-of-plane conductivity, and leading to a photocurrent response ratio of almost three orders of magnitude under AM1.5G illumination. Finally, an exclusively parallel oriented thin film of $(POE)_4AgBiI_8$ was integrated into a device to construct the first pure n = 1 Ruddlesden-Popper 2D double perovskite solar cell.

4.2 Introduction

Two-dimensional (2D) organic-inorganic metal halide perovskites are emerging as a promising class of semiconductors, not only owing to their superior intrinsic and extrinsic stability but also to their vast compositional and structural space.[1] Especially the organic component offers unique opportunities to tune the physical properties study the underlying physics of such materials and to control key features relevant for applications.[2] In the quest for more stable and less toxic alternatives to Pb-based perovskites, double perovskites (DP) based on Ag, Cu, Bi and Sb are at the focus of recent research efforts.[3,4] The flag-bearing DP $Cs_2AgBiBr_6$ has emerged as a stable alternative to Pb-based perovskites for applications in solar cells, photocatalysts or X-ray detectors.[5–8] The introduction of the corresponding 2D counterparts - referred to as 2D DPs - has further broadened their compositional space owing to their superior thermodynamic stability, thus giving access to iodide DPs and smaller band gaps. This, combined with the tunability of the organic intragallery phase makes them prototypical to study underlying physical properties such as electronic structure, charge-carrier dynamics, electrical conductivity and photoresponse.[9–12]

Generally, 2D Ruddlesden-Popper (RP) DPs have the chemical formula $(A^I)_4A_{2n-2}B(I)_nB(III)_nX_{6n+2}$, where A^I is a large monovalent organic cation, A is a small monovalent organic or inorganic cation, B(I) is a monovalent metal ion, B(III) is a trivalent metal ion, X is a halide anion and n is the number of corner-sharing metal halide $[B(I)X_6]^{5-}$ and $[B(III)X_6]^{3-}$ octahedral layers (Figure 4.1a). Due to the spatial separation of the inorganic and organic layers in the crystal structure, the resulting electronic band structure can be described as a multiple quantum well (QW) system.[13] The band alignment in QW systems is determined by the frontier orbital contributions of the large organic cation – i.e. its highest occupied molecular orbital (HOMO) and lowest unoccupied molecular orbital (LUMO) - and the inorganic layer band edges, namely its valence band maximum (VBM) and conduction band minimum (CBM). As shown in Figure 4.1b, the energetic alignment between the organic and inorganic bands yields an organic-inorganic heterojunction and four cases are possible, classified as Ia, Ib, IIa and IIb. In 2D perovskites, the most commonly formed heterojunction is the type Ib, where charge carriers or excitons are confined into the inorganic layer, thus yielding large exciton binding energies and charge transport anisotropy.[14] Since several optoelectronic device applications require directional charge transport (e.g. between contacts in solar cells) this anisotropy must be considered and adapted accordingly. However, attempts to control the crystallization direction of 2D perovskite thin films and understanding the relevant mechanisms to date have shown only limited success.[15,16] An alternative promising strategy is to

overcome the quantum confinement intrinsically, by modulating the frontier band energy levels through the use of electroactive, functional cations.[17–19] While this strategy has been recently employed for lead-based 2D perovskites, it remains mostly uncharted for 2D DPs.[20–24]

In this work, we present the synthesis of eight new n = 1 RP DPs based on naphthalene/pyrene containing cations in Ag-Bi-I and Cu-Bi-I inorganic frameworks. We investigate their structural and optoelectronic properties, with special regard to the electrical conductivity and the charge-carrier dynamics to finally construct the first solar cell based on this materials class.

4.3 Results and Discussion

4.3.1 Structural Characterization

The n = 1 RP structures are based on the inorganic frameworks containing either $[AgI_6]^{5-}$ + $[BiI_6]^{3-}$ or $[CuI_6]^{5-}$ + $[BiI_6]^{3-}$ octahedra, with organic cations based on the polycyclic aromatic systems naphthalene or pyrene, fused by an ether linkage to an ethyl- or propylammonium chain: naphthalene-O-ethylammonium (NOE), naphthalene-O-propylammonium (NOP), pyrene-O-ethylammonium (POE), pyrene-O-propylammonium (POP) (Figure 4.1c), yielding $(NOE)_4AgBiI_8$ (NOE-Ag), $(NOP)_4AgBiI_8$ (NOP-Ag), $(POE)_4AgBiI_8$ (POE-Ag), $(POP)_4AgBiI_8$ (POP-Ag), $(NOE)_4CuBiI_8$ (NOE-Cu), $(NOP)_4CuBiI_8$ (NOP-Cu), $(POE)_4CuBiI_8$ (POE-Cu) and $(POP)_4CuBiI_8$ (POP-Cu). The structures and high crystallinity of the thin films are confirmed by XRD (Figure 4.1d). The visible reflections in the low 2θ region correspond to the crystallographic planes orthogonal to their unit cells long axis, which in context of the layered structure is the out-of-plane direction. The length of this directly correlates with the size of the organic cations, as the organic layers consist of a double-layer of adjacent organic cations. The reflections shift downwards to smaller angles 2θ for increasing size of the cations along NOE < NOP < POE < POP (SI Table 4.2).

Additionally, single crystals of NOP-Ag, POE-Ag and POP-Ag were obtained through a vapor diffusion method, enabling us to obtain their structure solutions, with the exemplary 2D RP crystal structure of POE-Ag shown in Figure 4.1a. Due to the insufficient quality of the POE-Ag single crystals, we optimized the structure through DFT calculations for further discussion and for the band structure calculations (Section 2.2). Altough suitable single crystals for the NOE-Ag and Cu based materials could not be grown for reasons discussed in more detail in Figure 4.16 and 4.17, their 2D RP structure in thin film form was confirmed through GIWAXS, as well as room temperature Raman measurements (Figure 4.19). Furthermore, the crystalline orientation indicated earlier by the thin film XRD measurements was also confirmed through GIWAXS. The strong preferential orientation with the organic and inorganic layers parallel to the substrate surface is indicated in the GIWAXS data by the reflections of the set of planes along (00l) being located in the middle at $q_r = 0\,\mathrm{nm}^{-1}$, along the azimuthal angle $\chi = 0°$ (Figure 4.1e). The other observable reflections originate from the set of planes of (10l) and (01l), at $q_r \approx 8\,\mathrm{nm}^{-1}$ and from (11l) at $q_r \approx 11\,\mathrm{nm}^{-1}$.

All materials show very similar patterns, confirming the 2D RP structure, as they could either be indexed directly to their single crystal structural models (NOP-Ag, POE-Ag and POP-Ag) or to refined lattice parameters, originating from the other single crystal struc-

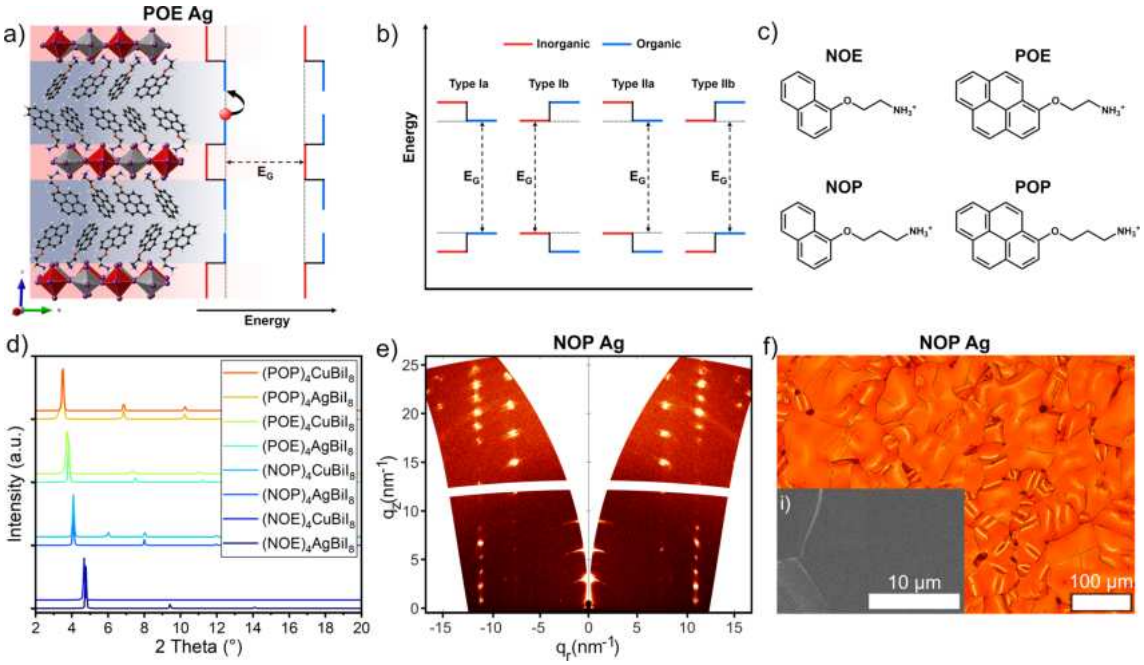

Figure 4.1: a) Exemplary crystal structure of the n = 1 RP DP phase POE-Ag with illustration of the electronic quantum well structure in context of the layered structure. A type IIb QW is shown, as determined by means of DFT calculations. In POE-Ag, the schematic hole (red sphere) is able to traverse the gap in the organic bilayer, as confirmed through conductivity data. b) Different possible types of electronic QWs in 2D perovskites. c) Structural formulas of the organic cations used in this work. d) Thin film XRD patterns of all eight materials displaying the characteristic, low 2θ reflections for parallel crystal orientation. Y-axis offset was added for visibility. e) GIWAXS data of a NOP-Ag thin film on ITO measured with a sample-detector distance (SDD) of 121 mm and incident angle α_i = 0.3°. f) Optical micrograph and scanning electron micrograph (inset i) of NOP-Ag thin film on ITO.

tures (full set of GIWAXS data and index parameters shown in Figures 4.8 to 4.15). The most notable difference in these patterns is seen in the pattern of NOE-Cu, where indexing revealed larger changes of the lattice parameters, most notably the different lengths of the a and b axes (a = 12.1 Å and b = 8.6 Å) and the strong deviation from 90 ° of the α and β angles compared to the other seven materials.

We further evaluated the morphology of thin film samples with visible light microscopy and scanning electron microscopy. The thin films, spincoated from DMF or DMSO solutions, form homogeneously at both the macroscopic and microscopic scale, showing complete coverage with large crystallites and domain sizes (Figure 4.1f shows NOP-Ag, with the remaining materials shown in Figure 4.18). The crystal structure of low n value 2D perovskites typically leads to the formation of large, oriented crystalline domains with lateral sizes ranging in the tens of microns. This phenomenon can be observed in many other thin films or the plate-like crystal habit of single crystals of these materials.[11]

Overall, the 2D RP structure is confirmed for all materials, as well as their exclusively parallel orientation when grown as thin films on substrates. This offers an attractive platform to investigate and understand the limitations of electronic anisotropy in the n = 1 2D

RP DPs and to evaluate the influence of the organic cations.

4.3.2 Electronic Structure and Band Alignment

The optimized crystal structure parameters of NOP-Ag, POE-Ag and POP-Ag, based on the single crystal structure solutions agree well as shown in table 4.3. The PBE+SOC calculated band gaps of NOE-Ag, POE-Ag and POP-Ag are smaller compared to the experimentally measured band gaps (Table 4.4). Nevertheless, PBE+SOC gives a reasonable qualitative description of band dispersion and band edge components.[25] For all the materials, the VBM and CBM are located at the Γ point, as shown in Figure 4.2a for POE-Ag and in Figure 4.20a and 4.21a for NOP-Ag and POP-Ag, leading to the direct band gaps.[10]

Moreover, the projected densities of states (DOS) are used to understand the atomic character of the frontier orbitals and the role of the different organic cations (NOP, POE and POP) on the transport properties. For NOP-Ag, as shown in Figure 4.20b, the VBM is composed of Ag-d orbitals and I-p orbitals, and the CBM is dominated by Bi-p and I-p orbitals, analogous to its 3D prototype Cs_2AgBiX_6 (X = Cl/Br).[26,27] Due to the dominant contribution of inorganic parts to the band edges, the VB and CB of NOP-Ag are dispersive. For POE-Ag and POP-Ag, the compositions of the VBM change. As shown in Figure 4.2b and Figure 4.21b, they are predominantly made up of the organic cations C-p and O-p orbitals instead of the inorganic orbitals, and therefore the band dispersions of the VB become smaller with respect to NOP-Ag. The components of the CBM for POE-Ag and POP-Ag are the same as that of NOP-Ag, namely the Bi-p and I-p orbitals. Besides the electronic structure, Figure 4.2c-d and 4.21c display the band alignment of POE-Ag, NOP-Ag and POP-Ag, respectively. NOP-Ag forms a type Ib heterojunction between the inorganic and organic parts, whilst POP-Ag forms a type IIb heterojunction. Notably, POE-Ag shows a unique band alignment. As shown in Figure 4.2c, in POE-Ag, there are overlapping states which are composed dominantly of the POE organic cations and a small portion of the inorganic component. The overlapping state around the VB is almost isoenergetic to the HOMO (VBM) with a difference of 0.18 eV, and the state above the CBM shows a separation of around 1 eV with the CBM. Their partial charge density is displayed in Figure 4.22. Such mixed states would benefit the transport of charge carriers in POE-Ag, providing joint transport channels.

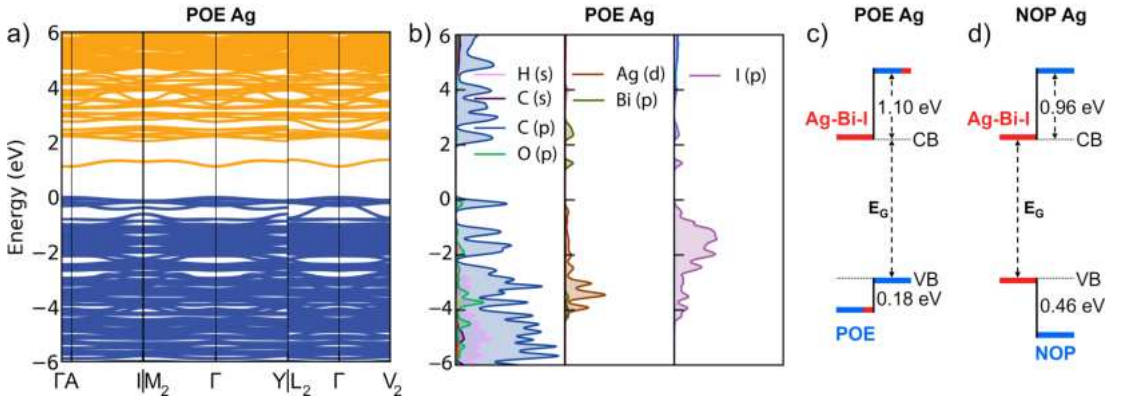

Figure 4.2: a) PBE+SOC calculated band structure with b) the partial density of states and c) the band alignment for POE-Ag. d) Band alignment for NOP-Ag (Band structure in Fig. S1).

In addition to the overlapping states, there are different molecular stacking types within the organic layers for NOP-Ag, POE-Ag and POP-Ag (Figure 4.23 to 4.25). In crystalline pyrene the stacking distance between the parallel oriented pyrene molecules is around 3.54 Å, which is within the typical interplanar distance range for π-π interaction between 3.4 – 3.7 Å.[28,29] This benefits the charge separation and transfer among molecules.[30] In POE-Ag, the pyrene moieties in the POE molecules are arranged in a similar manner, indicating a π-π interaction (Figure 4.23). In contrast, POP molecules in POP-Ag do not show this type of arrangement. Furthermore, POE molecules display an edge-face arrangement of the organic intralayer, i.e. along the out-of-plane direction, contrary to the edge-edge arrangement observed in POP-Ag and NOP-Ag (Figure 4.24). As demonstrated by Passarelli et al., edge-to-face interactions across the van der Waals gap yield better orbital overlap and enhanced out-of-plane conductivity as compared to edge-to-edge interactions.[22] These two factors combined, i.e. the electronic characters of the quantum wells and the structural arrangement of the organic cations enable better charge transport and photoresponse in POE-Ag compared to all other materials, as shown later on in section 4.3.4.

4.3.3 Optical Properties

Absorption

All materials based on the Ag-Bi inorganic framework show similar absorbance spectra with absorption edges and corresponding band gap energies between 2.15 - 2.19 eV, shown in Figure 4.3a, followed by two peaks indicated by droplines, that are characteristic for 2D iodide double perovskites.[11,24] One would tentatively assign these peaks to excitonic contributions, akin to their 2D lead perovskite counterparts, given that the systems here are also quantum confined systems, where Wannier-type excitonic species could be confined to the inorganic octahedral network. Contrarily, theoretical absorption spectra that exclude excitonic effects also result in the characteristic shape with one lower and one higher energy maximum.[11,24] Additionally, the emission for 2D DPs is not as typically narrow at cryogenic temperatures as one would expect for a purely excitonic origin, although as we showed for $(4\,FPEA)_4AgBiI_8$, a moderate narrowing can still be observed.[11] The complete picture for DPs and 2D DPs is not as clear as for other well-known semiconductors, since many effects and charge carrier species exist simultaneously. Firstly, since the heavy p-electron Bi atom introduces strong spin-orbit coupling, leading to a largely separated band in the CBM (Figure 4.2a, 4.20a and 4.21a), the first absorbance maximum should be related to the associated transitions, as was also shown for $Cs_2AgBiBr_6$.[31] Secondly, one can still expect the formation of indirect or self-trapped excitonic species from these states, as well as electron-phonon coupling which is known to be very strong in 3D DPs and even stronger in 2D DPs.[32–36] The observed double peak in 2D DPs could thus be a combination of the above effects but is not trivial to model without further spectroscopic and theoretical insights.

The materials NOP-Cu, POE-Cu and POP-Cu, based on the Cu-Bi inorganic framework show slightly smaller band gap energies, between 2.01 - 2.07 eV and do not exhibit the two peaks as clearly as seen in the Ag-Bi materials. The smaller band gaps of NOP-Cu, POE-Cu and POP-Cu should be related to the different electronic contributions to the band structure, since the inorganic VBM contributions are based on Ag/Cu-d and I-p orbitals and Cu 3d electrons have higher relative energy than Ag 4d electrons.[37] For Ag and Cu based materials, POE-Ag and POE-Cu both exhibit the respectively smallest band gap based on calculated and experimental values (Figure 4.3 and Table 4.4), as we showed due to the dominant contribution of POE to the VBM. NOE-Cu deviates from the other materials, in that its absorbance exhibits a blueshift with a band gap energy of 2.46 eV but again with a strong peak at 2.6 eV. Since Bi will still introduce spin-orbit coupling effects to the electronic structure of Cu-Bi based materials, the same reasoning for the maxima, mentioned before applies, with similar absorbance responses shown in

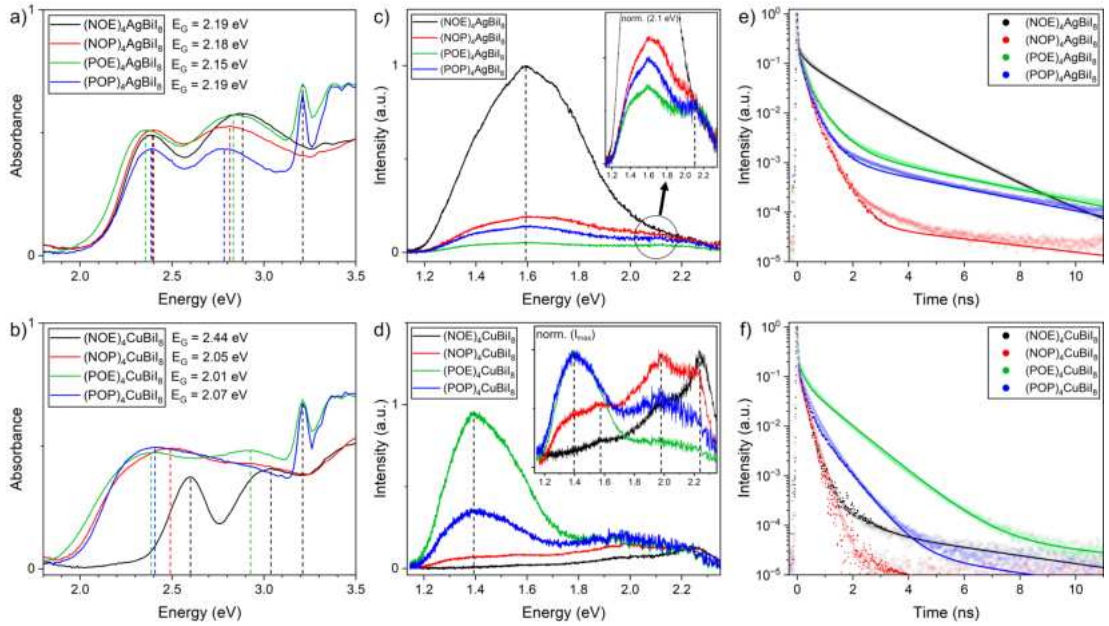

Figure 4.3: Thin film UV-Vis absorbance spectra of a) Ag-Bi and b) Cu-Bi based materials with an inset detailing the estimated band gap energies obtained with the Tauc method. The characteristic two maxima as well as the pyrene absorption are marked with droplines, in their respective color. c) and d) Steady-state photoluminescence spectra of Ag-Bi and Cu-Bi based materials with insets of spectra normalized to the second peak at 2.1 eV for Ag-Bi based materials and to the highest intensity peaks for Cu-Bi based materials (E_{exc} = 3.1 eV). Time-resolved photoluminescence spectra of e) Ag-Bi and f) Cu-Bi based materials, with the experimental data in semi-transparent points and the fitted transients overlayed as full points.

other works on Cu-Bi 2D DPs and 3D Cu-Bi DPs.[37,38] The less distinct peaks were also observed in Cu-Bi thin films elsewhere,[16] but still without a clear reason established. For the inorganic contributions to the electronic structure, the octahedral distortions, tilts and bond lengths play the major role, as this dictates the orbital overlap.[10,39] The formation of octahedra in double perovskites requires Cu or Ag to reside in a 6-fold coordination by halogen atoms. In fact, Cu(I) halides prefer to form 3- or 4-fold coordination as [CuX_3] polyhedra or [CuX_4] tetrahedra. Instead, Ag(I) can be 3-, 4- but also more easily 6-fold coordinated with halogen atoms. Especially for larger halogen atoms such as Br and I, based on Pauling's first rule, the smaller radius of Cu(I) ions may lead to more distortions with 6-fold coordination compared to Ag(I) ions.[40,41] Therefore there is so far also no report of Cu-Bi based 3-dimensional DPs, as far as we know. Next, one must also consider the modulating effect of the organic cations on the inorganic lattice. For NOE, the shorter ethyl-linkage leads to less freedom and possibly a shorter penetration depth of the anchoring ammonium moiety into the cuboctahedral cavities. This, combined with the reduced π-π interactions compared with POE and POP cations, NOE cations may have an inferior ability to modulate the inorganic framework. NOE-Cu does indeed show a very different GIWAXS pattern and lattice parameters compared to NOE-Ag as mentioned in section 4.3.1 and shown in Figure 4.12, possibly leading to the different absorption profile

compared to the other materials. The other three Cu-Bi based materials (NOP-Cu, POE-Cu and POP-Cu) display very similar GIWAXS patterns compared to their Ag-Bi based counterparts, in agreement with their similar absorbance profiles (Figure 4.12 and 4.3b). Finally yet importantly, the pyrene-based 2D DPs POE-Ag, POP-Ag, POE-Cu and POP-Cu, show increased absorbance in the UV region beyond 3.1 eV, compared to NOE and NOP based materials, with a strong peak at 3.21 eV. This fits the molecular absorption of pyrene, which has a strong absorption peak at 3.28 eV (378 nm) in its crystalline form, originating from its monomeric ^1L_b transition.[22,42–44]

Charge-Carrier Dynamics and Photoluminescence

Photoluminescence (PL) emission of thin films was recorded following excited by a laser with an energy of 3.1 eV. As shown in Figure 4.3c-f, the steady state and time resolved spectra exhibit characteristics similar to other 2D DPs, namely i) a broad emission spectrum, ii) weak emission intensity and iii) charge-carrier lifetimes on the order of nanoseconds. The Ag-Bi materials all show similar emission profiles, with an emission maximum centered at $\approx$ 1.6 eV and full-width half-maximum values of $\approx$ 500 meV at room temperature (RT). Furthermore, they show a second, weak feature centered around 2.1 eV. Normalized spectra reveal these emission bands to be identical for all four Ag-Bi materials (Figure 4.3c). The FWHM is very broad also in context of similar structures such as $(4\,FPEA)_4AgBiI_8$ showing a FWHM of 320 meV at RT.[11] As shown in previous publications, the origin of this broad emission does not exclusively lie in the excitonic band-to-band emission, but rather in the prevalence of various kinds of structural and electronic defects in these 2D double perovskites.[11,45,46] The broad emission can generally be observed in 3D double perovskites as well as in single-crystals of 2D double perovskites, which excludes lowered structural dimensionality or thin film crystal quality being a primary reason for the broad PL.[47,48] Structural defects such as iodine vacancies, molecular cation interactions with excitons or charge-carriers at defect sites, self-trapping and disorder between Ag and Bi metal octahedral sites have all been proposed as possible origins for this emission.[46,49] We note that the absolute intensities of this first feature decreases along NOE-Ag > NOP-Ag > POP-Ag > POE-Ag, with NOE-Ag showing a much larger intensity than the other materials (Figure 4.3c). As shown earlier, NOP-Ag forms a type Ib QW which should promote radiative band-to-band recombination from CBM to VBM, given the dominant contribution to the band edges of the inorganic sublattice. Due to the even stronger PL intensity of NOE-Ag, we can also assume a type Ib QW, since both cations are based on naphthalene and its electronic contribution is quite far below the VBM for NOP-Ag (around 0.46 eV lower, Figure 2d). Since the features at 1.6 eV are the energetically lowest, they could predominantly originate from excited states of the first

absorption feature, i.e. transitions into the separated CBM of the inorganic layers. The intensity trend supports this, since NOP-Ag, POE-Ag and POP-Ag have direct band gaps and for NOE-Ag it can be assumed to also be direct. The dispersive VBM in NOP-Ag and possibly also NOE-Ag, both dominantly inorganic, promotes radiative recombination from the dominantly inorganic CBM (for all materials) compared to the flat VBM in POE-Ag and POP-Ag, both dominantly organic. The broadness centered around this feature at 1.6 eV, would then also support the earlier mentioned origins, since almost all structural defects, such as various Schottky and Frenkel defects, especially the known influence of vacancies and disorder of equatorial iodines, self-trapping, octahedral disorder and color-centers, would be located in the inorganic sublattice.[6,26,46]

Besides the first main feature centered at 1.6 eV, there is a second feature centered at 2.1 eV (Figure 4.3c), with much lower intensity but the same profile for all four Ag-Bi materials (Figure 4.3c inset). The ratio between the emissions at 2.1 eV and 1.6 eV decreases along POE-Ag > POP-Ag $\geq$ NOP-Ag > > > NOE-Ag (Figure 4.26). Since for all four materials, there is a large energetic gap between the lowered inorganic band forming the CBM and the higher lying bands, made up of firstly organic contributions and growingly mixed inorganic-organic contributions (Figure 4.2, 4.20 and 4.21), radiative recombination at 2.1 eV would be favored for POE-Ag and POP-Ag, since their VBM is predominantly based on orbitals from the organic sublattice.

Next, we discuss steady-state spectra of Cu-Bi materials, where the first emission is centered at $\approx$ 1.4 eV for NOP-Cu, POE-Cu and POP-Cu. This redshift is consistent with the $\approx$ 0.2 eV smaller EG of the Cu-Bi materials compared to the Ag-Bi materials. The absolute intensity decreases along POE-Cu > POP-Cu > NOP-Cu, inverted to Ag-Bi materials (Figure 4.3d). This emission is only distinguishable for POE-Cu and POP-Cu with a FWHM $\approx$ 300 meV, being narrower than the Ag-Bi emission at 1.6 eV. NOE-Cu does not show this emission, which could be due to its larger E_G of 2.44 eV, i.e. the excitation energy being much closer than for the other materials, or due to different decay pathways in the structurally slightly different material. If this energetically lowest emission is related to similar origins as discussed for Ag-Bi materials, the observed inverted intensities could be due to the different contribution of the organic cations to the band structure for Cu-Bi materials, since the relative energy of Cu 3d electrons is larger, as mentioned earlier, which will result in relative changes of the organic cation energy levels. Looking at the absorbance data and the less pronounced maxima, the energetic separation of the CBM could also be smaller compared to Ag-Bi materials. The next emission peak, observable for NOE-Cu and NOP-Cu, lies at 1.58 eV (Figure 4.3d inset), which could be overshadowed by the larger emission at 1.4 eV for POE-Cu and POP-Cu. Furthermore, a third and fourth emission peak can be observed at 1.98 eV and 2.24 eV, where the former

is visible for all materials but the latter is predominantly seen in NOE-Cu and NOP-Cu (Figure 4.26). Due to the lack of crystal and band structure for Cu-Bi materials, we do not wish to speculate about the origins of the different emission spectra, with the exception, that the different spectrum observed for NOE-Cu is clearly due to its blueshifted absorption profile.

Next, we discuss the time resolved PL transients for all eight materials. They were fitted with a triexponential decay function (Tables 4.5-4.6). The transients show an initial, fast component on the order of less than 10 ps, followed by a second, longer-lived component in the range of ns and a third component up to 10 ns (Figure 4.3e-f), integrating over the whole spectral range. While the third component is evident in for example POE-Ag and POP-Ag, its intensity is on the low end of the signal (see amplitudes in Tables 4.5-4.6). We thus used the triexponential fit for all materials, although it most likely is just a very weakly emissive state caused by the slowest, possibly defect-related recombination process. The signal around 2.1 eV contains only the fast component, supporting an emissive state from a higher energy level, due to the band splitting and the intensity ratio between high and lower energy emissions, as discussed earlier (Figure 4.27). Accordingly, the slower component is most pronounced in NOE-Ag and POE-Cu, with both showing the strongest intensities for the low energy emissions at 1.6 eV and 1.4 eV, respectively (Figure 4.3c-f). These ultrafast decay times are in line with previous reports on 2D double perovskites and are most likely linked to a similar mechanism. Before the initial observed PL component, an ultrafast localization or self-trapping process of an excitonic polaronic state takes place, whos emission appears <10 ps. This state is possibly further mediated through defect-state recombination, which appear on the two following timescales in the range of ns.[11] This interpretation should be considered in addition to the previously discussed electronic band characteristics and QW structures. To determine the diffusion coefficients of the emissive species, we recorded time resolved PL across the confocal spot leaving the excitation beam stationary in a confocal microscope (Figure 4.4a-b).

From fitting the broadening of the gaussian-shaped confocal PL emission, we extracted the diffusion coefficients for two individual time scales (Figure 4.28). The first component appears on the ps timescale as an initial broadening in the rising signal. We attribute this to the ambipolar charge-carrier diffusion (Figure 4.4a) from free charge-carriers generated upon nonresonant photoexcitation, as further shown through optical-pump terahertz-probe (OPTP) spectroscopy measurements later on. The second component appears on the ns timescale, which we attribute to the excitonic polaron diffusion (Figure 4.4b) as a result of charge-carrier localisation processes already reported for different 2D and 3D DPs.[6,11,50] As further support for this attribution, we note that the diffusion coefficients for the initial free charge-carriers are around one to two orders of magnitude larger than

for the following polaron diffusion. Therefore, we propose the following mechanism: upon nonresonant photoexcitation mobile free ambipolar charge carriers are generated. These charge carriers rapidly localise and form an excitonic state, coupled to a phonon deforming the surrounding lattice (forming a polaron) which reduces their mobility, yet preserving a remnant mobility. For all materials, the diffusion coefficients of the fast component scatter around 0.8 $cm^2\ s^{-1}$ (dotted line Figure 4.4a), which is a combination of excitons and free charge-carriers. It is not possible to separate both signals. Observing the fast diffusion coefficient in the first picoseconds is in good agreement with the OPTP measurements having an ultrafast localization of the excited state. This is in agreement with the aforementioned strong electron- and exciton-phonon coupling in DPs.[33,35,50,51] In the soft, ionic lattice of DP crystals, lattice charge shielding effects or electron-phonon-coupling will occur, reducing the mobility of all charge-carriers. Since this PL diffusion signal appears at the noise free signal rise (Figure 4.28), these values are an estimation for an upper boundary of the free ambipolar charge carrier diffusion coefficient. The diffusion coefficients of the polaronic, excitonic state, on the longer time scale of up to 2 ns, vary for the different materials (Figure 4.4b). Hereby, the materials with POE and POP show the highest values up to 0.14 $cm^2\ s^{-1}$. The Cu-Bi based ones with NOE and NOP have the slowest mobile excited state at 0.01 $cm^2\ s^{-1}$. Comparing the measured polaron lifetime with the diffusion coefficients, it seems that the materials with higher mobility are connected to longer excited state lifetimes. One interpretation is that the organic molecules have an influence on quenching the excited states, which are not contributing anymore to further energy conversion of charge separation processes.

To further confirm the proposed mechanism, we investigate the early-time dynamics of free charge carriers by OPTP spectroscopy measurements. The THz photoconductivity following photoexcitation with the same energy (3.1 eV) shows a consistent ultrafast decay with a time constant of around 300 fs (Figure 4.4c) for all the studied thin films. The observed THz photoconductivity decay confirms the presence of an ultrafast transition between an initially photogenerated mobile state and an immobile state. A similar behavior has been reported for different 2D DPs and has been attributed to a phonon-mediated self-trapping process, which is a hallmark of Ag-Bi halide semiconductors.[6,11,52,53] It is worth noting that, given the high exciton binding energy in 2D DPs (generally in the range of $\approx$ 250 meV or higher for 2D DPs),[36,54] we expect the presence of strong excitonic interaction and the formation of a stable exciton population at room temperature, as predicted by the Saha equation.[55] Given this high exciton binding energy, which shifts intraexcitonic transition into the mid-IR range, the observed THz photoconductivity in the measured THz range (between 0.5 to 2.5 THz) can be safely attributed to free charge-carrier conductivity similarly to that reported for 3D DPs.[56] The estimated effective mo-

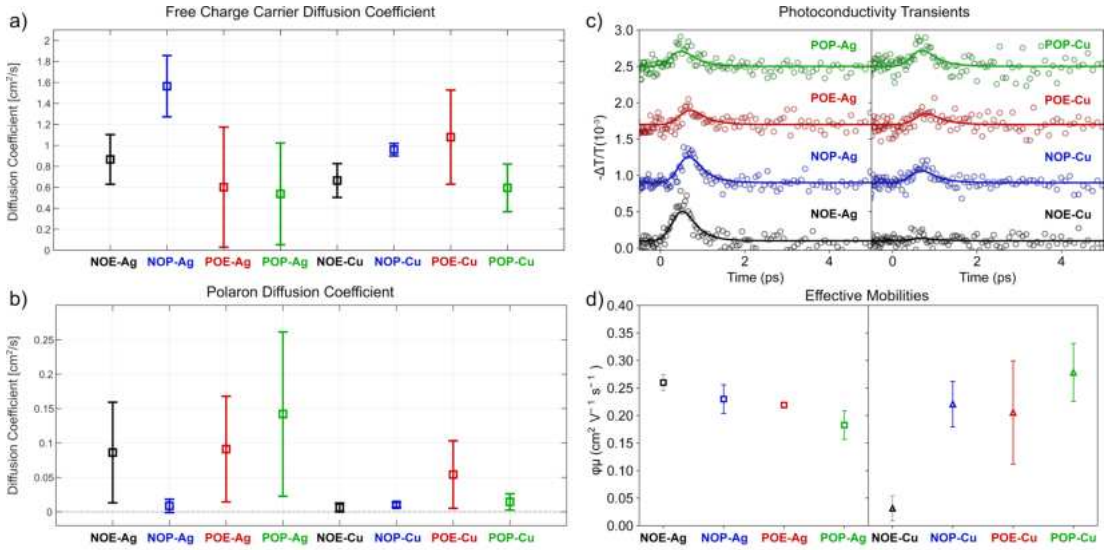

Figure 4.4: Diffusion coefficients extracted from fluorescence-lifetime imaging for a) the initial ultrafast component, attributed to free charge carriers and for b) the second, longer lived component, attributed to the polarons. c) Photoconductvity transients from optical-pump terahertz-probe spectroscopy and d) the extracted effective mobilities.

bilities are very similar for all the studied materials and lie between $\phi\mu \approx 0.2\,\mathrm{cm^2\,V^{-1}\,s^{-1}}$ to $0.3\,\mathrm{cm^2\,V^{-1}\,s^{-1}}$. Slightly higher mobility values are observed for NOE and NOP-based materials than for POE- and POP-based materials, except for NOE-Cu due to its larger E_G and for POP-Cu, which shows the highest mobility of all materials. We stress that, also considering the high exciton binding energies in these materials, charge-carrier mobilities reported here are effective mobilities, depending on the ratio between free charge carriers and excitons generated. Hence, the near absence of signal observed for NOE-Cu, could possibly be caused by the higher E_G (Figure 4.3b). Furthermore, we note that small variation in the estimated $\phi\mu$ can reflect either changes in the exciton binding energies or changes in the mobilities. Interestingly, observed charge-carrier mobility values are slightly lower than our previously reported mobility of $\approx 0.6\,\mathrm{cm^2\,V^{-1}\,s^{-1}}$ for $(4\,\mathrm{FPEA})_4\mathrm{AgBiI_8}$ (possibly due to different octahedral distortions) and an order of magnitude lower compared to mobilities for $\mathrm{Cs_2AgBiBr_6}$ of $\approx 1.3\,\mathrm{cm^2\,V^{-1}\,s^{-1}}$ (localized state) and $\approx 3\,\mathrm{cm^2\,V^{-1}\,s^{-1}}$ (delocalized state).[6,11] These ultrafast charge-carrier dynamics are consistent with all results on 2D DPs and can either be attributed to exciton formation or ultrafast charge carrier localization.[57] Finally, we note that the PL diffusion and the OPTP mobility measurements are both probing in-plane charge transport of thin film samples and thus can not give information about the out-of-plane transport and mobilities of these anisotropic 2D structures.

4.3.4 Photoconductivity and Photovoltaic Performance

To assess the suitability of the investigated 2D DPs for photoactive applications, we initially conducted simple in-plane photoconductivity measurements with top-evaporated contacts on thin films (note and Figure 4.29-4.30). Under dark conditions, only POE-Ag, POE-Cu and POP-Ag showed conductivity values above the instrument sensitivity of 1×10^{-10} A. At maximum bias voltage of 5 V, POE-Ag showed a current of around 1×10^{-9} A, while POE-Cu showed a higher current of around 1×10^{-7} A. Under illuminated conditions, different responses were observed. Materials based on NOE and NOP showed only slightly increased conductivities (Figure 4.5a-b). Materials based on POE and POP showed much larger photoresponses, with POE-Ag and POP-Ag having the highest on/off ratios with factors between one and three orders of magnitude. While POE-Cu did not feature a large on/off ratio, due to its higher conductivity under dark conditions its absolute conductivity under illuminated conditions was still the highest among the samples (Figure 4.6b). The photoresponse of POP-Cu was comparable to the small values of the materials based on NOE and NOP and was thus excluded from further investigation. Since POE-Ag showed the most promising photoresponse, we further investigated the influence of thin film synthesis conditions to optimize performance (Figure4.31 and Table 4.7), resulting in the values shown in Figure4.5a and b.

To compare the impact of the aromatic system in the organic cations, we also prepared $(4\,\mathrm{FPEA})_4\mathrm{AgBiI}_8$ as a reference material, under the exact same preconditions. The current under dark and light conditions as well as the on/off ratio is far below the values of POE-Ag, and is more similar to the values of NOE-Ag, NOE-Cu, NOP-Ag, NOP-Cu and POP-Cu. We note, that a clear differentiation between in- and out-of-plane contributions is not possible due to the device architecture featuring top-evaporated electrodes. Nonetheless, we assume that it is unlikely that all current is exclusively flowing through only the surface layer of the thin films, i.e. one or several atomic layers. Since all materials are exclusively oriented with the organic and inorganic layers parallel to the substrate surface, an improved in- and out-of-plane photoconductivity for POE-Ag, POE-Cu and POP-Ag can thus be assumed. Some materials exhibit a hysteresis in the photoconductivity scans, where the zero current points have an offset, namely at positive bias for the forward scan (-5 V to 5 V) and at negative bias for the backward scan (5 V to -5 V)(Figure 4.29). This points to a built-in potential or polarizability for some of the materials. Metal halide perovskites are ionic crystals and ionic mobility is a well known phenomenon.[58] Moreover, crystal lattices of 2D perovskites are known to be polarizable due to non-centrosymmetric space groups (which our results demonstrate for POE-Ag = Cc and POP-Ag = $C2$) or due to reorganization of the organic cations under voltage bias.[57] Another possible explanation for this phenomenon could be a charge buildup under bias, resembling simple

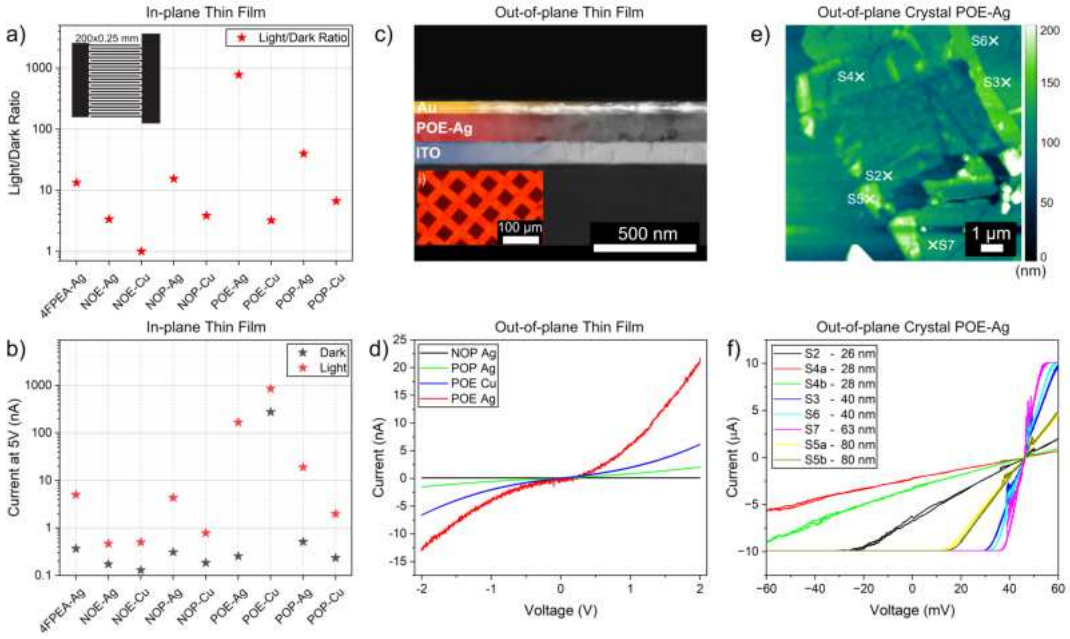

Figure 4.5: a) Light/dark in-plane conductivity ratios with an inset showing the top contact evaporation mask with channel length and width 200 x 0.25 mm. b) Current values at 5 V bias of thin film samples on ITO for all eight materials and 4FPEA-Ag as a reference material. c) SEM cross section of the cAFM thin film sample of POE-Ag on ITO, with top evaporated Au contacts, shown in an inset as an optical light microscopy top view. d) Out-of-plane cAFM IV curves of NOP-Ag, POE-Ag, POP-Ag and POE-Cu thin film samples. The increased signal/noise in the POE-Ag curve is due to a decreased sensitivity setting, due to the higher current flow in the sample. e) Height profile AFM image of exfoliated POE-Ag single crystal fragments on ITO with measured spots indicated as white crosses. f) The respective cAFM IV curves of different spots shown in e).

capacitive behavior, i.e. an insufficient conductivity for charge carriers to move through the lattice under applied voltage. In the case of POE-Ag this could be an explanation for the hysteresis under dark conditions, while the conductivity is greatly increased and no hysteresis is observable under light conditions (Figure 4.29 and 4.31).

To assess the out-of-plane conductivity of the most conducting materials POE-Ag, POP-Ag and POE-Cu compared to the moderately conducting NOP-Ag, we performed out-of-plane conductivity measurements on illuminated thin films with top electrodes and bottom indium doped tin oxide (ITO) substrates (Figure 4.5c-d). Top electrodes were contacted via a conductive atomic force microscopy (AFM) tip. The IV curves in Figure 4.5d show the largest current for POE-Ag and lower currents for POE-Cu and POP-Ag, while NOP-Ag shows no current response at all. This agrees well with the measured photoconductivity responses of macroscopic in-plane measurements (Figure 4.29).

Furthermore, an exfoliated single crystal sample of POE-Ag made through adhesive tape exfoliation of POE-Ag crystals onto an ITO substrate (Figure 4.6g) clearly confirms the significant out-of-plane conductivity, measured on multiple different spots at different crystal thickness with an AFM tip as top electrode in contact mode (Figure 4.5e-f).

Apparently, there is no clear thickness dependence of the measured currents, which could be caused by different contact resistances due to different crystal surfaces resulting from exfoliation or the different contact quality due to the volatility of the AFM tip in contact mode. Interestingly, a different type of hysteresis than previously mentioned, namely an increased current signal in the positive bias direction can be observed for out-of-plane thin film measurements of POE-Ag, POP-Ag and POE-Cu. Their IV-curves exhibit a non-linear behaviour (Figure 4.5d), in contrast to the linear ohmic behavior of the out-of-plane crystal samples (Figure 4.5f) and the in-plane thin film samples (Figure 4.29). The S-shape observed is typically caused by large contact interface resistance, which is plausible since out-of-plane thin film samples are contacted through a 30 μm^2 evaporated Au pad compared to the out-of-plane crystal sample, where the contact is directly the AFM tip with a tip radius > 25 nm. In contrast, in-plane thin film measurements do not exhibit this S-shape (Figure 4.29 and 4.32), although they are contacted through an evaporated Ag electrode with surface contact on the order of mm^2 (Figure 4.5a inset). The difference could either be caused by the different work functions of Ag (ϕ = 4.0 eV – 4.6 eV) and Au (ϕ = 5.2 eV – 5.4 eV),[59,60] or by the different measurement geometry at the same anisotropic, crystal orientation. More detailed views of the IV curves are shown in Figures 4.32-4.35 which show a clear Schottky barrier type behavior (Figure 4.33b) only for POE-Ag while POE-Cu and POP-Ag show the S-shaped IV curve. This could be caused by the larger out-of-plane photoconductivity of POE-Ag compared to the other materials. Since 2D perovskites are known to suppress ion migration, especially in the out-of-plane direction we attribute the S-shape in the out-of-plane thin film measurements to the different Schottky barrier heights at the Au contact and the different work functions of Ag and Au. Nonetheless, a small hysteresis upon multiple cycle measurement for out-of-plane thin film POP-Ag is observable, pointing towards small ionic movements and the build-up of an electric field (Figure 4.35).

Consistent with the above observations, it makes sense why the free charge carrier diffusion coefficients (Figure 4.4a) and effective mobilities (Figure 4.4d) are slightly higher for NOE-Ag and NOP-Ag compared to POE-Ag and POP-Ag. As shown earlier through DFT calculations, NOP-Ag has a type Ib QW structure and shows no significant out-of-plane conductivity. Thus the charge carriers are confined to the inorganic layers. POE-Ag and POP-Ag behave vice versa, showing smaller free charge carrier diffusion coefficients and mobilities (Figure 4.4a and d), while showing larger polaron diffusion coefficients (Figure 4.4b), compared to NOP-Ag. Since the polaron diffusion is the component with the much longer lifetime, it could be connected with the increased photoconductivities for POE and POP materials. With NOE-Ag lying between the values of the two cases, we hypothesize that it should also have a type Ib QW structure due to the similar energy levels

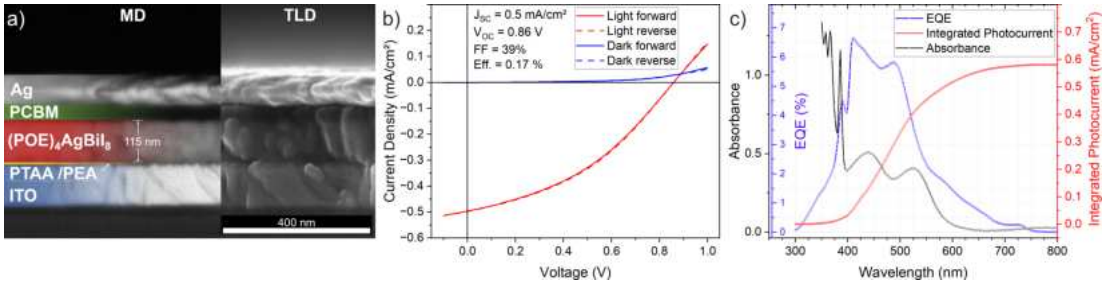

Figure 4.6: a) SEM cross section of the constructed solar cell with inverted p-i-n architecture ITO/PTAA/PEA/POE-Ag/PCBM/Ag for back-scattered electrons (MD = mirror detector) and secondary electrons (TLD = through lense detector). b) Corresponding JV curve and c) EQE and absorbance spectrum of the solar cell.

of its constituents like NOP-Ag. As discussed earlier, the organic intralayer arrangement also plays an important role in out-of-plane charge transport, which was shown to be favorable with the ethyl linkage compared to the propyl linkage (POE>POP), as is the case here with NOE compared to NOP.

Overall, the results establish the proof-of-concept for the enhancement of out-of-plane conductivity in samples featuring functional, organic cations with fused aromatic π-systems such as POE and POP, exhibiting favorable QW band alignment as well as favorable intra-organic layer alignment compared to other 2D DP materials.

Having identified POE-Ag as the most promising candidate of the eight materials for photoactive application, we constructed solar cells to assess the viability of 2D DPs in this context. We chose a planar architecture to ensure the parallel orientation of the POE-Ag active layer, consisting of ITO as the cathode substrate, a 2 nm thick poly[bis(4-phenyl)(2,4,6-trimethylphenyl)amine (PTAA) layer as the hole-transport-material (HTM), a phenethylammonium (PEA) interface passivation treatment (1 mg/ml) for increased wettability and better connection of the perovskite layer, POE-Ag as the active perovskite layer, [6,6]-Phenyl-C61-butyric acid methyl ester (PCBM) as the electron-transport-material (ETL) and Ag as the anode electrode (Figure 4.6a). To confirm the crystalline quality and the orientation of the POE-Ag layer, we measured GIWAXS on a functioning pixel of a full device (Figure S24). The non-optimized champion device produced a J_{sc} = 0.5 mA cm^{-2}, V_{oc} = 0.86 V, fill factor (FF) = 39% and power conversion efficiency (PCE) = 0.17% and the JV curve of the solar cell showed no hysteresis in the forward and reverse scan (Figure 4.6b). Statistical box plots are shown in Figure 4.38. As an evaluation criterion for working pixels, a V_{oc} above $0.4\ V$ was chosen, as it confirms a complete active layer and no short circuit in the diode structure. The solar cells were constructed from different POE-Ag solution concentrations (0.075 M, 0.0375 M and 0.01875 M) to achieve different thicknesses, since the results discussed above establish a strong impact of thickness on out-of-plane conductivity. For thicker layers, i.e. cells 1-4, almost no

J_{sc} could be measured, due to the perovskite layer being too thick for significant charge being extracted, as the mobility of free charge carriers is too small. For thinner active layers, i.e. cells 5-12, J_{sc} values above 0.15 mA cm^{-2} could be measured, indicating that the optimal thickness for charges to be extracted ranges from 100-200 nm. While a thinner layer should be able to produce higher JSC values, with a decreased thickness the continuity and complete coverage of the active layer becomes increasingly challenging with the fabrication of the solar cell, and the light capturing becomes less efficient. The champion device with a POE-Ag thickness of 115 nm (Figure 4.6a) consistently had all pixels producing an average J_{sc} of 0.47 mA cm^{-2}, with average V_{oc} values of 0.83 V. While this represents already a promising initial V_{oc}, the difference to the band gap of the material at 2.15 eV still indicates a significant voltage loss in the full device. Reasons could include defect states in the active material (trapping sites and sub bandgap states), as well as non-optimized energy alignment with the HTL and ETL materials. As most commercially available HTL and ETL materials are optimized for lead based perovskites and small band gap active materials, we envision that future transport layer optimisation will improve VOC values by a significant margin. The energy levels of POE-Ag have to be determined through ultraviolet photoelectron spectroscopy (UPS) to select and synthesize suitable transport materials. Furthermore, the low FFs between 30-40% indicate a large series resistance in POE-Ag solar cells, which is expected due to the low out-of-plane conductivity of 2D perovskites in general, as well as possibly high interfacial resistances. This is also evident in the S-shape of the out-of-plane IV curve shown in Figure 4.5d, due to contact resistances. Finally, to confirm the origin of the J_{sc} from the POE-Ag active layer, we performed external quantum efficiency (EQE) measurements (Figure 4.6c). With the absorbance of POE-Ag overlayed, it is clear that the generated current originates from the generation of charge carriers in the POE-Ag layer, as the spectral UV-vis absorption profile matches the EQE profile in good agreement. Furthermore, the predicted integrated photocurrent of 0.58 mA cm^{-2} is in good agreement with the solar cell's J_{sc} of 0.5 mA cm^{-2}. Interestingly, the absorbance peak at 390 nm, originating from the pyrene moiety, also contributes to the photocurrent as observed in the EQE peak at the same position. This is another key indication that (i) the organic layer contributes to the generation of mobile charge carriers and (ii) that these charge carriers can get extracted from the organic layer, providing further evidence of the out-of-plane charge carrier transport.

4.4 Conclusion

We synthesized eight new two-dimensional n = 1 RP double perovskites (DPs) based on Ag-Bi-I and Cu-Bi-I inorganic networks with large, organic cations NOE, NOP, POE and POP containing fused aromatic moeities. Thin films of these materials crystallize in the typical manner with their 2D layers oriented parallel to the substrate, allowing us to determine their anisotropic charge carrier and electrical conductivity properties. Through DFT calculations, we confirmed the formation of different quantum well structures of the type Ib for NOP-Ag and type IIb for POE-Ag and POP-Ag. All materials show similar optical properties for Bi-based DPs, with band gap energies around 2.2 eV for Ag-Bi materials and 2.0 eV for Cu-Bi materials, with the exception of NOE-Cu at 2.4 eV. The emissive and charge carrier properties were found to be similar to other reported 2D DPs, further confirming their intrinsic mechanism of ultrafast conversion of free charge carriers to less mobile states due to exciton formation, phonon-mediated self-trapping (i.e. small polaron formation) or other defect states. The diffusion coefficients of the free charge carriers average at around $0.8\,cm^2\,s^{-1}$ with associated picosecond lifetimes for all materials ($1.6\,cm^2\,s^{-1}$ for NOP-Ag), while the polaron diffusion coefficients (with associated lifetimes of nanoseconds) reach larger values between $0.09\,cm^2\,s^{-1}$ to $0.14\,cm^2\,s^{-1}$ only for NOE-Ag, POE-Ag, POE-Cu and POP-Ag. Accordingly, the electrical conductivity is greatest for these materials and POE-Ag showed a photoconductivity on/off ratio of 779. Due to the different QW types and the different intraorganic layer arrangement, POP-Ag, POE-Ag and POE-Cu showed out-of-plane conductivity with a 10x greater out-of-plane current for POE-Ag compared to POP-Ag. Finally, POE-Ag was employed as the active material for the construction of a solar cell with a J_{sc} = $0.5\,mA\,cm^{-2}$, V_{oc} = 0.86 V, FF = 39 % and PCE = 0.17 %. To the best of our knowledge, this is the first report of a functioning n = 1 lead-free, 2D DP solar cell in a planar architecture with exclusively parallel oriented layers. We envision that with further research aiming to achieve higher n value iodide 2D DPs i.e. lowering their EG towards optimum for reaching the Shockley-Queisser limit and by purposeful integration of functional organic cations to tune the charge carrier and transport properties, this material class can be a stable and lead-free alternative for constructing single-junction solar cells. Beyond the use in photovoltaics, the nanoscale integration of organic semiconducting materials and 2D lead-free perovskites offers numerous opportunities for designing novel heterostructures with widely tunable optoelectronic properties.

4.5 Experimental Section

Thin Film Synthesis

All substrates were cleaned by ultrasonication for 15 min in a solution of acetone, isopropanol, and ethanol (1:1:1). Afterward, the substrates were cleaned for 10 min under nitrogen plasma. Stoichiometric amounts of 1 eq. AgI (Sigma-Aldrich, 99%), 1 eq. CuI (Sigma-Aldrich, 99.995% trace metal basis), 1 eq. BiI3 (TCI, anhydrous >98%) and 4 eq. NOEI, NOPI, POEI, POPI (prepared according to Ref.[22]) were weighed in and dissolved in DMF (Sigma-Aldrich, anhydrous 99.8%), DMSO (Sigma-Aldrich, anhydrous >99.9%), GBL (Sigma-Aldrich >99%) or NMP (Sigma-Aldrich, anhydrous, 99.5%) in different ratios depending on the material and substrate, to receive the desired concentrations. The optimized solvent mixture and annealing temperatures for all materials are given in Table 4.1. If not specified elsewhere, thin films were prepared according to these conditions. All thin films were spin-coated in a glove box with N2 atmosphere. The spin-coating program consists of an initial step of 10 s at 3000 rpm, followed by a second step of 40 s at 5000 rpm. Spin-coating solutions were preheated at 70 °C and substrates were preheated at 100 °C.

Table 4.1: Optimized solvent and annealing parameters for the synthesis of all eight materials.

	Material	Solvent	Annealing 1 (1 min)	Annealing 2 (5 min)
1	$(NOE)_4AgBiI_8$	1:1 (DMSO:DMF)	140 °C	100 °C
2	$(NOP)_4AgBiI_8$	1:1 (DMSO:DMF)	140 °C	100 °C
3	$(POE)_4AgBiI_8$	1:1 (DMSO:DMF)	140 °C	100 °C
4	$(POP)_4AgBiI_8$	1:1 (DMSO:DMF)	140 °C	100 °C
5	$(NOE)_4CuBiI_8$	1:1 (DMSO:DMF)	140 °C	100 °C
6	$(NOP)_4CuBiI_8$	1:1 (DMSO:DMF)	140 °C	100 °C
7	$(POE)_4CuBiI_8$	1:1 (DMSO:DMF)	140 °C	100 °C
8	$(POP)_4CuBiI_8$	1:1 (DMSO:DMF)	140 °C	100 °C

Thin Film X-Ray Diffraction (TF-XRD)

TF-XRD measurements were carried out on a Bruker D8 Discover diffractometer in Bragg–Brentano geometry, with Ni-filtered Cu-Kα1 radiation (λ = 1.5406 Å) and a position sensitive LynxEye detector.

Single-Crystal X-Ray Diffraction (SC-XRD)

SC-XRD measurements were carried out on a Bruker D8 Venture Txs system equipped with a multilayer mirror monochromator and a Mo-Kα rotating anode X-ray tube (λ = 0.71073 Å). The frames were integrated with the Bruker SAINT software package. Data were corrected for absorption effects using the Multi-Scan method (SADABS). The structure was solved and refined using the Bruker Shelxtl Software Package.

Grazing-Incidence Wide Angle X-Ray Scattering (GIWAXS)

GIWAXS measurements were carried out on an Anton-Paar SAXSpoint 2.0 with a Primux 100 microfocus source with Cu-Kα1 radiation (λ = 1.5406 Å) and a Dectris Eiger R 1M 2D Detector.

Scanning Electron Microscopy (SEM)

SEM measurements were carried out on an FEI Helios NanoLab G3 UC Dual Beam microscope.

Optical Visible Light Microscopy

Optical microscopy measurements were carried out on a Leica - DM4 M light microscope equipped with a digital camera. Images were acquired in incident or transmission lighting settings and for single-crystals a polarization filter was used.

Computational methods

The calculations of electronic structure were carried out within the framework of density functional theory (DFT),[61,62] which was performed with the Vienna Ab initio Simulation Package (VASP).[63,64] The projector augmented-wave (PAW) method was employed to describe the interactions between core and valence electrons.[65] The plane wave cutoff energy was set to 520 eV, and a Γ-centered Monkhorst-Pack k-point mesh with a grid spacing of $2\pi \times 0.030$ Å^{-1} was used for Brillouin zone integration. The geometry optimization was performed until the energy and force reached less than $10^{-}6$ eV and 0.001 eV/Å, respectively. The Perdew-Burke-Ernzerhof (PBE) exchange-correlation functional with Tkatchenko-Scheffler (TS) van der Waals (vdW) corrections was employed to describe the long-range interaction.[66–68] The reliability of TS for low dimensional perovskite halides has been validated.[69,70] The optimized lattice parameters agree with experimental ones, which are listed in Table S3. It is noteworthy that unreasonable geometry optimization, viz. large difference, leads to the artificial Rashba splitting.[69–71] As the spin-orbit coupling (SOC) effect strongly influences the electronic structure of compounds containing heavy p-electron elements like Bi,[72,73] it was included here. In

the meantime, hybrid functional with SOC was not currently affordable for these large systems, as the computational resources are demanding and was thus not included. The post-processing of band structure and density of states were carried out by sumo.[74]

UV-Vis Absorption (UV-Vis)

UV-Vis spectra were taken on a Perkin-Elmer Lambda 1050 spectrometer equipped with a 150 mm integrating sphere. Thin films were measured in transmittance mode.

Raman Spectroscopy

FT-Raman measurements were performed on film samples with a RAM II extension of the Bruker Vertex 70 with a N_2 cooled germanium detector at an excitation wavelength of 1064 nm and a laser power of 300 mW. Spectra were recorded with a resolution of 4 cm^{-1} and averaged over 10000 scans.

Confocal Photoluminescence (PL)

For PL measurements, hyperspectral images and time resolved PL images, a home-built confocal laser scanning microscope was used. It is based on a microscope body (NIKON) which is combined with an xyz-piezo-scanning stage (PHYSIK INSTRUMENTE). The samples were measured upside down in epi-direction with an air objective (0.85 NA, NIKON). A beamsplitter (MELLES GRIOT 03BTL005) and a spectral, 490 nm long pass filter was used to separate the laser from the PL-light. A sub picosecond laser (ichrome TOPTICA) which is tunable from 476 nm to 645 nm was used for excitation. Here, the laser wavelength was set to 476 nm which was additionally filtered by a 473/10 nm band pass (CHROMA) in the excitation arm. The detection side consists of two parts, which are separated by a collapsible mirror. Additionally, a scannable mirror in the back focal plane was installed for the diffusion measurements scanning around the confocal spot. One arm in the detection has an avalanche photo diode (APD, type: MPD PDM, detector size 50 x 50 μm), which can be combined with Time Correlated Single Photon Counting (TCSPC) electronics (BECKER UND HICKEL) measuring time resolved PL-transients. The second part consists of a spectrometer (ANDOR SHAMROCK SRi303) combined with an open electrode CCD camera (ANDOR NEWTON DU920) recording spectra. The data were recorded using a customized LABVIEW (NATIONAL INSTRUMENTS) program that combines the manufacturers' software to our desired measurements. Further processing and analysis were carried out using MATLAB (MATHWORKS) to obtain the PL spectra, TCSPC transients and the images.

External Quantum Efficiency (EQE)

EQE Measurements were performed on a homemade system with a halogen lamp, a monochromator and a silicon reference diode. The light was chopped at 330 Hz and the signal was detected through a lock-in amplifier.

In-Plane-Conductivity

Electrical in-plane conductivity was measured by constructing thin films on isolating glass substrates. For contacts, Ag was evaporated on top of the thin films, through a shadow mask with interdigitated electrode pattern (Figure 4.5a inset). Measurements were taken with a standard white light LED spectrum, calibrated to the intensity of 1 sun, and under dark conditions through a voltage sweep between -5 V and 5 V using a Keithley 2401 source meter.

Out-of-Plane-Conductivity

The electrical measurements for out-of-plane conductivity on thin films and flakes (Figure 4.5 in the main manuscript) were performed with an atomic force microscope (Jupiter Oxford) under ambient atmosphere. A conductive AFM tip (SCM-PIT-W from NanoWorlds, Width: 28 µm; Length: 225 µm; resonance frequency: 75 kHz; force constant: 2.8 N/m) was used to contact the top side of the sample. The conducting substrate ITO was grounded with Ag paste. For the thin film samples additional top electrodes (100 nm Au, 30 µm x 30 µm) were thermally evaporated with shadow masks to increase the area of charge injection. The IV-curves were recorded completely by the AFM program without additional measurement equipment. Mention should be made of the quantitative values of such measurement. Many factors are preventing to read out exact values for the out-of-plane conductivity. For instance, tip degeneracy, tip pressure, surface roughness. To minimize the influence of these and other factors we performed multiple IV-curves at different spots while using the same tip. This enables a qualitative comparison between the materials.

Solar Cell characterization

Current density–voltage (JV) characteristics were measured using a Newport OrielSol 2A solar simulator with a Keithley 2401 source meter. The devices were illuminated through a shadow mask, yielding an active area of 0.0831 cm^2. The JV curves were recorded under standard AM 1.5G illumination from a xenon lamp, and calibrated to a light intensity of 100 mW cm^{-2} with a Fraunhofer ISE certified silicon diode.

Mechanical exfoliation of the $(POE)_4AgBiI_8$ crystals

The POE-Ag crystal was carefully picked up by tweezers and placed on a low adhesion tape (ELP BT-150P-LC from Nitto). A new piece of low adhesion tape was slightly pressed on the attached crystal on the tape and quickly removed. Two mirrored crystal areas on the tapes were thus created. The tapes were then pressed together and removed for 4-5 times, where each time the two tapes are slightly misplaced in order to avoid crystal areas overlapping. Then tape with exfoliated crystal was firmly pressed on a plasma cleaned ITO glass substrate. The substrate was placed on a hot plate and heated to 70 °C for 10 minutes. At the end, the tape was gently removed and the POE-Ag thin sheets remained on the substrate.

4.6 Acknowledgements

The authors gratefully thank Dr. Steffen Schmidt for the SEM measurements and Dr. Peter Mayer for the SC-XRD measurements and structure solutions. Furthermore, the authors thank the Bavarian research network Solar Technologies go Hybrid, the Deutsche Forschungsgemeinschaft (DFG) Excellence Cluster e-conversion (EXC 2089/1 – 390776260) and the DFG focus program SPP 2196 for funding. L.M.H. acknowledges support through a Hans Fischer Senior Fellowship from the Technical University of Munich's Institute for Advanced Study, funded by the German Excellence Strategy. L.M.H. and M.R. acknowledge funding from the UK Engineering and Physical Sciences Research Council (EPSRC).

4.7 Supporting Information

Overcoming Intrinsic Quantum Confinement and Ultrafast Self-Trapping in Ag-Bi-I and Cu-Bi-I Based 2D Double Perovskites through Electroactive Cations This chapter is based on the following publication:

R. Hooijer†, S. Wang†, A. Biewald, C. Eckel, M. Righetto, M. Chen, Z. Xu, D. Blätte, D. Han, H. Ebert, L. M. Herz, R. T. Weitz, A. Hartschuh, T. Bein, submitted.

Table 4.2: Angle 2 Theta (°) of the first characteristic reflection of the thin film diffractograms and its corresponding lattice spacing distance d (nm), for all eight materials. Visualization in Figure 4.7 below.

Material	First Reflection 2 Theta (°)	d (nm)
$(NOE)_4AgBiI_8$	4.76	1.857
$(NOP)_4AgBiI_8$	4.02	2.200
$(POE)_4AgBiI_8$	3.80	2.323
$(POP)_4AgBiI_8$	3.43	2.574
$(NOE)_4CuBiI_8$	4.65	1.899
$(NOP)_4CuBiI_8$	4.07	2.172
$(POE)_4CuBiI_8$	3.86	2.291
$(POP)_4CuBiI_8$	3.49	2.535

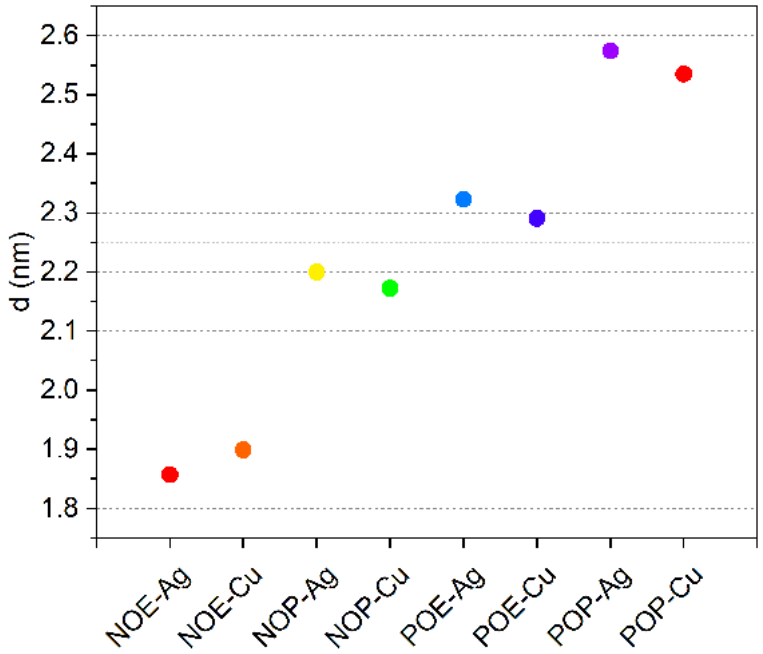

Figure 4.7: Visualization of the data in Table S2, the lattice spacing d (nm) of the first characteristic reflections of the thin film diffractograms of all eight materials.

The observed trend in Table 4.2 and Figure 4.7 corresponds to the increasing size of the organic bilayer due to the increasing size of NOE < NOP < POE < POP. Between two materials with the same organic cation a small difference is observable between the Ag and Cu material. While NOE-Ag < NOE-Cu, the remaining materials are the opposite, i.e. NOP-Ag > NOP-Cu, POE-Ag > POE-Cu, POP-Ag > POP-Cu. Reasons for the small differences could include different axial bond lengths in $[Ag/CuI_6]^{5-}$ octahedra, as for Ag-I they tend to be larger than for Cu-I, due to the different electronic configuration and ionic size, as well as due to the stronger Jahn-Teller distortion in Cu over Ag complexes/coordination. Furthermore, the distortion of the octahedral layers of the materials can be different. Thirdly, the organic cations have some degree of freedom regarding their orientation within the organic layer itself, which also strongly affects the lattice spacing distance.

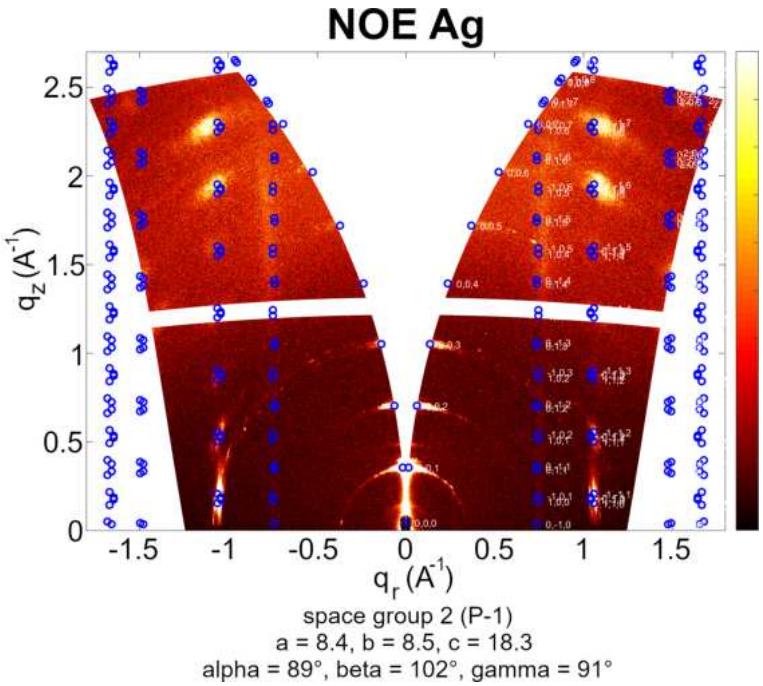

Figure 4.8: Indexed GIWAXS images for Ag-Bi materials on ITO substrates. Measurement time was 30 minutes with an incident angle α_i = 0.3° and a sample detector distance (SDD) = 121 mm. The unit cell length parameters are given in Å.

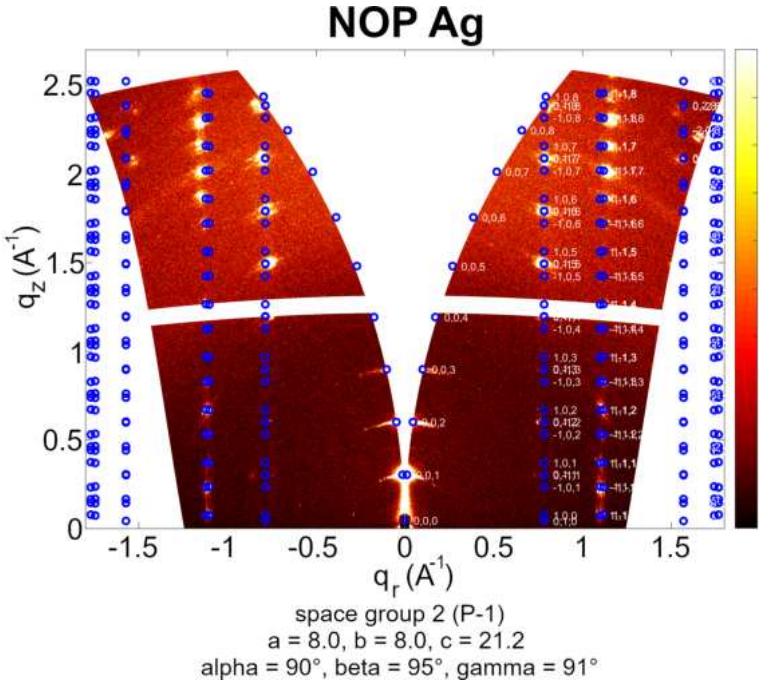

Figure 4.9: Indexed GIWAXS images for Ag-Bi materials on ITO substrates. Measurement time was 30 minutes with an incident angle α_i = 0.3° and a sample detector distance (SDD) = 121 mm. The unit cell length parameters are given in Å.

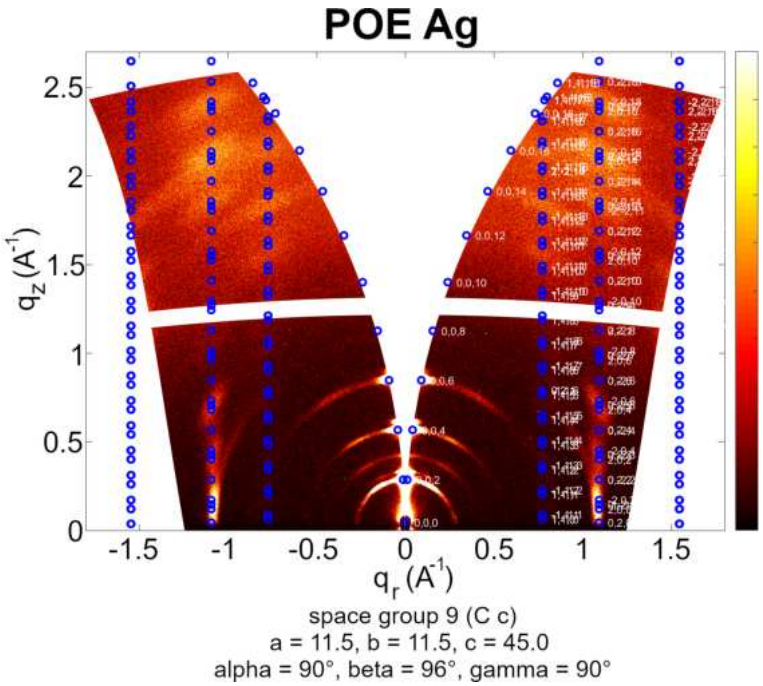

Figure 4.10: Indexed GIWAXS images for Ag-Bi materials on ITO substrates. Measurement time was 30 minutes with an incident angle α_i = 0.3° and a sample detector distance (SDD) = 121 mm. The unit cell length parameters are given in Å.

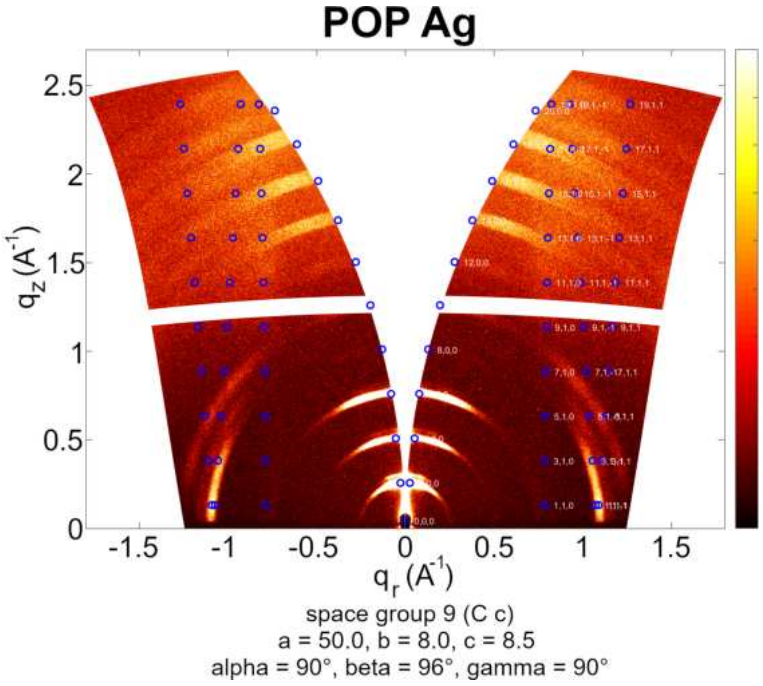

Figure 4.11: Indexed GIWAXS images for Ag-Bi materials on ITO substrates. Measurement time was 30 minutes with an incident angle α_i = 0.3° and a sample detector distance (SDD) = 121 mm. The unit cell length parameters are given in Å.

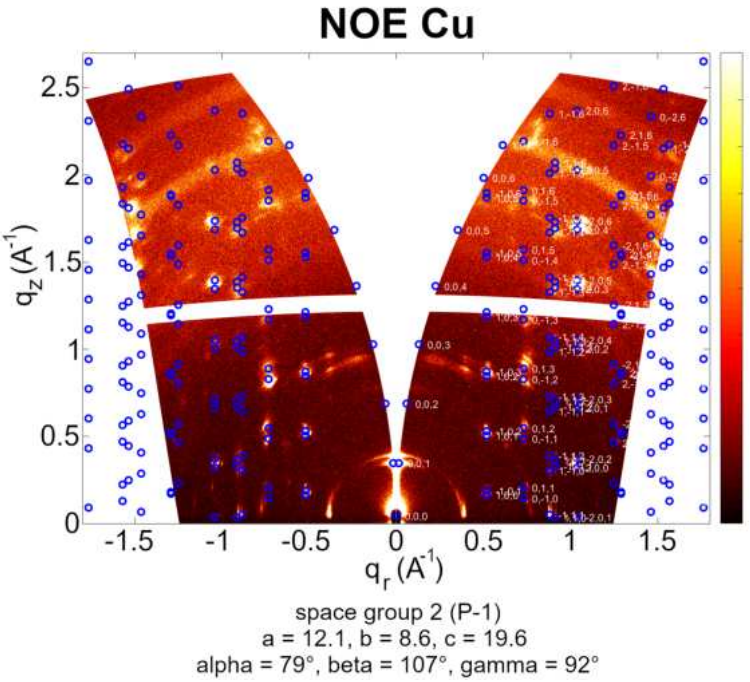

Figure 4.12: Indexed GIWAXS images for Cu-Bi materials on ITO substrates. Measurement time was 30 minutes with an incident angle α_i = 0.3° and a sample detector distance (SDD) = 121 mm. The unit cell length parameters are given in Å.

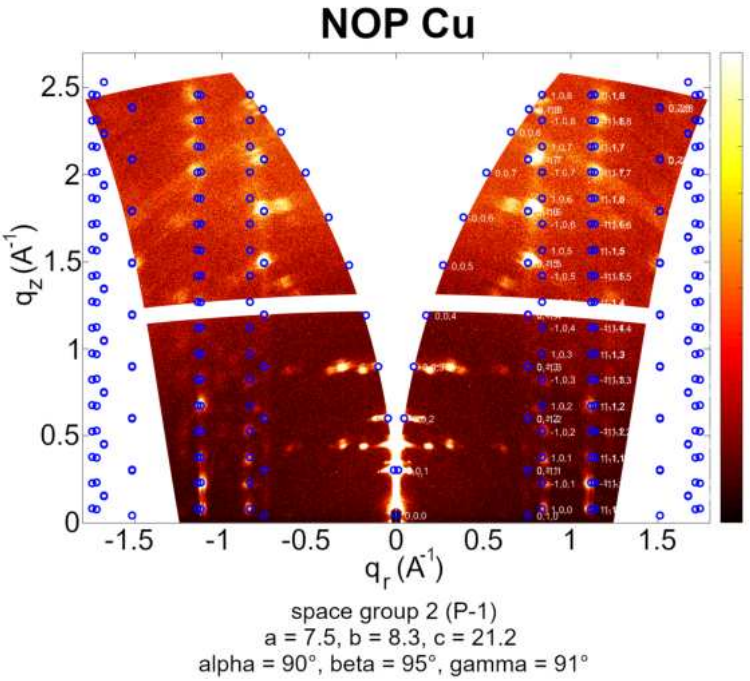

Figure 4.13: Indexed GIWAXS images for Cu-Bi materials on ITO substrates. Measurement time was 30 minutes with an incident angle α_i = 0.3° and a sample detector distance (SDD) = 121 mm. The unit cell length parameters are given in Å.

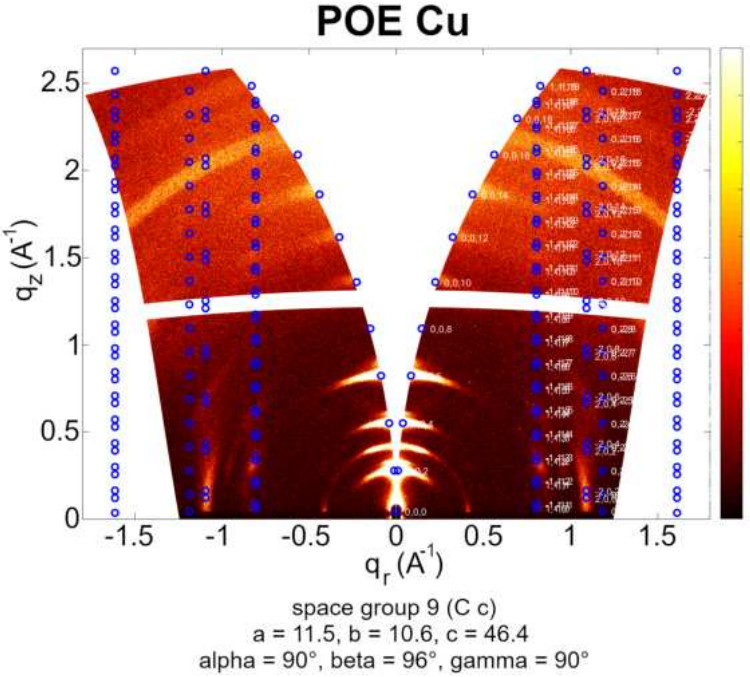

Figure 4.14: Indexed GIWAXS images for Cu-Bi materials on ITO substrates. Measurement time was 30 minutes with an incident angle α_i = 0.3° and a sample detector distance (SDD) = 121 mm. The unit cell length parameters are given in Å.

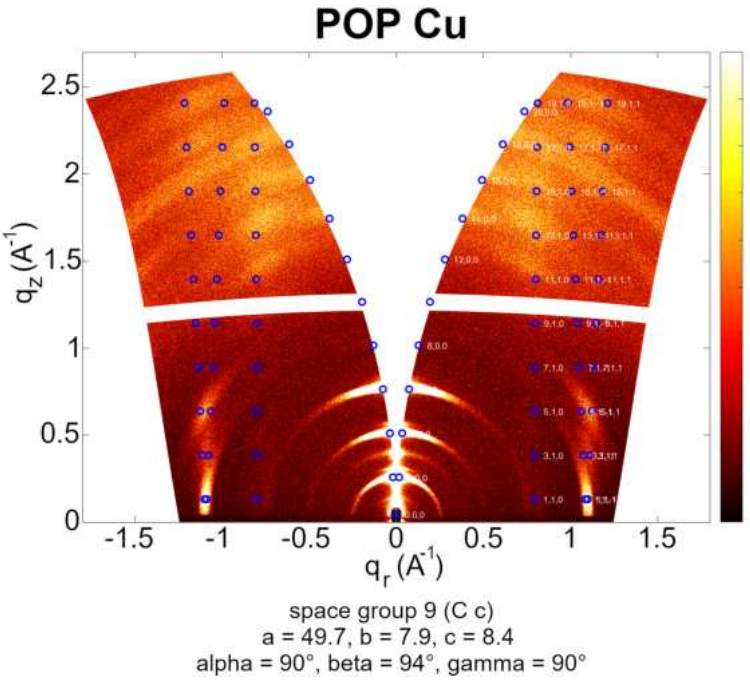

Figure 4.15: Indexed GIWAXS images for Cu-Bi materials on ITO substrates. Measurement time was 30 minutes with an incident angle α_i = 0.3° and a sample detector distance (SDD) = 121 mm. The unit cell length parameters are given in Å.

To confirm the 2D Ruddlesden-Popper double perovskite structures, all thin films were measured and indexed according to our single crystal structure solutions from NOP-Ag, POE-Ag and POP-Ag (see CIF files or Tables 4.7-4.8). GIWAXS signals are generally somewhat broadened, on the one hand due to the polycrystalline nature of macroscopically probed thin films and on the other hand due to the different scattering events in thin film GIWAXS under the distorted wave Born-approximation, as a result of combinations of refraction at the film surface, reflection at film/substrate interface and diffraction of the film material. This, combined with broadened reflections due to thin film quality and thermal stress exerted on thin film structures during annealing, gives an approximation of lattice parameters through indexing, but is not directly comparable to single crystal solutions and DFT optimization results. Nonetheless, the 2D RP DP structure and the well-defined thin film orientation can be confirmed for all eight materials in this work.

All resulting lattice parameters and space groups are listed below the respective GIWAXS image (Figure 4.8 to 4.15). For the calculation of the diffraction positions, the lattice planes corresponding to the out-of-plane 2D orientation were chosen to be parallel to the substrate surface plane, i.e. (001) for NOE-Ag, NOP-Ag, POE-Ag, NOE-Cu, NOP-Cu and POE-Cu and (100) for POP-Ag and POP-Cu. For NOE-Ag and NOP-Ag, the calculated positions agree well with the observed signals, since the diffraction signals are well defined. For POE-Ag the orientational distribution is not as well defined as for example for NOP-Ag, but still dominantly parallel to the substrate (observable for the (002), (004) and (006) signals). This distribution can vary depending on the sample and substrate, but as shown in Figure S16 for the POE-Ag solar cell, it is exclusively parallel to the substrate surface. The weaker signals observable slightly above the (002), (004) and (006) diffractions are due to the scattering events that include reflection at the film/substrate surface, i.e. intrinsic to the GIWAXS measurement setup. An additional signal is observable in the middle of the (002) and (004) signals. In space group 9 Cc, the reflections where h + l is odd should be extinct, here this would be the (003) reflection. This could arise due to a deviation from the ideal Cc symmetry through for example twinning or stacking faults, which in fact are very likely for these 2D RP materials, as we observed often in the growth of single crystals (Figure 4.16 and 4.17). The terrace like growth along the c or out-of-plane direction can be observed in Figure 4.16a and Figure 4.17, demonstrating the proneness to stacking faults, while the twinning growth of four crystals can be observed in the polarized light microscopy image in Figure 4.16b. For POP-Ag films, less distinct oriented diffraction is observed, similar to POE-Ag, but still dominantly parallel to the substrate, indicating a mixed orientation of crystal domains in the polycrystalline film. For POE-Cu the lattice parameters show the strongest deviations from the other materials, most notably a larger difference between parameters a and b,

as well as the angle α and β. As mentioned in the main article, the absorption data and band gap value extracted for this sample being very different to the other materials, point to a different structural arrangement or octahedral bond lengths and distortions, which could explain the different lattice parameters. Single crystal analysis would be needed to further confirm this, but attempts towards growing single crystals have not been successful so far. The indexed parameters for NOE-Cu agree well with the observed diffraction pattern with a dominant orientation of the (001) direction parallel to the substrate surface, although a partial orientation vertical to the substrate can be observed for signals close to the (001) diffraction, at q_r = –0.4 Å^{-1} and 0.4 Å^{-1}. For NOP-Cu the indexed parameters also agree well with orientation parallel to the substrate, with the exception of some additional signals most notably between the (001) and (002) diffractions, and next to the (003) reflection, at q_z = 0.4 Å^{-1} and 0.9 Å^{-1}, respectively. For POE-Cu and POP-Cu the observed pattern again agrees well with the indexed parameters and the calculated positions, with a dominant parallel orientation but again less defined, similar to POE-Ag and POP-Ag. Both show an additional signal between the (002) and (004) reflection for POE-Cu and between (200) and (400) for POP-Cu, as also observed for POE-Ag and NOP-Cu, probably due to crystal twinning, as discussed before and shown in Figure 4.16.

Overall, the 2D RP DP structures and the (predominantly) parallel orientations of the 2D perovskite sheets on the substrates can be confirmed, as required for the study addressing the anisotropic electrical conductivity.

Single crystal growth

Single crystals of NOP-Ag, POE-Ag and POP-Ag were obtained through a vapor diffusion method of dichloromethane (DCM) into γ-butyrolactone (GBL) solutions of the 2D DPs. Similar methods were attempted for the other five materials, but were unsuccessful for different reasons. Due to the different alkyl linkage chain length, NOE and POE are more soluble compared to NOP and POP, because of which we could not recrystallize NOE-Ag-solutions successfully. Furthermore, Cu-Bi based material organic solutions showed signs of degradation, i.e. a color change to dark red, possibly linked to the oxidation of Cu^+. Crystallization attempts from concentrated aqueous hydroiodic acid were also unsuccessful, due to the strong hydrophobicity of all organic cations.

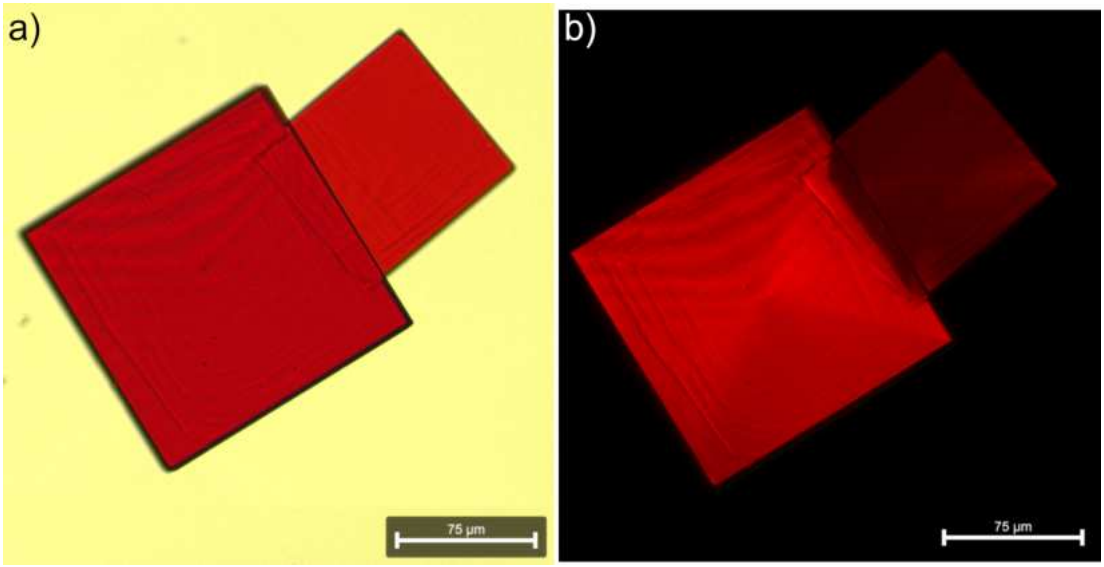

Figure 4.16: Optical light microscopy images of POE-Ag single crystals with transmission lighting a) without and b) with polarization filter. In b) the twinning of four crystals can be observed with a fourfold rotational axis originating in the center of the crystal.

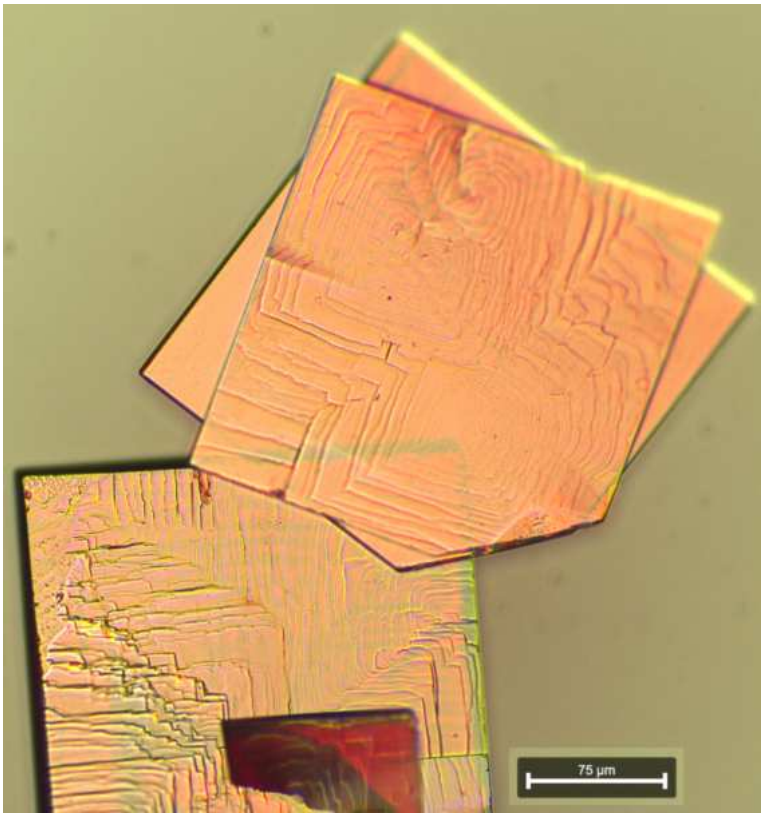

Figure 4.17: Optical light microscopy image of POE-Ag single crystals with transmission lighting, showing the terrace like growth in the c or out-of-plane direction.

The micrographs in Figure 4.16 and 4.17 show the issue with the quality of the single crystal structure solution for POE-Ag. The proneness to twinning (Figure 4.16b) and stacking faults (Figure 4.17) result in broadened diffraction signals. The crystal structure was hence refined by theoretical calculations as shown in Table 4.3 and the appended CIF-file for the optimized POE-Ag structure.

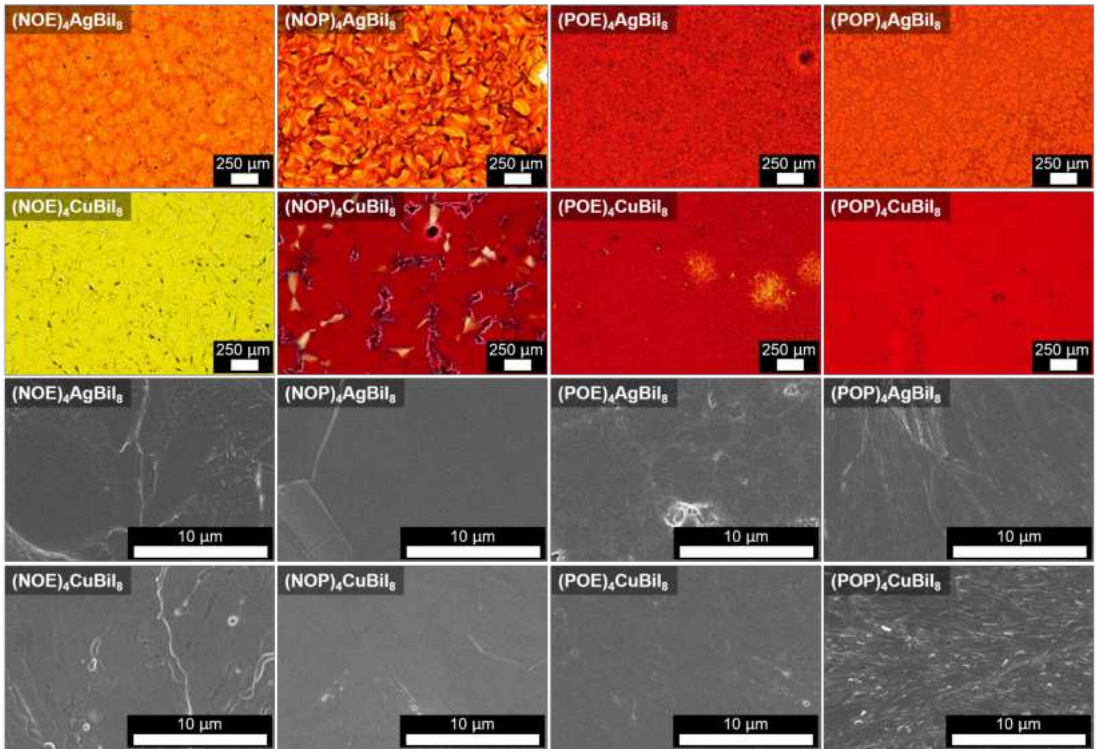

Figure 4.18: Optical visible light (top) and scanning electron (bottom) micrographs of all eight materials synthesized as thin films on ITO substrates.

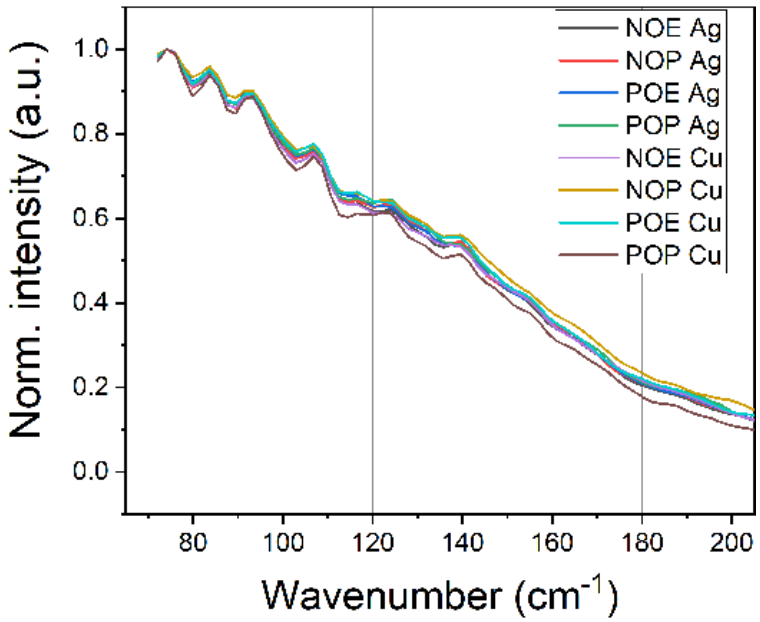

Figure 4.19: Raman spectra for all eight materials indicating the similar phonon modes and inorganic framework structures being present.

Recently, first detailed Raman studies of 2D double perovskites have been published with special focus on the electron-phonon coupling to gain insight into the crystal structure and possible phase transitions.[75,76] Although we cannot provide such detailed investigations, our room temperature Raman measurements in the 70-200 cm^{-1} region, where information about the lattice modes would be visible, feature the same peak positions and similar relative intensities for all 8 materials. Thus, indicating similar phonon bands of the inorganic lattice.

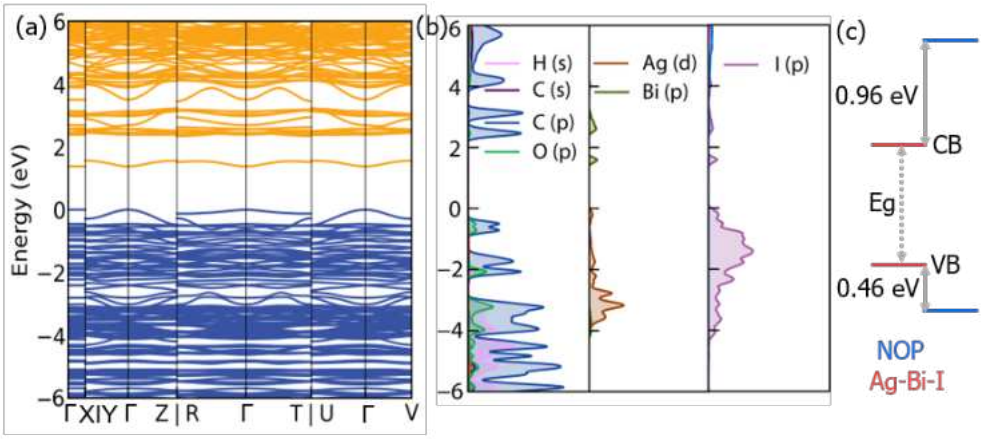

Figure 4.20: a) PBE+SOC calculated band structure with b) the partial density of states and c) the band alignment for NOP-Ag.

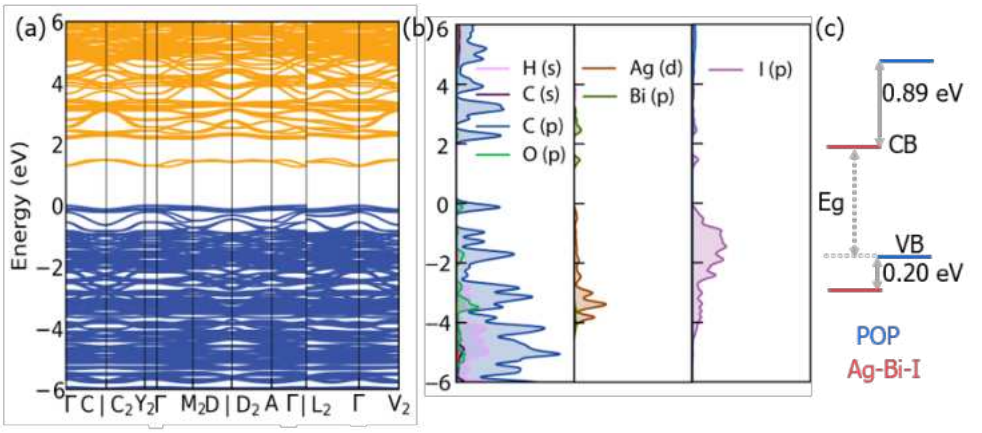

Figure 4.21: a) PBE+SOC calculated band structure with b) the partial density of states and c) the band alignment for POP-Ag.

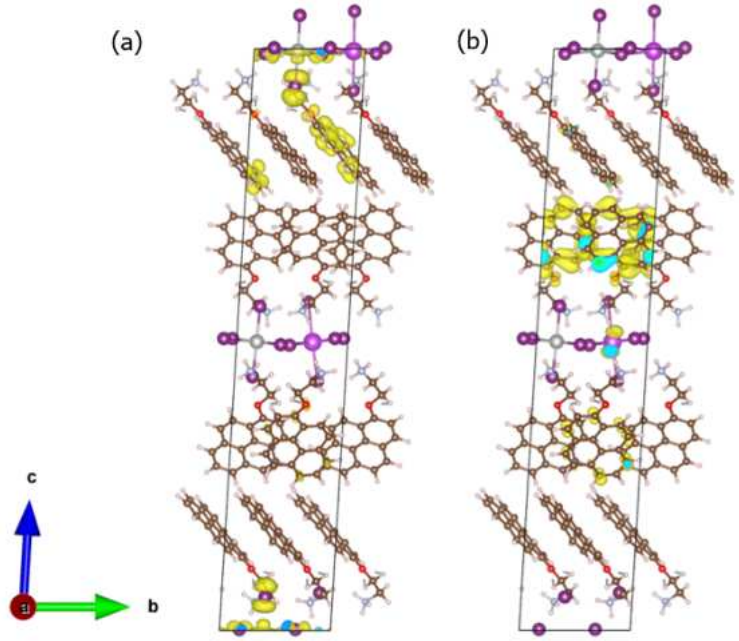

Figure 4.22: The partial charge density for the (a) overlapping states below the VB and (b) overlapping states above the CB in POE-Ag. The yellow contours show the isosurface of the norm squared wavefunction with the isovalue at 0.0005.

Table 4.3: Lattice parameters of NOP-Ag, POE-Ag, POP-Ag from theoretical optimization (ISIF 3) and experimental single crystal solutions.

Material	Theo. a, b, c (Å); α, β, γ (°); space group (No.)	Exp. a, b, c (Å); α, β, γ (°); space group (No.)
$(NOP)_4AgBiI_8$	22.556, 8.913, 7.908; 89.828, 98.333, 90.632; P-1 (2)	22.526, 8.931, 8.163; 90.220, 95.284, 90.415; P-1 (2)
$(POE)_4AgBiI_8$	8.707, 8.707, 46.665; 86.309, 93.691, 89.701; Cc (9)	8.786, 8.786, 47.097; 85.491, 94.509, 90.138; Cc (9)
$(POP)_4AgBiI_8$	51.964, 8.033, 9.129; 90.000, 94.523, 90.000; C2 (5)	52.957, 8.162, 9.117; 90.000, 94.641, 90.000; C2 (5)

Table 4.4: PBE and PBE+SOC calculated and experimental band gaps of NOP-Ag, POE-Ag, POP-Ag.

Material	PBE (eV)	PBE+SOC (eV)	Expt. (eV)
$(NOP)_4AgBiI_8$	1.9920	1.3791	2.18
$(POE)_4AgBiI_8$	1.7688	1.0938	2.15
$(POP)_4AgBiI_8$	1.8161	1.2620	2.19

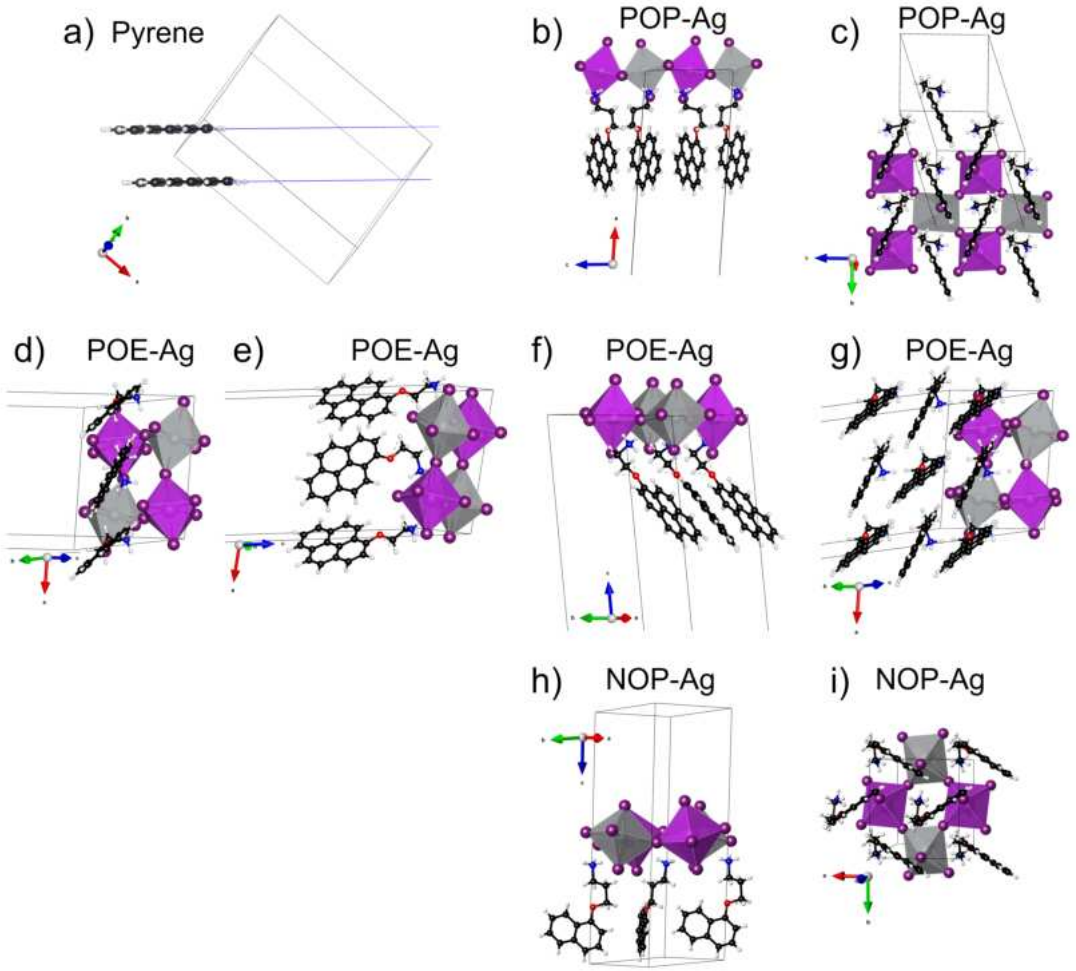

Figure 4.23: Comparison of the molecular alignment of a) crystalline pyrene to the organic cation alignment in b) and c) of POP-Ag; d-g) of POE-Ag and h) and i) of NOP-Ag. b) f) and h) highlight a similar point of view for the organic half-layer arrangement from the side for POP-Ag, POE-Ag and NOP-Ag. c), g) and i) highlight a similar point of view for the organic half-layer arrangement from below for POP-Ag, POE-Ag and NOP-Ag. d) and e) highlight the face-face arrangement of POE-Ag cations in one column of the organic half-layer, most closely resembling that of pyrene in a), potentially giving rise to π-π interactions, compared to POP-Ag and NOP-Ag where the arrangement show angles which make π-π interaction unlikely, i.e. POP-Ag showing a herringbone arrangement (c) and NOP-Ag showing almost 90° angles between naphthalene moieties (h and i).

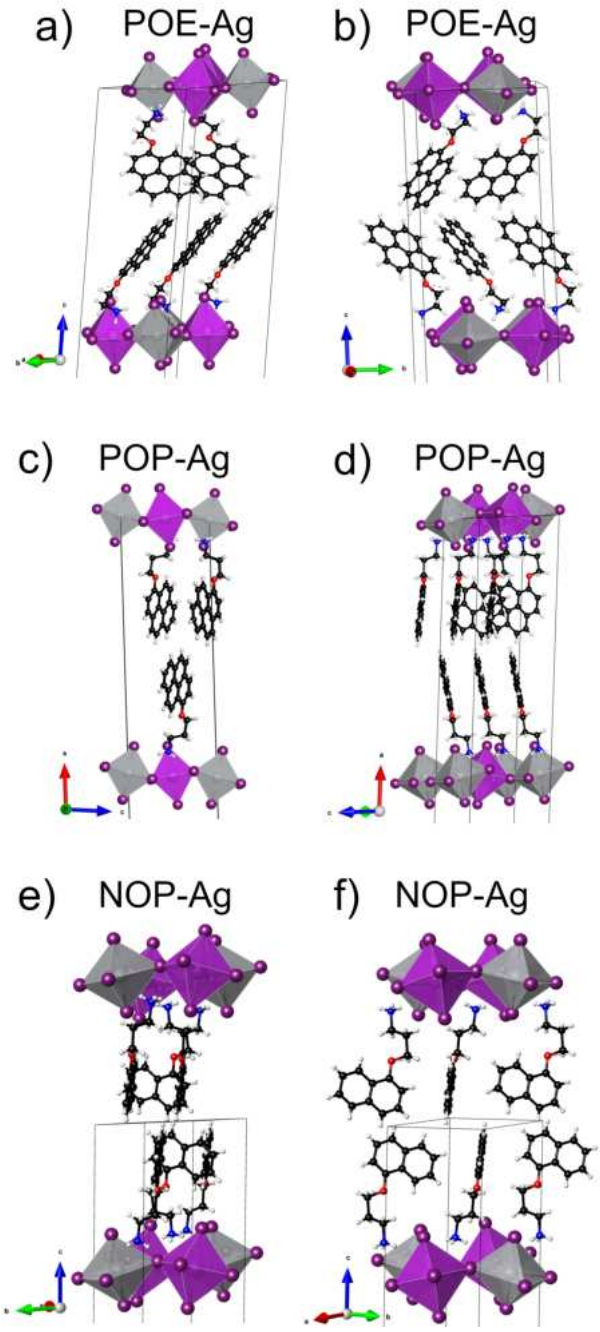

Figure 4.24: Comparison of the organic bilayer and intralayer arrangement for POE-Ag in a) and b), for POP-Ag in c) and d) and for NOP-Ag in e) and f). While POE-Ag displays an edge-face arrangement within the organic bilayer, shown to be favorable for orbital coupling and charge transport, POP-Ag and NOP-Ag display an edge-edge arrangement, shown to be unfavorable for orbital coupling and charge transport.[1].

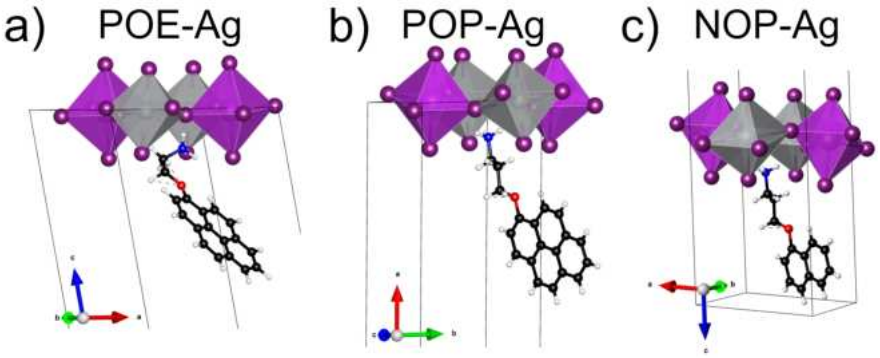

Figure 4.25: Comparison of the proximity of the pyrene and naphthalene moieties in a) POE-Ag, b) POP-Ag and c) NOP-Ag, to the inorganic octahedral lattice, highlighting the different angle, being almost 45° for POE-Ag and almost 90° for POP-Ag and NOP-Ag, which should further lead to an increased orbital overlap for POE-Ag. Moreover, this depiction highlights the different conformation of the ethyl- vs. the propyl-linkage moeities.

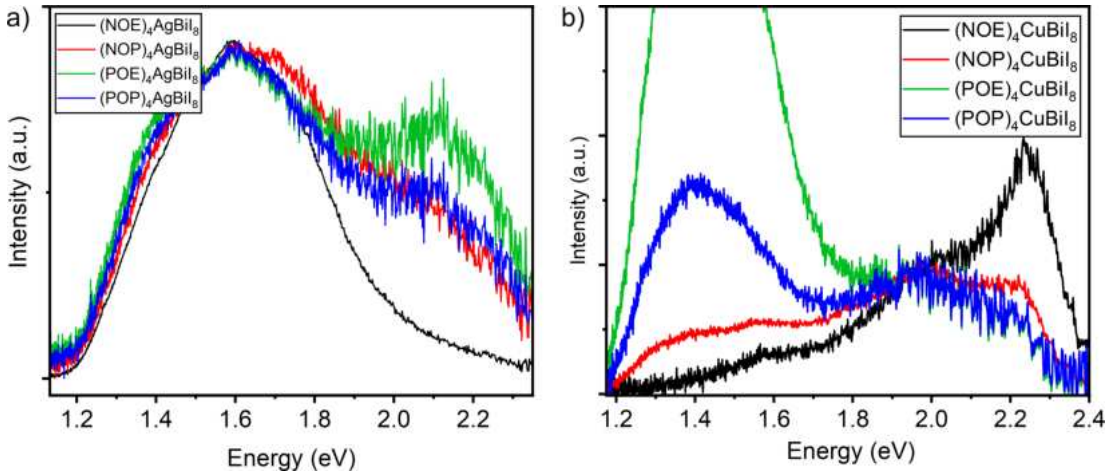

Figure 4.26: a) PL steady state spectra normalized at 1.6 eV for the Ag-Bi materials, highlighting the similar emission shape of the first feature at 1.6 eV and the different ratios of the first to the second feature at 2.1 eV. b) PL steady state spectra normalized at 1.97 eV for the Cu-Bi materials, for better comparison of the emissive features, as discussed in the main text.

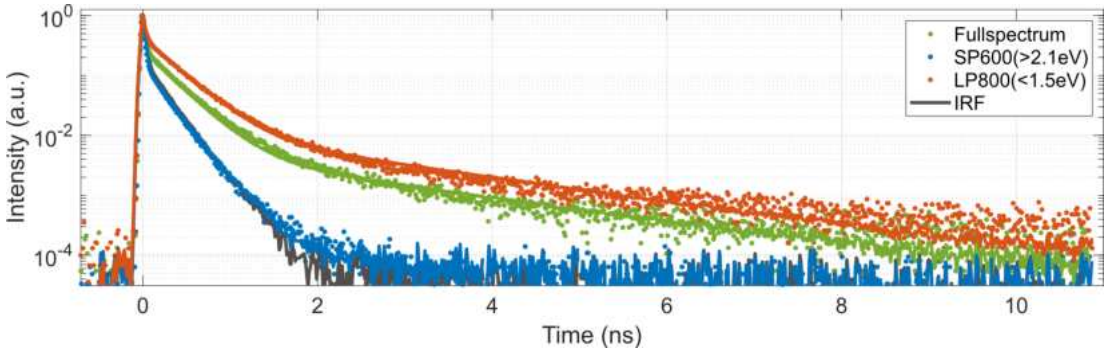

Figure 4.27: PL transients of POE-Ag at room temperature with full spectrum (green), short-pass filter 600 nm (blue) and long-pass filter 800 nm (red). Solid lines represent tri-exponential function fits to the data with lifetime parameters τ_1 < 10 ps, τ_2 = 280 ps, and τ_3 = 2ns. The fitted tri-exponential model function was convoluted with the instrument response function (IRF) of the setup (grey curve). Note that the lifetime parameters are slightly different to the values reported in table 4.5, but still on the same order of magnitude. This is due to the fact that here (4.27) an exfoliated crystal flake of POE-Ag was measured compared to the thin film samples on glass measured in tables 4.5 and 4.6.

The transient PL spectra were fitted according to a triexponential decay function shown below:

$$f(t) = A_1 e^{\frac{t}{\tau_1}} + A_2 e^{\frac{t}{\tau_2}} + A_3 e^{\frac{t}{\tau_3}} \tag{4.1}$$

Table 4.5: Transient PL fit parameters for Ag-Bi materials. Due to the IRF being 28 ps, the first, ultrafast component has a large standard deviation. Nonetheless, the fast process happens on timescales <=20 ps.

	NOE-Ag	NOP-Ag	POE-Ag	POP-Ag
A_1/sum(A_1)	0.97	0.99	0.99	0.99
A_2/sum(A_2)	0.03	0.006	0.01	0.01
A_3/sum(A_3)	0.001	0.00002	0.0004	0.0003
τ_1 (ns)	0.01 $\pm$0.01	0.02 $\pm$0.01	0.01 $\pm$0.01	0.01$\pm$0.01
τ_2 (ns)	1.241 $\pm$0.06	0.419 $\pm$0.06	0.538 $\pm$0.06	0.442$\pm$0.06
τ_3 (ns)	2.44 $\pm$0.5	6.51 $\pm$0.5	3.80 $\pm$0.5	3.89 $\pm$0.5

Table 4.6: Transient PL fit parameters for Cu-Bi materials. Due to the IRF being 28 ps, the first, ultrafast component has a large standard deviation. Nonetheless, the fast process happens on timescales <=20 ps.

	NOE-Cu	NOP-Cu	POE-Cu	POP-Cu
A_1/sum(A_1)	1	1	0.98	0.99
A_2/sum(A_2)	0.0004	0.00005	0.02	0.01
A_3/sum(A_3)	0.00005	0.000006	0.00005	0.00001
τ_1 (ns)	0.01 $\pm$0.01	0.01 $\pm$0.01	0.01 $\pm$0.01	0.01$\pm$0.01
τ_2 (ns)	0.681 $\pm$0.06	0.819 $\pm$0.06	0.952 $\pm$0.06	0.620 $\pm$0.06
τ_3 (ns)	5.36 $\pm$0.5	5.45 $\pm$0.5	8.33 $\pm$0.5	5.28 $\pm$0.5

Analysis of the remote detected time resolved emission data

From remote detected time resolved PL, the diffusion coefficient is extracted via a 2 Gaussian fit for every step. One Gaussian with a fixed width is representing a nonmoving species which stays constant in width according to the resolution limit. The second Gaussian curve represents the diffusive excited states. Since we assumed that this is 2D diffusive transport, the change in width has the following relation:

$$\sigma^2(t) = 2Dt \tag{4.2}$$

Two time scales can be observed, one in the signal rise, the second on longer time scales, which we assign to two different species, the free ambipolar charge carriers and the polaronic excitons.

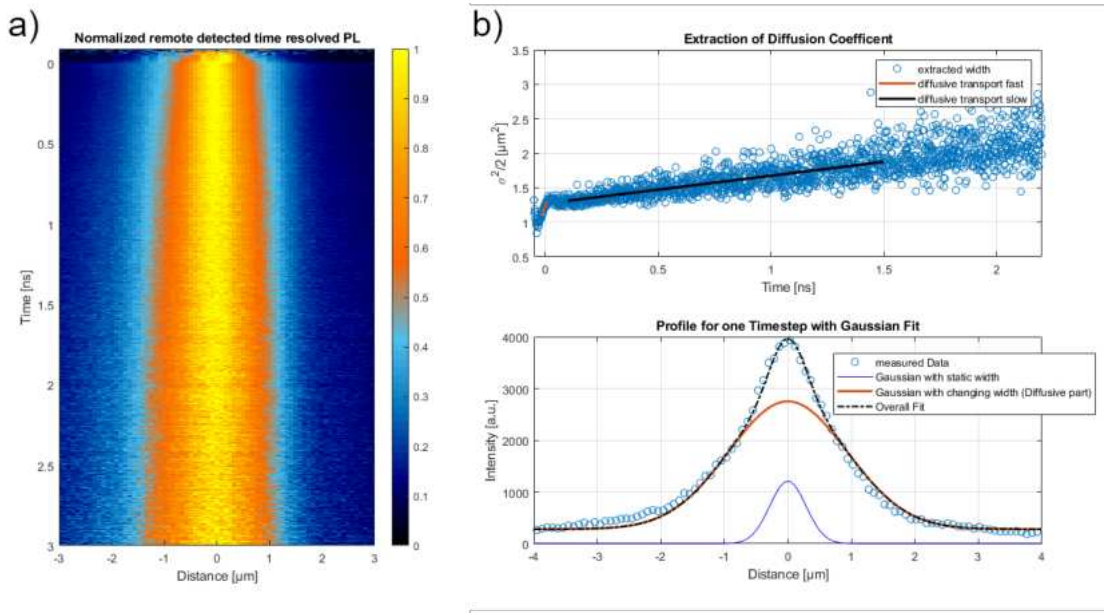

Figure 4.28: a) Normalized remote detected time resolved PL. b) Extraction of diffusion coefficient and the Gaussian fit used for the extraction as described above.

Photoconductivity measurements

We fabricated thin films on isolating glass substrates with top evaporated, interdigitated 100 nm Ag electrodes. The conductivity was measured through a voltage sweep from -5 V to 5 V in dark and light conditions. The illumination source was a standard white light spectrum LED, calibrated to the intensity of 1 sun. To exclude the influence of thin film morphologies, we evaluated the thin film quality in terms of homogeneity, thickness and continuity regarding large grain boundaries through optical microscopy, ensuring similar conditions. Cross section SEM images are shown in Figure 4.30, displaying continuous and homogeneous thin films. The noise or fine structure, observable for current signals below 10^{-9} A are due to the signal resolution limit of the Keithley source meter and most likely correspond to a minimal charge buildup. The fine structure is connected to the step-size of the measurement.

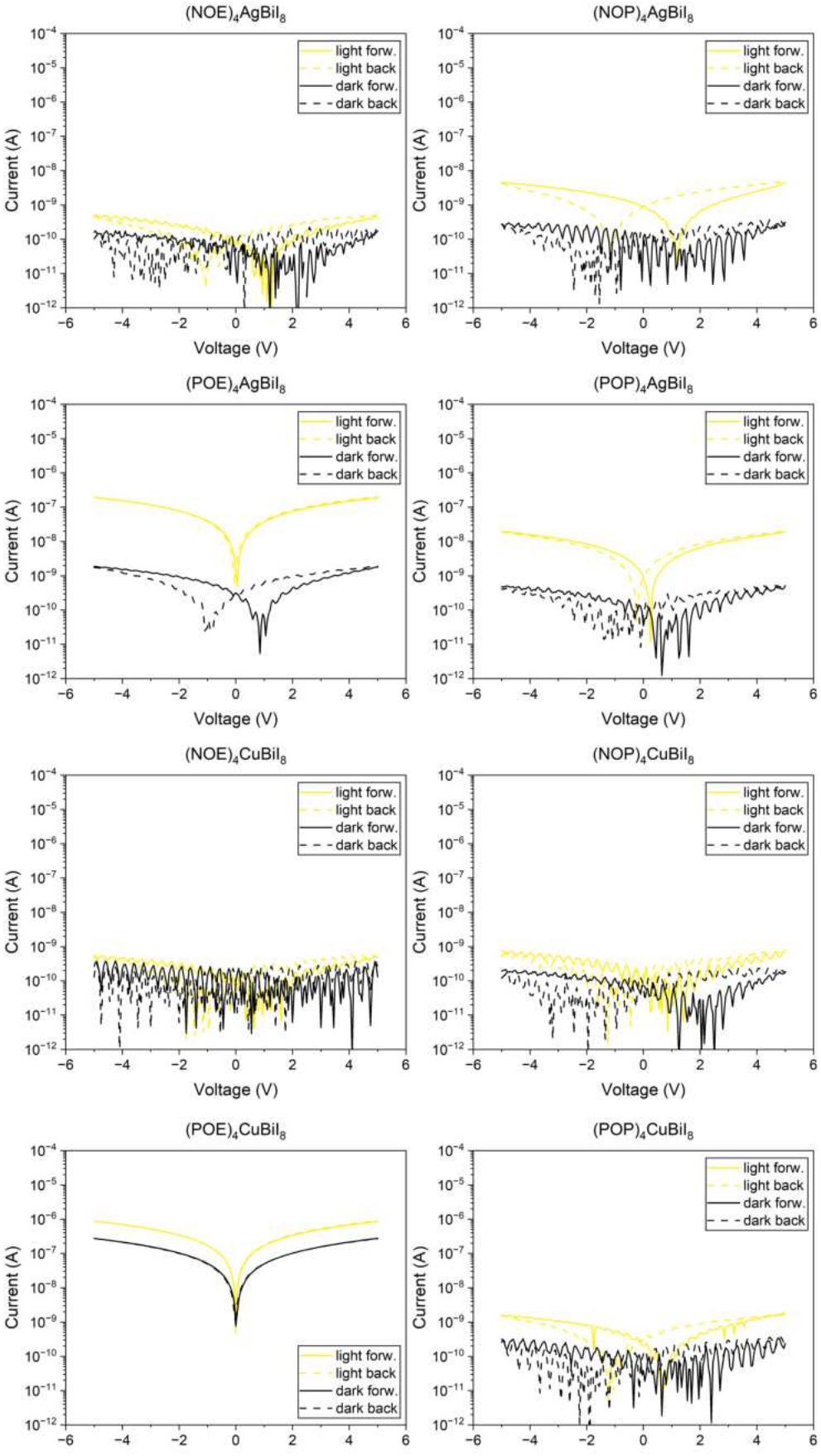

Figure 4.29: Photoconductivity IV curves for all eight materials under dark and light conditions.

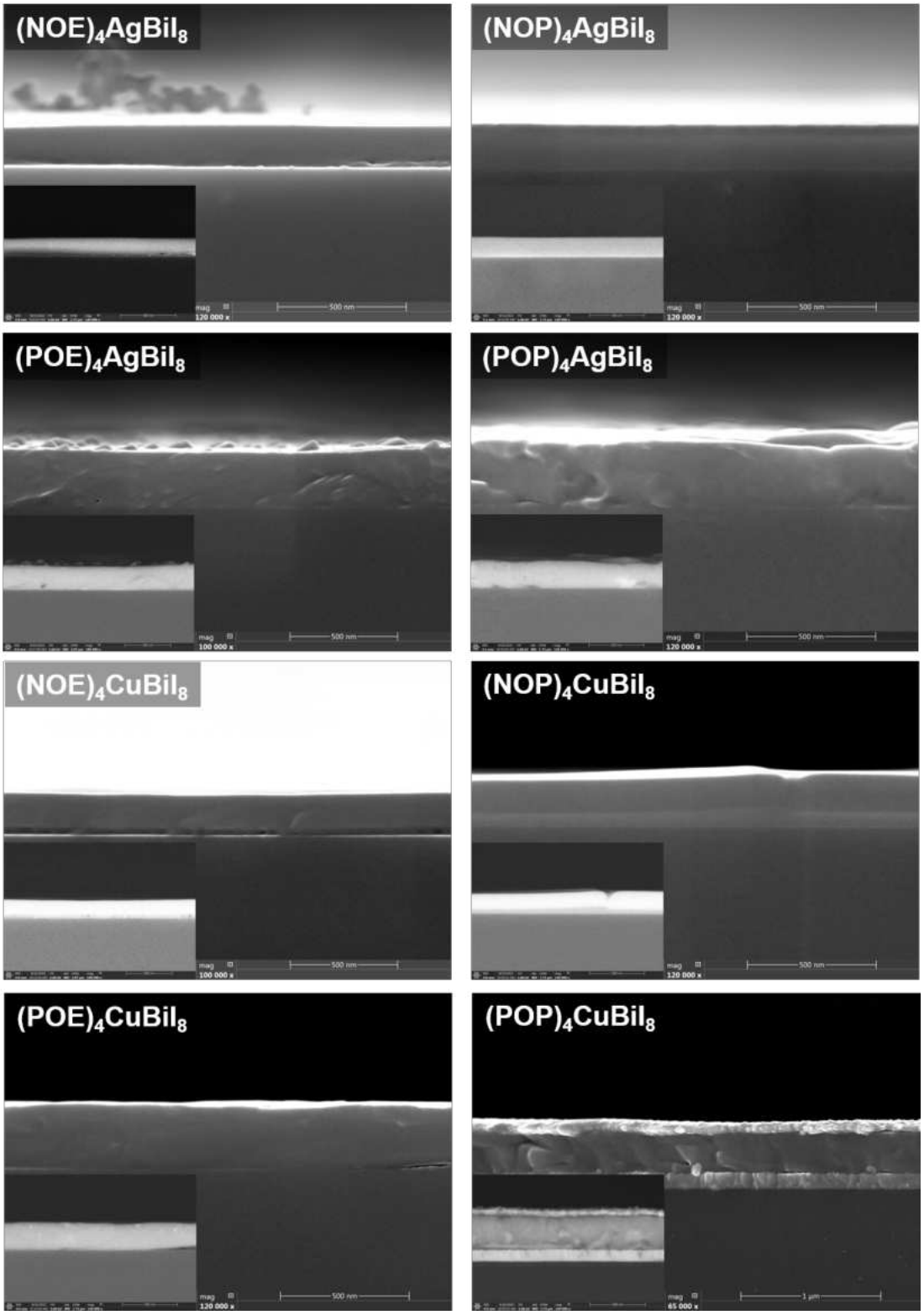

Figure 4.30: SEM cross section images for all eight materials using secondary electrons; the inset shows images obtained with back-scattered electrons. All samples show dense, continuous and homogeneous morphology, confirming the comparability for the conductivity measurements shown in Figure 4.28 for top evaporated Ag electrodes (Ag electrodes are visible in the micrograph of POP-Cu).

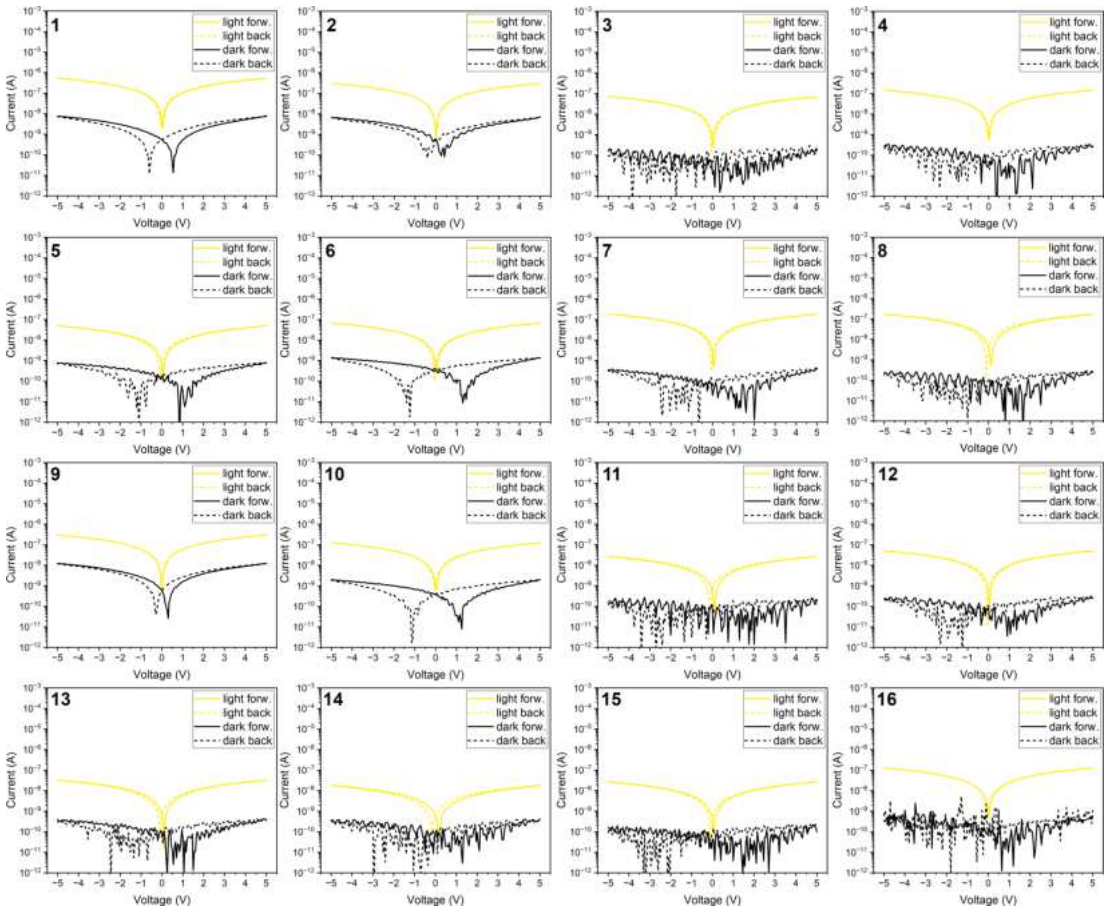

Figure 4.31: Optimization row for POE-Ag thin films for top-evaporated in-plane conductivity measurements based on different synthesis conditions shown below in Table 4.6. As evident, different synthesis parameters result in different light and dark current responses and ratios. We selected sample 7 to be the best performing sample in terms of light/dark ratio (x779), while sample 1 showed the highest absolute current response ($5.04 \text{x} 10^{-7}$ A at 5V).

Table 4.7: Synthesis conditions for POE-Ag thin film samples for top-evaporated in-plane conductivity measurements shown in Figure S19. Solvents were varied to test the different crystallization behavior. Concentrations were varied to test the influence of different thin film thicknesses. Antisolvent chlorobenzene (CB) was tested to potentially improve crystallinity and surface smoothness. Annealing temperatures and times were kept constant, to ensure the formation of the desired phase.

	Material	Solvent	c (mol/L)	AS	Annealing 1 (1 min)	Annealing 2 (5 min)
1	POE-Ag	DMF	0.3	-	140 °C	100 °C
2	POE-Ag	DMF	0.3	CB 500 μL	140 °C	100 °C
3	POE-Ag	DMSO:DMF 1:1	0.3	-	140 °C	100 °C
4	POE-Ag	DMSO:DMF 1:1	0.3	CB 500 μL	140 °C	100 °C
5	POE-Ag	GBL:DMF 1:1	0.3	-	140 °C	100 °C
6	POE-Ag	GBL:DMF 1:1	0.3	CB 500 μL	140 °C	100 °C
7	POE-Ag	NMP:DMF 1:1	0.3	-	140 °C	100 °C
8	POE-Ag	NMP:DMF 1:1	0.3	CB 500 μL	140 °C	100 °C
9	POE-Ag	DMF	0.15	-	140 °C	100 °C
10	POE-Ag	DMF	0.15	CB 500 μL	140 °C	100 °C
11	POE-Ag	DMSO:DMF 1:1	0.15	-	140 °C	100 °C
12	POE-Ag	DMSO:DMF 1:1	0.15	CB 500 μL	140 °C	100 °C
13	POE-Ag	GBL:DMF 1:1	0.15	-	140 °C	100 °C
14	POE-Ag	GBL:DMF 1:1	0.15	CB 500 μL	140 °C	100 °C
15	POE-Ag	NMP:DMF 1:1	0.15	-	140 °C	100 °C
16	POE-Ag	NMP:DMF 1:1	0.15	CB 500 μL	140 °C	100 °C

The influence of CB as antisolvent on the conductivity was negligible. The influence of the precursors concentration, i.e. the resulting thickness of the thin films, shows a decreased absolute current for thinner samples obtained from c = 0.15 mol/L, compared to their counterparts from c = 0.3 mol/L. This is another indication that POE-Ag does indeed have an out-of-plane component in its conductivity, since otherwise the film thickness should not have a large influence, as charge transport would be limited to the topmost atomic layers of the 2D DP thin films. The dark currents are very low, at the detection minimum for the employed setup, for solutions based on DMSO:DMF 1:1, and NMP:DMF 1:1 (i.e. samples 3, 4, 7, 8, 11, 12, 15, 16). Samples based on pure DMF or GBL:DMF 1:1 show increased responses, which should be based on better crystallization of the thin film. This can result in a number of factors improving the conductivity, such as improved homogeneity, fewer defects, larger crystallites or better intergrown crystallite/domain boundaries, or even slightly different orientations.

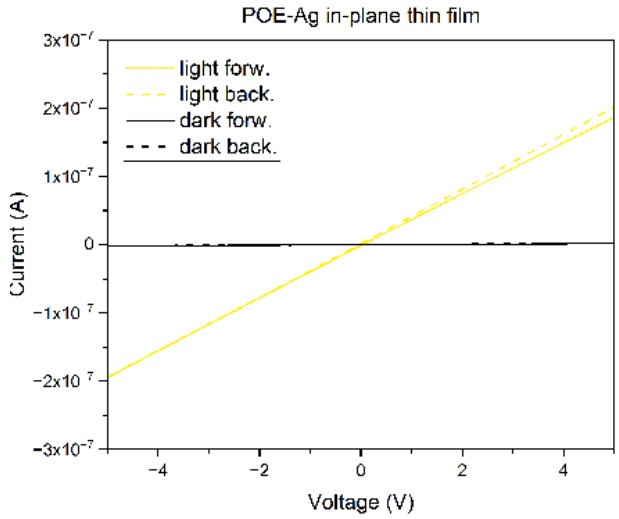

Figure 4.32: Linear IV¬ curve plot for POE-Ag in-plane thin film samples with evaporated top Ag contacts, displaying a linear, ohmic behavior.

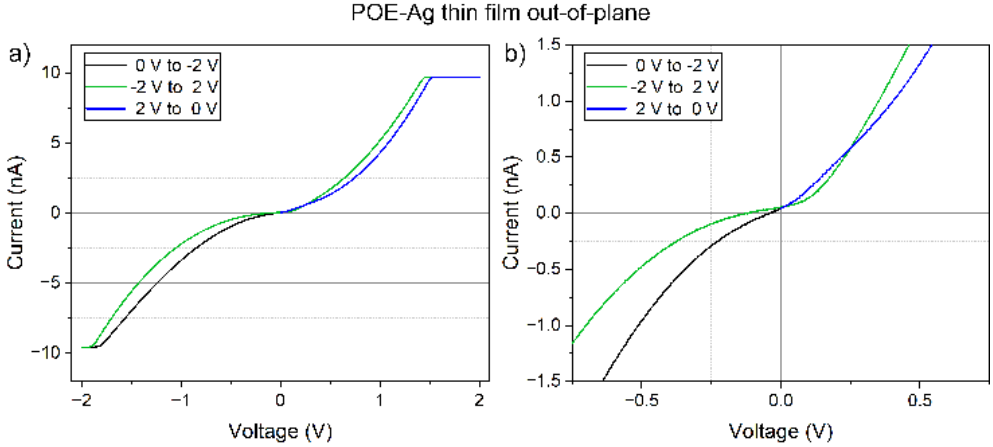

Figure 4.33: a) IV curves of POE-Ag thin film out-of-plane measurement and b) zoom-in around the axes origin, revealing the Schottky barrier type behavior.

Out-of-plane conductivity

In the following figures a detailed view of the thin film out-of-plane IV curves is shown to display the characteristics.

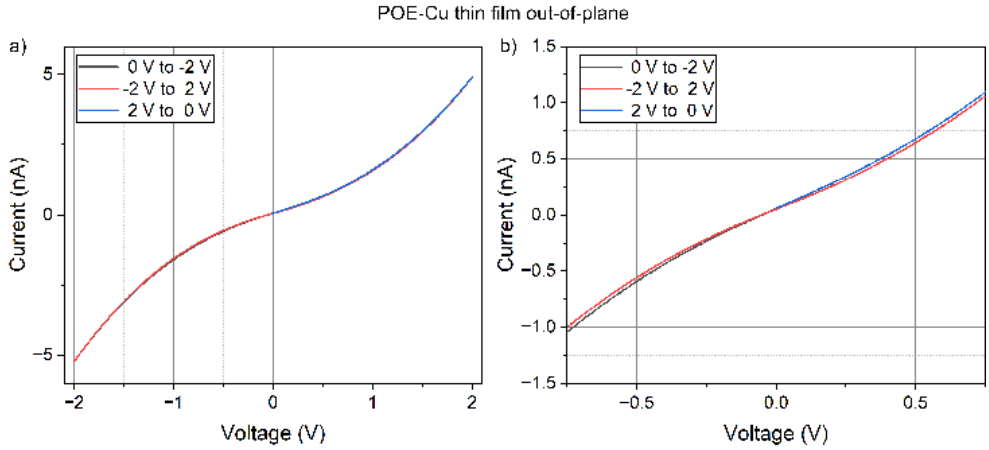

Figure 4.34: a) IV curves of POE-Cu thin film out-of-plane measurement and b) zoom-in around the axes origin. The S-shape is observable but no distinct Schottky barrier type behavior is exhibited compared to POE-Ag in Figure 4.32.

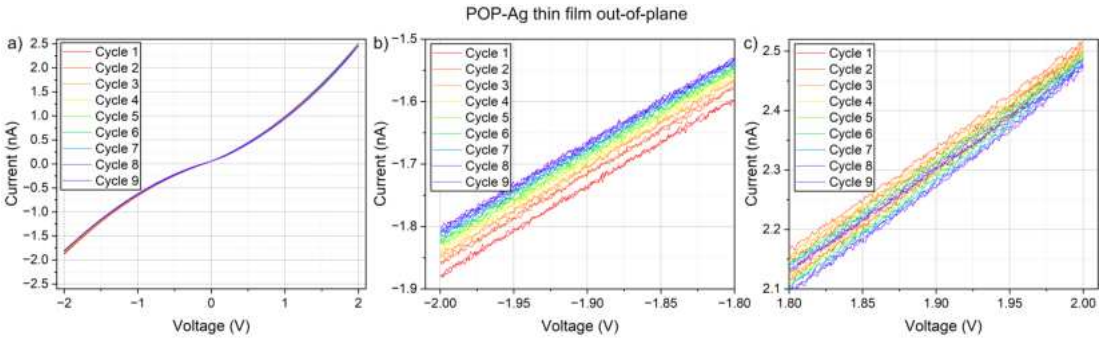

Figure 4.35: a) IV curves of POP-Ag thin film out-of-plane measurement measured for 9 cycles with zoom-in at the negative voltage maximum bias in b) and positive voltage maximum bias in c). The S-shape is observable but no distinct Schottky barrier type behavior is exhibited compared to POE-Ag in Figure 4.32. The cycling shows a very small hysteresis, observable in b) and c), where upon multiple cycles the maximum currents shift towards lower values.

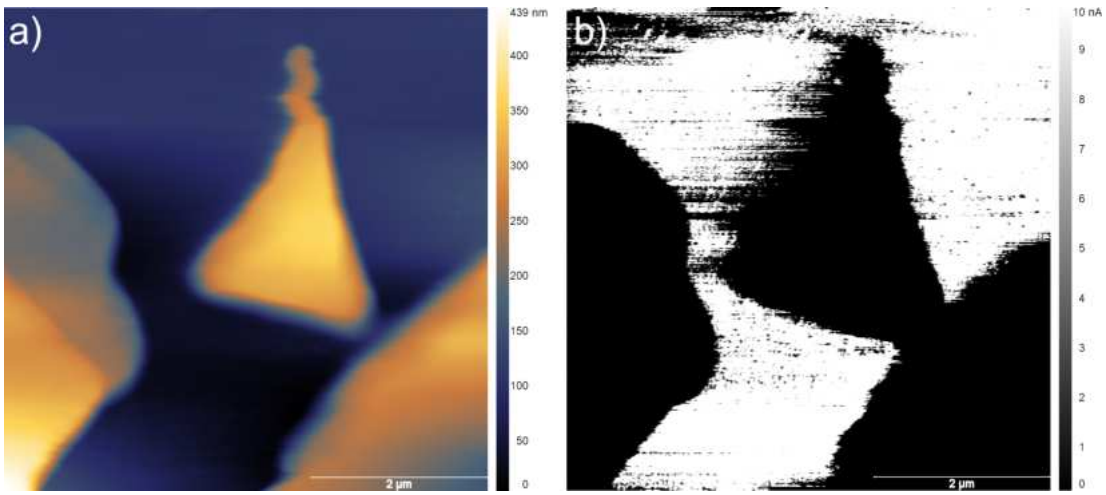

Figure 4.36: a) AFM height profile image and b) cAFM image of exfoliated 4FPEA-Ag crystals on ITO substrate. 4FPEA-Ag does not show any out-of-plane conductivity.

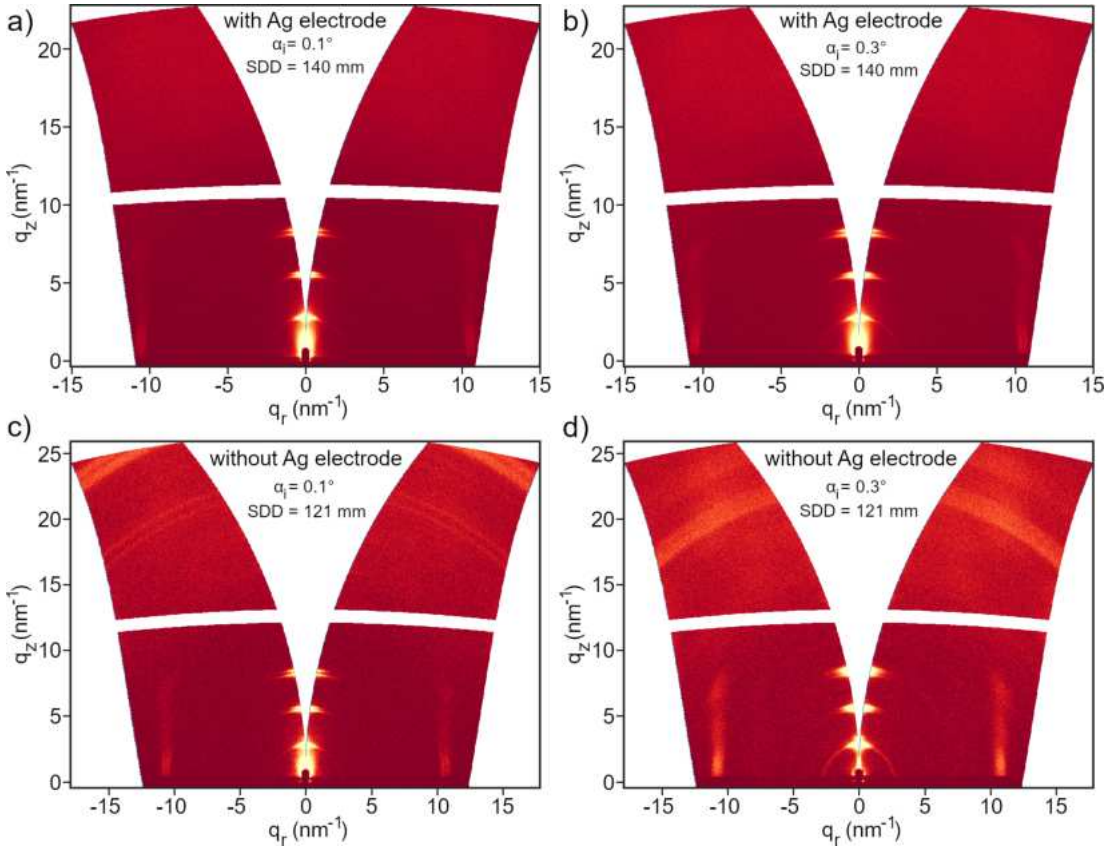

Figure 4.37: GIWAXS data of a pixel of the champion solar cell constructed with POE-Ag. Measurements were taken with at sample detector distances 121 mm and 140 mm, an incident angle of 0.3° to probe deep into the device, as well as at 0.1° to probe predominantly the surface, on two different spots with a) and b) a PCBM/silver electrode terminated surface and c) and d) only a PCBM terminated surface. As shown in Figure 4.8, independent of the depth, the 2D perovskite layer is exclusively oriented parallel to the substrate surface. Note, that for measurements taken with a silver terminated surface, the reflections split up due to the additional reflectance and scattering as the X-ray beam travels through the silver layer and an additional interface.

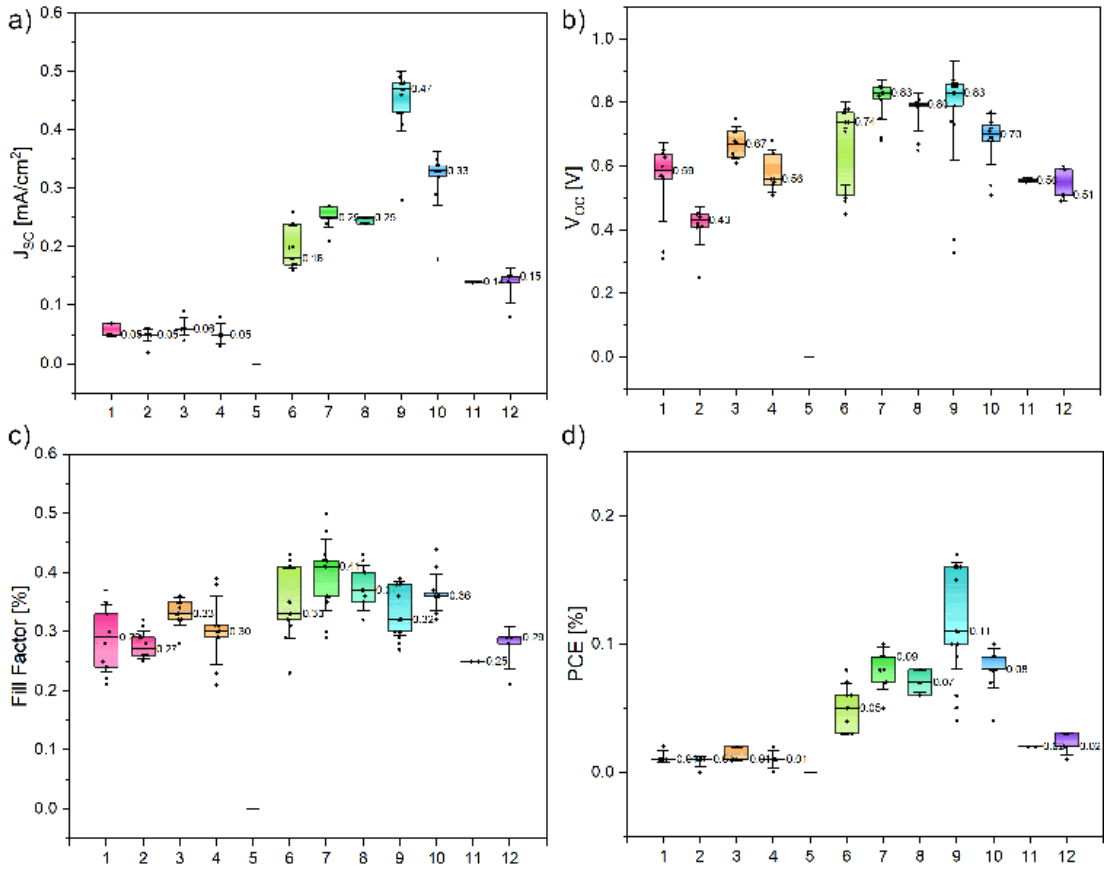

Figure 4.38: Statistical box plots of the solar cell characteristics with POE-Ag as the active layer with a) the J_{sc}, b) the V_{oc}, c) the Fill Factor and d) the power conversion efficiency. The sample numbers on the x-axis correspond to the sample synthesis conditions listed in table S8, primarily resulting in different thicknesses.

Solar cells were prepared on glass/ITO substrates, which were patterned by etching with zinc-powder and 3 M HCl, cleaned with a detergent followed by washing with acetone and ethanol and dried under an air stream. Before applying the hole transport layer (HTL), substrates were nitrogen plasma cleaned for 10 minutes. The HTL PTAA (Sigma-Aldrich, 2 mg/mL in 1:1 chlorobenzene/toluene, doped with 2 μL/mL of a 1 mg/mL F4TCNQ solution in DMF) was spincoated with 60 μL at 6000 rpm for 35 seconds and annealed at 100 °C for 5 minutes. Then PEAI (1 mg/mL DMF) was spincoated on the PTAA layer with 100 μL at 3000 rpm for 30 seconds and annealed at 100 °C for 5 minutes. Subsequently the active layer POE-Ag was spincoated as specified in Table S8. The electron transport layer (ETL) PCBM (20 mg/mL in 1:1 chlorobenzene/toluene, 60 μl) was spincoated at 2000 rpm for 30 seconds and annealed at 100 °C for 5 minutes. Finally, 100 nm Ag electrodes were evaporated through thermal evaporation.

Table 4.8: Synthesis conditions for the active layer POE-Ag in the solar cells shown in Figure 4.38 and discussed in the main text (cell number 9). Spin-coating volume is 70 μL. Solutions were preheated to 60 °C and substrates were preheated to 80 °C.

	cation	metal	solvent	M	Annealing 1	Annealing 2
1	POE	Ag	DMF	0.075	60 °C 4 min	100 °C 5 min
2	POE	Ag	DMF	0.075	60 °C 4 min	140 °C 2 min
3	POE	Ag	DMF	0.075	60 °C 8 min	100 °C 5 min
4	POE	Ag	DMF	0.075	60 °C 8 min	140 °C 2 min
5	POE	Ag	DMF	0.0375	60 °C 4 min	100 °C 5 min
6	POE	Ag	DMF	0.0375	60 °C 4 min	140 °C 2 min
7	POE	Ag	DMF	0.0375	60 °C 8 min	100 °C 5 min
8	POE	Ag	DMF	0.0375	60 °C 8 min	140 °C 2 min
9	POE	Ag	DMF	0.01875	60 °C 4 min	100 °C 5 min
10	POE	Ag	DMF	0.01875	60 °C 4 min	140 °C 2 min
11	POE	Ag	DMF	0.01875	60 °C 8 min	100 °C 5 min
12	POE	Ag	DMF	0.01875	60 °C 8 min	140 °C 2 min

4.8 References

[1] X. Li, J. M. Hoffman, M. G. Kanatzidis, *Chemical reviews* **2021**, *121*, 2230–2291.

[2] J. Sun, K. Wang, K. Ma, J. Y. Park, Z.-Y. Lin, B. M. Savoie, L. Dou, *Journal of the American Chemical Society* **2023**, *145*, 20694–20715.

[3] Y. Wei, W. Wang, Z. Wang, H. Yang, X. You, Y. Zhao, P. Dang, H. Lian, J. Hao, G. Li, et al., *Advanced Functional Materials* **2023**, *33*, 2205829.

[4] X. Chen, M. Jia, W. Xu, G. Pan, J. Zhu, Y. Tian, D. Wu, X. Li, Z. Shi, *Advanced Optical Materials* **2023**, *11*, 2202153.

[5] M. T. Sirtl, R. Hooijer, M. Armer, F. G. Ebadi, M. Mohammadi, C. Maheu, A. Weis, B. T. van Gorkom, S. Häringer, R. A. Janssen, et al., *Advanced Energy Materials* **2022**, *12*, 2103215.

[6] A. D. Wright, L. R. Buizza, K. J. Savill, G. Longo, H. J. Snaith, M. B. Johnston, L. M. Herz, *The journal of physical chemistry letters* **2021**, *12*, 3352–3360.

[7] Z. Zhang, Y. Liang, H. Huang, X. Liu, Q. Li, L. Chen, D. Xu, *Angewandte Chemie International Edition* **2019**, *58*, 7263–7267.

[8] W. Pan, H. Wu, J. Luo, Z. Deng, C. Ge, C. Chen, X. Jiang, W.-J. Yin, G. Niu, L. Zhu, et al., *Nature photonics* **2017**, *11*, 726–732.

[9] P. Vishnoi, R. Seshadri, A. K. Cheetham, *The Journal of Physical Chemistry C* **2021**, *125*, 11756–11764.

[10] B. A. Connor, A. C. Su, A. H. Slavney, L. Leppert, H. I. Karunadasa, *Chemical science* **2023**, *14*, 11858–11871.

[11] R. Hooijer, A. Weis, A. Biewald, M. T. Sirtl, J. Malburg, R. Holfeuer, S. Thamm, A. A. Y. Amin, M. Righetto, A. Hartschuh, et al., *Advanced Optical Materials* **2022**, *10*, 2200354.

[12] B. Chen, R. Yu, G. Xing, Y. Wang, W. Wang, Y. Chen, X. Xu, Q. Zhao, *ACS Energy Letters* **2024**, *9*, 226–242.

[13] Y. Gao, E. Shi, S. Deng, S. B. Shiring, J. M. Snaider, C. Liang, B. Yuan, R. Song, S. M. Janke, A. Liebman-Peláez, et al., *Nature chemistry* **2019**, *11*, 1151–1157.

[14] C. Liu, W. Huhn, K.-Z. Du, A. Vazquez-Mayagoitia, D. Dirkes, W. You, Y. Kanai, D. B. Mitzi, V. Blum, *Physical Review Letters* **2018**, *121*, 146401.

[15] Y. Xu, M. Wang, Y. Lei, Z. Ci, Z. Jin, *Advanced Energy Materials* **2020**, *10*, 2002558.

[16] L.-Y. Bi, T.-L. Hu, M.-Q. Li, B.-K. Ling, M. S. Lassoued, Y.-Q. Hu, Z. Wu, G. Zhou, Y.-Z. Zheng, *Journal of materials chemistry A* **2020**, *8*, 7288–7296.

[17] J. V. Passarelli, C. M. Mauck, S. W. Winslow, C. F. Perkinson, J. C. Bard, H. Sai, K. W. Williams, A. Narayanan, D. J. Fairfield, M. P. Hendricks, et al., *Nature chemistry* **2020**, *12*, 672–682.

[18] D. B. Mitzi, K. Chondroudis, C. R. Kagan, *Inorganic chemistry* **1999**, *38*, 6246–6256.

[19] Y. Boeije, W. T. Van Gompel, Y. Zhang, P. Ghosh, S. J. Zelewski, A. Maufort, B. Roose, Z. Y. Ooi, R. Chowdhury, I. Devroey, et al., *Journal of the American Chemical Society* **2023**, *145*, 21330–21343.

[20] M. Braun, W. Tuffentsammer, H. Wachtel, H. Wolf, *Chemical physics letters* **1999**, *303*, 157–164.

[21] M. Braun, W. Tuffentsammer, H. Wachtel, H. Wolf, *Chemical physics letters* **1999**, *307*, 373–378.

[22] J. V. Passarelli, D. J. Fairfield, N. A. Sather, M. P. Hendricks, H. Sai, C. L. Stern, S. I. Stupp, *Journal of the American Chemical Society* **2018**, *140*, 7313–7323.

[23] D. Han, S. Chen, M.-H. Du, *The Journal of Physical Chemistry Letters* **2021**, *12*, 9754–9760.

[24] M. K. Jana, S. M. Janke, D. J. Dirkes, S. Dovletgeldi, C. Liu, X. Qin, K. Gundogdu, W. You, V. Blum, D. B. Mitzi, *Journal of the American Chemical Society* **2019**, *141*, 7955–7964.

[25] M.-H. Du, *The journal of physical chemistry letters* **2015**, *6*, 1461–1466.

[26] Z. Xiao, W. Meng, J. Wang, Y. Yan, *ChemSusChem* **2016**, *9*, 2628–2633.

[27] D. Han, M. Ogura, A. Held, H. Ebert, *ACS applied materials & interfaces* **2020**, *12*, 37100–37107.

[28] A. Camerman, J. Trotter, *Acta Crystallographica* **1965**, *18*, 636–643.

[29] Z. Zhao, S. Chen, J. W. Lam, Z. Wang, P. Lu, F. Mahtab, H. H. Sung, I. D. Williams, Y. Ma, H. S. Kwok, et al., *Journal of Materials Chemistry* **2011**, *21*, 7210–7216.

[30] Y. Ge, Y. Wen, H. Liu, T. Lu, Y. Yu, X. Zhang, B. Li, S.-T. Zhang, W. Li, B. Yang, *Journal of Materials Chemistry C* **2020**, *8*, 11830–11838.

[31] A. Schmitz, L. L. Schaberg, S. Sirotinskaya, M. Pantaler, D. C. Lupascu, N. Benson, G. Bacher, *ACS energy letters* **2020**, *5*, 559–565.

[32] S. Zelewski, J. M. Urban, A. Surrente, D. K. Maude, A. Kuc, L. Schade, R. Johnson, M. Dollmann, P. Nayak, H. Snaith, et al., *Journal of Materials Chemistry C* **2019**, *7*, 8350–8356.

[33] J. A. Steele, P. Puech, M. Keshavarz, R. Yang, S. Banerjee, E. Debroye, C. W. Kim, H. Yuan, N. H. Heo, J. Vanacken, et al., *ACS nano* **2018**, *12*, 8081–8090.

[34] L. Zhang, S. Li, H. Sun, Q. Jiang, Y. Wang, Y. Fang, Y. Shi, D. Duan, K. Wang, H. Jiang, et al., *Angewandte Chemie* **2023**, *135*, e202301573.

[35] R. Kentsch, M. Scholz, J. Horn, D. Schlettwein, K. Oum, T. Lenzer, *The Journal of Physical Chemistry C* **2018**, *122*, 25940–25947.

[36] M. Palummo, S. Postorino, C. Borghesi, G. Giorgi, *Applied Physics Letters* **2021**, *119*.

[37] A. Bala, V. Kumar, *Physical Review Materials* **2021**, *5*, 095401.

[38] M. Chen, X. Dong, Z. Shan, Z. Xu, S. F. Liu, *The Journal of Physical Chemistry C* **2022**, *126*, 14824–14831.

[39] J. T. Race, T. Liu, P. M. Woodward, *Crystal Growth & Design* **2024**.

[40] S. Wang, D. Han, C. Maheu, Z. Xu, A. Biewald, H. Illner, R. Hooijer, T. Mayer, A. Hartschuh, H. Ebert, et al., *APL Materials* **2023**, *11*.

[41] Z. Xiao, K.-Z. Du, W. Meng, D. B. Mitzi, Y. Yan, *Angewandte Chemie* **2017**, *129*, 12275–12279.

[42] J. Ferguson, *The Journal of Chemical Physics* **1958**, *28*, 765–768.

[43] B. Stevens, *Spectrochimica Acta* **1962**, *18*, 439–448.

[44] R. D. Pensack, R. J. Ashmore, A. L. Paoletta, G. D. Scholes, *The Journal of Physical Chemistry C* **2018**, *122*, 21004–21017.

[45] S. Kahmann, D. Meggiolaro, L. Gregori, E. K. Tekelenburg, M. Pitaro, S. D. Stranks, F. De Angelis, M. A. Loi, *ACS Energy Letters* **2022**, *7*, 4232–4241.

[46] A. S. Rury, A. M. Sanni, D. Konadu, T. Danielson, *The Journal of Chemical Physics* **2023**, *158*.

[47] X. Zhang, T. Zhu, C. Ji, Y. Yao, J. Luo, *Journal of the American Chemical Society* **2021**, *143*, 20802–20810.

[48] J. Y. Park, R. Song, J. Liang, L. Jin, K. Wang, S. Li, E. Shi, Y. Gao, M. Zeller, S. J. Teat, et al., *Nature Chemistry* **2023**, *15*, 1745–1753.

[49] M. D. Smith, H. I. Karunadasa, *Accounts of chemical research* **2018**, *51*, 619–627.

[50] J. G. Mann, F. He, Q. A. Akkerman, T. Debnath, J. Feldmann, *The Journal of Physical Chemistry Letters* **2024**, *15*, 2169–2176.

[51] B. Martín-García, D. Spirito, M.-L. Lin, Y.-C. Leng, S. Artyukhin, P.-H. Tan, R. Krahne, *Advanced Optical Materials* **2022**, *10*, 2200240.

[52] M. Righetto, Y. Wang, K. A. Elmestekawy, C. Q. Xia, M. B. Johnston, G. Konstantatos, L. M. Herz, *Advanced Materials* **2023**, *35*, 2305009.

[53] S. Lal, M. Righetto, A. M. Ulatowski, S. G. Motti, Z. Sun, J. L. MacManus-Driscoll, R. L. Hoye, L. M. Herz, *The Journal of Physical Chemistry Letters* **2023**, *14*, 6620–6629.

[54] M. Pantaler, V. Diez-Cabanes, V. I. Queloz, A. Sutanto, P. A. Schouwink, M. Pastore, I. García-Benito, M. K. Nazeeruddin, D. Beljonne, D. C. Lupascu, et al., *Jacs Au* **2021**, *2*, 136–149.

[55] M. N. Saha, *Proceedings of the Royal Society of London. Series A Containing Papers of a Mathematical and Physical Character* **1921**, *99*, 135–153.

[56] M. Righetto, S. Caicedo-Dávila, M. T. Sirtl, V. J.-Y. Lim, J. B. Patel, D. A. Egger, T. Bein, L. M. Herz, *The Journal of Physical Chemistry Letters* **2023**, *14*, 10340–10347.

[57] S. G. Motti, M. Kober-Czerny, M. Righetto, P. Holzhey, J. Smith, H. Kraus, H. J. Snaith, M. B. Johnston, L. M. Herz, *Advanced Functional Materials* **2023**, *33*, 2300363.

[58] T. P. Schneider, J. Glaser, J. Horn, F. Schmitz, T. Gatti, D. Schlettwein, *ACS Applied Electronic Materials* **2024**.

[59] N. Lang, W. Kohn, *Physical Review B* **1971**, *3*, 1215.

[60] H. L. Skriver, N. Rosengaard, *Physical Review B* **1992**, *46*, 7157.

[61] P. Hohenberg, W. Kohn, *Physical review* **1964**, *136*, B864.

[62] W. Kohn, L. J. Sham, *Physical review* **1965**, *140*, A1133.

[63] G. Kresse, J. Furthmüller, *Physical review B* **1996**, *54*, 11169.

[64] G. Kresse, D. Joubert, *Physical review b* **1999**, *59*, 1758.

[65] P. E. Blöchl, *Physical review B* **1994**, *50*, 17953.

[66] J. P. Perdew, K. Burke, M. Ernzerhof, *Physical review letters* **1996**, *77*, 3865.

[67] A. Tkatchenko, R. A. DiStasio Jr, R. Car, M. Scheffler, *Physical review letters* **2012**, *108*, 236402.

[68] T. Bučko, S. Lebègue, J. Hafner, J. G. Angyan, *Physical Review B* **2013**, *87*, 064110.

[69] M. K. Jana, R. Song, H. Liu, D. R. Khanal, S. M. Janke, R. Zhao, C. Liu, Z. Valy Vardeny, V. Blum, D. B. Mitzi, *Nature communications* **2020**, *11*, 4699.

[70] D. Han, S. Chen, M.-H. Du, *The Journal of Physical Chemistry Letters* **2021**, *12*, 9754–9760.

[71] S. Yu, G. Na, S. Luo, O. Rubel, L. Zhang, *Journal of Applied Physics* **2020**, *128*.

[72] D. Han, C. Feng, M.-H. Du, T. Zhang, S. Wang, G. Tang, T. Bein, H. Ebert, *Journal of the American Chemical Society* **2021**, *143*, 12369–12379.

[73] M.-H. Du, *The journal of physical chemistry letters* **2015**, *6*, 1461–1466.

[74] A. M. Ganose, A. J. Jackson, D. O. Scanlon, *Journal of Open Source Software* **2018**, *3*, 717.

[75] B. Martín-García, D. Spirito, G. Biffi, S. Artyukhin, F. Bonaccorso, R. Krahne, *The Journal of Physical Chemistry Letters* **2020**, *12*, 280–286.

[76] B. Martín-García, D. Spirito, M.-L. Lin, Y.-C. Leng, S. Artyukhin, P.-H. Tan, R. Krahne, *Advanced Optical Materials* **2022**, *10*, 2200240.

Chapter 5

Cu/Ag-Sb-I Rudorffite Thin Films for Photovoltaic Applications

This chapter is based on the following publication:

R. Hooijer†, A. Weis†, W. Kaiser, A. Biewald, P. Dörflinger, C. Maheu, O. Arsatiants, D. Helminger, V. Dyakonov, A. Hartschuh, E. Mosconi, F. De Angelis, T. Bein, Chemistry of Materials **2023**, 35(23), 9988-10000.

†R.H. and A.W. contributed equally to this work.

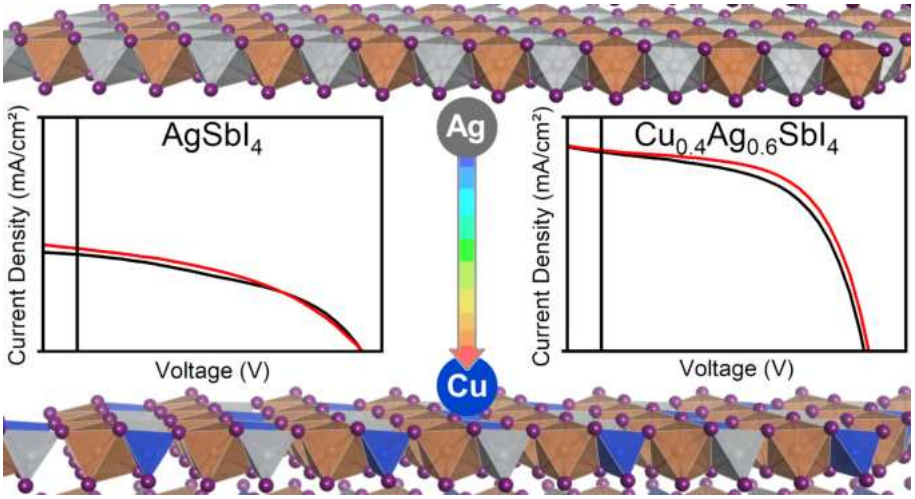

The following work was performed by R. Hooijer and A. Weis: conception, synthesis of thin films. R. Hooijer performed structural analysis through XRD and SEM. A. Weis performed analysis and fitting of absorption and EQE data. R. Hooijer manufactured and analysed the solar cells. W. Kaiser performed DFT calculations. P. Dörflinger performed TRMC measurements and analysis. C. Maheu performed UPS measurements and analysis. O. Arsatiants and D. Helminger worked on the project through internships. A. Weis wrote the initial draft of the manuscript. R. Hooijer and A. Weis edited until the final version. R. Hooijer performed the submission and revision process.

5.1 Abstract

In the search for lead-free perovskites, silver pnictohalides recently gained attention as novel perovskite-inspired materials for photovoltaics due to their high stability, low toxicity, and promising early efficiencies, especially for indoor applications. Recent research on such "rudorffites" mainly addresses silver bismuth iodides (Ag-Bi-I), while their antimony analogues are hardly investigated due to intrinsic challenges in the synthesis of Sb-based thin films. Here, we establish a synthetic route to prepare Ag-Sb-I thin films by employing thiourea as a Lewis-base additive. Thin film morphologies were further optimized by alloying them with Cu, resulting in solar cells with an improved power conversion efficiency of 0.7% by reducing undesired side phases. Density functional theory calculations and optical characterization methods support the incorporation of Cu into a $Cu_{1-x}Ag_xSbI_4$ phase, keeping the overall stoichiometry and band gap virtually unchanged upon alloying. Our results further reveal the detrimental role of Ag point defects representing trap states in the band gap, being responsible for low open-circuit voltages and subgap absorption and emission features. Moreover, additional minor amounts of Bi are shown to boost the efficiency and stabilize the performance over a wider compositional range. Despite the remaining challenges regarding device performance, we demonstrate a strong increase in external quantum efficiency when reducing the light intensity, highlighting the potential of Ag-Sb-I rudorffites for indoor photovoltaics.

5.2 Introduction

Lead-halide perovskites have drawn enormous interest for optoelectronics applications, particularly photovoltaics, from industry and research alike. Still, the practical applications of these materials remain limited by their notorious instability coupled with the high toxicity of the constituents and degradation products.[1–4] Nonetheless, through the recent upsurge of emerging semiconducting materials, the focus of photovoltaic research has greatly shifted from purely inorganic materials such as silicon or CIGS (Cu-In-Ga-Se) with high energy demands for production to novel compounds that combine favorable optoelectronic properties with remarkable defect tolerance, in combination with low-temperature solution syntheses.[5–9]

Starting from the prototypical methylammonium lead iodide, $MAPbI_3$, a classical strategy to circumvent the toxicity issues is homovalent or heterovalent substitution of the central lead atom while retaining the perovskite structure. This is commonly achieved through elements with the same ns^2 electronic configuration, as this was repeatedly suggested to be the basis of the exceptional defect tolerance in lead-halide perovskites.[10–12] An obvious and intensely studied candidate for substitution is the group IV neighbor tin, which was shown to be both efficient and less problematic than lead in terms of environmental impact.[13,14] Nonetheless, $MASnI_3$ and other Sn(II) based compounds are highly sensitive towards oxidation, requiring pure precursor chemicals and non-oxidizing solvents, which still hampers the successful implementation of these materials.[15–18] Alternative approaches combine adjacent elements of tin and lead in the periodic table, namely trivalent antimony(III) and bismuth(III), which still showcase the characteristic electronic ns^2 configuration, with monovalent cations like silver and copper, as prominently seen and studied in the archetype double-perovskite $Cs_2AgBiBr_6$.[19,20] Although this compound exhibits several promising properties like long charge carrier lifetime and high environmental stability, the photovoltaic efficiency is limited by rapid non-radiative recombination and a large bandgap.[19–21]

If the monovalent metal ion is omitted entirely in the above systems, the original perovskite structure is sacrificed, leading to another class of perovskite-derived materials with the general structural formula $A_3B_2X_9$, which also suffer from detrimental factors such as high exciton binding energies, strong exciton-phonon coupling and low dimensionality, among others.[22–25] Herein, the A-site cations are mostly derived from the lead-based perovskite counterparts, namely methylammonium, formamidinium or cesium(I). Many reports have already shown the significant influence of these cations, not only on the electronic properties but also as structure directing agents.[26,27]

Most recently, a new class of Sb/Bi-based materials has emerged, with the accom-

panying monovalent A cations being silver and/or copper, featuring the general structural formula $A_xB_yX_{x+3y}$ and straying even further away from the original perovskite lattice. These compounds were termed "rudorffites"[28] in previous reports and are comprised of interconnected $[A/B]X_6$ octahedra, where the A and B cations share equivalent lattice positions, thereby inducing a high degree of stoichiometric freedom. Notably, these pnictohalides show favorable bandgaps for single-junction solar cell devices and high absorption coefficients.[28,29] The hitherto published materials are mostly based on Ag-Bi-I and were shown to already surpass 5% PCE within only a couple of years time.[30] Moreover, rudorffites were also employed successfully in other types of devices like X-ray detectors,[31] memristors[32] or, as of latest, as highly efficient indoor light harvesters,[33,34] competing with commercial solar cells in this field. Alloying and substituting Ag with Cu was also shown to be an efficient way to tailor their structural and electronic properties.[33,34]

While research efforts to date have been mostly focused on Bi-based rudorffite structures, only few reports concerning pure (Ag/Cu)-Sb-I materials can be found, some of which being inconclusive about important properties like color, bandgap and structure.[35,36] This may be due to synthetic difficulties when working with SbI_3 as precursor,[37] which exhibits a high vapor pressure and is prone to evaporation when using film annealing temperatures above 100 °C. Furthermore, instability of the pristine $AgSbI_4$ under ambient conditions was reported as well.[35]

Herein, we demonstrate the thin-film synthesis of $Cu_xAg_{1-x}SbI_4$ (CASI) rudorffites using a Lewis-base assisted approach. We establish the formation of the crystalline materials in thin films and furthermore we highlight the beneficial effect of an optimal ratio of 40% Cu to Ag on the morphology, reducing grain boundaries and improving the overall coverage. Notably, substitution of Sb with only 5% of Bi led to a further morphology improvement over a broader range up to a Cu content of 90%, which can also be seen in the photovoltaic performance. Density functional theory (DFT) calculations investigate the impact of the stoichiometry of various (Cu/Ag)-Sb-I phases, highlighting the incorporation of Cu into the layered CASI composition. X-ray photoelectron spectroscopy (XPS) measurements demonstrate the disappearance upon Cu addition of other trivalent oxide or metallic antimony states like SbO_x, SbI_3 and Sb_0 as side phases likely created through degradation and surface oxidation. UV-Vis spectroscopy and photoluminescence measurements further reveal the presence of deep defect states and broad emission with large Stokes shift, confirmed by DFT calculations pointing to extraordinarily low Ag point defect formation energies of 0.16 eV. Additionally, photoluminescence measurements reveal static emission and lifetime characteristics over the whole doping range, which we discuss in view of varying charge carrier mobilities and photovoltaic performance. Con-

ceptually, we connect the luminescence behavior to the thin film morphology via hyperspectral optical measurements, explaining the improved performance in solar cells when using an optimal Cu content. Lastly, external quantum efficiency measurements reveal a much-improved photocurrent at low photon flux when no white light bias is employed, indicating the great potential of these materials for indoor photovoltaic applications.

5.3 Results and Discussion

To synthesize thin films based on CASI, a common approach was employed by dissolving the corresponding halide precursors (CuI/AgI/SbI_3) in a mixture of 1:1 DMF:DMSO to achieve a concentration of 0.6 M, followed by spin-coating on different substrates (glass/FTO/ITO/mp-TiO_2). Furthermore, a small amount of the Lewis base thiourea (TU) was added to retard the crystallization of the thin film, a crucial step in controlling the formation of the CASI material, which has been reported to exhibit significant formation issues.[35,36,38] This is a necessary step to obtain working devices and circumvent recurrent problems of the halide precursors, with AgI being only hardly soluble in organic solvents like DMF that are commonly used for spin-coating. The influence of the additive on the behavior of the precursor solution is presented in Figure 5.6 in the Supporting Information (SI). Similar effects have been shown for lead-based and lead-free perovskites.[39–42] Furthermore, SbI_3 is known to have a high equilibrium vapor pressure[37] which prohibits the use of elevated annealing temperatures, shown to be crucial for the formation of the Bi analogue.[29] In this work, we therefore employed a ramped thermal annealing approach from 50 °C for 1 h to 80 °C for a minute to anneal the films. An 'inverse' technique based on one short immediate heating step for 1 min at 120 °C leads to improved crystallinity but less complete coverage, as shown in the XRD graphs and SEM images in FigureSI 5.8.

Materials based on $A_xB_yI_{x+3y}$ stoichiometries, with A being a monovalent transition metal cation (Ag^+/Cu^+) and B being a trivalent pnictogen cation (Bi^{3+}/Sb^{3+}), are constructed of alternating occupied and unoccupied positions of edge-sharing octahedra $[AI_6]^{5-}$, $[BI_6]^{3-}$, and $[\Delta X_6]^{6-}$ (Δ = vacancy).[38] By maintaining the edge-sharing octahedral lattice and the charge neutrality through vacancies, the entire A-B-I phase space can be defined.[28] $AgSbI_4$ and Ag_3SbI_6 are the most reasonable structural models based on space group $R3\bar{m}$ (no. 166) as more Sb-rich phases have very high formation energies and very small band gap energies around 0.4 eV, as discussed later based on DFT calculations. Because of the aforementioned disorder, exact crystal structure analysis of such materials was shown to be a challenge, especially since the diffraction patterns are extremely similar and different symmetry groups with partial positional occupations can produce satisfactory crystal structure and profile refinements.[28,38,43–47] Furthermore, for

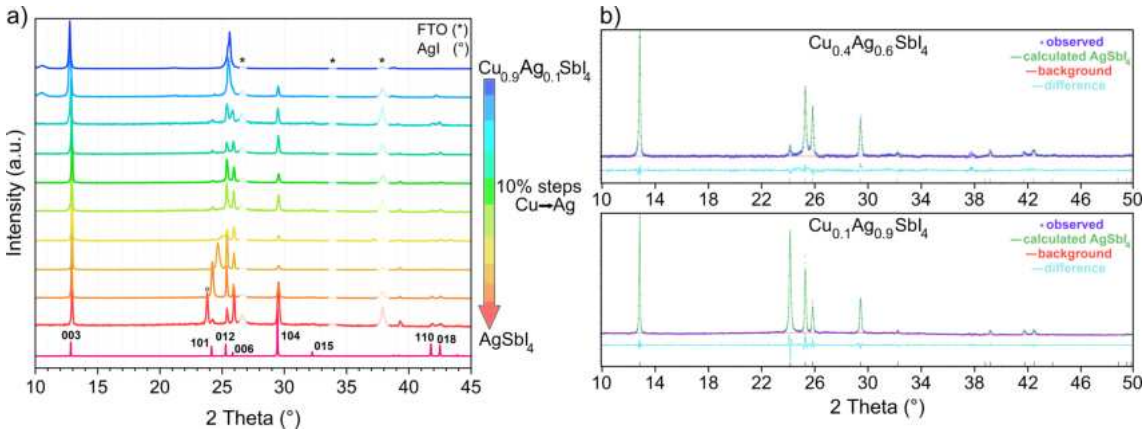

Figure 5.1: Thin film XRD data are normalized to the highest intensity. (a) CASI thin films on FTO substrates. Increasing Cu concentrations in steps of 10% coded from red to blue with theoretical patterns from Gray et al.[36] FTO reflections are transparent and marked with an asterisk (*). (b) Peak profile refinements with the Le Bail method for $Cu_{0.1}Ag_{0.9}SbI_4$ and $Cu_{0.4}Ag_{0.6}SbI_4$.[48]

Ag- or Cu-rich compositions, the monovalent A cations may occupy the 3b positions in-between the octahedral slabs.[38,47] Our DFT calculations discussed below show slightly preferential formation of the 1:1:4 composition rather than the 3:1:6 composition, which both, however, appear to be metastable. Also, large losses in V_{oc}, as discussed later, suggest the presence of imperfect phases. Thus, we will limit our discussion to the 1:1:4 composition.

The diffractograms of CASI films on FTO are shown in Figure 5.1a for the incremental replacement of Ag with Cu in 10% steps. They match well with the theoretical patterns of $AgSbI_4$ extracted from the Bi analog $AgBiI_4$, up to a Cu substitution of 80%, i.e., $Cu_{0.8}Ag_{0.2}SbI_4$ and $Cu_{0.9}Ag_{0.1}SbI_4$ assuming the same space group ($R3\bar{m}$) and a related crystal structure based on the $CdCl_2$ prototype, in line with Gray et al.[36,47] For the thin film of pure $AgSbI_4$ (without Cu), a significant contribution of the AgI side phase can be observed at 23.8° (Figure 5.1a red), which can be completely avoided with the first substitution step to $Cu_{0.1}Ag_{0.9}SbI_4$ (Figure 5.1a, orange). Good agreement with the theoretical structure is shown in the bottom part of Figure 5.1b through a profile peak refinement using the Le Bail method. Note that a profile refinement with the Ag_3BiI_6 structure results in a similar agreement (FigureSI 5.22). Interestingly, within the next two substitution steps, the relative intensity of the (101) reflection is reduced to a minimum, and for $Cu_{0.2}Ag_{0.8}SbI_4$ (light orange), a second strong reflection at 24.66° appears, which has a weak intensity and is shifted to higher angles, at 25° for $Cu_{0.3}Ag_{0.7}SbI_4$ (yellow). These reflections are absent after inclusion of 40% Cu and higher, as shown in the top part of Figure 5.1b for $Cu_{0.4}Ag_{0.6}SbI_4$, agreeing well with the structure of $AgSbI_4$. As the true origin of these reflections is nontrivial and would require detailed solid state and structural analysis, which is beyond the scope of this article, we suggest a few con-

siderations. Upon substitution of Ag with Cu, we expect the octahedral coordination to be strongly distorted, as Cu^+ generally prefers tetrahedral coordination. This, along with the smaller ionic radius of Cu^+ (0.6 Å for tetrahedral coordination and 0.77 Å for octahedral coordination) compared to that of Ag^+ (1.15 Å for octahedral coordination), should lead to deformations of the octahedral symmetry and the lattice parameters, as shown below in Figure 5.4b, where Ag/Cu coordination was optimized to a tetrahedral coordination through DFT calculations.[49] As most reflections in the sequence of XRD patterns do not change their position as drastically as the (101) reflection, a large change in the unit cell parameters is not plausible here. The shift and the increased width of the aforementioned reflections at 24.66° and 25° further indicate the presence of overlapping reflections, which can also be observed for $Cu_{0.8}Ag_{0.2}SbI_4$ and $Cu_{0.9}Ag_{0.1}SbI_4$ for the (003), (012), and (006) reflections (see Figure 5.1). Since the inclusion of Cu distorts the octahedral structure, a reduction in symmetry from $R3\bar{m}$ to $C2/m$ or other lower symmetry subgroups is possible. Profile refinement using the structural solution from DFT, as discussed later, in the triclinic space group $P1$ agrees well with the observed thin film diffractogram (FigureSI 5.23). Lastly, for $Cu_{0.8}Ag_{0.2}SbI_4$ and $Cu_{0.9}Ag_{0.1}SbI_4$, the decreased crystallinity, the decreased number of observable reflections, and the appearance of a reflection at 10.48° suggest a structural breakdown and formation of a different phase than $AgSbI_4$. Consistently, the photovoltaic performance of materials with Cu contents of more than 60% is substantially reduced, as discussed below.

Previous reports suggested an intrinsic instability of the $AgSbI_4$ phase, whereas the Bi-based analog with a larger ionic radius was shown to be highly stable under synthesis and in ambient conditions.[36] Moreover, Al-Anesi et al. showed local symmetry enhancement through Sb doping of Cu_2AgBiI_6, thereby improving photovoltaic efficiency through enhanced local structural symmetry and thus reducing defect density.[34] Consequently, we also prepared a system with only a small addition of 5% Bi, resulting in a decrease in band gap (discussed later) and improved morphology. The corresponding XRD patterns show no significant change when comparing Bi-alloyed structures versus pure antimony thin films (see FigureSI 5.9).

In the following, we focus on samples with 0, 40, and 60% Cu/Ag as they are exemplary for the electronic and morphological changes in this system. The SEM images of those samples, shown in Figure 5.2a-f, highlight the strong impact of the monovalent halide precursor on the morphology and crystallization. First of all, the addition of Bi seems to generally aid the crystallization, resulting in films with significantly better coverage and homogeneous morphologies. Enhanced lattice stability may further rationalize the increased coverage and high homogeneity at 40% Cu, resulting in overall homogeneously covered films. Beyond 50% Cu, the homogeneity decreases again.

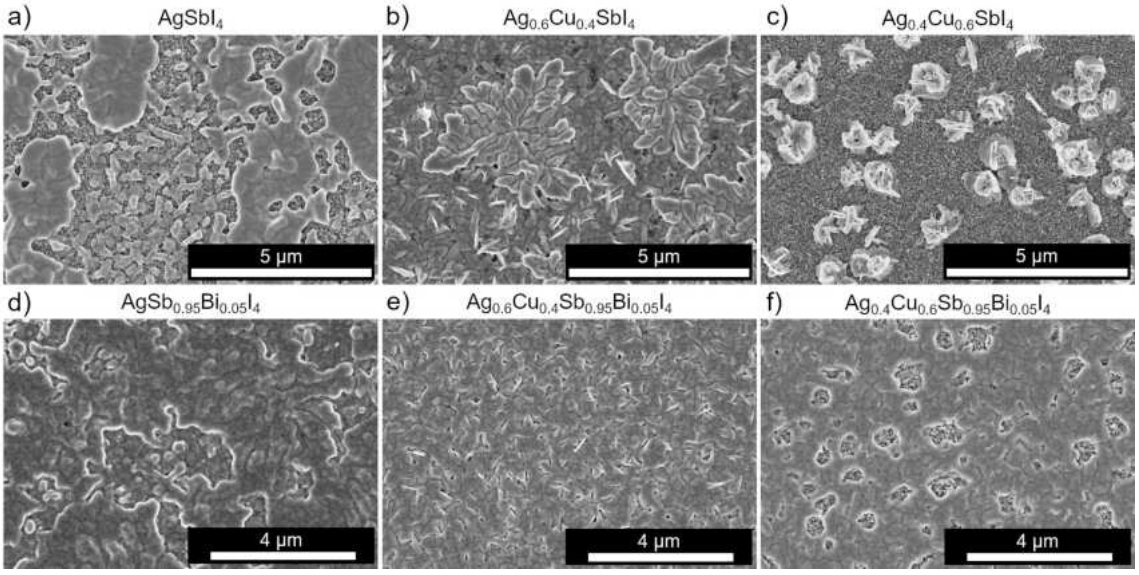

Figure 5.2: Scanning electron microscopy images of CASI thin films on FTO/c-TiO_2/mp-TiO_2. (a-c) Increasing amount of Cu (0, 40, and 60%) and (d-f) increasing amount of Cu (0, 40, and 60%) combined with 5% Bi/Sb-substitution.

XPS spectra confirm the incorporation of Cu and the presence of the expected elements (e.g., Ag 3d and Sb 3d), verifying the formation of the pure silver and copper-alloyed phases; see FigureSI 5.7a-c. A characteristic energy difference of 367.2 eV between Ag $3d_{5/2}$ and the VB onset was measured for the Cu-Ag-Sb/Bi-I thin films. Interestingly, the XPS spectra of the pure $AgSbI_4$ (FigureSI 5.7c) show additional states at approximately 528.7 eV (i.e., 2.0 eV below the characteristic peak of Sb^{3+}. According to the literature, it is assigned to Sb_0.[50] This side phase vanishes when Cu is added to the system (FigureSI 5.7).

We now employ a combined fitting procedure following Elliott's method for the absorption coefficient close to the band edge and Urbach tail to quantify the band gap and sub-band gap states.[51] The band gap of $AgSbI_4$ lies within the range of 2.0-2.2 eV, as in Figure 5.3a for $AgSbI_4$ (green), $Cu_{0.4}Ag_{0.6}SbI_4$ (blue), $Bi_{0.05}AgSbI_4$ (orange), and $Bi_{0.05}Cu_{0.4}Ag_{0.6}SbI_4$ (red). Changing the Cu/Ag ratio does not significantly alter the band gap, while the addition of Bi reduces the band gap by 0.2 eV. The decrease in band gap upon Bi/Sb alloying has previously been successfully assigned to the formation of aggregates rich of either Sb or Bi for similar materials, being the source of the reduction in the electronic band gap.[25,52] Furthermore, the Urbach tails all converge to the same energy of around 1.6 eV, indicating the presence of trap states. This deep contribution is reduced through the incorporation of 40% Cu, which is most likely tied to the improved crystallinity and morphology, suggesting that fewer defects are introduced in the synthesis compared to the reference systems, as confirmed by absorbance log plots (FigureSI 5.11). These disorder-related deep levels are also confirmed by the PL emission,

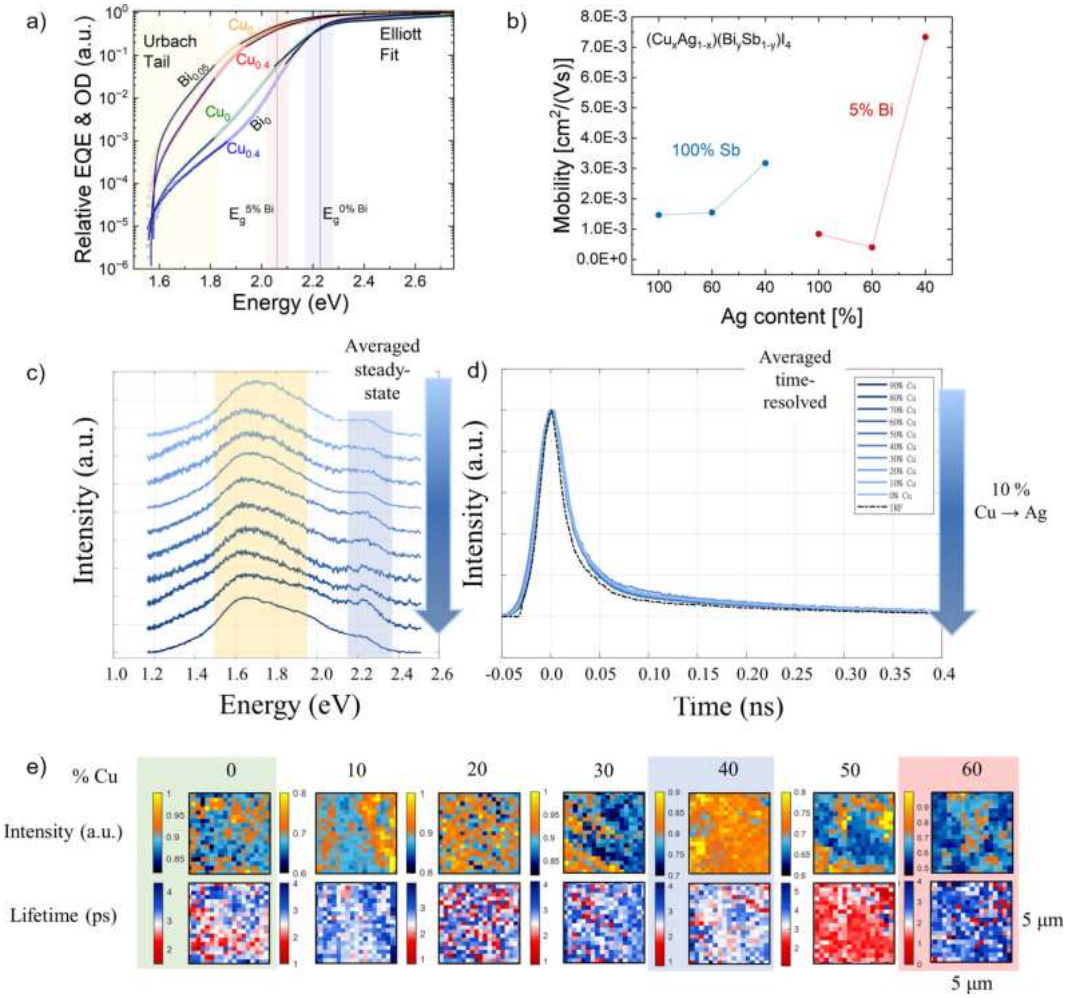

Figure 5.3: (a) Fitted absorption coefficient of $AgSbI_4$ (green), $Cu_{0.4}Ag_{0.6}SbI_4$ (blue), $AgBi_{0.05}Sb_{0.95}I_4$ (yellow), and $Cu_{0.4}Ag_{0.6}Bi_{0.05}Sb_{0.95}I_4$ (red). Red and blue boxes highlight the band gap extracted from the Elliott fits. The straight lines around the band edge are fitted with Elliott's method and the black lines in the band gap are exponential Urbach tails. (b) Mobility values extracted from time-resolved microwave conductivity measurements for Ag concentrations of 100, 60, and 40% without (blue) and with 5% Bi-substitution (red). (c) Averaged spectra from PL measurements for incremental Cu percentage from 0 to 100% without Bi addition (dark to light blue: increasing Cu content). The yellow box highlights the selftrapped exciton emission and the light blue box highlights the band-to-band emission. (d) Averaged time-resolved PL measurements for incremental Cu percentage from 0 to 100% without Bi addition (dark to light blue: increasing Cu content). (e) Hyperspectral images of the PL intensity and time-resolved PL intensity distribution on a 5 μm $\times$ 5 μm large area of a CASI thin film with composition ranging from 0 to 60% Cu/Ag ratio.

as seen in Figure 5.3c, where the main emission maximum lies at around 1.6 eV as well, with only a small contribution at the band edge (2.3 eV), which agrees well with the band gap obtained from the Elliott fits. This low energy emission is probably caused by self-trapped excitons and defects dominating the emission behavior, which was reported to be induced by exciton-phonon coupling and the resulting ultrafast carrier localization in multiple lead-free perovskite materials.[53–55] Furthermore, the lifetimes are also unaffected by additional Cu doping and occur in the range of only picoseconds (Figure 3d).

The detailed spectral trends of PL and lifetime measurements for all samples are shown in FigureSI 5.13, with only negligible intensity and lifetime differences evident.

Mobility values for the thin films, extracted from time-resolved microwave conductivity (TRMC), highlight an overall increase when the silver content is reduced, as shown in Figure 5.3b. This is in line with previous reports on the related $Cu_{4x}(AgBi)_{1-x}I_4$ compound, where small polaron formation was found to be responsible for ultrafast charge carrier localization that could be mitigated via the introduction of Cu.[53,54] Note that the extracted charge carrier mobility is a lower estimate, limited by the sensitivity of the setup. Nevertheless, a comparison is feasible, indicating relatively low mobility compared to other lead-free perovskites like $Cs_2AgBiBr_6$ ($3\,cm^2\,V^{-1}\,s^{-1}$ to $5\,cm^2\,V^{-1}\,s^{-1}$).[56] Moreover, Bi addition does not increase the overall mobility in the pure $AgSbI_4$, but it significantly boosts the mobility for systems with Cu in excess of 60%.

To connect the optical properties with the morphology changes upon Cu doping, we performed fluorescence-lifetime imaging microscopy (FLIM) measurements; the results are shown in Figure 5.3e. Here, the intensity of the PL emission and the lifetime are spectrally and spatially resolved on a film area of the size $5\,\mu m \times 5\,\mu m$. These results confirm the trend of increased homogeneity of the surface of film samples alloyed with 40% Cu, showing the most consistent lifetimes overall and the best (homogeneous) distribution of luminescence intensity. The latter decreases sharply at 50% Cu and above, drastically decreasing the lifetime of the whole sample area. Keeping in mind the similar electronic characteristics over the whole substitution range, these measurements reveal the important role of the A cation in such structures, directing morphology, excitation behavior over a bigger sample size, and, as shown in Figure 5.5, device performance and statistics.

DFT calculations were then performed to shed light on the impact of composition on the Ag-Sb-I and Cu/Ag-Sb-I rudorffite phases. The ionic positions and cell parameters were optimized on the PBE level of theory, including D3 dispersion corrections, with refined PBE0 + SOC calculations for formation energies and electronic band gaps; see computational details in the Supporting Information. The cubic $ThZr_2H_7$-type $AgSb_2I_7$ stoichiometry,[43,56–58] see FigureSI 5.14, is unlikely to form as seen in the large formation energies of 4.86 eV/f.u., see Table 5.1. Additionally, predicted band gaps of 0.39 eV, far below the experimental values, rule out the existence of $AgSb_2I_7$ stoichiometry, in line with studies on its Bi-based counterpart.[43] $AgSbI_4$ and Ag_3SbI_6 phases show disorder in their positions of Sb and Ag ions; see FiguresSI 5.15 and 5.16. Starting from the structure of the Bi-based counterparts,[56,59,60] a configurational screening was performed to obtain low energy configurations using DFT. Both compositions ($AgSbI_4$ and Ag_3SbI_6) show low energy structures with formation energies of -0.01 and 0.03 eV with band gaps of 2.07 and 1.78 eV for $AgSbI_4$ and Ag_3SbI_6, respectively. Recalling the experimental band gap

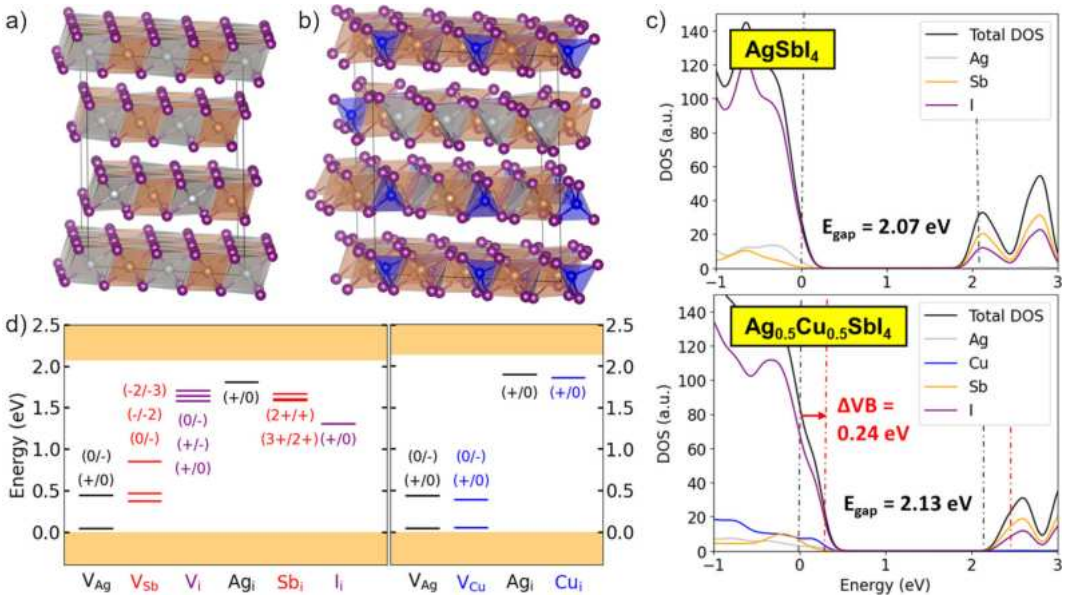

Figure 5.4: (a,b) Structural representation of $AgSbI_4$ and $Cu_{0.5}Ag_{0.5}SbI_4$, respectively, with the following color codes: Ag = silver, Cu = blue, Sb = orange, and I = purple. (c) Density of states on the PBE0+SOC level of theory of (top) $AgSbI_4$ and (bottom) $Cu_{0.5}Ag_{0.5}SbI_4$. Electronic band gap values are given in each panel. The potential of the considered systems has been aligned with respect to the vacuum level to obtain the VB shift between $AgSbI_4$ and $Cu_{0.5}Ag_{0.5}SbI_4$, as highlighted in red. The VB maximum of the $AgSbI_4$ phase has been set to zero energy. (d) Thermodynamic ionization levels (TILs) of point defects, vacancies V_X, and interstitials X_i for each element X = (Ag, Cu, Sb, and I), based on hybrid PBE0 + D3 DFT calculations with inclusion of SOC. Orange parts highlight the VB band (bottom) and conduction band (top). Right box: comparison of Ag and Cu TILs. Computational details on the defect calculations are provided in the Supporting Information.

values of $\sim$ 2.0-2.2 eV, supports the existence of layered $AgSbI_4$ phases, see Figure 5.4a, while Ag_3SbI_6-rich side phases may contribute to the subgap absorption and emission features. The DOS of the $AgSbI_4$ phase shows the expected dominant role of iodide at the valence band (VB) edge, while the conduction band edge is dominated by Sb and I states from the SbI_6 octahedra, with limited contribution from Ag; see Figure 5.4b. Note that entropic contributions, neglected in our study, likely contribute to the phase stabilization of such disordered phases.

Moving to the (Cu/Ag)-Sb-I compositions, especially the Cu_2AgSbI_6 phase has recently been proposed to form in the Bi counterparts.[61] The structure of the given phase is highly disordered, with many cations occupying the same lattice positions, requiring a configurational screening; see FigureSI 5.17. The proposed low-energy structure shows a formation energy of 0.42 eV/f.u., containing layers of Ag/Cu-I without Sb incorporated; see configuration c11 in Figure 5.17, which is substantially lower than fully mixed structures; see TableSI 5.3. This may point to favorable phase segregation in such compounds. Electronic band gap values of 1.90 eV are in fair agreement with experiments. Still, the successful incorporation of Cu ions over a wide range of Cu/Ag alloying in our experimental investigation raises concerns about the relevance of the Cu_2AgSbI_6 phase. Thus,

Table 5.1: Optimized Lattice Parameters (PBE,D3) of the Low Energy Configuration of the Ag-Sb-I and Cu/Ag-Sb-I Rudorffite Phases[a].

system	formation energy (eV/f.u.)	band gap (eV)	lattice constants (Å)	cell angles (°)
$AgSb_2I_7$	4.86	0.39	$a = b = c = 14.637$	$\alpha = \beta = \gamma = 90$
$AgSbI_4$	-0.01	2.07	$a = 8.671$	$\alpha = 88.97$
			$b = 8.665$	$\beta = 91.11$
			$c = 20.804$	$\gamma = 120.58$
Ag_3SbI_6	0.03	1.78	$a = 9.178$	$\alpha = 86.57$
			$b = 8.751$	$\beta = 92.47$
			$c = 20.763$	$\gamma = 122.65$
Cu_2AgSbI_6	0.42	1.90	$a = 8.551$	$\alpha = 89.96$
			$b = 8.252$	$\beta = 90.11$
			$c = 21.452$	$\gamma = 119.52$
$Cu_{0.5}Ag_{0.5}SbI_4$	0.14	2.13	$a = 8.671$	$\alpha = 88.97$
			$b = 8.665$	$\beta = 91.11$
			$c = 20.804$	$\gamma = 120.58$

[a]Formation energies per formula unit and electronic band gaps are given at the PBE0 level of theory with the inclusion of SOC corrections on the PBE+D3 optimized geometries. TableSI 5.3 summarizes a configurational analysis for each composition.

we performed DFT calculations on the $Cu_{0.5}Ag_{0.5}SbI_4$ composition, keeping the overall A-B-X stoichiometry of 1-1-4 and replacing half of the Ag ions by Cu, as suggested by our XRD data in Figure 5.1. Interestingly, the formation energy of the $Cu_{0.5}Ag_{0.5}SbI_4$ phase, see Figure 5.4b, decreases to 0.14 eV/f.u., with a band gap of 2.13 eV, in excellent agreement with our experimental thin films. We further predict an upshift of the VB edge by 0.24 eV compared to the $AgSbI_4$ phase; see Figure 5.4c. Notably, VB XPS spectra (FigureSI 5.7d) show an increase in the VB energy upon Cu addition by ∼0.15-0.25 eV. The energy difference between the VB onset and the Fermi level (binding energy of 0 eV) decreases from 1.1 eV ($AgSbI_4$) to 0.8 eV (40% Cu) and depends on the Cu content and the presence of Bi. In addition, 0.15 eV binding energy shifts of the core levels such as Cu $2p_{3/2}$, Sb $3d_{5/2}$, or Ag $3d_{5/2}$ (FigureSI 5.7a-c) are also observed for these samples, meaning that the Fermi level position inside the band gap is modified by 0.15-eV and that the VB onset is also shifted by 0.15 eV to higher energy. It confirms our DFT results and, most importantly, underlines the existence of the 1:1:4 stoichiometry in our synthesized thin films. Thus, we can expect that the 1:1:4 stoichiometry is accessible over a large range of Cu/Ag alloying. In addition, it can be noted that combining the optical band gap and the energy difference between the VB onset and the Fermi level indicates that the (Cu/Ag)-Sb-I composition materials are rather intrinsic semiconductors.

We further calculate the defect formation energies (DFEs), see FiguresSI 5.19 and 5.20, and thermodynamic ionization levels (TILs), see Figure 5.4d, for the pure $AgSbI_4$ and the

alloyed $Cu_{0.5}Ag_{0.5}SbI_4$ compounds. All geometries were optimized on the PBE + D3 level of theory with refined calculations for DFE and TILs based on the PBE0 level of theory with the inclusion of spin-orbit coupling corrections. We observe low DFEs of 0.16 eV for Ag vacancies (V_{Ag}^-) and interstitials (Ag_i^+), representing hole and electron trap states at 0.44 eV above the VBM and 0.25 eV below the CBM; see Figures 5.4d and 5.19. This suggests that subgap emission features at 1.6 eV (i.e., 0.6 eV below the band gap measured in Figure 5.3a) may likely be caused by the recombination of electrons trapped at Ag vacancies. The low formation energies of Ag point defects further are in line with features of Ag-Bi-I compounds that previously have been considered for ionic conduction due to their mobile Ag ions.[60] Notably, Sb and I point defects also act as trap states within the band gap; see Figure 5.4d, while showing moderate formation energies of ∼0.7 to 0.9 eV, thus being of less relevance for the optoelectronic properties of $AgSbI_4$. Moving toward the alloyed $Cu_{0.5}Ag_{0.5}SbI_4$, we observe negligible differences in the TILs and DFEs (FigureSI 5.20) for Ag and Cu vacancies and interstitials, in line with the low dependence of subgap emission on Cu/Ag alloying, as shown in Figure 5.4c. This suggests further that the reduction of subgap absorption upon Cu addition is due to the growth of more homogeneous morphologies (see Figure 5.2) rather than a suppression of point defect formation. Consequently, Cu alloying is mainly relevant for reducing AgI-rich side phases, while the concentration of incremental Cu alloying shifts the type of detrimental defects between Ag and Cu.

After the structural and electronic properties of the CASI rudorffites were elaborated, photovoltaic devices were fabricated in the n-i-p architecture with increasing amounts of Cu. Mesoporous TiO_2 was used as the electron transport layer and PTAA as the hole transport layer.[28,29,62] The statistical analysis of the device performance can be seen in Figure 5.5a-f. First, the overall performance increases significantly when employing only a small substitution of 5% Bi, attributed to the band gap decrease. Second, Cu addition also increases the overall performance until an optimal concentration of 40%, while the performance breaks down at a higher level. Interestingly, the minor incorporation of Bi additionally stabilizes the performance over a wider range of Cu/Ag ratios, almost up to 80%. We attribute this impact of Bi to the improved homogeneity of the morphology as seen in Figure 5.2f, hinting at a highly beneficial role of BiI_3 in the precursor solution. In the Bi-free series, samples prepared with 40% Cu are generally the most efficient, showing the overall highest PCE, mostly due to the increased current density. Notably, the low open circuit voltage is the main bottleneck in these systems, as also suggested previously.[29,30] In our studies, only samples with added Bi surpass the 0.4 V open circuit voltage in some cases, whereas Cu-alloyed samples show only small improvements. We attribute the low voltage to nonradiative recombination processes mediated by Ag

point defects, representing trap states with low formation energies as shown by our DFT calculations, and ultrafast carrier localization.[51,53]

To further estimate the potential of Sb-based rudorffites for indoor photovoltaics, external quantum efficiency (EQE) measurements were carried out on well-performing solar cells with and without white light background illumination. As shown in Figure 5.5g, the EQE measured under white light illumination at 100 mW cm^{-2} is comparably small, with a maximum of 20% for Cu-alloyed films at 450 nm without Bi and at 550 nm with Bi. Interestingly, when using a chopped white light source without a white light bias, the overall EQE increases significantly by approximately 10% for all thin films, except $Cu_{0.4}Ag_{0.6}SbI_4$. This could be explained by a different recombination mechanism at high fluence intensities in this system, as seen in the TRMC curves in Figure 5.12b. The EQE increase is in line with the behavior of Cu_2AgBiI_6 rudorffites, where the efficiency for indoor light illumination almost doubles up to 10% iPCE,[34] being attributed to reduced nongeminate recombination, which seems to be an intrinsic feature of (Cu/Ag)-(Sb/Bi)-I-based materials.

Although the initial performance falls behind Bi-based "rudorffites",[28,34,57] this class of materials offers great potential for indoor applications while being easily tunable. Furthermore, our results demonstrate the compositional freedom of solution-processed rudorffites. We propose that through stoichiometry tweaking and precursor engineering-i.e., by employing acetates or other metal sources[15,22]-or further additive modification, the performance could be strongly improved to offer a viable alternative for low-cost indoor photovoltaics.

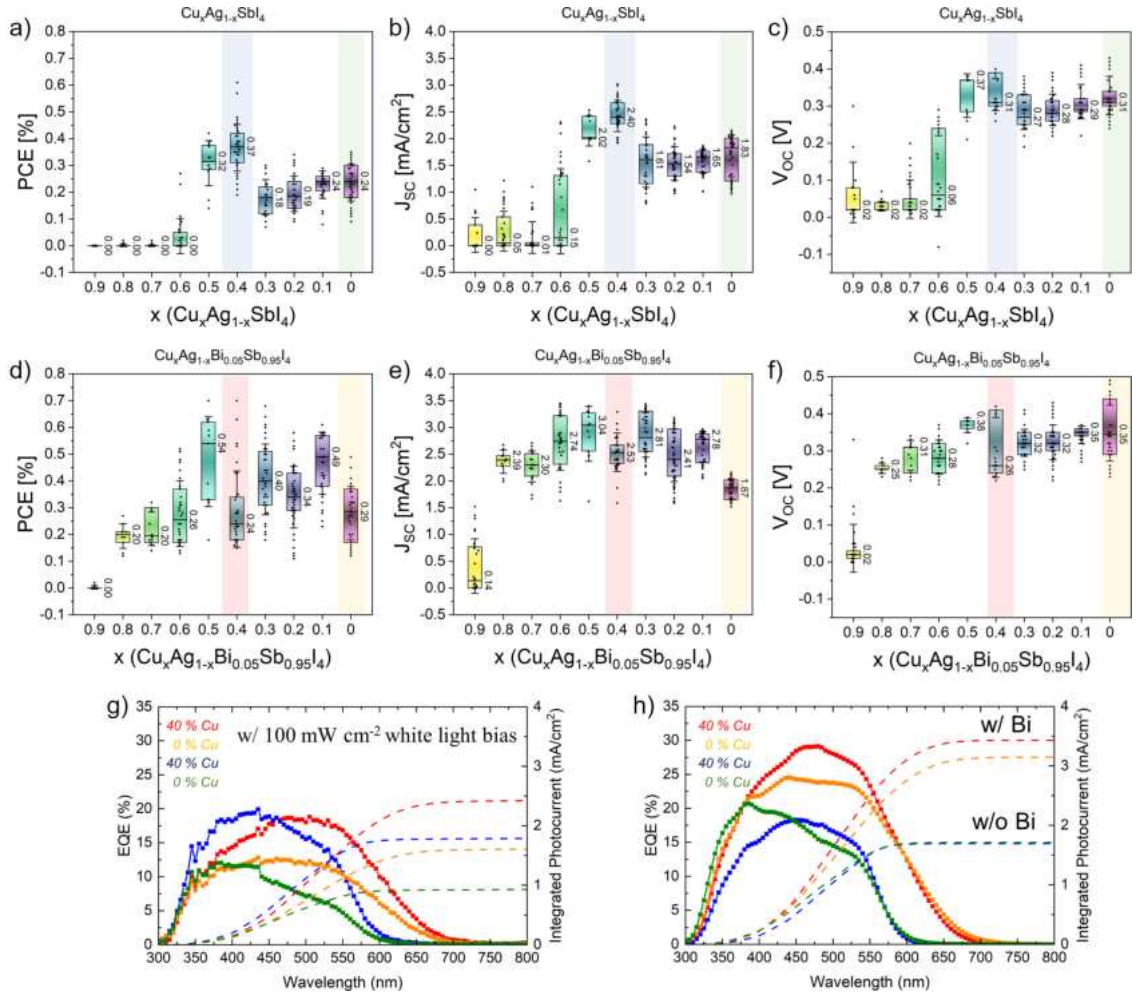

Figure 5.5: Characterization of the photovoltaic devices. (a-c) PCE, Jsc, and Voc statistical box plots with median, interquartile range, and statistical outliers for 10% changes of the Cu/Ag ratio from $Cu_{0.9}Ag_{0.1}SbI_4$ to $Cu_{0.0}Ag_{1.0}SbI_4$. The same color scheme for the colored boxes as for Figure 5.4a was used to highlight the reference and the most efficient alloying step. (d-f) PCE, J_{sc}, and V_{oc} statistical box plots with median, interquartile range, and statistical outliers for 10% changes of Cu/Ag ratio with fixed 5% Bi content from $Cu_{0.9}Ag_{0.1}Bi_{0.05}Sb_{0.95}I_4$ to $Cu_{0.0}Ag_{1.0}Bi_{0.05}Sb_{0.95}I_4$. The same color scheme for the colored boxes as for Figure 5.4a was used to highlight the reference and the most efficient alloying step. (g,h) EQE spectra and integrated photocurrent density of the most efficient solar cells for $AgSbI_4$ (green), $Cu_{0.4}Ag_{0.6}SbI_4$ (blue), $AgBi_{0.05}Sb_{0.95}I_4$ (orange), and $Cu_{0.4}Ag_{0.6}Bi_{0.05}Sb_{0.95}I_4$ (red). The data in (g) were measured with a constant 100 mW cm^{-2} white light source in the background, while the data in (h) were measured without white light bias.

5.4 Conclusions

To summarize, we successfully synthesized "rudorffite"-type Cu/Ag-Sb-I thin films using the Lewis-base additive thiourea. We establish control of the thin film morphology by partial alloying of Ag with Cu atoms, resulting in homogeneous coverage, which was even improved upon partial substitution with Bi. DFT calculations and optical characterization point to the formation of a $AgSbI_4$ phase in the pure Ag case and the incorporation of Cu ions, partially replacing Ag and forming $Cu_{1-x}Ag_xSbI_4$. Other phases that have been previously discussed for the Bi-based counterparts could be ruled out due to larger formation energies or lower predicted band gaps. Our results further reveal the detrimental role of Ag point defects, which induce sub-band gap electronic states that may act as recombination centers, resulting in subgap emission and absorption features. We further demonstrate that Cu alloying does not significantly alter the electronic band gap, which consequently represents a facile strategy for the optimization of Sb-based rudorffites. Solar cells based on Sb-based rudorffites show low power conversion efficiencies of around 0.3%, mainly limited by large losses in the V_{oc}. Substituting the optimal ratio of Cu/Ag with a small amount of 5% bismuth to $Cu_{0.4}Ag_{0.6}Sb_{0.95}Bi_{0.05}I_4$ raises the efficiencies to up to 0.7%, mainly through a reduction of the electronic band gap and an increased J_{sc}. We observe an apparent stabilization of current density and open-circuit voltage upon addition of Bi over a wide range of Cu/Ag alloys. Finally, white light bias-free EQE measurements suggest a much-improved performance of these materials for indoor photovoltaic applications, which we attribute to reduced geminate recombination at low light intensity. These observations offer opportunities for the control and design of novel Sb-based rudorffites as perovskite-inspired semiconductors with the potential for diverse optoelectronic applications such as indoor photovoltaics.

5.5 Experimental/Methods

Precursor Solution. To synthesize (Cu/Ag)-(Bi/Sb)-I films, the corresponding iodides were dissolved in a 1:1 vol% mixture of DMF/DMSO in a 0.6 M precursor solution with a 1 wt% additive of TU.

Table 5.2: Precursors and Respective Weights/Substance Amounts for the Thin Film Synthesis of CASI Thin Films.

	x (molar ratio)					
	0	0.1	0.2	0.3	0.4	0.5
AgI (Sigma-Aldrich)	140.8/0.6	126.8/0.54	112.7/0.48	98.6/0.42	84.5/0.36	70.4/0.3
CuI (Sigma-Aldrich)	0/0	11.4/0.06	22.9/0.12	34.3/0.18	45.7/0.24	57.1/0.3
SbI_3 (Alfa Aesar)	301.4/0.6	301.4/0.6	301.4/0.6	301.4/0.6	301.4/0.6	301.4/0.6
	x (molar ratio)					
	0.6	0.7	0.8	0.9	1.0	
AgI (Sigma-Aldrich)	56.3/0.24	42.3/0.18	28.2/0.12	14.1/0.06	0/0	
CuI (Sigma-Aldrich)	68.6/0.36	80.0/0.42	91.4/0.48	102.8/0.54	114.27/0.6	
SbI_3 (Alfa Aesar)	301.4/0.6	301.4/0.6	301.4/0.6	301.4/0.6	301.4/0.6	

1 mL of precursor solutions for the CASI systems were weighed in as follows: x is the molar ratio ($Cu_xAg_{1-x}SbI$); the masses are given in weight/amount of substance [mg/mmol] (Table 5.2). To these mixtures, 1 wt% with respect to the total precursor weight of TU was added (4.42 mg, 0.06 mmol, Sigma-Aldrich) and dissolved in 0.5 mL DMF and 0.5 mL DMSO. Furthermore, for 5% Bi-substitution, 17.69 mg (0.03 mmol) BiI_3 was added, and only 286.4 mg (0.57 mmol) SbI_3 was used.

Thin Film Deposition. All solutions were heated at 70 °C on a hot plate in a nitrogen atmosphere for 30 min prior to spin-coating. For thin film deposition, 70 μL of the precursor solution was spincoated on different substrates at 3000 rpm for 10 s, followed by 6000 rpm for 50 s. Varying substrate types were cleaned with oxygen plasma under vacuum (up to 10^{-4} mbar). Glass and fluorine-doped tin oxide (FTO) substrates were cleaned at 50% power for 5 min with a Diener Femto Plasma Etcher.

X-ray Analysis. XRD data of thin films were recorded on a Bruker D8 Discover instrument operating at 40 kV and 30 mA with Cu Kα radiation (λ = 1.5406 Å) and a position-sensitive LynxEye detector. XRD patterns were measured in the range of 2θ = 5-60° with a step size of 0.05°. Powders were measured on a STOE STADI P diffractometer with Cu Kα radiation (λ = 1.5406 Å) and a Ge(111) single-crystal monochromator equipped with a DECTRIS solid-state strip detector MYTHEN 1K, which was used for wide-angle X-ray diffraction measurements in transmission mode. Powder patterns were measured in the range of 2θ = 5-60° with a resolution of 0.05° and a step size between 0.5 and 4°

with a counting time of 20-90 s per step.

Device Fabrication. A sol-gel approach was used to deposit the compact TiO_2 layer from a solution containing 0.23 M titanium isopropoxide (Sigma-Aldrich, 99.999%) and 0.013 M HCl in isopropanol (IPA). The solution of 250 μL per 6 $\times$ 6 cm^2 substrate size was spin-coated dynamically on top of the substrate at 2000 rpm for 45 s, dried at 150 °C for 10 min, and annealed at 500 °C for 45 min.

In devices with a mesoporous TiO_2 layer, an approximately 150 nm thick, mesoporous (mp)-TiO_2 layer was applied by spin-coating 100 μL of a TiO_2 nanoparticle paste (Dyesol DSL 18NR-T) diluted in absolute ethanol (1:6 weight ratio) onto the above compact TiO_2 layer at 2500 rpm for 30 s, followed by subsequent annealing at 500 °C for 45 min under ambient conditions.

PTAA (12 mg, average molecular weight Mn = 30,000) was dissolved in 1 mL of toluene, and the resulting solution was filtered using a syringe filter (pore diameter 0.45 μm). A 70 μL aliquot of the filtered solution was spin-coated on top of the active layer in a single-step spin coating program at 3000 rpm for 35 s, and the obtained films were annealed at 100 °C for 5 min.

The top electrode with a thickness of 40 nm was deposited by thermally evaporating gold under a vacuum (at 10^{-7} mbar).

SEM Measurements. For analysis of the thin film morphology, thickness, and composition, scanning electron microscopy (SEM) was performed on an FEI Helios Nanolab G3 UC-DualBeam SEM with an acceleration voltage between 2 and 5 keV.

X-ray Photoelectron Spectroscopy. The samples were sealed in a nitrogen atmosphere and delivered to Darmstadt, where they were opened in a glovebox filled with N_2, and then transferred under vacuum to the DAISY-SOL lab cluster tool. XPS was then performed with a Thermo Fisher VG Escalab 250 spectrometer in an analytic chamber with a pressure kept below 3×10^{-9} mbar. A monochromatic Al Kα X-ray source (hv = 1486.6 eV) operating at 12.5 mA and 14.2 kV was used for the XPS experiment without a charge neutralizer. The measurement mode was adjusted to get a lateral resolution of 650μm in diameter and overcome possible inhomogeneity at the sample surface.

The high-resolution spectra were acquired with a pass energy of 10 eV, a step size of 0.05 eV, and a dwell time of 50 ms; up to 60 scans were made to increase the signal-to-noise ratio.

XPS spectra were calibrated using the Fermi level of silver (0 eV) as well as the binding energy of the Au $4f_{7/2}$ emission line (84.0 eV), the Ag $3d_{5/2}$ emission line (368.26 eV-fwhm at a pass energy of 10 eV equal to 0.53 eV), and the Cu $2p_{3/2}$ emission line (932.67 eV). The Fermi level value was determined with a sigmoid fit and taking the position where the intensity is at 50%. Before the measurement, all calibration samples

were cleaned by using Ar sputtering (3 kV, for 180 s). The instrumental resolution was measured using the Fermi level of the cleaned silver, which was 0.44 eV for XPS (pass energy of 10 eV).

UV-Vis Spectroscopy. UV-vis spectroscopy was conducted with a PerkinElmer Lambda 1050 instrument equipped with a 150 mm integrating sphere. A tungsten-halogen and a deuterium lamp were used to create visible and ultraviolet light. The measurement interval was chosen from 350 to 900 nm with a monochromator step size of 2 nm.

PL Measurements. For PL measurements, hyperspectral images, and time-resolved PL images, a home-built confocal laser scanning microscope was used. It is based on a microscope body (NIKON) that is combined with an xyz-piezo-scanning stage (PHYSIK INSTRUMENTE). The samples were measured upside down in the epi-direction with an air objective (1.4 NA, Apo-Chromat, NIKON). A beamsplitter (MELLES GRIOT 03BTL005) and a spectral 490 nm long-pass filter were used to separate the laser from the PL light. A sub-picosecond laser (iChrome TOPTICA), which is tunable from 476 to 645 nm, was used for excitation. Here, we measured only with the 476 nm laser light, which was additionally filtered by a band-pass of 473/10 nm (CHROMA) in the excitation arm. The detection side consists of two parts that are separated by a flippable mirror. One has an avalanche photo diode (APD, type: MPD PDM, detector size 50 $\times$ 50 μm), which can be combined with timecorrelated single-photon counting (TCSPC) electronics (BECKER UND HICKEL) to measure time-resolved PL-transients. The second part consists of a spectrometer (ANDOR SHAMROCK SRi303) combined with an open electrode CCD camera (ANDOR NEWTON DU920) for recording spectra. The data were recorded using a customized LABVIEW (National Instruments) program that combines the manufacturers' software with our desired measurements. Further processing and analysis were carried out using MATLAB (MATHWORKS) programs to obtain the PL spectra, TCSPC transients, and the images.

TRMC Measurements. Thin films on sapphire substrates were placed in a microwave cavity. The TRMC technique was used to measure the change in reflected microwave (9 GHz) power after pulsed excitation (repetition rate 1 kHz) of the samples at 355 nm using the third harmonic of a Nd/YAG laser. The layers were illuminated from the glass side.[55]

Solar Cell Characterization. Photovoltaic device performance was measured with a Keithley 2400 source meter in air at 25 °C under illumination by a Newport Oriel Sol2A solar simulator, which was calibrated to 100 mW cm^{-2} with a Fraunhofer ISE-certified silicon cell with a mismatch factor of 1.01. The active area of the solar cell was defined with a square metal aperture mask of 0.0831 cm^2.

EQE Measurements. Measurements were performed on a homebuilt setup with a

halogen lamp, a monochromator, and a silicon reference diode. The light was chopped at 330 Hz, and the signal was detected through a lock-in amplifier. The setup was calibrated with a silicon solar cell, and no bias light was applied.

Computational Details. DFT calculations were performed on Ag-Sb-I and alloyed Cu/Ag-Sb-I rudorffites. Cell parameters were refined within the Quantum ESPRESSO software package66 (vc-relax) using the GGA-PBE exchange correlation functional.[63] Electron-ion interactions were described by scalar relativistic ultrasoft pseudopotentials (Ag, 11 electrons, $5s^2$, $4p^9$; Cu, 11 electrons, $4s^2$, $3d^9$; Sb, 5 electrons, $5s^2$, $5p^3$; and I, 7 electrons, $5s^2$, $5p^5$). Plane-wave basis set cutoffs for the smooth part of the wave functions and the augmented density were 40 and 320 Ry, respectively. The Brillouin zone was sampled using a 4 $\times$ 4 $\times$ 1 Monkhorst-Pack grid.[64] Dispersion corrections were accounted for by the DFT-D3 scheme.[65]

Accurate electronic band gaps were calculated using the PBE0 functional,[66] including spin-orbit coupling within the Quantum ESPRESSO package.[67] Here, we used full relativistic norm-conserving pseudopotentials (Ag, 19 electrons, $4s^2$, $4p^6$, $4d^10$, $5s^2$, $4p^9$; Sb, 15 electrons, $4d^10$, $5s^2$, $5p^3$; and I, 7 electrons, $5s^2$, $5p^5$) with a cutoff on the wave functions of 40 and 80 Ry on the Fock grid and sampling the Brillouin zone using a 2 $\times$ 2 $\times$ 1 Monkhorst-Pack grid. PDOS plots were generated with a Gaussian smearing of 0.1 eV.

5.6 Acknowledgements

The authors acknowledge funding from the Bavarian Network 'Solar Technologies Go Hybrid', the German Science Foundation (DFG) focus program SPP 2196 (projects BE 1042/10-1, 424101351, 506623857, 423746744 and 424707803), and the DFG Excellence Cluster e-conversion (EXC 2089/1-390776260). The authors thank Dr. Steffen Schmidt for performing the SEM measurements. W.K., E.M., and F.D.A. acknowledge funding from the European Union's Horizon Europe research and innovation programme under grant agreement no. 101082176-VALHALLA and from the European Union- NextGenerationEU under the Italian Ministry of University and Research (MUR) National Innovation Ecosystem grant ECS00000041-VITALITY. The views and opinions expressed are, however, those of the author(s) only and do not necessarily reflect those of the European Union or CINEA. Neither the European Union nor the granting authority can be held responsible for them. F.D.A. acknowledges Universita degli Studi di Perugia and MUR for support within the project Vitality.

5.7 Supporting Information

Cu/Ag-Sb-I Rudorffite Thin Films for Photovoltaic Applications

R. Hooijer†, A. Weis†, W. Kaiser, A. Biewald, P. Dörflinger, C. Maheu, O. Arsatiants, D. Helminger, V. Dyakonov, A. Hartschuh, E. Mosconi, F. De Angelis, T. Bein, Chemistry of Materials **2023**, 35(23), 9988-10000.

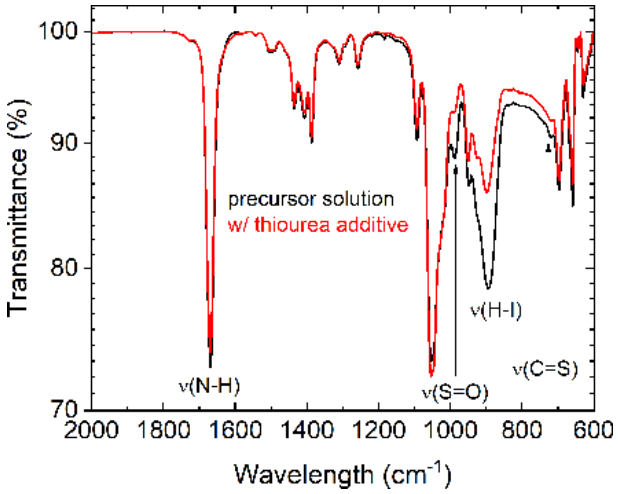

Figure 5.6: **S1** Infrared spectrum of two 1.0 M solutions of $AgSbI_4$ with (red) and without (black) 1 wt% (with respect to total precursor weight) thiourea additive. Characteristically changing vibrations are highlighted.

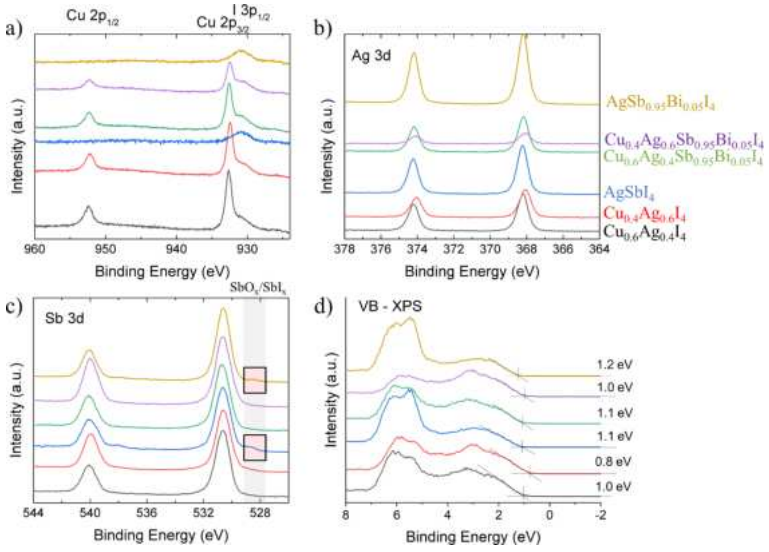

Figure 5.7: **S2** XPS spectra for AgSbI4 thin films with and without Bi (5%) and Cu (40%, 60%) replacement. a) Cu $2p_{1/2}$ and I $3p_{1/2}$ regions. b) Ag 3d states. c) Sb 3d states with an inset of SbO_x/SbI_x states. d) Valence band XPS data with valence band edge for all samples.

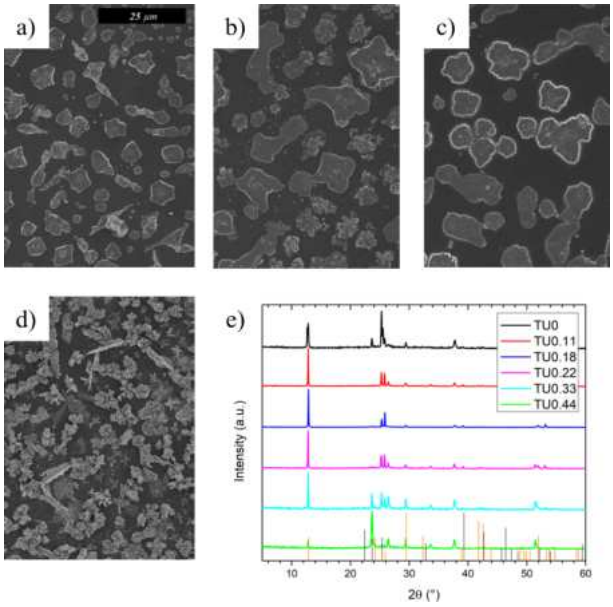

Figure 5.8: **S3** SEM images on compact TiO_2 and XRD data of $AgSbI_4$ thin films synthesized by annealing a 1 M precursor solution prepared as described in the methods section at 110 °C for 1 min to 70 °C for 1 h. a) Addition of 0 mol/L, b) 0.11 mol/L, c) 0.18 mol/L, and d) 0.33 mol/L thiourea. e) XRD patterns for different thiourea concentrations with theoretical patterns for $AgBiI_4$ (orange) and AgI (grey).

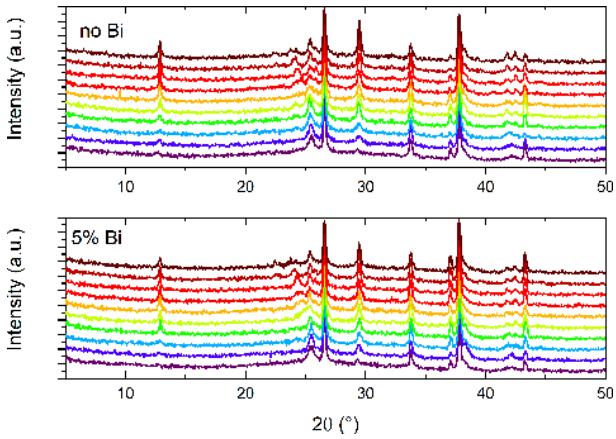

Figure 5.9: **S4** Thin film XRD data obtained on FTO/c-TiO_2/mp-TiO_2 for $Cu_xAg_{1-x}SbI_3$ thin films with increasing Cu concentrations (10% steps) from red (0%) to blue (100%). (upper panel: films without added Bi, lower: 5% Bi additive)

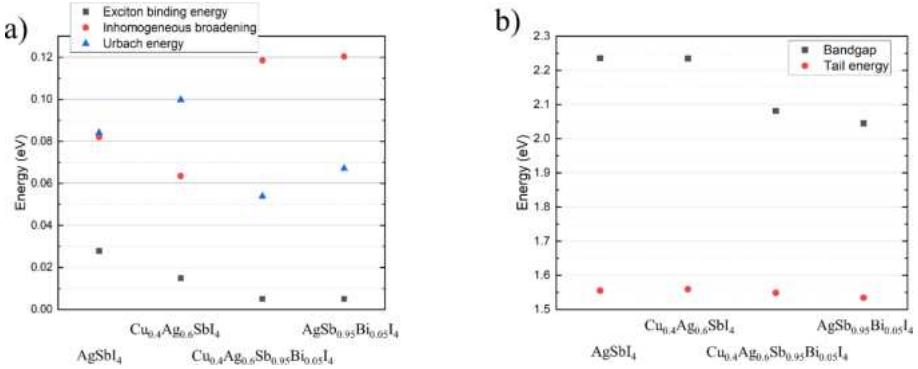

Figure 5.10: **S5** a) Fitting parameters for the Elliott fits in Figure 5.4a with exciton binding energy, inhomogeneous broadening and Urbach energy. b) Bandgap trend and tail energy of the exponential Urbach tails for the sample subset.

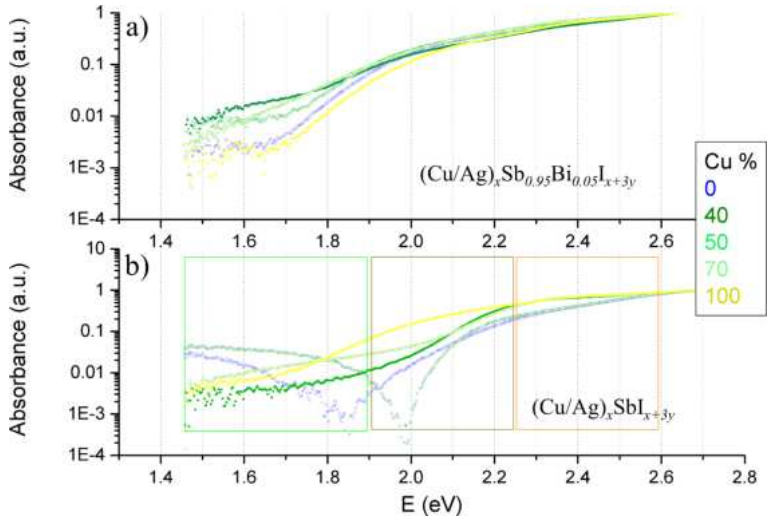

Figure 5.11: **S6** Logarithmic absorbance data for $Cu_xAg_{1-x}SbI_4$ thin films on glass with (a) and without (b) 5% Bi additive. In (b), the deep sub bandgap region beyond the Urbach tail is highlighted in green, the shallow sub bandgap region in dark yellow and the bandgap edge in orange.

Urbach and Elliot Fit:

Absorbance data near the band edge for the reference material $AgSbI_4$ were fitted with a leastsquares approach via Elliott's method with added thermal broadening as described by D'Innocenzo et al,[68] shown in equation 5.1 (with E_b being the exciton binding energy, n an integer describing the continuum transitions, $h\upsilon$ the photon energy, Γ the inhomogeneous broadening parameter, E_G the bandgap and $m_r b$ a factor determining the parabolicity of the fitting curve).

$$\alpha(\hbar\omega) = \alpha_0^{3D}\left[\sum_{n=1}^{\infty}\frac{4\pi E_b^{3/2}}{n^3}Sech\left(\frac{\hbar\omega - E_G - \frac{E_b}{n^2}}{\Gamma}\right) + \int_{Eg}^{\infty} Sech\left(\frac{\hbar\omega-\epsilon}{\Gamma}\right) \times \frac{\frac{2}{\pi}\sqrt{E_b}}{1-e^{-2\pi\sqrt{E_b/h\upsilon - E_G}}} \times \frac{1}{\frac{8m_r b}{h^3}(\epsilon - E_G)}d\epsilon\right] \tag{5.1}$$

To fit the absorbance in the bandgap, a simple Urbach fit[63,69] as shown in equation 5.2 was employed (with α_0 and E_1 being fitting parameters and E_0 the Urbach energy).

$$\alpha(E) = \alpha_0 e^{\frac{E-E_1}{E_0}} \tag{5.2}$$

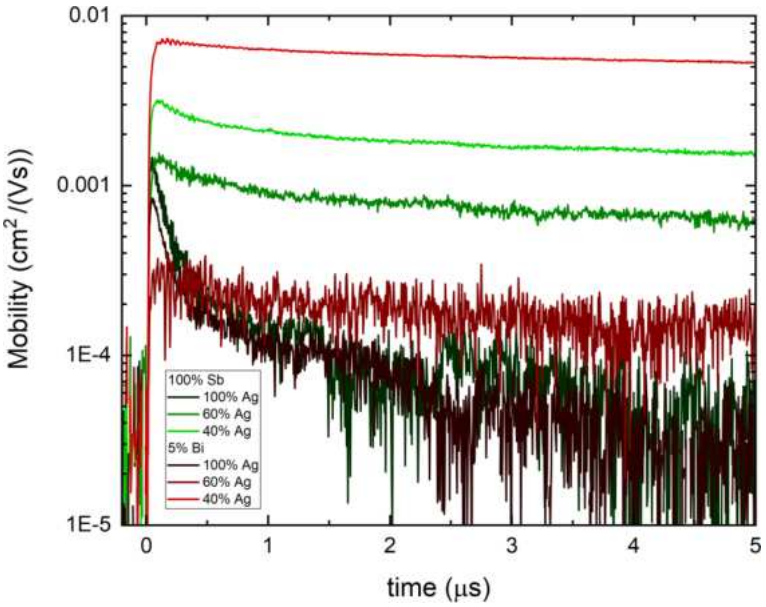

Figure 5.12: **S7** Traces of the TRMC measurements for thin films with and without Bi and 100%, 60% and 40% Cu/Ag ratio. The charge carrier mobility is extracted by the peak value of each transient, excited with a laser intensity of 3×10^{13} photons/cm^{-2}. The mobility is a lower estimate limited by the sensitivity of the setup due to the overall low signal for the 60% Cu/Ag ration sample with Bi.

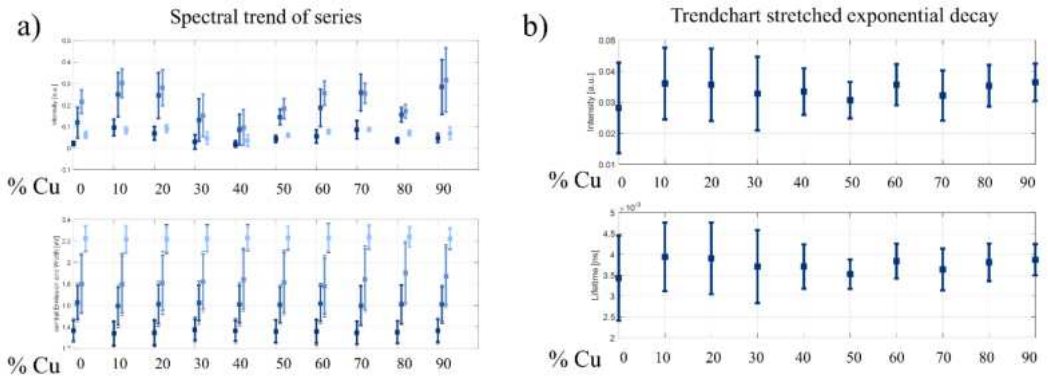

Figure 5.13: **S8** a) Spectral trend chart of photoluminescence measurements with intensity distribution and emission width. b) Spectral trend chart of the time-resolved photoluminescence traces fitted with an exponential decay function, with intensity and lifetime shown.

Compositional Analysis

Due to the presence of disorder in the lattice, we considered several permutations to obtain a low energy structure for further analysis. Formation energies are calculated with respect to the bulk phases of the precursors (CuI/AgI/SbI_3) matching the stoichiometry of the final composition.

First, we consider the cubic $ThZr_2H_7$-type crystal structure resulting in the $AgSb_2I_7$ stoichiometry,[70–72] FigureSI 5.14. Optimized lattice parameters of $a = b = c = 14.64$ Åare obtained with a zero band gap at the PBE level of theory. Notably, large formation energies are observed, suggesting an intrinsic instability of this compound. This is in line with previous studies on the Bi-based analog,[71] which allows us to rule out the given geometry.

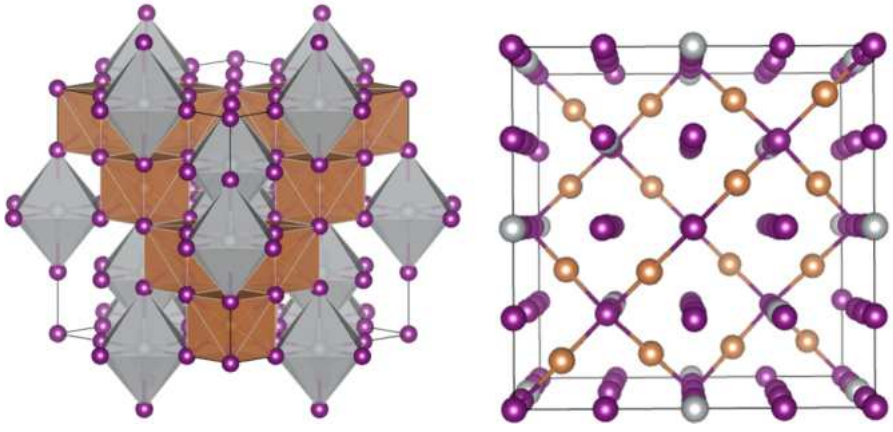

Figure 5.14: **S9** Optimized geometry (PBE, D3) of the $AgSb_2I_7$ composition resulting in a cubic structure with cell parameters $a = b = c = 14.64$ Å. At the PBE level of theory, this composition shows metallic behavior with a band gap of 0 eV. Colors are as follows: Sb, brown; Ag, silver; I, purple.

Next, we consider the $CdCl_2$-type crystal structures, in particular $AgSbI_4$ and Ag_3SbI_6, which have been frequently proposed for the Bi-based analogs.[59,71] Starting from $AgSbI_4$, a $CdCl_2$-type crystal with 1/2 Sb and 1/2 Ag occupation of the octahedral centers emerges, see FigureSI 5.15. We observe low differences in energies and cell parameters, see TableSI 5.3, with the c2 configuration that contains alternating Ag and Sb centers being most favorable.

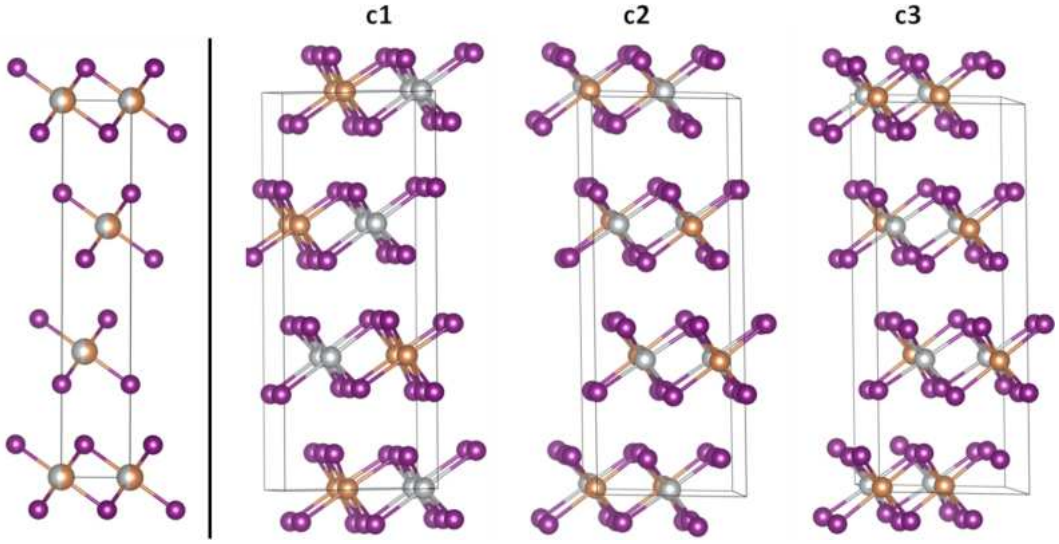

Figure 5.15: **S10** (left) $CdCl_2$-type structure with $AgSbI_4$ stoichiometry with metal centers occupied by 1/2 Sb and 1/2 Ag. (right) Permutations of the $AgSbI_4$ geometries, labeled with c1 to c3. Colors are as follows: Sb, brown; Ag, silver; I, purple.

Next, we focus on the crystal structure of Ag_3SbI_6. Starting from the structure proposed by Oldag et al.,[59] we consider various permutations and perform optimizations of the ionic positions and the cell parameters. Starting from the $AgSbI_4$, a $CdCl_2$-type crystal with 1/2 Sb and 1/2 Ag occupation of the octahedral centers, see FigureSI 5.16. We observe low differences in energies and cell parameters, see TableSI 5.3, for final cell parameters, energies, and band gaps. Notably, the Ag_3SbI_6 structures show a reduction in electronic band gap compared to the $AgSbI_4$ ones and further feature larger formation energies, thus being less likely to appear.

Upon Cu addition, we consider the formation of a Cu_2AgSbI_6 phase as reported from recent studies on the Bi-based counterpart.[33] The fundamental crystal structure is modeled by replacing Bi of the Cu_2AgBiI_6[61] by Sb. As shown in FigureSI 5.17, there is disorder in the Ag/Sb sites and a plentitude of potential positions for Cu, highlighting the large disorder in this system. To derive low energy structures, we constructed a variety of several configurations, FigureSI 5.17, following some fundamental rules:

- Random distribution of Sb, Ag, and vacancies, with at least three Ag or Sb ions being in each layer.

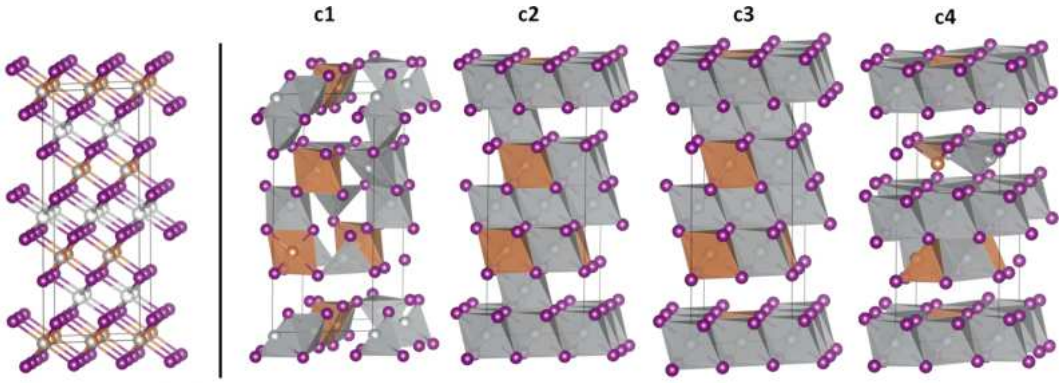

Figure 5.16: **S11** (left) $CdCl_2$-type structure with Ag_3SbI_6 stoichiometry following Oldag et al..[59] Metal centers in the mixed Sb/Ag layers are occupied by 1/3 Sb and 2/3 Ag. The sites in the interlayers are populated by 1/3 Ag to complete the stoichiometry. (right) Permutations of Ag_3SbI_6, labeled with c1 to c4. Colors are as follows: Sb, brown; Ag, silver; I, purple.

- The charge of the Sb, Ag, and Cu ions in each layer should balance the charge of the 8 iodide ions. Thus, according to the amount of Sb and Ag placed in between the iodides, Cu ions are added randomly to bond undercoordinated I ions.
- We place maximal as many Cu ions in between the Sb/Ag layer as Ag or Sb are present. The remaining Cu ions are placed

Note that this certainly does not sample the full compositional space, but provides fundamental insight into the structural and electronic properties of the Cu_2AgSbI_6. We further note that the resulting structures show similar features as the low energy structures predicted by Sansom et al.[61] for the Bi-based system.

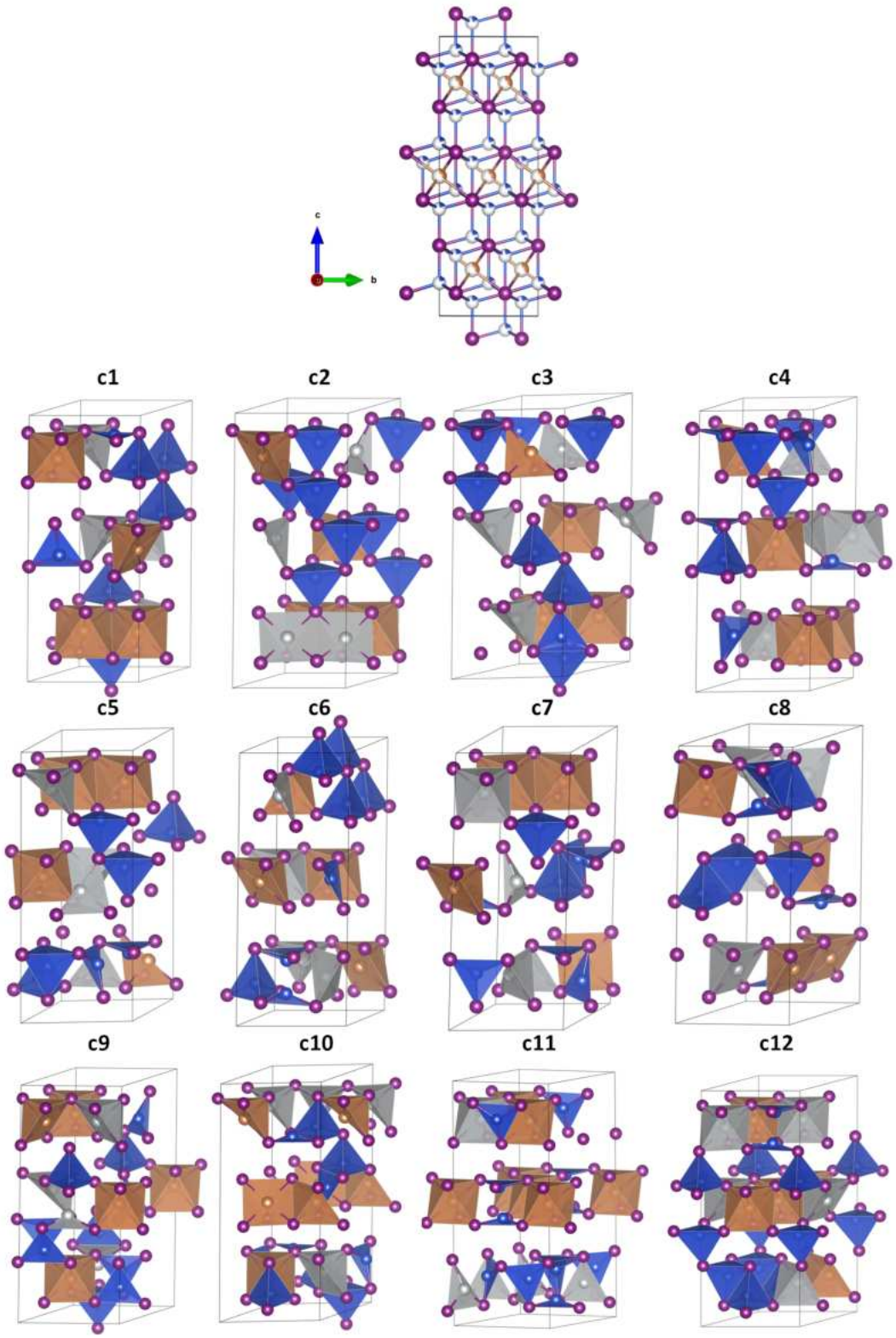

Figure 5.17: **S12** (Top) Visualization of the $CdCl_2$-type structure with Cu_2AgSbI_6 stoichiometry with partial occupations highlighted, following Sansom et al..[61] (Bottom) Exemplary structural configurations of the Cu_2AgSbI_6 stoichiometry. Colors are as follows: Sb, brown; Cu, blue; Ag, silver; I, purple.

Table 5.3: Optimized lattice parameters (PBE, D3) of the Ag-Sb-I and the Cu/Ag-Sb-I rudorffites. Formation energies and electronic band gaps are given at the PBE level of theory; refined band gaps and formation energies are calculated on the PBE0 level of theory with inclusion of SOC corrections on the PBE+D3 optimized geometries.

System	Config.	Formation Energy (eV/f.u.) PBE/PBE0	Band Gap (eV) PBE/PBE0	Lattice constants (Å)	Cell Angles (°)
$AgSb_2I_7$	-	$4.09/4.86$	$0/0.39$	$a = 14.637$ $b = 14.637$ $c = 14.637$	$\alpha = 90$ $\beta = 90$ $\gamma = 90$
$AgSbI_4$	c1	$0.03/0.00$	$1.07/2.13$	$a = 8.684$ $b = 8.579$ $c = 20.828$	$\alpha = 89.99$ $\beta = 89.26$ $\gamma = 119.60$
	c2	$0.01/-0.01$	$1.03/2.07$	$a = 8.671$ $b = 8.665$ $c = 20.804$	$\alpha = 88.97$ $\beta = 91.11$ $\gamma = 120.58$
	c3	$0.03/-0.01$	$1.06/2.10$	$a = 8.696$ $b = 8.692$ $c = 20.870$	$\alpha = 89.22$ $\beta = 90.79$ $\gamma = 120.77$
Ag_3SbI_6	c1	$0.24/0.12$	$0.43/1.54$	$a = 8.569$ $b = 8.983$ $c = 20.829$	$\alpha = 90.03$ $\beta = 91.81$ $\gamma = 120.88$
	c2	$0.15/0.03$	$0.76/1.70$	$a = 9.123$ $b = 8.659$ $c = 20.852$	$\alpha = 87.35$ $\beta = 91.76$ $\gamma = 121.84$
	c3	$0.14/0.03$	$0.82/1.78$	$a = 9.178$ $b = 8.751$ $c = 20.763$	$\alpha = 86.57$ $\beta = 92.47$ $\gamma = 122.65$
	c4	$0.59/0.52$	$0.23/0.70$	$a = 8.685$ $b = 8.684$ $c = 20.383$	$\alpha = 89.66$ $\beta = 90.31$ $\gamma = 119.59$
Cu_2AgSbI_6	c1	$0.54/1.13$	$0.54/0.43$	$a = 8.640$ $b = 8.588$ $c = 20.720$	$\alpha = 90.11$ $\beta = 89.89$ $\gamma = 119.94$
	c2	$0.17/0.56$	$0.45/1.50$	$a = 8.567$ $b = 8.539$ $c = 20.991$	$\alpha = 89.81$ $\beta = 90.45$ $\gamma = 119.60$
	c3	$0.58/0.97$	$0.12/0.45$	$a = 8.786$ $b = 8.572$ $c = 20.953$	$\alpha = 87.17$ $\beta = 89.96$ $\gamma = 121.03$
	c4	$0.16/0.52$	$0.81/2.04$	$a = 8.574$ $b = 8.635$ $c = 21.161$	$\alpha = 89.43$ $\beta = 90.85$ $\gamma = 120.69$
	c5	$0.18/0.73$	$0.96/2.03$	$a = 8.593$ $b = 8.611$ $c = 21.051$	$\alpha = 90.70$ $\beta = 90.32$ $\gamma = 119.98$
	c6	$0.20/0.41$	$0.81/1.89$	$a = 8.571$ $b = 8.598$ $c = 21.242$	$\alpha = 90.69$ $\beta = 90.75$ $\gamma = 120.39$

	c7	0.19/0.63	0.99/2.09	$a = 8.674$ $b = 8.548$ $c = 21.196$	$\alpha = 90.02$ $\beta = 90.58$ $\gamma = 120.65$
	c8	0.18/0.57	0.74/1.82	$a = 8.593$ $b = 8.539$ $c = 21.323$	$\alpha = 88.20$ $\beta = 89.88$ $\gamma = 120.14$
	c9	0.18/0.52	0.71/1.79	$a = 8.728$ $b = 8.654$ $c = 20.792$	$\alpha = 89.57$ $\beta = 90.41$ $\gamma = 120.64$
	c10	0.30/0.64	0.29/1.29	$a = 8.688$ $b = 8.618$ $c = 20.906$	$\alpha = 88.49$ $\beta = 91.12$ $\gamma = 120.48$
	c11	0.06/0.42	0.86/1.90	$a = 8.551$ $b = 8.525$ $c = 21.452$	$\alpha = 89.96$ $\beta = 90.11$ $\gamma = 119.52$
	c12	0.33/0.68	0.02/0.85	$a = 8.574$ $b = 8.618$ $c = 20.884$	$\alpha = 88.96$ $\beta = 90.51$ $\gamma = 120.32$
$Cu_{0.5}Ag_{0.5}SbI_4$	-	0.06/0.14	0.83/2.13	$a = 8.671$ $b = 8.665$ $c = 20.804$	$\alpha = 88.97$ $\beta = 91.11$ $\gamma = 120.58$

Defect Calculations

Electronic structure and defect calculations of the optimized geometries were performed using 2×2×1 supercells. The PBE0 functional[66] including spin-orbit coupling and DFT-D3 dispersion corrections[65] were employed within the Quantum Espresso package.[67] Here, we used full relativistic norm-conserving pseudopotentials (Ag, 19 electrons, $4s^2$, $4p^6$, $4d^{10}$, $5s^2$, $4p^9$; Sb, 15 electrons, $4d^{10}$, $5s^2$, $5p^3$; I, 7 electrons, $5s^2$, $5p^5$) with a cutoff on the wave functions of 40 Ry and 80 Ry on the Fock grid, an increased fraction of exact exchange in the HSE06 functional of $\alpha = 0.43$ and sampling the Brillouin zone at the gamma point. PDOS plots have been generated with a Gaussian smearing of 0.1 eV.

Defect formation energies (DFE) and thermodynamic ionization levels (TIL) were calculated as follows:[73,74]

$$\begin{aligned} DFE[X^q] &= E[X^q] - E[prist] - \sum_i n_i\mu_i + q(E_{VBM} + E_F) + E^q_{corr} \\ TIL[q/q'] &= \frac{DFE[X^q; E_F = 0] - DFE[X^{q'}; E_F = 0]}{q' - q} \end{aligned} \tag{5.3}$$

where $E[X^q]$ is the energy of the defective supercell with defect X in charge state q, $E[prist]$ is the energy of the pristine supercell, n_i and μ_i are the number and chemical potential of the added and subtracted species, respectively, E_{VBM} and E_F are the valence band energy and the Fermi energy, respectively, and E^q_{corr} are electrostatic potential cor-

rections due to the finite size of the supercell. Electrostatic finite-size effects have been accounted for using the Makov-Payne correction scheme.[75]

Static dielectric constants of $AgSbI_4$ were obtained using the density functional perturbation theory (DFPT)[76] in the Vienna ab initio simulation package (VASP),[68] with PBE exchangecorrelation functional[63] and the projector-augmented wave (PAW) method[69] using a 400 eV plane-wave cutoff, 6×6×1 Monckhorst-Pack k-point sampling, and a tightly converged electronic wavefunction (within 10-8 eV).

Table 5.4: Electronic (ϵ_{elec}) and ionic contributions and (ϵ_{ion}), respectively, to the static dielectric constant for $AgSbI_4$. The averaged static dielectric constant, ϵ_0, is used for all defect calculations.

System	ϵ_{elec}	ϵ_{ion}
$AgSbI_4$	$\epsilon_{xx} = 7.46$	$\epsilon_{xx} = 32.88$
	$\epsilon_{yy} = 7.99$	$\epsilon_{yy} = 36.65$
	$\epsilon_{zz} = 5.84$	$\epsilon_{zz} = 1.50$
	$\epsilon_0 = 15.39$	

Role of the functional during defect geometry optimization on TILs

In lead-halide perovskites, defect geometries and TILs were shown to depend also on the role of the used functional during geometry optimization. Hybrid PBE0 calculations have been performed for geometry optimization of the ionic positions using the freely available CP2K software package,[77] keeping the Fock exchange α at 0.25 and including van der Waals interactions with the DFT-D3 scheme including Becke-Johnson damping.[78,79] Kohn-Sham orbitals are expanded in a double-zeta basis set (DZVP-MOLOPT)[80] in combination with the norm-conserving Goedecker-Teter-Hutter (GTH)[81] pseudopotentials, and a cutoff of 600 Ry for expansion of the electron density in plane waves. The auxiliary density matrix method with the cFIT auxiliary basis set was applied to accelerate the optimization of ionic positions within hybrid functional calculations.[82]

The TILs, shown in FigureSI 5.6, show low dependence on the utilized exchange correlation functional during geometry optimization for the PBE and PBE0 level of theory. The most relevant Ag point defects show limited changes with the functional. Geometry optimizations with the PBE0 level of theory impose further challenges, resulting in large changes in the layered structures, and require further investigation. Consequently, we report the defect properties with geometries from PBE optimization in the manuscript.

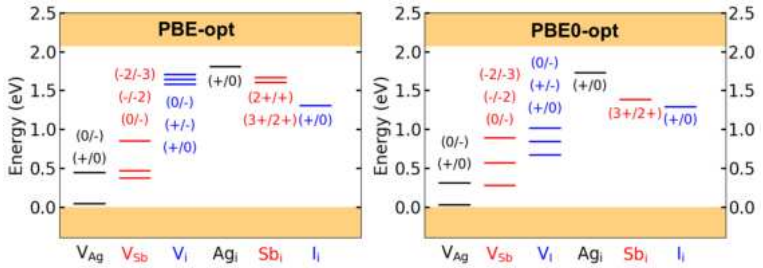

Figure 5.18: **S13** Role of exchange correlation functional during geometry optimization on the defect TILs.

Defect formation energies

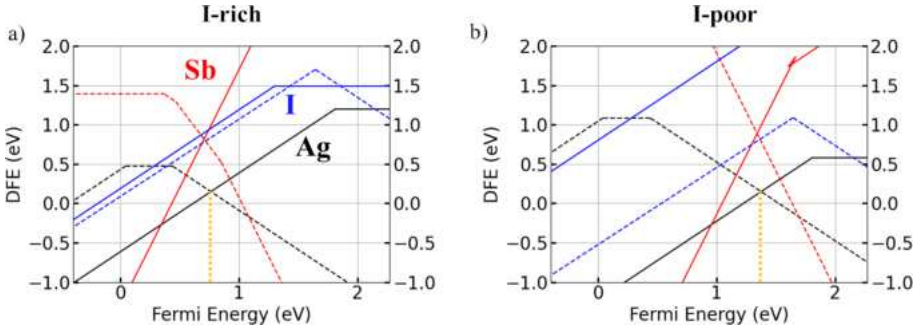

Figure 5.19: **S14** Defect formation energies in $AgSbI_4$ under (a) I-rich and (b) I-poor conditions. Solid lines give the DFE for interstitials, dashed lines visualize DFEs for vacancies. The Fermi level of the system, dominated by the defect equilibrium between Ag vacancies and Ag interstitials, is highlighted by the dotted vertical line.

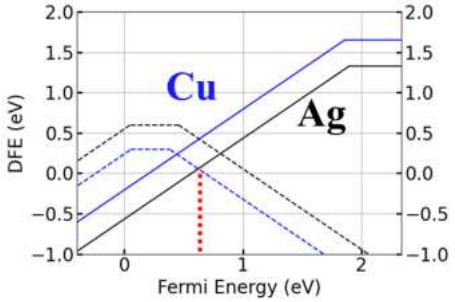

Figure 5.20: **S15** Defect formation energies of $Cu_{0.5}Ag_{0.5}SbI_4$ under I-rich conditions. Solid lines give the DFE for interstitials, dashed lines visualize DFEs for vacancies. The Fermi level of the 16 system, dominated by the defect equilibrium between Ag vacancies and Cu interstitials, is highlighted by the dotted vertical line.

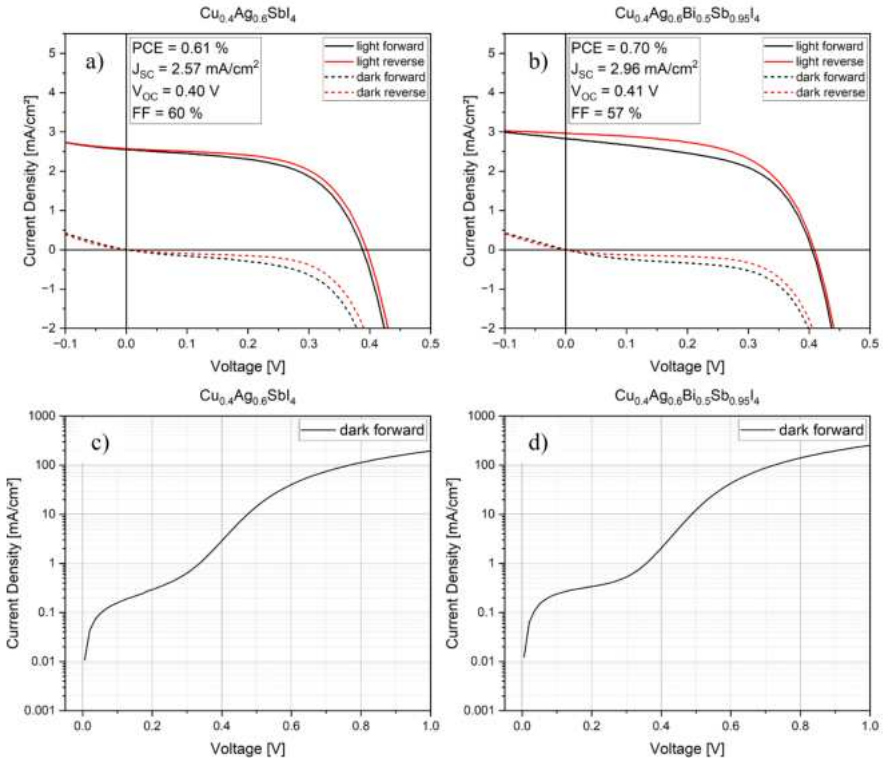

Figure 5.21: **S16** Light (a,b) and logarithmic dark (c,d) current-voltage curves for the record pixels (solar cells) discussed in the main text. (a,d) $Cu_{0.4}Ag_{0.6}SbI_4$ without Bi additive, and (b,c) with 5% Bi added.

The JV-curves in Fig. S16 a) and b) show a slight hysteresis between the forward and the reverse scan. This is most likely due to moderate ion mobilities as Ag-Cu rudorffites have shown to be ionic conductors for Ag and Cu ions.[59] The S-shape of the dark scans in Fig. S16 c) and d) point to inefficient charge extraction due to energetic barriers at the interfaces or increased electrical resistance of the layers.[83]

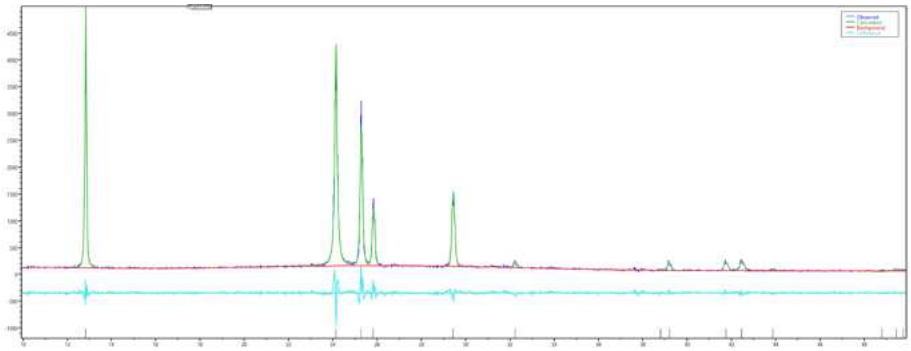

Figure 5.22: **S17** Peak profile refinement with the Le Bail method for $Cu_{0.1}Ag_{0.9}SbI_4$ with the Ag_3BiI_6 structure type.[59] Cell parameters $a = 4.32149$ Å, $b = 4.32149$ Å, $c = 20.66504$ Å, alpha = 90.000°, beta = 90.000°, gamma = 120.000°, Cell volume: 334.22 Å^3. Background modelled by a Chebyshev polynomial of degree 14. Profile shape function: Pearson VII.[48]

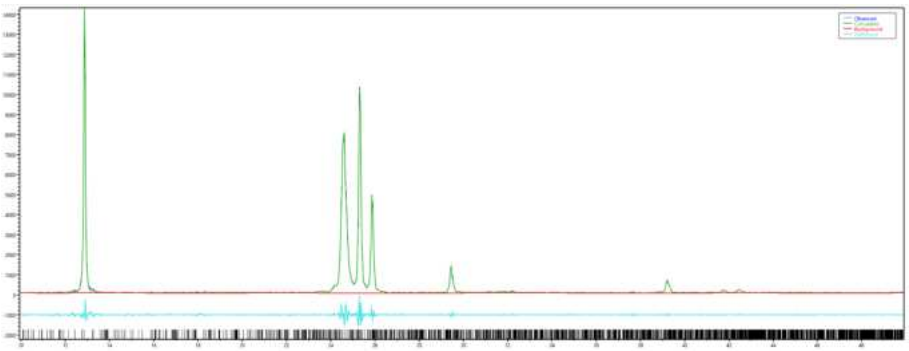

Figure 5.23: **S18** Peak profile refinement with the Le Bail method for $Cu_{0.2}Ag_{0.8}SbI_4$ with the $Cu_{0.5}Ag_{0.5}SbI_4$ structure based on the optimized DFT structure (TableSI 5.3). Cell parameters $a = 19.44139$ Å, $b = 16.59001$ Å, $c = 20.86535$ Å, alpha = 85.499°, beta = 92.705°, gamma = 123.778°, Cell volume: 5576.44 Å^3. Background modelled by a Chebyshev polynomial of degree 14. Profile shape function: Pearson VII.[48]

Main text profile refinement specifications:

Fig. 1 b) top: Cell parameters $a = 4.32149$ Å, $b = 4.32149$ Å, $c = 20.66504$ Å, alpha = 90.000°, beta = 90.000°, gamma = 120.000° Cell volume: 334.22 Å^3. Background modelled by a Chebyshev polynomial of degree 14. Profile shape function: Pearson VII.

Fig. 1 b) bottom: Cell parameters $a = 4.32118$ Å, $b = 4.32118$ Å, $c = 20.66747$ Å, alpha = 90.000°, beta = 90.000°, gamma = 120.000°, Cell volume: 334.21 Å^3. Background modelled by a Chebyshev polynomial of degree 14. Profile shape function: Pearson VII.

5.8 References

[1] G. Divitini, S. Cacovich, F. Matteocci, L. Cinà, A. Di Carlo, C. Ducati, *Nature Energy* **2016**, *1*, 1–6.

[2] C. C. Boyd, R. Cheacharoen, T. Leijtens, M. D. McGehee, *Chemical reviews* **2018**, *119*, 3418–3451.

[3] S. P. Dunfield, L. Bliss, F. Zhang, J. M. Luther, K. Zhu, M. F. van Hest, M. O. Reese, J. J. Berry, *Advanced Energy Materials* **2020**, *10*, 1904054.

[4] L. Schmidt-Mende, V. Dyakonov, S. Olthof, F. Ünlü, K. M. T. Lê, S. Mathur, A. D. Karabanov, D. C. Lupascu, L. M. Herz, A. Hinderhofer, et al., *APL Materials* **2021**, *9*.

[5] M. Grätzel, *Accounts of chemical research* **2017**, *50*, 487–491.

[6] F. C. Krebs, N. Espinosa, M. Hösel, R. R. Søndergaard, M. Jørgensen, *Advanced Materials* **2014**, *26*, 29–39.

[7] H. Li, W. Zhang, *Chemical Reviews* **2020**, *120*, 9835–9950.

[8] G.-W. Kim, A. Petrozza, *Advanced Energy Materials* **2020**, *10*, 2001959.

[9] K. X. Steirer, P. Schulz, G. Teeter, V. Stevanovic, M. Yang, K. Zhu, J. J. Berry, *ACS Energy Letters* **2016**, *1*, 360–366.

[10] A. M. Ganose, C. N. Savory, D. O. Scanlon, *Chemical Communications* **2017**, *53*, 20–44.

[11] R. C. Kurchin, P. Gorai, T. Buonassisi, V. Stevanovic, *Chemistry of Materials* **2018**, *30*, 5583–5592.

[12] R. E. Brandt, J. R. Poindexter, P. Gorai, R. C. Kurchin, R. L. Hoye, L. Nienhaus, M. W. Wilson, J. A. Polizzotti, R. Sereika, R. Zaltauskas, et al., *Chemistry of Materials* **2017**, *29*, 4667–4674.

[13] G. Nasti, A. Abate, *Advanced Energy Materials* **2020**, *10*, 1902467.

[14] L. Serrano-Lujan, N. Espinosa, T. T. Larsen-Olsen, J. Abad, A. Urbina, F. C. Krebs, *Advanced Energy Materials* **2015**, *5*, 1501119.

[15] A. Weis, P. Ganswindt, W. Kaiser, H. Illner, C. Maheu, N. Gluck, P. Dörflinger, M. Armer, V. Dyakonov, J. P. Hofmann, et al., *The Journal of Physical Chemistry C* **2022**, *126*, 21040–21049.

[16] T. Leijtens, R. Prasanna, A. Gold-Parker, M. F. Toney, M. D. McGehee, *ACS Energy Letters* **2017**, *2*, 2159–2165.

[17] D. Ricciarelli, D. Meggiolaro, F. Ambrosio, F. De Angelis, *ACS Energy Letters* **2020**, *5*, 2787–2795.

[18] M. Aldamasy, Z. Iqbal, G. Li, J. Pascual, F. Alharthi, A. Abate, M. Li, *Physical Chemistry Chemical Physics* **2021**, *23*, 23413–23427.

[19] W. Tress, M. T. Sirtl, *Solar RRL* **2022**, *6*, 2100770.

[20] R. L. Hoye, L. Eyre, F. Wei, F. Brivio, A. Sadhanala, S. Sun, W. Li, K. H. Zhang, J. L. MacManus-Driscoll, P. D. Bristowe, et al., *Advanced Materials Interfaces* **2018**, *5*, 1800464.

[21] M. T. Sirtl, R. Hooijer, M. Armer, F. G. Ebadi, M. Mohammadi, C. Maheu, A. Weis, B. T. van Gorkom, S. Häringer, R. A. Janssen, et al., *Advanced Energy Materials* **2022**, *12*, 2103215.

[22] N. Giesbrecht, A. Weis, T. Bein, *Journal of Physics: Energy* **2020**, *2*, 024007.

[23] K. M. McCall, C. C. Stoumpos, S. S. Kostina, M. G. Kanatzidis, B. W. Wessels, *Chemistry of Materials* **2017**, *29*, 4129–4145.

[24] K. M. McCall, C. C. Stoumpos, O. Y. Kontsevoi, G. C. Alexander, B. W. Wessels, M. G. Kanatzidis, *Chemistry of Materials* **2019**, *31*, 2644–2650.

[25] G. Giovilli, B. Albini, V. Grisci, S. Bonomi, M. Moroni, E. Mosconi, W. Kaiser, F. De Angelis, P. Galinetto, L. Malavasi, *Journal of Materials Chemistry C* **2023**, *11*, 10282–10291.

[26] P. C. Harikesh, H. K. Mulmudi, B. Ghosh, T. W. Goh, Y. T. Teng, K. Thirumal, M. Lockrey, K. Weber, T. M. Koh, S. Li, et al., *Chemistry of Materials* **2016**, *28*, 7496–7504.

[27] D. B. Mitzi, *Journal of the Chemical Society Dalton Transactions* **2001**, 1–12.

[28] I. Turkevych, S. Kazaoui, E. Ito, T. Urano, K. Yamada, H. Tomiyasu, H. Yamagishi, M. Kondo, S. Aramaki, *ChemSusChem* **2017**, *10*, 3754–3759.

[29] C. Lu, J. Zhang, H. Sun, D. Hou, X. Gan, M.-h. Shang, Y. Li, Z. Hu, Y. Zhu, L. Han, *ACS Applied Energy Materials* **2018**, *1*, 4485–4492.

[30] N. Pai, J. Lu, T. R. Gengenbach, A. Seeber, A. S. Chesman, L. Jiang, D. C. Senevirathna, P. C. Andrews, U. Bach, Y.-B. Cheng, et al., *Advanced Energy Materials* **2019**, *9*, 1803396.

[31] S. Tie, W. Zhao, W. Huang, D. Xin, M. Zhang, Z. Yang, J. Long, Q. Chen, X. Zheng, J. Zhu, et al., *The Journal of Physical Chemistry Letters* **2020**, *11*, 7939–7945.

[32] H. Ye, B. Sun, Z. Wang, Z. Liu, X. Zhang, X. Tan, T. Shi, Z. Tang, G. Liao, *Journal of Materials Chemistry C* **2020**, *8*, 14155–14163.

[33] G. K. Grandhi, B. Al-Anesi, H. Pasanen, H. Ali-Löytty, K. Lahtonen, S. Granroth, N. Christian, A. Matuhina, M. Liu, A. Berdin, et al., *Small* **2022**, *18*, 2203768.

[34] B. Al-Anesi, G. K. Grandhi, A. Pecoraro, V. Sugathan, N. Viswanath, H. Ali-Löytty, M. Liu, T.-P. Ruoko, K. Lahtonen, D. Manna, et al., **2023**.

[35] R. Nishikubo, H. Kanda, I. Garcia-Benito, A. Molina-Ontoria, G. Pozzi, A. M. Asiri, M. K. Nazeeruddin, A. Saeki, *Chemistry of Materials* **2020**, *32*, 6416–6424.

[36] M. B. Gray, E. T. McClure, N. P. Holzapfel, F. P. Evaristo, W. Windl, P. M. Woodward, *Journal of Solid State Chemistry* **2021**, *297*, 121997.

[37] D. Ferro, B. Nappi, V. Piacente, *The Journal of Chemical Thermodynamics* **1979**, *11*, 193–201.

[38] A. Chakraborty, N. Pai, J. Zhao, B. R. Tuttle, A. N. Simonov, V. Pecunia, *Advanced Functional Materials* **2022**, *32*, 2203300.

[39] H. Luo, J. Wu, X. Liu, Y. Yang, Q. Liu, M. Zhang, P. Yuan, W. Sun, Z. Lan, J. Lin, *ACS Applied Energy Materials* **2018**, *1*, 6700–6706.

[40] J. V. Patil, S. S. Mali, C. K. Hong, *Nanoscale* **2019**, *11*, 21824–21833.

[41] S. Wang, Z. Ma, B. Liu, W. Wu, Y. Zhu, R. Ma, C. Wang, *Solar Rrl* **2018**, *2*, 1800034.

[42] Y. Yang, C. Liu, M. Cai, Y. Liao, Y. Ding, S. Ma, X. Liu, M. Guli, S. Dai, M. K. Nazeeruddin, *ACS applied materials & interfaces* **2020**, *12*, 17062–17069.

[43] Z. Xiao, W. Meng, D. B. Mitzi, Y. Yan, *The journal of physical chemistry letters* **2016**, *7*, 3903–3907.

[44] B. Cucco, L. Pedesseau, C. Katan, J. Even, M. Kepenekian, G. Volonakis, *Solar RRL* **2022**, *6*, 2200718.

[45] L. F. Mashadieva, Z. S. Aliev, A. V. Shevelkov, M. B. Babanly, *Journal of alloys and compounds* **2013**, *551*, 512–520.

[46] A. Kulkarni, F. Ünlü, N. Pant, J. Kaur, C. Bohr, A. K. Jena, S. Öz, M. Yanagida, Y. Shirai, M. Ikegami, et al., *Solar RRL* **2021**, *5*, 2100077.

[47] A. Koedtruad, M. Goto, M. A. Patino, Z. Tan, H. Guo, T. Nakamura, T. Handa, W.-T. Chen, Y.-C. Chuang, H.-S. Sheu, et al., *Journal of Materials Chemistry A* **2019**, *7*, 5583–5588.

[48] A. Altomare, C. Cuocci, C. Giacovazzo, A. Moliterni, R. Rizzi, N. Corriero, A. Falcicchio, *Journal of Applied Crystallography* **2013**, *46*, 1231–1235.

[49] R. D. Shannon, *Acta crystallographica section A: crystal physics diffraction theoretical and general crystallography* **1976**, *32*, 751–767.

[50] L. Bodenes, A. Darwiche, L. Monconduit, H. Martinez, *Journal of Power Sources* **2015**, *273*, 14–24.

[51] A. Merker, M. Morgenroth, M. Scholz, T. Lenzer, K. Oum, *The Journal of Physical Chemistry C* **2023**, *127*, 1487–1498.

[52] L. R. Buizza, H. C. Sansom, A. D. Wright, A. M. Ulatowski, M. B. Johnston, H. J. Snaith, L. M. Herz, *Advanced Functional Materials* **2022**, *32*, 2108392.

[53] R. Hooijer, A. Weis, A. Biewald, M. T. Sirtl, J. Malburg, R. Holfeuer, S. Thamm, A. A. Y. Amin, M. Righetto, A. Hartschuh, et al., *Advanced Optical Materials* **2022**, *10*, 2200354.

[54] A. D. Wright, L. R. Buizza, K. J. Savill, G. Longo, H. J. Snaith, M. B. Johnston, L. M. Herz, *The journal of physical chemistry letters* **2021**, *12*, 3352–3360.

[55] M. T. Sirtl, M. Armer, L. K. Reb, R. Hooijer, P. Dörflinger, M. A. Scheel, K. Tvingstedt, P. Rieder, N. Glück, P. Pandit, et al., *ACS applied energy materials* **2020**, *3*, 11597–11609.

[56] Y. Kim, Z. Yang, A. Jain, O. Voznyy, G.-H. Kim, M. Liu, L. N. Quan, F. P. García de Arquer, R. Comin, J. Z. Fan, et al., *Angewandte Chemie International Edition* **2016**, *55*, 9586–9590.

[57] H. Zhu, A. Erbing, H. Wu, G. J. Man, S. Mukherjee, C. Kamal, M. B. Johansson, H. Rensmo, M. Odelius, E. M. Johansson, *ACS Applied Energy Materials* **2020**, *3*, 7372–7382.

[58] K.-C. Hsiao, Y.-F. Yu, C.-M. Ho, M.-H. Jao, Y.-H. Chang, S.-H. Chen, Y.-H. Chang, W.-F. Su, K.-M. Lee, M.-C. Wu, *Chemical Engineering Journal* **2023**, *451*, 138807.

[59] T. Oldag, T. Aussieker, H.-L. Keller, C. Preitschaft, A. Pfitzner, *Zeitschrift für anorganische und allgemeine Chemie* **2005**, *631*, 677–682.

[60] A. Crovetto, A. Hajijafarassar, O. Hansen, B. Seger, I. Chorkendorff, P. C. Vesborg, *Chemistry of Materials* **2020**, *32*, 3385–3395.

[61] H. C. Sansom, L. R. Buizza, M. Zanella, J. T. Gibbon, M. J. Pitcher, M. S. Dyer, T. D. Manning, V. R. Dhanak, L. M. Herz, H. J. Snaith, et al., *Inorganic Chemistry* **2021**, *60*, 18154–18167.

[62] J. W. Park, Y. Lim, K.-Y. Doh, M. T. Jung, Y. I. Jeon, I. S. Yang, H.-s. Choi, J. Kim, D. Lee, W. I. Lee, *Sustainable Energy & Fuels* **2021**, *5*, 1439–1447.

[63] J. P. Perdew, K. Burke, M. Ernzerhof, *Physical review letters* **1996**, *77*, 3865.

[64] H. J. Monkhorst, J. D. Pack, *Physical review B* **1976**, *13*, 5188.

[65] S. Grimme, J. Antony, S. Ehrlich, H. Krieg, *The Journal of chemical physics* **2010**, *132*.

[66] C. Adamo, V. Barone, *The Journal of chemical physics* **1999**, *110*, 6158–6170.

[67] P. Giannozzi, S. Baroni, N. Bonini, M. Calandra, R. Car, C. Cavazzoni, D. Ceresoli, G. L. Chiarotti, M. Cococcioni, I. Dabo, et al., *Journal of physics: Condensed matter* **2009**, *21*, 395502.

[68] A. S. Botana, M. R. Norman, *Physical Review Materials* **2019**, *3*, 044001.

[69] P. E. Blöchl, O. Jepsen, O. K. Andersen, *Physical Review B* **1994**, *49*, 16223.

[70] Y. Kim, Z. Yang, A. Jain, O. Voznyy, G.-H. Kim, M. Liu, L. N. Quan, F. P. García de Arquer, R. Comin, J. Z. Fan, et al., *Angewandte Chemie International Edition* **2016**, *55*, 9586–9590.

[71] Z. Xiao, W. Meng, D. B. Mitzi, Y. Yan, *The journal of physical chemistry letters* **2016**, *7*, 3903–3907.

[72] H. Zhu, A. Erbing, H. Wu, G. J. Man, S. Mukherjee, C. Kamal, M. B. Johansson, H. Rensmo, M. Odelius, E. M. Johansson, *ACS Applied Energy Materials* **2020**, *3*, 7372–7382.

[73] A. Alkauskas, P. Deák, J. Neugebauer, A. Pasquarello, C. G. Van de Walle, *Advanced Calculations for Defects in Materials: Electronic Structure Methods*, John Wiley & Sons, **2011**.

[74] D. Meggiolaro, F. De Angelis, *ACS Energy Letters* **2018**, *3*, 2206–2222.

[75] M. Leslie, N. Gillan, *Journal of Physics C: Solid State Physics* **1985**, *18*, 973.

[76] S. Baroni, S. De Gironcoli, A. Dal Corso, P. Giannozzi, *Reviews of modern Physics* **2001**, *73*, 515.

[77] T. D. Kühne, M. Iannuzzi, M. Del Ben, V. V. Rybkin, P. Seewald, F. Stein, T. Laino, R. Z. Khaliullin, O. Schütt, F. Schiffmann, et al., *The Journal of Chemical Physics* **2020**, *152*.

[78] O. Trott, A. J. Olson, *J. Comp. Chem* **2009**, *31*, 456–461.

[79] S. Ehrlich, J. Moellmann, W. Reckien, T. Bredow, S. Grimme, *ChemPhysChem* **2011**, *12*, 3414–3420.

[80] J. VandeVondele, J. Hutter, *The Journal of chemical physics* **2007**, *127*.

[81] S. Goedecker, M. Teter, J. Hutter, *Physical Review B* **1996**, *54*, 1703.

[82] M. Guidon, J. Hutter, J. VandeVondele, *Journal of chemical theory and computation* **2010**, *6*, 2348–2364.

[83] R. Saive, *IEEE journal of photovoltaics* **2019**, *9*, 1477–1484.

Chapter 6

Conclusions and Outlook

The search for lead-free perovskites and other alternative materials that can deliver similar outstanding optoelectronic properties while also being nontoxic, long-term stable and resource abundant perfectly illustrates the never-ending pursuit of perfection, curiosity and human advancement in the natural sciences. While this is an ambitious goal and its success is uncertain, progress is continuously being made in both lead-based and lead-free perovskites. At the time of this thesis, lead perovskites are still pushing the physical performance limits of photovoltaics while steadily improving their long term device stabilities. Meanwhile, lead-free alternatives have shown their potential, placing them firmly into the field of material sciences but they still face challenges that are at the core of contemporary research efforts. Double perovskites and their 2D phases exhibit great structural stability combined with non toxicity and the abundance of their organic and inorganic constituent elements such as Ag, Cu, Bi, Sb and the halogens Cl, Br and I. Their charge-carrier properties on the other hand limit their performance in photovoltaics and other applications.

In the first chapter, the n = 1 Ruddlesden-Popper phases deriving from $Cs_2AgBiBr_6$ were newly synthesized using the organic cation 4-fluoro-phenethylammonium to yield $(4\,FPEA)_4AgBiX_8$, where X = Cl, Br or I. The use of this strongly polar and interacting organic molecule enables the formation of the otherwise inaccesible iodide phase, enabling smaller band gap energies around 2 eV, while the dimensional reduction achieves direct band gaps. The crystallization of these materials as thin films was investigated and found to be highly oriented with the layers being oriented exclusively parallel to different substrates. The charge-carrier properties were found to be limited by an ultrafast self-trapping process or the formation of small polarons, rendering these materials to be inefficient with regards to charge-carrier extraction. Furthermore, the multiple quantum well structure due to the alternating inorganic and organic layers inhibits out-of-plane

conductivity due to the insulating nature of the 4FPEA cation.

In the second chapter, the synergetic effect of a 3D/2D heterostructure active layer based on $Cs_2AgBiBr_6$/$(PEA)_4AgBiBr_8$ was employed to improve the performance of double perovskite solar cells. The interfacial strategy adding a 2D double perovskite layer between the 3D double perovskite and the hole transport material Spiro-O-MeTAD improves the contact selectivity through a combination of a more homogenous morphological barrier between $Cs_2AgBiBr_6$ and the HTM and an improved energy level alignment, enabling a better electron-blocking and hole-extraction towards the anode. This improves the J_{sc} by 0.22 mA/cm^2 and the V_{oc} by 70 meV leading to increased champion efficiencies from 2.15% (3D) to 2.46% (3D/2D).

In the third chapter, key intrinsic challenges of 2D double perovskites, namely the electronic anisotropy and the multiple quantum well structure were rationally addressed by employing electroactive organic cations based on napthalene and pyrene moeities. Eight new materials were synthesized with inorganic frameworks of Ag-Bi-I and Cu-Bi-I and large organic cations NOE, NOP, POE and POP. The charge-carrier properties and the polaron formation were further elucidated, identifying the in-plane diffusion coefficients for initial free charge-carriers and excitons, followed by reduced diffusion coefficients for the self-trapped small polarons, as well as the initial photoconductivity for free charge-carriers. Based on single-crystal structures, DFT calculations were performed which confirmed different types of quantum well structures, where type IIb was found for $(POE)_4AgBiI_8$ and $(POP)_4AgBiI_8$, enabling charge transport in the valence band for both the inorganic and organic layers and in the conduction band for the inorganic layers. This, combined with the out-of-plane conductivity confirmed for POE and POP based materials, allowed us to prepare the first functioning n = 1 lead-free, 2D double perovskite solar cell in a planar architecture with exclusively parallel oriented layers using $(POE)_4AgBiI_8$.

In the fourth chapter, perovskite inspired, rudorffite type Cu/Ag-Sb-I thin films were successfully synthesized overcoming the synthetic difficulty to include Sb, compared to the more conventional Bi based rudorffites. Through Cu/Ag substituion in the $Cu_{1-x}Ag_xSbI_4$ phase combined with a 5% Bi substitution the crystallinity and morphology was greatly improved, leading to larger charge-carrier mobilities and reduced deep trap states, while the Bi inclusion reduces the band gap energy by 0.2 eV to around 2.05 eV. DFT calculations reveal the detrimental effect of Ag and Cu point defects, demonstrating intrinsic challenges in these disordered rudorffite type structures, where Cu, Ag, Sb and Bi occupy the same Wyckoff positions. The optimally substituted material $Cu_{0.4}Ag_{0.6}Sb_{0.95}Bi_{0.05}I_4$

could almost double the solar cell efficiency to 0.7%, compared to the pure $AgSbI_4$ phase. The increased efficiency at low light intensity under indoor illumination further indicated promise for these type of materials for indoor photovoltaics.

In this thesis, n = 1 2D double perovskites have been explored as pure materials identifying their strengths and weaknesses. The strengths can be utilized in 3D/2D perovskite heterostructures or possibly in other applications than photovoltaics, such as X-ray detectors or field effect transistors. To overcome the weaknesses, other perovskite-inspired materials such as rudorffites can also be explored. Most intriguingly, some intrinsic challenges can also be addressed directly as was shown in chapter three. After establishing n = 1 2D iodide double perovskites, a synthetic outlook would be the successful synthesis of higher n value phases, which would lower the band gap energy further towards the optimum for reaching the Shockley-Queisser limit in photovoltaics. Another challenge for 2D double perovskites is still the desirable full control over the crystallization and orientation in thin film form, enabling the directed use of their anisotropic properties. Finally, the organic cations and the nanoscale integration of organic semiconducting materials and 2D lead-free perovskites offers numerous opportunities for the design of novel heterostructures beyond photovoltaics.

Chapter 7

Publications and Conference Contributions

7.1 List of Publications

Rik Hooijer*, Shizhe Wang*, Alexander Biewald, Christian Eckel, Marcello Righetto, Meizhu Chen, Zehua Xu, Dominic Blätte, Dan Han, Hubert Ebert, Laura M. Herz, Thomas Weitz, Achim Hartschuh, Thomas Bein, *Overcoming Intrinsic Quantum Confinement and Ultrafast Self-Trapping in Ag-Bi-I and Cu-Bi-I Based 2D Double Perovskites through Electroactive Cations*, *under review*.

Rik Hooijer*, Andreas Weis*, Waldemar Kaiser, Alexander Biewald, Patrick Dörflinger, Clément Maheu, Oleksandr Arsatiants, David Helminger, Vladimir Dyakonov, Achim Hartschuh, Edoardo Mosconi, Filippo De Angelis, Thomas Bein, *Cu/Ag-Sb-I Rudorffite Thin Film for Photovoltaic Applications*, Chemistry of Materials, **2023**, 35(23), 9988-10000.

Rik Hooijer, Andreas Weis, Alexander Biewald, Maximilian T. Sirtl, Julian Malburg, Rico Holfeuer, Simon Thamm, Amir Abbas Yousefi Amin, Marcello Righetto, Achim Hartschuh, Laura M. Herz, Thomas Bein, *Silver-Bismuth Based 2D Double Perovskites* $(4\,FPEA)_4AgBiX_8$ *(X= Cl, Br, I): Highly Oriented Thin Films with Large Domain Sizes and Ultrafast Charge-Carrier Localization*, Advanced Optical Materials, **2022**, 10(14), 2200354.

Maximilian T. Sirtl, **Rik Hooijer**, Melina Armer, Firouzeh G. Ebadi, Mahdi Mohammadi, Clément Maheu, Andreas Weis, Bas T. van Gorkom, Sebastian Häringer, René A.J. Janssen, Thomas Mayer, Vladimir Dyakonov, Wolfgang Tress, Thomas Bein, *2D/3D Hybrid* $Cs_2AgBiBr_6$ *Double Perovskite Solar Cells: Improved Energy Level Alignment for Higher Contact-Selectivity and Large Open Circuit Voltage*, Advanced Energy Materials, **2022**, 12(7), 2103215.

Maximilian T. Sirtl, Melina Armer, Lennart K. Reb, **Rik Hooijer**, Patrick Dörflinger, Manuel A. Scheel, Kristofer Tvingstedt, Philipp Rieder, Nadja Glück, Pallavi Pandit, Stephan V. Roth, Peter Müller-Buschbaum, Vladimir Dyakonov, Thomas Bein, *Optoelectronic Properties of $Cs_2AgBiBr_6$ Thin Films: The Influence of Precursor Stoichiometry*, ACS Applied Energy Materials, **2020**, 3(12), 11597-11609.

Shizhe Wang, Dan Han, Clément Maheu, Zehua Xu, Alexander Biewald, Hannah Illner, **Rik Hooijer**, Thomas Mayer, Achim Hartschuh, Hubert Ebert, Thomas Bein, *Room-temperature Synthesis of Lead-free Copper(I)-Antimony(III)-based Double Perovskite Nanocrystals*, APL Materials, **2023**, 11(4).

Ali Semerci, Ali Buyruk, Saim Emin, **Rik Hooijer**, Daniela Kovacheva, Peter Mayer, Manuel A. Reus, Dominic Blätte, Marcella Günther, Nicolai Hartmann, Soroush Lotfi, Jan P. Hofmann, Peter Müller-Buschbaum, Thomas Bein, Tayebeh Ameri, *A Novel Multi-Functional Thiophene-Based Organic Cation as Passivation, Crystalline Orientation, and Organic Spacer Agent for Low-Dimensional 3D/1D Perovskite Solar Cells*, Advanced Optical Materials, **2023**, 11, 2300267.

Armin Klumpp, **Rik Hooijer**, Nina Krüger, Jamila Boudaden, Florian Wolf, Markus Döblinger, Thomas Bein, *Study on the Properties of Wafer-scale Grown MoS_2 Deposited via Thermally Induced Chemical Vapor Deposition with $Mo(CO)_6$ and H_2S Precursors*, Materials Research Express, **2023**, 10(9), 095903.

7.2 Contributions to International Conferences

Materials for Sustainable Development Conference (MATSUS) | ***Talk*** March 2024

A Silver-Bismuth Based 2D Double Perovskite Solar Cell - Overcoming Intrinsic Quantum Confinement and Ultrafast Self-trapping — Barcelona, Spain

Materials Research Society (MRS) Spring Meeting | ***Talk*** April 2023

Synthetic Control of the Structural, Electronic and Optical Properties of Lead-Free Two-Dimensional Double Perovskites — San Francisco, USA

Hybrid and Organic Photovoltaics (HOPV) | ***Talk*** May 2022

Silver-Bismuth based 2D Double Perovskites $(4\,FPEA)_4AgBiX_8$ (X=Cl, Br, I): Highly Oriented Thin Films with Large Domain Sizes and Ultrafast Charge-Carrier Localization — Valencia, Spain